TECHNISCHE UNIVERSITÄT MÜNCHEN

Lehrstuhl E23 für Technische Physik

Walther-Meißner-Institut für Tieftemperaturforschung
der Bayerischen Akademie der Wissenschaften

Microwave circuit-electromechanics in a nanomechanical hybrid system

Fredrik J. Hocke

Vollständiger Abdruck der von der Fakultät für Physik der Technischen
Universität München zur Erlangung des akademischen Grades eines

Doktors der Naturwissenschaften

genehmigten Dissertation.

Vorsitzende: Univ.-Prof. Dr. N. Brambilla

Prüfer der Dissertation: 1. Univ.-Prof. Dr. R. Gross

                           2. Hon.-Prof. Dr. G. Rempe

Die Dissertation wurde am 08.07.2013 bei der Technischen Universität München eingereicht
und durch die Fakultät für Physik am 13.09.2013 angenommen.

*The most exciting phrase to hear in science, the one that heralds new discoveries, is not,
"Eureka!" ("I found it!") but rather, "Hmm... that's funny..."*
Isaac Asimov

Abstract

The young field of optomechanics focuses on the interaction of the quantized modes of a light field in an optical cavity with the vibrational modes of a mechanical oscillator. This gives rise to a variety of interesting phenomena such as cooling and amplification of mechanical motion. These effects are not limited to the purely optical domain, but can be transferred to the microwave regime by combining superconducting microwave resonators with nanometer-sized mechanical beams. In this way the new field of circuit nano-electromechanics has been established, which allows to couple the quantized modes of a microwave resonator to the vibrational modes of a mechanical system and thereby to do quantum mechanics with mechanical systems.

In this thesis, we present a comprehensive study on a microwave-nanomechanical hybrid device at millikelvin temperatures. It consists of a niobium/silicon nitride low loss nanobeam, capacitively coupled to the voltage node of a niobium microwave cavity establishing an on-chip all integrated electromechanical hybrid system.

A careful investigation of the mechanical degree of freedom shows that our system allows for the study of the mechanical loss mechanisms in nanobeams. In particular, the investigation of the nonlinear mechanical oscillation regime (Duffing regime) allows to extract the mechanical properties of nanobeams incorporating multiple material layers. The complete pre-characterization of the sample further includes the microwave cavity and the coupling mechanism between cavity and nanobeam establishing our electromechanical hybrid system. By application of frequency noise calibration we determine the electromechanical vacuum coupling including a calibration of the input wiring of the cryogenic setup. The experimental and theoretical investigation of the basic electromechanical phenomena including sideband cooling of the vibrational mode to an average occupation number of 13 confirms good control and detailed understanding of the system under study.

The extension of our experiments to two-tone spectroscopy allows for the detailed analysis of interference effects between a weak probe field and a strong drive field. We investigate two of the most prominent interference phenomena: Electromechanically induced transparency and absorption, leading to enhanced or reduced transmittance of the probe tone, respectively. Our comprehensive study includes the mapping of nonlinear mechanical motion into the microwave regime as well as the analysis of the impact of high mechanical oscillation amplitudes on the cavity resonant frequency.

We also investigate the dynamic properties of the system in the time domain, where the focus is on a direct measurement of the group delay and the switching dynamics of the induced transparency effect. The strong dispersive phase shift in the case of electromechanically induced transparency makes our device promising for the realization of group delays of microwave pulses of several $10\,\mathrm{ms}$. Exploiting this feature, we generate slow light with group velocities in the pedestrian regime. The achieved control over the propagation of microwave fields is not limited to classical light fields and offers the perspective to synchronize quantized microwave fields generated by spatially separated systems.

Time domain measurements of the ring up and ring down behavior of the nanobeam's amplitude reveal the counterintuitive fact that not the slowest dynamics in the device – the

mechanical ring down – limits electromechanical switching of the transmitted probe field, but the cavity's ring down time. Hereby, we provide the basis for complete storage and retrieval of a microwave quantum state in long-lived mechanical excitations, contributing to the study of quantum decoherence in macroscopic mechanical systems.

Zusammenfassung

Die Optomechanik ist ein junges Gebiet in der Physik, welches sich mit der Wechselwirkung zwischen den quantisierten Moden eines Lichtfeldes in einer optischen Kavität und den Vibrationsmoden eines mechanischen Oszillators beschäftigt.

Diese Kopplung manifestiert sich in einer Vielzahl an interessanten Effekten wie die Kühlung und die Verstärkung der Bewegung mechanischer Schwingungen. Dabei sind optomechanische Phänomene nicht nur auf den sichtbaren Spektralbereich beschränkt, sondern können auch auf den Mikrowellenbereich übertragen werden, indem ein supraleitender Mikrowellenresonator mit einer schwingenden mechanischen Saite auf nanometer Skala kombiniert wird. Dies hat das neue Feld der circuit (Schaltkreis) nano-Elektromechanik hervorgebracht, welches erlaubt die quantisierten Moden eines Mirkowellen-Resonators und die Vibrationsmoden eines mechanischen Oszillators zu koppeln und dadurch Quantenmechanik in mechanischen Systemen zu untersuchen.

In der vorliegenden Dissertation präsentieren wir eine umfassende Analyse eines solchen Mikrowellen-Nanomechanik Hybrid Systems bei millikelvin Temperaturen. Es besteht aus einer verlustarmen Niob/Silizium Nitrid Nanosaite, welche kapazitiv und den Spannungsbauch eines Niob Mikrowellenresonators gekoppelt ist, wodurch ein vollständig auf der Probe intergriertes elektromechanisches Hybridsystem entsteht.

Eine Sorgfältige Analyse des mechanischen Freiheitsgrades zeigt, dass sich unser System dazu eignet mechanische Verlustmechanismen in Nanosaiten zu untersuchen. Insbesondere zeigt eine Untersuchung des nichtlinearen mechanischen Verhaltens (Duffing-Regime), dass wir hiermit die mechanischen Eigenschaften von nano-Seiten bestimmen können, welche aus mehreren Materialschichten bestehen. Die vollständige Vorcharakterisierung der Probe schließt zusätzlich zum mechanischen Freiheitsgrad den Mikrowellenresonator und die Kopplungsmechanismen zwischen Resonantor und nano-Saite ein, woraus das elektromechanische System entsteht. Eine Kalibration des Frequenzrauschspektrums (frequency noise calibration) erlaubt es sowohl die elektromechanische Vakuumkopplung zu bestimmen, als auch die Eingangsleitung des kryogenen Aufbaus zu kalibrieren. Experimentelle und theoretische Untersuchungen von grundlegenden optomechanischen Phänomenen, einschließlich Seitenband-Kühlung des mechanischen Freiheitsgrades zu einer mittleren Besetzungzahl von 13, bestätigen die gute Kontrolle und detailliertes Verständnis des untersuchten Systems.

Die Erweiterung auf Zwei-Ton Spektroskopie ermöglicht eine detailierte Analyse von Inteferenzeffekten zwischen dem schwachen Mikrowellenfeld des Testtons und einem intensiven Feld eines Antriebstons. In diesem Zusammenhang wurden die prominenten Interferenz Phänomene der elektromechanisch induzierten Transparenz und Absorption untersucht, welche jeweils zu einer verstärkten oder reduzierten Transmission des Testtons führen. Unsere umfangreiche Untersuchung schließt das Abbilden von nichtlinearen mechanischen Effekten in den Mikrowellenbereich und den Einfluss von hohen mechanischen Amplituden auf die Resonanzfrequenz des Mikrowellenresonators ein.

Zusätzlich wurden die dynamischen Eigenschaften der induzierten Mikrowellentransparenz in der Zeitdomäne untersucht, wobei der Fokus auf dem direkten Nachweis von

Gruppenverzögerungen und die Schaltdynamik des induzierten Tranparenzeffekts liegen. Mit dem Transparenzeffekt geht ein stark dispersiver und über die Antriebsleistung einstellbarer Phasenschub einher, was das System zu einer guten Plattform zur Erzeugung von Gruppenlaufzeitverzögerungen von Mikrowellenpulsen im Bereich von mehreren $10\,\mathrm{ms}$ macht. Wir nutzen diese Eigenschaft um langsames Licht zu erzeugen, wobei die Gruppengeschwindigkeiten im Bereich von Fußgängern liegen. Zu bemerken ist, dass die Kontrolle über die Ausbreitungsgeschwindigkeit von Mikrowellenfeldern, welche wir erreichen, nicht auf klassische Felder beschränkt ist und die Aussicht quantisierte Mikrowellenfelder zu synchronisieren, welche von räumlich getrennten Systemen erzeugt werden, eröffnet.

Zeitdomänen-Messungen des Auf- und Abschwingverhaltens des Transparenzeffektes, verursacht durch die Amplitude der Nanosaite, zeigen die nicht erwartete Beobachtung, dass nicht die langsamste Zeitkonstante des Systems – das mechanische Abschwingen – elektromechanisches Schalten des Testfeldes begrenzt, sondern vielmehr das Abschwingverhalten des Mikrowellenresonators für die Dynamik begrenzend ist. Mit diesen Messungen legen wir den Grundsein für vollständiges Speichern und Wiederherstellen eines quantisierten Zustandes im Mikrowellenbereich in einer langlebigen mechanischen Anregung, was einen Beitrag zu Untersuchungen von Quanten Dekohärenz in makroskopischen mechanischen Systemen darstellt.

Contents

Chapter 1

Introduction

The nature of light has fascinated many generations of scientists. One of the most intriguing features of light is the transfer of momentum onto matter. The idea behind this phenomenon dates back to the 17th century when Kepler noted that comet tails point away from the sun[1]. Yet it took more than two centuries until Maxwell laid down the foundations of the so-called radiation pressure within his framework of electrodynamics [1].

The first experimental demonstration of radiation pressure with a torsional balance used as a light mill [2, 3] took place in 1901. With the advent of intensive coherent light sources in form of masers and lasers, the focus soon shifted from demonstration to utilization of radiation pressure. Hänsch and Shawlow [4] and almost at the same time Wineland and Dehmelt [5] recognized the ability of light to cool the vibrational modes of atoms and ions to the quantum ground state and proposed schemes to trap electromagnetic particles exploiting radiation pressure.

Within quantum mechanics on the other hand, the study of interactions between light and matter has developed to one of the most prominent fields in research called Quantum Optics, awarded with the Nobel prize in 2012. In this field, quantized modes of electromagnetic waves (photons) interact with atoms or ions via both their electric and magnetic dipole moment and thus a lot of effort is undertaken to prepare the atoms in states with a large dipole moment – the Rydberg state.

Together with the implementation of so-called laser cooling of microscopic particles mentioned above, the access to atomic systems with large dipole moments enabled the investigation of these particles in their motional ground state in optical cavities. The enhancement and storage of coherent light fields in cavities increased the probability of interaction between photons and the object under study due to the reduced photonic loss rate, allowing for repeated interactions before the photon leaves the cavity. In 1985, the strong coupling of light to atoms in the optical regime [6] (in the microwave regime, a Rabi splitting was observed in 1992 [7]) has been achieved, where the coupling rate is exceeding both the loss rates of the cavity and the atoms. This was the starting point of a successful new research direction in Quantum Optics called Cavity Quantum Electrodynamics (CQED). For a review of experiments in this field see Refs. [8, 9]. Besides the fundamental study of quantum mechanical properties of matter and light, quantum

---

[1]Although this effect inspired Kepler to think about the concept of radiation pressure, it is caused by solar winds.

optical setups are useful for applications in the field of quantum information. The long coherence times of atoms and ions allows us to implement quantum two-level systems (so-called quantum bits or qubits) and to use them for quantum information processing and storage. Ref. [10] draws a comparison of different atomic systems in this domain. Moreover, Photons are ideal candidates for so-called flying qubits allowing for coherent transfer of quantum information over a long distance.

The properties of atomic systems are predetermined by nature and cannot be tuned and designed for specific applications. This triggered another field of research aiming for the implementation of solid state circuits with discrete energy levels similar to the ones in atoms but tunable by design; so-called artificial atoms. Different realizations of such systems include superconducting loops with one or more Josephson junction, semiconductor quantum dots or defect states in solid state systems, reviewed and compared in Ref. [11]. With the advance in the realization of superconducting artificial atoms and microfabrication technology in mind, Blais *et al.* proposed to transfer the concepts already established in cavity QED to all integrated solid state systems operating in the microwave regime [12] using coplanar waveguide resonators as cavities and Cooper pair boxes as artificial atoms. In 2004, Wallraff *et al.* [13] implemented the concept of CQED by engineered solid state quantum circuits, starting a new research direction named circuit quantum electrodynamics (cQED). Refs. [14,15] review the ideas behind and the development in circuit quantum electrodynamics. Compared to the optical counterpart the coupling between qubit and photonic excitations is much stronger due to the large dipole moments associated with the much larger size of the artificial solid state atoms. Recently, even the ultra-strong coupling regime has been reached, where the coupling rate becomes of the same order of magnitude than the qubit and resonator transition frequencies [16]. Additionally, they offer more design flexibility and tunability since the system parameters can be engineered and tuned in-situ. On the other hand, on-chip superconducting qubits are not as well isolated from the environment as atomic systems in an optical trap. A comparison of both systems in terms of quantum computation is provided in Ref. [17].

Recently, more quantum systems have been coupled to microwave resonators, like quantum dots [18–21] or the spins in solid state systems [22–29] providing a new class of quantum hybrid systems. Of particular interest for quantum information processing is the coupling of superconducting qubits to spin systems. Here, superconducting qubits are used to implement a quantum processor due to their strong interaction with the environment while the long coherence times of spin systems enable storage of quantum information. Two proof of principle experiments couple a qubit directly to NV centers in diamond [30] or use a frequency tunable microwave cavity as a bus [31].

Coupling a superconducting qubit to a mechanical drum oscillator operating in the GHz regime allowed the first demonstration of quantized mechanical vibration [32], although in this experiment the mechanical decoherence time underruns the qubit decoherence time. Other experiments used a nanobeam to read out a qubit [33] and to parametrically amplify and squeeze the mechanical vibration by exploiting the nanobeam-qubit coupling [34]. Etaki *et al.* [35] suspended one side of a dc SQUID to detect the mechanical vibration and recently Pirkkalainen *et al.* [36] monitored the vibration of a mircobeam via a transmon qubit capacitively coupled to it.

Yet, to transfer quantum information over long distances, photons at optical wavelengths are unprecedented. Thus, a particular focus of research is to exploit the advantages

of systems working in different frequency regimes to bring quantum information processing and quantum computers into reach. In this context, a key requirement is a transducer, capable of (nearly) lossless, coherent transfer of quantum information between those systems. A good candidate is found within the relatively young field of optomechanics. Here, the photons inside a cavity couple parametrically to the position of a mechanical oscillator, allowing for coherent state transfer from the optical to the mechanical mode [37]. Thus, coupling two different optical modes to one mechanical oscillator allows for coherent state transfer between those modes [38–42]. In this thesis, we investigate optomechanics in a device operating in the microwave regime – a so-called electromechanical system – in the context of control over the propagation of microwave fields and the transfer of information to the mechanical mode.

In Chapter 2, we provide a brief historical overview on how optomechanics evolved. Hereby, we also review the zoo of realizations of optomechanical systems. The cryogenic apparatus in which the experiments take place is described in Chapter 3. We present our electromechanical system in Chapter 4, including a detailed pre-characterization of the microwave cavity, the suspended nanobeam forming the mechanical oscillator and the electromechanical coupling mechanisms. Basic optomechanical features are studied both on the theoretical and experimental side in Chapter 5. We investigate electromechanical linewidth broadening, the optical spring effect and cooling of the mechanical mode. We also estimate the electromechanical coupling and the detection sensitivity of the mechanical amplitude. In Chapter 6 we analyze interference effects called electromechanical induced transparency (EMIT) and absorption (EMIA) for our device in a two-tone configuration, where a strong drive field manipulates the transmission of a weak probe field. We further use this configuration to demonstrate the mapping of mechanical nonlinearities into the microwave regime and to investigate the cavity sidebands and the Kerr-like cavity resonance shift as a consequence of high amplitude mechanical motion. The discussion of a two-tone configuration is shifted to time domain in Chapter 7. We exploit the strong dispersion coming along with EMIT to control the propagation of probe pulses and demonstrate slow light in the microwave regime in an electromechanical system. By switching the drive tone, we further investigate the switching behavior in our electromechanical device and hereby reveal the counterintuitive fact that the probe field's switching dynamics is not limited by the slow decay of the mechanical amplitude. A discussion of the results in context of the progress in the field of opto-/electromechanics is given in Chapter 8.

Chapter 2

Optomechanics – An overview

In this Chapter, we summarize the history of experiments and accompanying theory developing optomechanics to an own field within physical research. To demonstrate the vast of different devices obeying the optomechanical Hamiltonian, we present a few realizations of optomechanical systems. Further, we give an overview over some of the most important achievements of the last years, demonstrating the rapid progress within this field. Since the mechanical oscillator in our device is a doubly clamped nanobeam, we end the Chapter with a brief review of nanomechanics, the second field of research accessible with our system geometry.

2.1 Historical overview

The foundations of optomechanics were developed by Braginsky in 1970 [43] observing the influence of mechanical vibrations inside a microwave cavity onto the intra-cavity light field. Later Braginsky and coworkers embedded this into a theory of quantum non-demolition (QND) measurements in the context of gravitational wave detection [44], where a light field inside a cavity exerts dynamical backaction on a suspended mirror (as depicted in Figure 2.1):

The photons inside a cavity transfer momentum onto the suspended mirror. The movement of the mirror periodically changes the length of the cavity, subsequently changing its resonance frequency. For a fixed input field, this modulates the number of intra-cavity photons. A parametric coupling between the photonic mode and the position of the mirror is established. The vibration of the mirror can be observed by spectral analysis of the response of the cavity, allowing for high precision readout of the mechanical mode [45–49].

Braginsky also recognized that the retarded nature of the force acting on the mirror can be used to cool or amplify the mechanical motion. The photons inside the cavity either lead to positive or negative damping of the vibration, what Braginsky demonstrated experimentally in 1970 [43]. The influence of pondermotive quantum noise, ultimately limiting the readout precision of the mechanical mode was theoretically addressed in 1981 by Caves [50].

Only some experiments studied this type of coupling [51–53] until in the 1990's theoretical studies of optomechanical effects including QND measurements of the intra-cavity photon number [54,55], the reduction of quantum noise [56,57], the generation of nonclas-
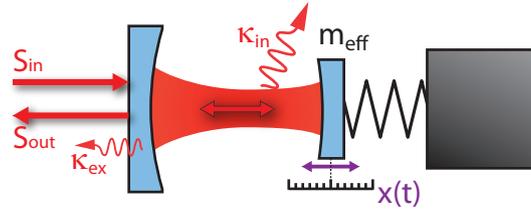
Figure 2.1: Schematic of an optomechanical system. A Fabry-Perot cavity with one vibrating
mirror (with effective mass m_{eff}) couples the number of photons inside the cavity to the mirror
position. An input field S_{in} populates the cavity. The emitted field S_{out} leaving the cavity due
to the finite coupling κ_{ex} to the external light field carries information about the mechnical
position $x(t)$. The internal dissipation of light into the environment is defined by κ_{in}.

sical states [58, 59] and the cooling of the mechanical mode via feedback [60] impressively
demonstrated some of the various phenomena in optomechanics and triggered new experiments.

Cohadon *et al.* demonstrated feedback cooling of the vibrations of an end-mirror
in in 1999 [61]. This effect was later transferred to low temperatures in the range of
several Kelvin [62, 63] with smaller mirrors, cooling the mechanical mode to an effective
temperature in the millikelvin regime. These experiments were the first in a series to cool
the vibration of a macroscopic object close to the quantum ground state.

Scientists started to study optomechanical interaction between radiation inside a cavity
and a mechanical degree of freedom in devices different from the standard Fabry-Perot
cavity, showing that optomechanical physics resides in a huge variety of systems. Here,
one aspect of optomechanics becomes obvious: The possibility to realize at first sight
completely different samples, working in different frequency regimes considering the optical
and mechanical frequencies but still obeying the same (optomechanical) Hamiltonian.

The optomechanical capabilities of microtoroids were demonstrated by investigation of
the parametric instability of the breathing mode in these devices in 2005 [64–66]. Coupling
a cantilever [67] and a nanobeam [68, 69] to an LC-resonator transferred optomechanics
to electronic systems in 2007, establishing cavity nano-electromechanics. The coupling
of the collective vibrational mode of a Bose-Einstein-Condensate (BEC) to the light field
of a cavity in 2008 [70, 71] triggered cavity optomechanics with ultracold atomic systems
offering the lowest effective mass of the mechanical mode.

2.2   Overview of optomechanical systems

We show some realizations of optomechanical systems with mechanical masses ranging
from the kilogram scale down to the zeptogram scale, a range of more than 20 orders of
magnitude. Although we cover most principal realizations, the list is far from complete.
For a recent, more detailed review of different sample geometries see Ref. [72].

Figure 2.2 shows different optomechanical systems. The colored boxes indicate one
specific system class.

Fabry-Perot cavity: The most generic optomechanical system is a single sided Fabry-
Perot cavity. The orange box in Figure 2.2 shows three mechanical oscillators used
in such a geometry though their masses are separated by ten orders of magnitude:
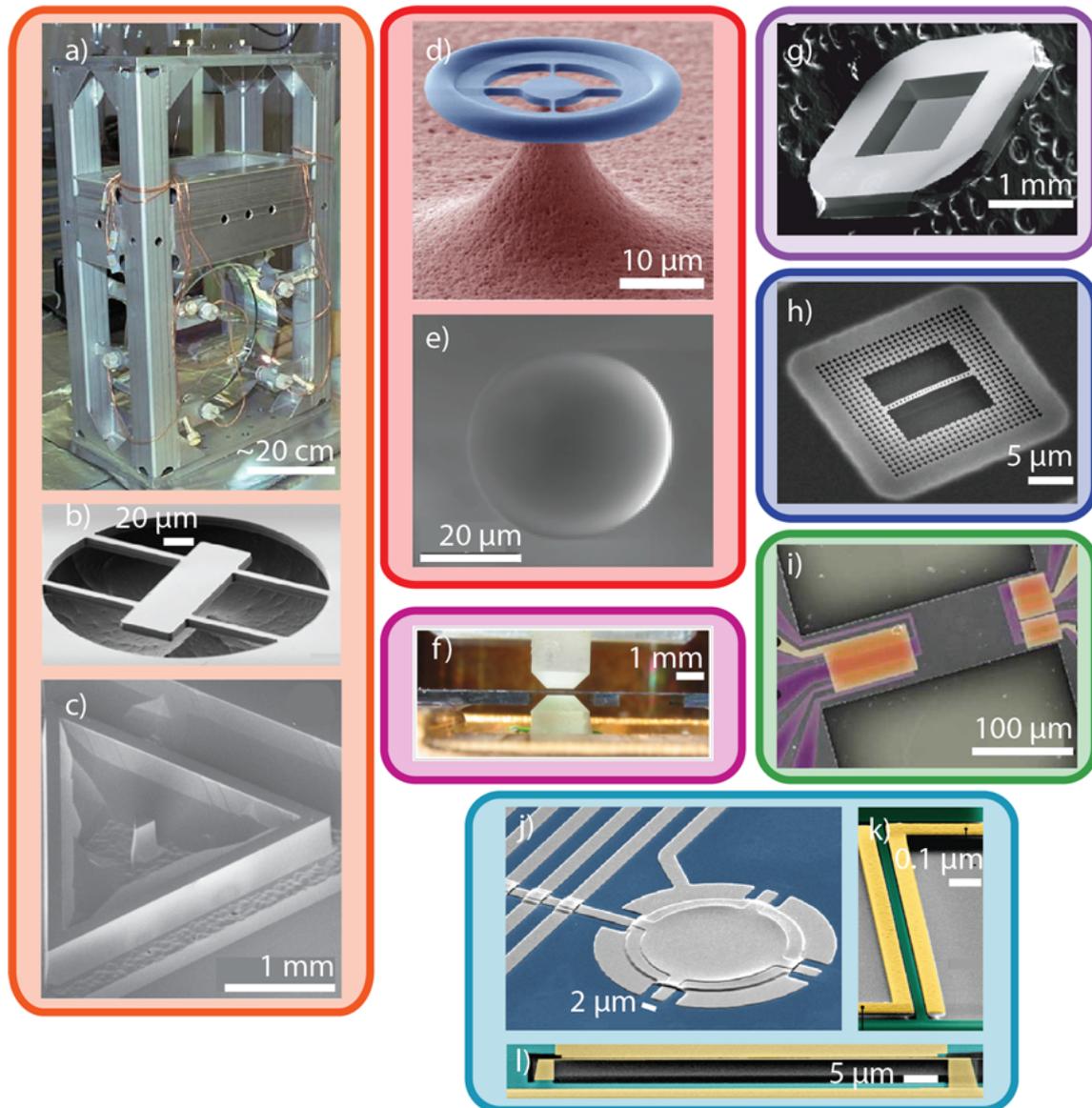
Figure 2.2: Overview of different optomechanical systems. For more details see the main text. Sources of the Figures: a) "`http://www.sr.bham.ac.uk/gwgroup/sounds_of_space/press_info/photos/`", b) Ref. [73], c) Ref. [74], d) Ref. [75], e) Ref. [76], f) "`http://ultracold.physics.berkeley.edu/pmwiki/Main/E3`", g) Ref. [77], h) Ref. [78], i) Ref. [79], j) Ref. [80], k) Ref. [81], l) Ref. [82].

Figure 2.2a presents a photo of a suspended mirror with a mass of 40 kg used for gravitational wave detection in the laser interferometer gravitational-wave observatory (LIGO) [83]. In Figure 2.2b we show a micromechanical free-free suspended mirror [73]. Figure 2.2c shows an optical cavity quartz micropillar, supported by a membrane, forming the vibrating end of a Fabry-Perot cavity [74].

Whispering gallery mode cavity: A different type of optical cavity is shown in the red box in Figure 2.2. Here, the light is stored in a closed loop by total internal reflection, a so-called whispering gallery mode named after the effect in St. Pauls cathedral in London. The whole cavity performs breathing-like mechanical oscillations, what effectively changes the length of the loop providing the parametric coupling between

optical and mechanical mode. In Figure 2.2d we show a micro-toroid [75], in Figure 2.2e a microsphere [76]. These systems have a lower mode volume than free-space cavities giving high optomechanical single photon couplings.

Atomic cloud inside a cavity: The vibrational mode of a BEC influences the light field inside an optical cavity as well. One can show that this configuration forms an optomechanical system. A photo of the optical cavity including the atom chip to trap the cold atoms is shown in Figure 2.2f. The collective motion of the atomic cloud forms the mechanical oscillator with the smallest mass of up to a million atomic masses. Here the mechanical mode is already in the ground state, enabling the observation of quantum backaction to the light [84].

Membrane in the middle: Placing a dielectric membrane as shown in Figure 2.2g (purple box) inside a Fabry-Perot cavity can generate an optomechanical coupling [85] or a quadratic coupling [77] depending on whether the membrane is placed in a node or antinode of the standing light field, respectively. Membranes are promising tools to couple an optomechanical system working in the optical regime to a system in the microwave regime [39].

Photonic crystal cavity: Manipulation of the refractive index in a material (typically silicon) by periodic structures on a size smaller than the light field's wavelength allows to store light fields inside these structures, called photonic crystal cavities. A suspended photonic crystal cavity changes its refraction index additionally due to stress generated by the vibrations of the structure. Here a coupling to longitudinal vibrations allows for analysis of high Q mechanical modes in the GHz regime. Figure 2.2h (blue box) shows such a system, including perforation of the supports to suppress leakage of mechanical excitations into the substrate [86].

Phonon-cavity electromechanics: An optomechanical system without optical cavity has been implemented by Mahboob *et al.* [79], see Figure 2.2i. Here, the optical mode is replaced by a second vibrational mode. Tension due to the mechanical oscillation couples both mechanical modes, proving that the physics of optomechanics is not limited to cavities storing photonic excitations.

Optomechanics in the microwave regime – Circuit electromechanics: The light blue box in Figure 2.2 shows systems working in the microwave regime. Here the cavity is an electric LC-oscillator. Systems working in this regime are called electromechanical systems. The mechanical oscillator is coupled to the cavity by manipulating its overall capacitance. It is easy to show that these systems follow the optomechanical Hamiltonian. Figure 2.2j shows an electromechanical system with a mechanical oscillator provided by the vibrations of the top of a plate capacitance of a lumped element microwave cavity [80]. The image in Figure 2.2k shows a suspended silicon nitride nanobeam (green) modulating the capacitance between two gold wires (yellow) due to changes of the dielectric constant inside the capacitor [81]. In contrast to most electromechanical systems, this structure does not require low temperatures. The microwave cavity consists out of copper, giving a low quality factor but allowing for measurements at room temperature. Figure 2.2l shows a nanobeam made from a silicon nitride/niobium sandwich structure [82,87], coupled

to the center conductor of a coplanar waveguide microwave cavity. Together with the ground plane, the nanobeam forms a capacitor modulating the cavity resonance frequency.

2.3   Experimental achievements

The zoo of different opto- or electromechanical systems leads to a rapid progress in exploring the physical phenomena. Reviews of optomechanics are found in Refs. [39, 72, 88–92].

The first demonstration of microtoroids as optomechanical systems in 2005 explored the regime of mechanical self oscillations [64–66]. A blue detuned drive tone reduced the mechanical damping until the mechanical motion becomes undamped allowing for the observation of phonon lasing [52, 53, 93–99].

In 2006 three groups demonstrated optomechanical cooling of the mechanical mode by radiation pressure [100–102]. On the theoretical side, a quantum description of optomechanical cooling was derived and the limits were studied depending on system parameters [103–105] and on technical limitations [106–108].

Although low occupation numbers of the mechanical mode were reported before [47, 76, 109–111] and the strong coupling limit was reached showing normal mode splitting [80, 112], it took until 2011 before cooling of the mechanical motion close to the ground state (what means an average mechanical occupation less than one) was reported independently in an electromechanical system [113] and in an optomechanical photonic crystal structure [78]. The sideband asymmetry of Stokes and anti-Stokes scattered light due to the low mechanical occupation is studied in [114].

Two-tone spectroscopy experiments successfully demonstrated optomechanically induced transparency [80, 87, 115, 116], predicted by Agarwal and Sumei [117] and optomechanically induced absorption [82, 116]. Here two excitation pathways from a pump and a probe tone interfere inside the cavity resulting from the coupling to the mechanical mode. As a consequence the transmission of the probe tone is either enhanced for a red detuned pump tone (transparency effect) or reduced for a blue detuned pump tone (absorption effect), respectively. These effects are the optomechanical analogues to electromagnetically induced transparency [118] and absorption [119] in atomic media. The effective interaction Hamiltonian on the blue sideband allowed to generate a mechanical parametric amplifier from an electromechanical system [120].

Inspired by the generation of slow light by induced transparency in atomic systems [121–124], two teams generated group delays of light pulses in an optomechanical and an electromechanical system [87, 116]. Optomechanical arrays are predicted to increase the delays, eventually leading to stopping of light pulses [125].

Optomechanis with pulsed schemes attracted a growing interest recently. Principally, pulsed schemes can be used to generate entanglement between optical and mechanical states [126], optimize cooling [127] or to perform a state tomography and squeezing of the mechanical state [128]. Vanner *et al.* [129] recently demonstrated tomography of a vibrating mirror in the classical regime.

Pulsed multi-tone spectroscopy offers access to the dynamics of optomechanical systems. The study of the switching dynamics of a continuous probe tone for a pulsed drive field reveals that the long mechanical coherence times impose no limit of the transmission dynamics [87].

Schemes with pulsed drive and probe fields induce the transfer of quantum information between optical and mechanical mode, an effect of high interest in connection with quantum decoherence in macroscopic systems [72]. On the other hand it offers practical use in storing quantum information in mechanical systems due to their long coherence times. Experiments have demonstrated the first necessary steps towards the transfer of a quantum state to mechanical excitation [37, 75, 130, 131].

As mentioned in the beginning, coupling a mechanical mode to two cavities operating at different frequencies will allow coherent state transfer between the cavities [39–42]. First proof of principle experiments show the transfer of classical, coherent light between two modes of one optical cavity [132, 133].

2.4   Nanomechanics

Besides contributing to the rapid progress in the domain of optomechanics, the electromechanical system studied in this work (see Figure 2.2l) gives opportunity for research in a second field; the behavior of nanomechanical oscillators, here in the form of a doubly clamped nanobeam. For a review focusing on mechanical oscillators in different hybrid structures see [134]. Further reviews of the advances in nanomechanics are provided by Refs. [135–137].

One focus is the understanding of damping mechanisms in these devices [138–145], identifying various mechanisms:

Viscous damping of mechanical vibrations in a gas or fluid environment [146, 147], phonon-phonon interaction and so-called thermoelastic losses originate from redistribution of phonons due to different thermal equilibria of the surfaces of bent materials [148–151]. Depending on the expansion coefficients of the nanobeam and the underlying substrate, the eigenfrequency and Q-factor changes [69, 152] with decreasing temperature. The anchoring of mechanical oscillators provide the loss mechanism that fundamentally places a lower bound to the dissipation by phonon tunneling into the clamps and the substrate [141, 151, 153–159]. Strategies to minimize these losses include free-free clamping of the beam [160] or structuring of the substrate to prohibit phonons with the beam's resonance frequency in these areas [78]. Another loss mechanism is the interaction of mechanical excitation with intrinsic two level systems in the material [161–166].

Moreover, mechanical oscillators offer a platform to study the nonlinear regime of mechanical vibrations. For example, the Duffing regime accessible in various systems [164, 167–173].

A light field in close vicinity to a nanobeam driving the mechanical motion gave insight to phononic heat transport in solids [153, 174]. Intrinsic amplitude and frequency noise attracted interest with the advance of high quality factor oscillators [175]. Here, doubly clamped highly stressed silicon nitride nanobeams offer high Q-factors [176–178] up to seven million at room temperature [144].

One team coupled two nanobeams to study chaotic behavior [179]. Noise squeezing of mechanical modes, reviewed in [180, 181] reduce the noise properties and are promising building blocks for electronic clocks.

Multiple vibration modes are present in most nanomechanical structures. The embedding of a dielectric nanobeam into a microwave cavity [182] or strong driving of one mode [183] was found to generate coupling between two modes. As mentioned above,

this coupling allows to build a purely electromechanical system where one vibration mode replaces the optical cavity [79].

Coupling to other systems like the spin of a silicon nitrogen vacancy [184] provides a new family of hybrid systems. Nanomechanical systems have also been used as platform for implementations like the mechanical analogue of a laser [99,185], mechanical bit [186] or memory operations [187], thermometry [188] and audio mixing [189]. Scientists have demonstrated a broad range of sensing applications with mechanical oscillators like ultra sensitive mass sensing [190–193], detecting changes in magnetization [194], spin flips [195] or mutations in RNA [196].

Chapter 3

Cryogenic setup

Systems incorporating on-chip high-Q microwave cavities require low temperatures. First, these devices are usually made from superconducting materials like niobium or aluminum. Second, the energies of photons in the microwave regime correspond to temperatures in the millikelvin regime (a photon with a frequency of $1\,\text{GHz}$ corresponds to approximately $50\,\text{mK}$). To avoid thermal population of the cavity, the experimental temperature needs to be below the equivalent single photon temperature.

Although it is impossible to cool a mechanical oscillator working in the MHz regime into its ground-state as achieved with a bulk dilatational resonator with GHz eigenfrequencies [32], low temperatures allow for a reduction of mechanical quanta to the range of hundreds. An ideal experimental environment provides a temperature as low as possible for arbitrarily high drive powers. Actual setups compromise between high input power and low temperatures.

The experiments discussed in this thesis were performed at temperatures between 30 and $600\,\text{mK}$, far below the critical temperature of niobium ($T_\text{c} = 9.2\,\text{K}$).

3.1   Cryostat No.1

Dilution fridge No.1 with an actual base temperature of $80\,\text{mK}$ was completely designed and constructed at the WMI, focussing initially on transport experiments at millikelvin temperatures in magnetic fields. To allow for measurements in the frequency regime of GHz, we modified the setup to increase the volume of the vacuum chamber at $4\,\text{K}$ containing the still and the mixing chamber. The additional space allows to include coaxial high frequency cables, attenuators a bias-tee, a circulator and a low noise high electron mobility transistor (HEMT) amplifier. Additionally a thermal shield anchored at the still protect the mixing chamber from radiation. The temperature of the device is recorded by an in-house calibrated temperature sensor.

Figure 3.1 shows photos of the microwave (MW) setup of the fridge and a schematic wiring scheme. Three coaxial stainless steel cables guide signals in and out of the fridge. The input line directs the microwaves to the device. To thermalize the center conductor and to suppress thermal noise, it is attenuated by $20\,\text{dB}$ at $4\,\text{K}$. The $10\,\text{dB}$ attenuators at the still and the mixing chamber further thermalize the inner conductor and reduce the number of thermal photons applied to the sample. A bias-tee (UMTCC BT-S000-
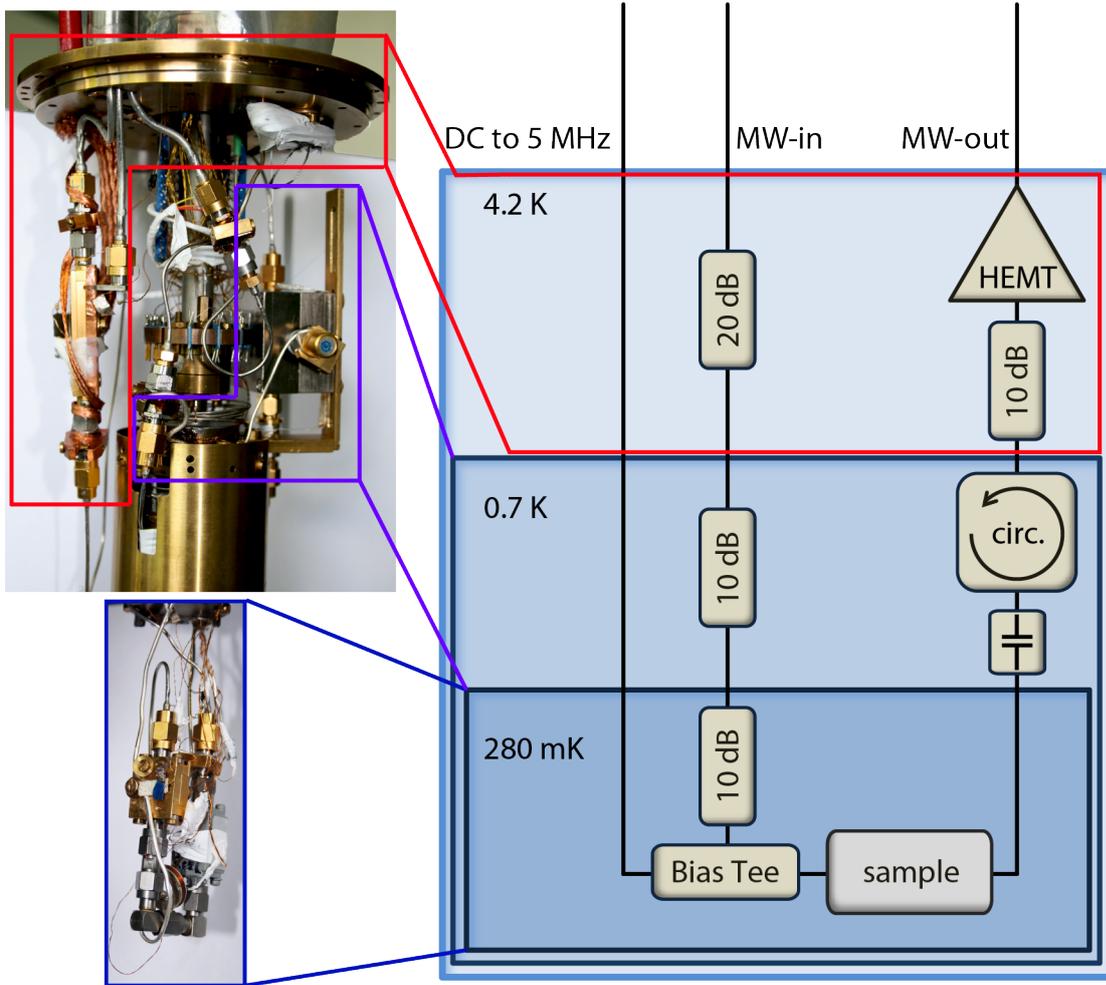
Figure 3.1: Schematic of the wiring of cryostat No.1. See the main text for further details.

HS) at the mixing chamber stage allows to combine the microwave input signals with a low frequency tone of up to $2\pi \times 200\,\mathrm{MHz}$. In total we estimate an overall attenuation of $59\,\mathrm{dB}$, distributed over the attenuators ($40\,\mathrm{dB}$), the bias tee ($10\,\mathrm{dB}$) and the cables ($9\,\mathrm{dB}$). This value is in agreement[1] with the calibration obtained from the measurement of the coupling constant g_0 detailed in Section 5.2.2 together with the measurement of the mechanical linewidth broadening in an EMIT configuration, discussed in Section 6.1.4.

For the DC-line, we estimate an overall attenuation of $70\,\mathrm{dB}$ at a frequency of $2\pi \times 1.45\,\mathrm{MHz}$ typically used to drive the nanobeam. Here the bias-tee contributes with an attenuation of approximately $60\,\mathrm{dB}$.

After transmission through the sample and a DC-block (minicircuits BLK-18-S+), a circulator (QuinStar CTH0408KCS) with one output terminated with a $50\,\Omega$ connector protects the experiment from noise stemming from the HEMT-amplifier. A $10\,\mathrm{dB}$ attenuator at $4\,\mathrm{K}$ prevents the following amplifier from saturation. The HEMT amplifier (Low Noise Factory LNF-LNC4_8A) is anchored at $4\,\mathrm{K}$ and amplifies the signal by $40\,\mathrm{dB}$. a low noise temperature of approximately $3\,\mathrm{K}$. Not shown in Figure 3.1 is a second HEMT amplifier at room temperature amplifying the signal again by $30\,\mathrm{dB}$.

---

[1]Note, that the value stated in the discussion of the experimental calibration includes the room temperature wiring.
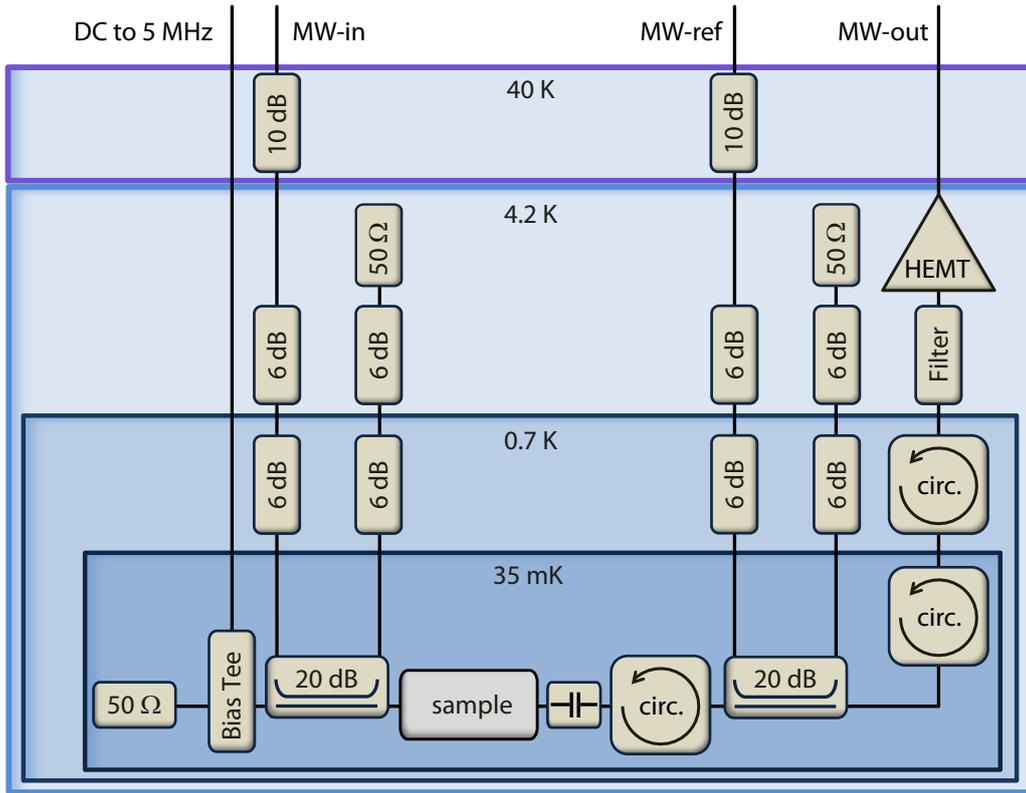
Figure 3.2: Schematic of the wiring of cryostat No.2. See the main text for further details

3.2   Cryostat No.2

The second dilution fridge used in this thesis is a commercial Oxford TRITON dilution fridge with a base temperature of 30 mK. This cryostat is a so-called dry dilution fridge, meaning that it works without the need of being supplied with cryogenic liquids [197]. Accompanied by the advantage of continuous operation without the need of refilling the cryogenics, it offers an tremendously increased space on all temperature stages.

The wiring of the high frequency lines is similar to fridge No.1, but owing to the increased space we implemented additional microwave components as schematically shown in Figure 3.2.

Again, a DC-line is fed to a bias-tee (UMTCC BT-S000-HS) used to apply low frequency signals and to thermalize the center conductor. The MW-input of the bias-tee is terminated with $50\,\Omega$.

The signal line ("MW-in" in Figure 3.2) consists of multiple connected coaxial cables spanning from one temperature stage to the next one. We use less attenuation than compared to the first setup, but the built in connectors add additional 20 dB of attenuation. To minimize the heat load on the mixing chamber when using high microwave drive powers, the signal is fed into a directional coupler (MITEQ-Estonia CPL4000-8000-20-C) transmitting most of the signal back to the 4 K stage where it is terminated. Attenuators prevent thermal noise from reaching the mixing chamber. The fraction of $-20\,$dB is fed into the signal line coming from the bias-tee. A DC-block (minicircuits BLK-18-S+) after the sample box again prevents a current from flowing when a DC-voltage is applied.

After transmission through the sample box, a second input line ("MW-ref" in Fig-

ure 3.2), set-up completely analogous to the first one, feeds a reference tone with an adjusted phase and power to annihilate the drive signal by destructive interference. However, all information from interaction with the sample is preserved. The electromechanical interaction of microwave cavity and mechanical oscillator generates additional frequency contributions to the drive tone that will not be annihilated by interference with the reference (for a more detailed discussion of the measurement, see Section 5.1). This part of the setup is particulary important when operating with high drive powers to prevent saturation of the amplifier.

To prevent the reference tone from interaction with the sample, a circulator (QuinStar CTH0408KCS) is placed between sample and reference line.

Note, that no experiments presented in this thesis were performed at microwave power levels sufficiently high to saturate the amplifier and thus we did not use the reference input.

Two additional circulators of the above type anchored at the mixing chamber and the still further isolate the sample from thermal noise and backscattering of photons from the amplifier. A bandpass filter (minicircuits MC-VBFZ-5500+) blocks low frequency contributions that arise when driving the mechanical mode via the "DC" input.

At $4\,\mathrm{K}$, a low noise HEMT amplifier (Low Noise Factory LNF-LNC4_8A) amplifies the signal before it leaves the cryostat. Again, not shown in Figure 3.2 is a second HEMT amplifier at room temperature amplifying the signal by $30\,\mathrm{dB}$.

Chapter 4

Sample fabrication and pre-characterization

In Chapter 2 we have presented different realizations of opto- and electromechanical systems. Here, we first discuss the analogy between optomechanics and electromechanics. We then present the system studied in this work, including the design, the production steps and sample parameters. Further, we characterize in detail the microwave cavity, give an approximation of the electromechanical coupling based on the sample geometry and study the nanobeam. A study of its temperature dependence reveals that coupling of phonons to two level systems (TLS) provide the most prominent loss mechanism, also influencing the mechanical eigenfrequency. Driving of the mechanical resonator to high amplitudes provides access to the so-called Duffing regime, helping to extract effective material parameters of the nanobeam's double layer structure.

4.1   From optomechanics to electromechanics

At first sight the capacitive coupling of a mechanical oscillator to a LC-circuit has no similarities to a Fabry-Perot cavity with a vibrating mirror or other optomechanical systems. Here, we discuss the analogy of the coupling between "optical" and mechanical degree of freedom, albeit the fact that both cavities operate at different frequencies and employ different concepts to enhance the intra-cavity field.

Essential for an opto-/electromechanical system is the parametric coupling between "optical" and mechanical mode. Hereby, the intra-cavity photon number couples to the position of the mechanical oscillator, allowing for, among other effects, cooling/amplification of the mechanical mode or precise monitoring of the vibration (see one of the reviews [39, 72, 88–92] for more details on the consequences of an opto-/electromechanical coupling). From the point of the cavity, such a coupling implies a linear change of the optical eigenfrequency $\widetilde{\omega}_\mathrm{c}$ with the mechanical amplitude x depending on the coupling constant G:

$$\omega_\mathrm{c}(x) = \widetilde{\omega}_\mathrm{c} - \frac{\partial \widetilde{\omega}_\mathrm{c}}{\partial x} x \equiv \widetilde{\omega}_\mathrm{c} + Gx \ . \tag{4.1}$$

The Hamiltonian describing the coupled system reads [198]:

$$\hat{H} = \hbar\widetilde{\omega}_\mathrm{c} \left(\hat{n}_\mathrm{c} + \frac{1}{2} \right) + \hbar\Omega_\mathrm{m} \left(\hat{n}_\mathrm{m} + \frac{1}{2} \right) + \hbar G \hat{n}_\mathrm{c} \hat{x} \ . \tag{4.2}$$

Figure 4.1: Schematic showing an optomechanical system as a single sided Fabry-Perot cavity with one vibrating mirror (left) and a equivalent circuit scheme of an elecromechanical system (right). The input and output fields are indicated by S_{in} and S_{out}, respectively. The losses into the environment and into the feeds are indicated by κ_{in} and κ_{ex}, respectively. Both systems are described by the same Hamiltonian defined in equation 4.2.

Here, $\bar{n}_{\text{c}}$ is the photon number operator, $\hat{x}$ the mechanical position operator and Ω_{m} the mechanical resonance frequency. We discuss the Hamiltonian under different aspects in the following chapters.

For a generic optomechanical system consisting of a Fabry-Perot cavity with one movable mirror as shown on the left side in Figure 4.1, it is easy to see that the eigenfrequency scales linearly with small displacements of the mirror. In contrast, for most other systems it is typically more subtle to understand the mechanism and the functional dependence of the optical frequency change induced by the mechanical amplitude.

In the following of this thesis, we will focus on a system consisting of a coplanar waveguide microwave (CPW) cavity coupled to a vibrating nanobeam. An equivalent circuit diagram is shown on the right side in Figure 4.1. The microwave cavity is represented as a grounded LC-oscillator with overall inductance L and overall capacitance C, coupled to a feedline via a coupling capacitance C_{ex}. The nanobeam forms an additional capacitance together with the opposite ground plane, coupled parallel to the circuit. Figure 4.2 shows false colored images of the actual device studied in this work, showing a top view of the microwave cavity (a), a top view of the nanobeam (b) and a tilted zoom to the nanobeam's clamping region (c). Considering that the eigenfrequency of the "optical" mode is proportional to the $1/\sqrt{C}$ [199] and identifying the nanobeam as one side of a plate capacitance $C_{\text{g}}(x)$ according to the right side in Figure 4.1 allows to review the coupling in this system. We write the eigenfrequency of the μ-wave cavity as follows:

$$\omega_{\text{c}}(x) = \frac{1}{\sqrt{L(C + C_{\text{g}}(x))}} = \widetilde{\omega}_{\text{c}} \frac{1}{\sqrt{1 + C_{\text{g}}(x)/C}} \ , \tag{4.3}$$

The resonance frequency of a bare microwave cavity without a nanobeam is called $\widetilde{\omega}_{\text{c}}$ in this work. Further, we have ignored the contribution of C_{ex} from coupling the cavity to the feed line, as this capacitance is almost three orders of magnitude smaller than the overall capacitance C. We find for a series expansion (valid as long as $C_{\text{g}}/C \ll 1$) of Equation (4.3) to first order in the the displacement x

$$\omega_{\text{c}}(x) = \widetilde{\omega}_{\text{c}} \left(1 - \frac{1}{2C} \frac{\partial C_{\text{g}}}{\partial x} x \right) = \widetilde{\omega}_{\text{c}}(1 - \text{const} \cdot x) \ . \tag{4.4}$$

For small amplitudes, the cavity eigenfrequency changes linearly with the displacement. Therefore, this is the electric counterpart of an optomechanical system; a so-called electromechanical system. The prefactor of x in Equation (4.4) multiplied with $\widetilde{\omega}_{\text{c}}$ defines the
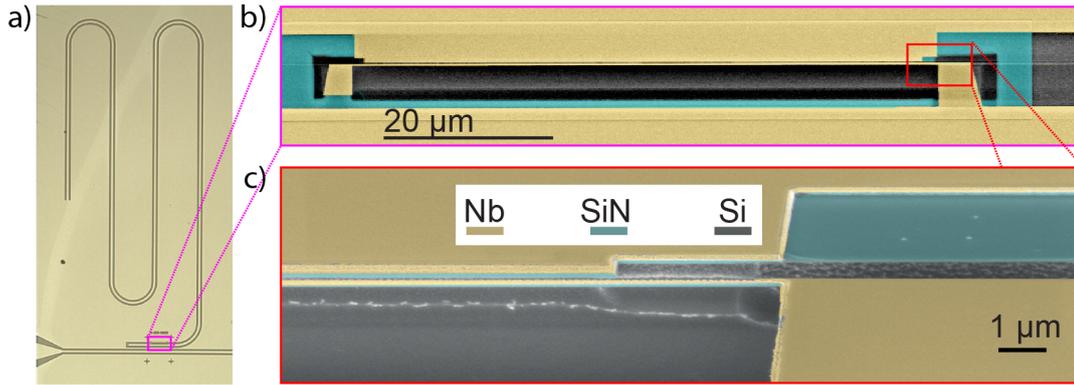
Figure 4.2: An optical micrograph of the μ-wave cavity is shown in a). b) shows a false colored scanning electron microscope image of a zoom to the voltage antinode revealing the mechanical resonator. The tilted view of the clamping section of the nanobeam in c) shows the undercut and the nanobeam's two layer structure. Yellow colored areas are niobium, green indicates silicon nitride and grey the silicon substrate.

electromechanical coupling constant G. We will derive an expression for G in Section 4.4. Before turning to the individual components of our electromechanial device, we present an overview over relevant device parameters including the design and materials system:

The circuit nano-electromechanical device studied in our experiments is a hybrid system, consisting of a superconducting CPW microwave resonator and a nanomechanical beam, capacitively coupled to the center conductor of the microwave resonator at the voltage antinode (see Figure 4.2). Our nano-electromechanical system is similar to that studied by Regal *et al.* [69]. However, in contrast to the purely metallic nanobeams (Al) in [69], we use nanobeams consisting of Nb/Si_3N_4 bilayers to increase the resonant frequency and the quality factor of the mechanical oscillator. Furthermore, the superconducting CPW resonator is made of Nb with a high critical temperature of $9.2\,$K, resulting in a higher internal quality and lager critical photon number of the microwave resonator. The latter is fabricated by patterning a quarter-wave CPW structure into a $130\,$nm thick Nb film, which has been deposited on a silicon substrate by sputter deposition [16, 200] (see Section 4.2 for more details). The resonator is capacitively coupled to a $50\,\Omega$ CPW feedline at one end and shortened at the other (one-sided cavity, see Figure 4.2a and Figure 4.6). By choosing the resonator length an eigenfrequency of $\widetilde{\omega}_c/2\pi = 6.07\,$GHz is obtained. We note that the resonant frequency $\widetilde{\omega}_c$ also depends on the additional capacitances C_g and C_{ex} due to the capacitive coupling to the nanomechanical beam and the feedline, respectively. The coupling to the feedline results in a coupling rate of $\kappa_{ex}/2\pi = 339\,$kHz. Comparing this coupling rate to the measured cavity linewidth (total loss rate) of $\kappa/2\pi = 759\,$kHz yields a coupling rate $\eta_c = \kappa_{ex}/\kappa \simeq 0.45$ close to the critical coupling $\eta_c = 1/2$ where the best contrast is obtained. The corresponding quality factors are $Q = 7910$ and $Q_{ex} = 17535$ (see Section 4.3 for more details).

The nanomechanical resonator (NR) consists of a Nb/Si_3N_4 nanobeam which is clamped on both ends (see Figure 4.2b). The Nb/Si_3N_4 bilayer shown in Figure 4.2c is fabricated out of a $130\,$nm thick Nb film sputtered on top of a $70\,$nm thick layer of highly strained (tensile) Si_3N_4 layer, grown by low pressure chemical vapor deposition on a silicon wafer. The beam has a high aspect ratio with a length of $60\,\mu$m and a width of $140\,$nm. The structure is patterned by electron beam lithography, followed by an anisotropic and an isotropic

reactive ion etching process [87] (see Section 4.2 for more details). The high tensile strain in the Si_3N_4 layer accounts for a high mechanical eigenfrequency of $\Omega_m/2\pi = 1.45\,\mathrm{MHz}$ and a narrow linewidth of down to $\Gamma_m/2\pi = 2.59\,\mathrm{Hz}$ at a temperature of $T = 32\,\mathrm{mK}$, corresponding to a quality factor of $Q_m = 5.60 \times 10^5$ [146, 176] at $32\,\mathrm{mK}$. Unfortunately, the compressive strain in the Nb film partly compensates the tensile strain in Si_3N_4. This reduces the mechanical eigenfrequency below the value of $5 - 6\,\mathrm{MHz}$ expected for pure Si_3N_4, depending on the detailed amount of the tensile strain [176]. Nevertheless, since $\Omega_m/2\pi$ is about twice the cavity linewidth $\kappa/2\pi$ ($\Omega_m/\kappa \simeq 1.91$), the system is sufficiently far in the resolved-sideband regime to be able to neglect the anti-Stokes field in the theoretical modeling, what will become relevant when discussing the theory of electromechanics in the remaining chapters. The finite coupling capacitance C_g gives rise to the electromechanical coupling $g_0 = Gx_{zpf}$ between the mechanical displacement and the microwave mode inside the CPW resonator. For the coupling distance of this device of $200\,\mathrm{nm}$, the normalized vacuum coupling $g_0/2\pi = 1.26\,\mathrm{Hz}$ is determined experimentally by frequency noise calibration in Section 5.2. With the zero point fluctuation amplitude of the beam, $x_{zpf} = \sqrt{\hbar/2m_{eff}\Omega_m} \simeq 30\,\mathrm{fm}$ ($m_{eff} \simeq 7\,\mathrm{pg}$), the equivalent linear electromechanical interaction can be determined to $G = g_0/x_{zpf} = 2\pi \times 36.3\,\mathrm{s^{-1}/nm}$ giving reasonable agreement to a geometric estimate, discussed in Section 4.4. At a temperature of $T = 32\,\mathrm{mK}$, the parameters above correspond to a low thermal decoherence rate of $\Gamma_m \bar{n}_m \approx 2\pi \times 1.29\,\mathrm{s^{-1}}$, with the mean thermal phonon number $\bar{n}_m = k_B T/\hbar\Omega_m \approx 497$ of the mechanical mode. We will show in Section 6.1 that the effective electromechanical coupling $g = g_0\sqrt{\bar{n}_c}$ scales with the square root of the average number of drive photons $\bar{n}_c$ in the cavity. This exceeds the thermal decoherence rate about more than one order of magnitude, placing our system in a regime where quantum coherent exchange of excitations between "optical" and mechanical mode is possible [75].

All material parameters of the sample are given in table A.1.

4.2 Sample fabrication and preparation

In this Section we discuss the principle fabrication steps necessary to produce the device displayed in Figure 4.2. For more details, in particular all the process parameters, we refer to the PhD thesis of X. Zhou (EPFL Lausanne) [201], since this device stems from a very fruitful collaboration with the group of Tobias Kippenberg located at the EPFL. Parameters, used to pattern similar samples at the WMI are given in appendix A.4.

After cleaning, a highly tensile stressed silicon nitride film with a thickness of $100\,\mathrm{nm}$ is deposited onto a $10 \times 6\,\mathrm{mm^2}$ silicon substrate with low pressure chemical vapour deposition (see Figure 4.3a and b). The silicon nitride layer allows to fabricate nanobeams with high quality factors [146]. Unfortunately, we observed a strong absorption of microwaves in highly stressed silicon nitride, preventing the fabrication of high quality factor superconducting microwave resonators directly on Si_3N_4 layers. This observation is corroborated by Ref. [202] and results in the the necessity to remove the Si_3N_4 layer from the wafer, except from the positions where the nanobeams will be structured eventually. For this purpose, a negative electron-beam (ebeam) resist on the sample (see Figure 4.3c) is patterned with rectangles by electron beam lithography at the later beam positions. After development all resist except from the exposed positions is removed (see Figure 4.3d). Using anisotropic reactive ion etch (RIE), the silicon nitride is selectively removed. The
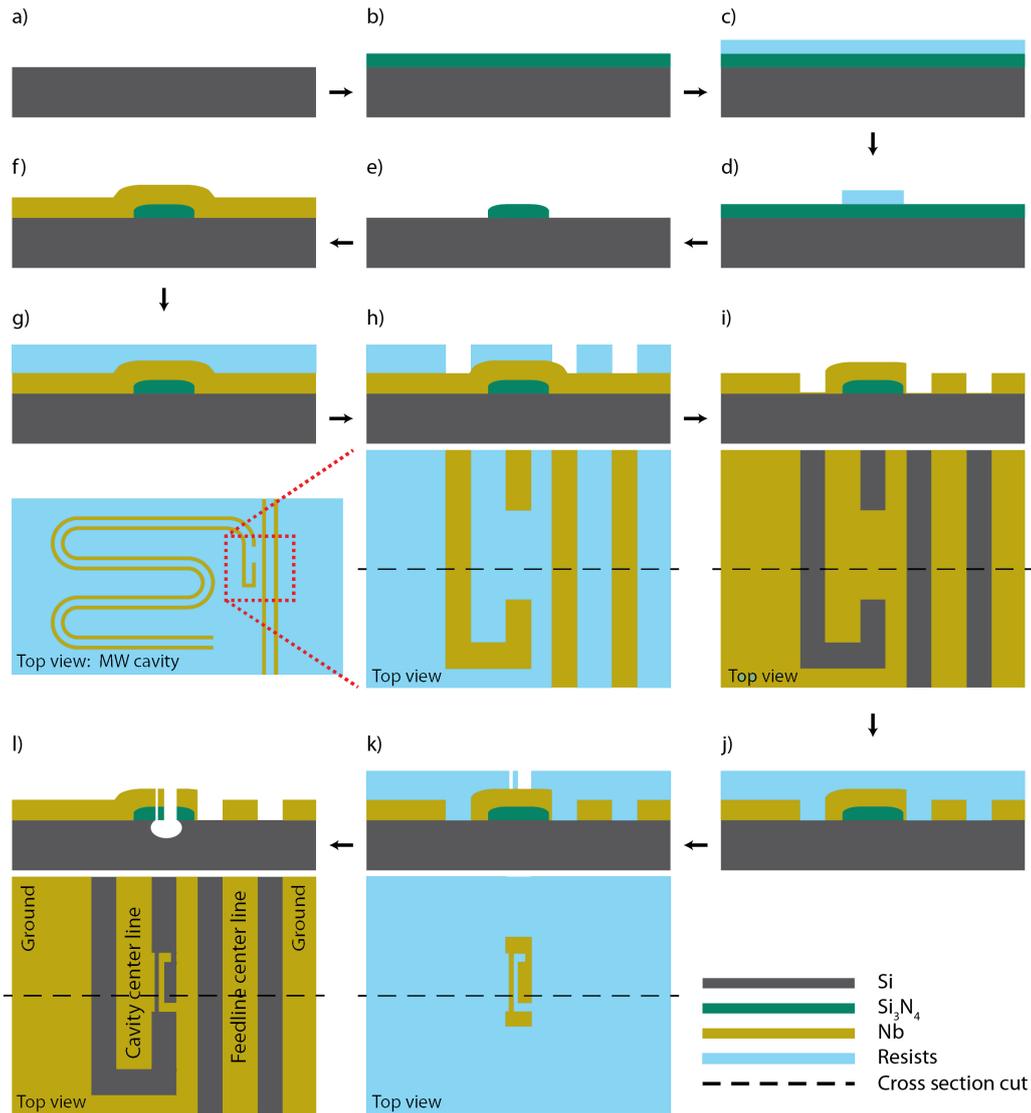
Figure 4.3: Schematic of the different fabrication steps to produce the electromechanical sample studied in this work. Details are found in the main text. This figure is taken from the supplementary information in Ref. [87].

next step is a cleaning process to remove the remaining resist. Further, the remainders of couple of nanometers thick silicon nitride layer at the unpatterned areas is removed with buffered hydrogen fluoride (BHF). This ensures a smooth silicon surface, since the selectivity between silicon nitride and silicon is orders of magnitude higher than in RIE processes [203]. The remaining silicon nitride layer at the patches is hereby thinned to approximately 70 nm and the edges are smoothed out (see Figure 4.3e). The rounded edges of the silicon nitride patches prevent breaks in the 130 nm thick niobium layer, deposited onto the sample in the next step by DC-magnetron sputtering (see Figure 4.3f). An additional electron beam lithography step followed by an anisotropic RIE defines the feedline and the microwave cavities (seven per sample). Here, a positive resist protects the Nb-layer at the non-exposed areas (see Figure 4.3g-i). The top view in Figure 4.3i shows a connection between ground plane and center conductor of the μ-wave cavity. In this region, the nanobeam is patterned in the next step using electron beam lithography
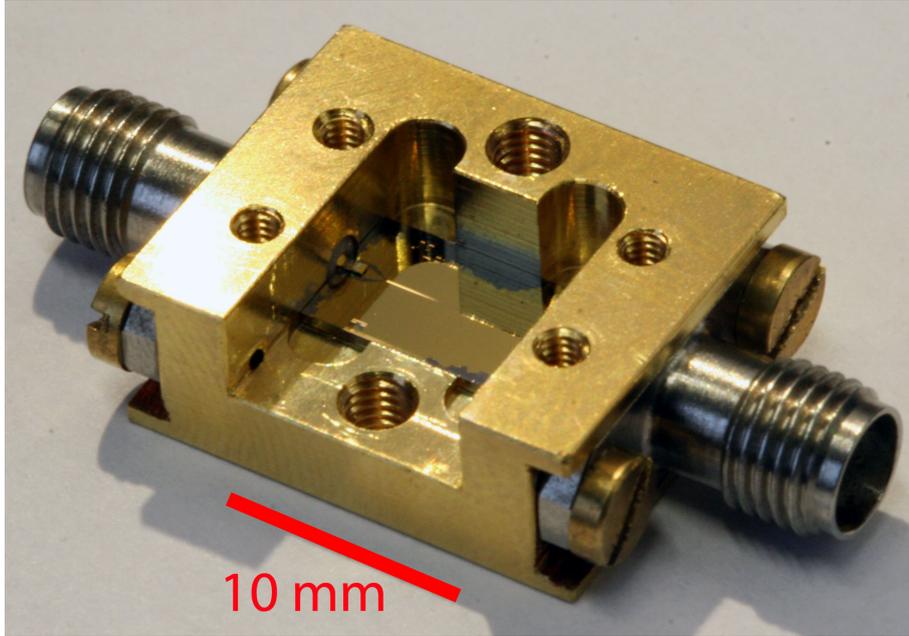
Figure 4.4: Photo of the sample box without cover, including a sample of the same size as the electromechanical one used in this work.

followed by two RIE steps; first an anisotropic one to pattern the beam, and second an isotropic one to release it (see Figure 4.3j-l). These steps are the most critical; the negative resist, acing as a protection mask must be very resistant to RIE processes, since the etch process has to remove the niobium layer as well as the silicon nitride and the isotropic step still attacks the Nb film.

As shown in Figure 4.4, the final sample is mounted in a gold plated copper box built by the WMI workshop to exactly fit a sample of the given size. The pins of two SMA adaptors screwed to the box are connected to the center conductor of the feedline with silver paint. By mounting the adaptors to the coaxial lines of the cryostat, the sample is wired to the experimental setup. The connection between the sample ground and the box is provided by silver paint as well. To minimize additional unwanted resonances and to electrically shield the sample, the box is closed with a fitting top, locked into position with two screws.

4.3   Characterization of the microwave cavity

In the following we start with the first of the two fundamental building blocks of the electromechanical device – the "optical" cavity – here operating in the microwave regime.

Superconducting on-chip cavities have become an important building block for a variety of research fields in solid state based systems during the last decade. The use of superconducting materials allows to build devices without Ohmic losses (but require experimental temperatures below the critical temperature of the material), permitting high Q-factors in the order of 10^5 [204, 205]. Even Q-factors up to millions have been reported in niobium structures [206], still not necessarily limited by internal dissipation [207]. This corresponds to photon storage times in the microsecond regime. In combination with the energy gap between Cooper pairs and single electrons, they serve as so-called lumped ele-
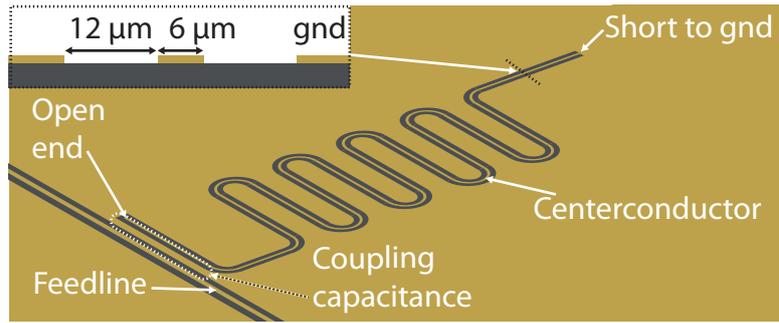
Figure 4.5: Schematic of a $\lambda/4$ coplanar waveguide (CPW) resonator. Yellow represents niobium, grey the silicon substrate. A feedline provides signal in- and output, the resonator consists out of a center strip capacitively coupled to the feedline, open on one end and shorted to ground on the other. The inset shows a cross-sectional view of the coplanar waveguide structure including the significant values.

ment microwave kinetic inductance detectors. An incoming photon with energy exceeding twice the gap energy breaks one Cooper pair, changing the kinetic inductance and thus the resonance frequency [200]. Coupling these devices to superconducting qubits has spawned circuit quantum electrodynamics [13]. The coupling of superconducting cavities to spin systems [22–26] or ferrimagnetic materials [27] allow for coherent exchange of excitations between both systems or can be exploited to test the dynamics of these systems [28]. Kubo *et al.* [31] use a microwave cavity as a bus to mediate quantum information between a qubit and a spin system, creating new quantum hybrid systems and bringing quantum computing into reach. In cavity electromechanics, the coupling of a microwave resonator to a nanobeam or micromembrane have triggered many experiments. Prominent examples are the ground state cooling of a mechanical oscillator [113], the building of a mechanical parametric amplifier [120] or the generation of huge group delays of microwave pulses [87] (see Section 7.1).

These on-chip cavities consist of distributed superconducting transmission lines, guiding the electromagnetic field[1]. The mirrors of an optical cavity take hereby the form of discontinuities in the waveguide impedance, i.e. a capacitance or a short, leading to reflection of the electromagnetic field.

Characteristics of $\lambda/4$ coplanar waveguide cavities

Many realizations of on-chip μ-wave cavities exist. Lumped element cavities [205, 208] offer the highest coupling to a nanobeam in an electromechanical system [48, 80, 120], because the ratio between overall capacitance C to the coupling capacitance C_{g} is highest in this case. The drawback is that higher harmonics are not supported. In contrast, stripline cavities suffer from lower quality factors. Moreover, the impedance depends more strongly on the underlying substrate, leading to a worse scalability than CPW structures [199]. The electromechanical system we study in this work incorporates a coplanar waveguide structure with one open and one shorted end similar to the one in Ref. [69], first introduced by Day *et al.* [200].

---

[1]Any microwave cavity can be understood as an *LC*-circuit. We ignore Ohmic losses since the resonators in this work consist out of superconducting materials and dielectric losses dominate in the temperature/frequency regime presented here.
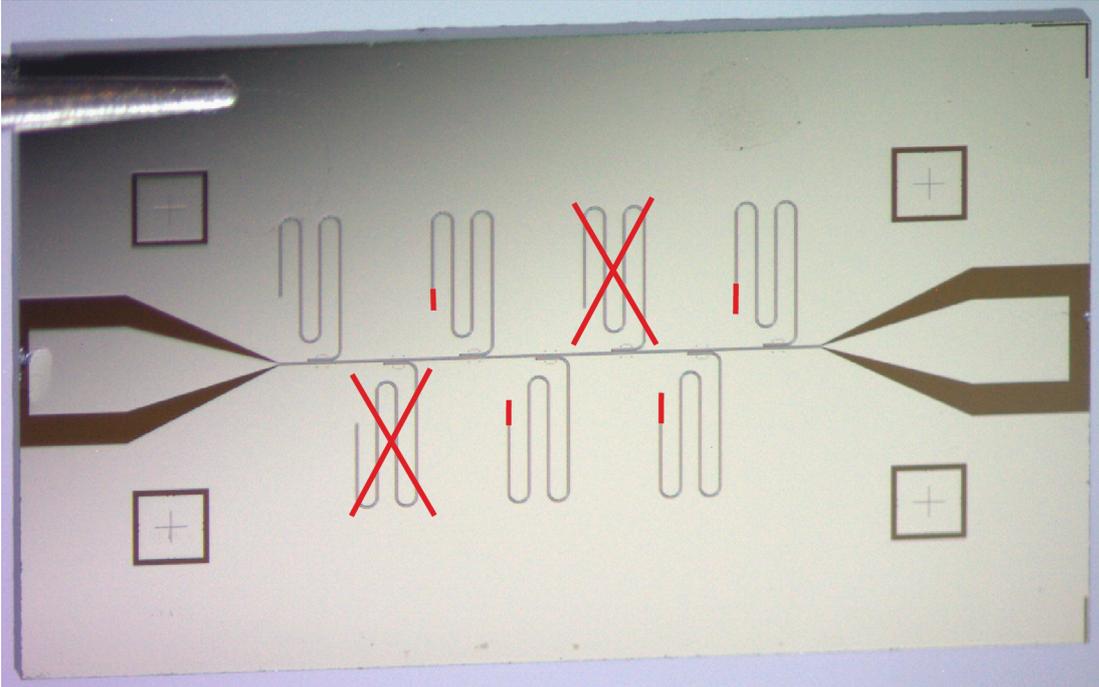
Figure 4.6: Optical micrograph of the microwave cavities on one sample. The box around the pictures show the approximate sample size of 10×6 mm^2. The red lines indicate the post processing with a focused ion beam to increase the cavity lengths, the red crosses show the intensionally broken cavities.

This implementation supports a standing waves with a voltage node on one side (defined by the capacitance) and a voltage antinode on the other side (defined by the short) and is called a $\lambda/4$ resonator (see Figure 4.5 for a schematic). These resonators have the advantage of being short compared to other realizations like $\lambda/2$ resonators, since their length is given by one quarter of the fundamental mode's wavelength. Together with their easy connection to a transmission line in an absorptive configuration the realization of multiple resonators on one chip is simple.

We present the most important parameters and equations for superconducting μ-wave cavities, more details and derivations of the presented formulas can be found in Refs. [199, 209, 210].

Coplanar waveguides are two-dimensional coaxial cables consisting out of a center conductor and ground planes, separated by a gap as schematically shown in the inset of Figure 4.5. For sufficiently thin metallization layers (but still exceeding the London penetration depth), its impedance is defined by the substrate material's dielectric parameters and the ratio of the width of the center conductor and the width of the gap. This allows to operate CPW resonators for a wide range of parameters, e.g. their lateral dimensions can range from micrometers up to centimeters.

The boundary conditions of one shorted and one open end (see Figure 4.5) lead to the support of modes with multiples of a quarter wavelength $\lambda = 4l/(2n+1)$, with n an integer. The capacitive boundary condition corresponds to a voltage node (current antinode), the shorted one to a voltage antinode (current node).

The particular sample discussed in this thesis contains seven cavities with different frequencies placed on a 10×6 mm^2 silicon substrate as shown in Figure 4.6. The cavities
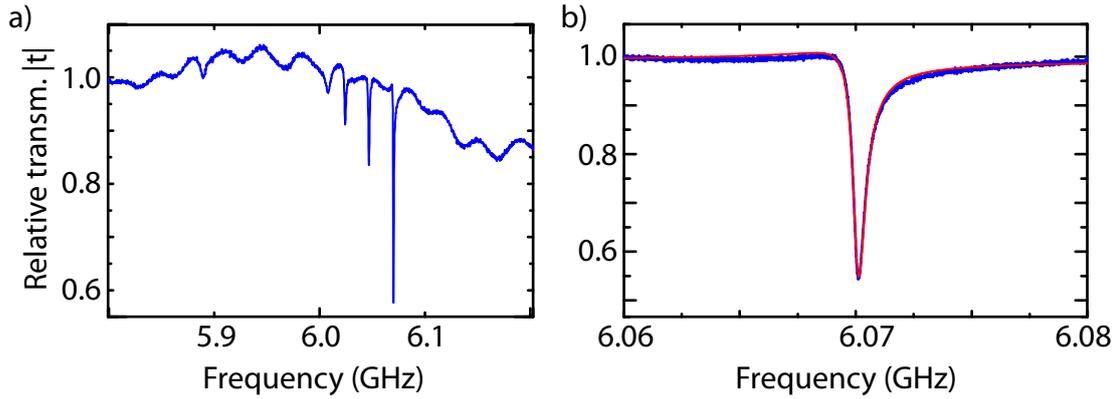
Figure 4.7: Transmission spectra of the electromechanical sample. a) Spectrum from 5.8 to 6.2 GHz showing the characteristic absorption spectrum of three cavities between 6.0 GHz and 6.1 GHz. A zoom around the only cavity not post processed is shown in b). The red line is a fit to the data. The temperature is $T \approx 80$ mK the probe power is $P_{\mathrm{p}} \approx -110$ dBm.

have lengths of approximately 5 mm, what is long compared to the center strip width of $12\,\mu$m and a gap size of $6\,\mu$m. One feedline capacitively couples to all cavities and carries signals to and from each resonator. The impedances of the resonators and the feedline are $Z = 50\,\Omega$.

The eigenfrequency of this type of microwave cavity is given by $\widetilde{\omega}_{\mathrm{c}} = 2\pi/4\sqrt{LC}$. The overall inductance L and overall capacitance C are proportional to the length l of the structure [199]. The relative transmission spectrum of each cavity corresponds to the one of an absorptive harmonic oscillator and reads [210]:

$$t(\omega) = 1 - \frac{\kappa_{\mathrm{ex}}/2}{\kappa/2 + i(\omega - \widetilde{\omega}_{\mathrm{c}})} = \frac{\kappa_{\mathrm{in}}/2 + i(\omega - \widetilde{\omega}_{\mathrm{c}})}{\kappa/2 + i(\omega - \widetilde{\omega}_{\mathrm{c}})} \; . \tag{4.5}$$

The total loss rate $\kappa = \kappa_{\mathrm{ex}} + \kappa_{\mathrm{in}}$ of the cavity includes the external losses κ_{ex} due to the loss of photons into the feedline and the internal losses κ_{in} in due to absorption and radiation leaking into the environment (see the right of Figure 4.1). The loss rates allow to calculate the quality factor Q, a value useful to compare the performance of cavities with different eigenfrequencies. It is given by

$$Q = \frac{\widetilde{\omega}_{\mathrm{c}}}{\kappa} \; . \tag{4.6}$$

The internal (external) quality factor is defined by $Q_{\mathrm{int}} = \widetilde{\omega}_{\mathrm{c}}/\kappa_{\mathrm{in}}$ ($Q_{\mathrm{ex}} = \widetilde{\omega}_{\mathrm{c}}/\kappa_{\mathrm{ex}}$). Another parameter allowing to quantify the relation between internal and external losses is $\eta_{\mathrm{c}} = \kappa_{\mathrm{ex}}/\kappa_{\mathrm{in}}$. For $\eta_{\mathrm{c}} = 1/2$ the cavity is critically coupled; we obtain the best contrast in this case. The cavity is overcoupled (undercoupled) for $\eta_{\mathrm{c}} > 1/2$ ($\eta_{\mathrm{c}} < 1/2$), meaning that the external (internal) loss rate dominates. Undercoupled systems have the drawback of dissipating more information than transferred into the signal lines.

Experimental characterization of the μ-wave cavity

When producing the sample, a design flaw led to the same length l in all cavities. To compensate for this, some of the cavities were post processed with a focused ion beam to increase their lengths (red lines in Figure 4.6) or to render the cavity unusable (red crosses
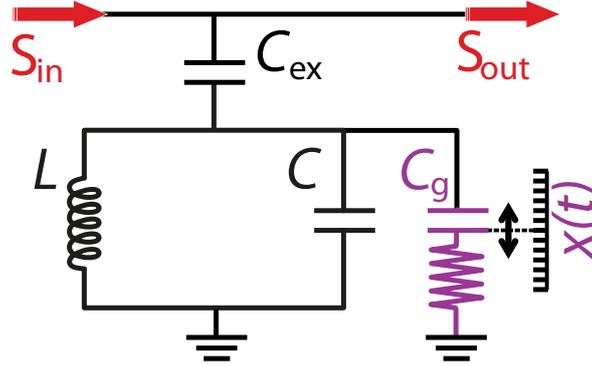
Figure 4.8: Equivalent circuit diagram of the electromechanical system. A vibrating capacitance C_g is connected parallel to the microwave cavity represented by a LC equivalent circuit.

in Figure 4.6). The increased lengths result in lowered eigenfrequencies. The unchanged cavity is thus easily recognized as the one with the highest resonance.

To characterize the sample, we measure the microwave transmission through the sample with a vector network analyzer at a temperature of 80 mK. The probe power was increased from approx. -120 dBm to approx. -50 dBm without showing any power dependency of the recorded transmission. Changes of the sample temperature from 32 mK to more than 600 mK leave the measured quality factors and eigenfrequencies unchanged as well.

Figure 4.7a shows that three of the four cavities with resonances between 6.0 GHz and 6.1 GHz and different absorption depths, indicating varying external quality factors. Figure 4.7b shows a zoom of the spectrum belonging to the unmodified cavity with the highest frequency. The red line is a fit to the absolute value of Equation (4.5), where we have taken into account a small dispersive shift to account for the asymmetry of the spectrum (see Appendix A.5). The spectrum in Figure 4.7b is obtained from the cavity coupled to the most promising nanobeam, with a cavity eigenfrequency of $\widetilde{\omega}_c/2\pi = 6.070$ GHz. We have normalized the transmission to unity close to the absorbtion spectrum of this cavity, since this is the regime that we calibrate in Section 5.2 and all frequencies that are used in the following experiments are situated in this regime. The coupling to the feedline results in a coupling rate of $\kappa_{ex}/2\pi = 339$ kHz. Comparing this coupling rate to the measured cavity linewidth of $\kappa/2\pi = 759$ kHz yields a coupling rate $\eta_c = \kappa_{ex}/\kappa \simeq 0.45$. The corresponding quality factors are $Q = 7910$ and $Q_{ex} = 17535$. The resonance at $\widetilde{\omega}_c/2\pi = 6.045$ GHz ($\widetilde{\omega}_c/2\pi = 6.024$ GHz) shows $Q = 5084$ ($Q = 3794$). We attribute higher internal losses for decreasing the quality factor as a result of the post processing with a focused ion beam. For the rest of this work, we restrict ourselves to the analysis of the cavity centered around $\widetilde{\omega}_c/2\pi = 6.070$ GHz and the nanobeam coupled to this cavity building an electromechanical system.

4.4 Electromechanical coupling between a CPW μ-wave cavity and a nanobeam

Before studying the nanomechanical oscillator, we will calculate the expected coupling between the mechanical and optical modes in our electromechanical system. In Section 4.1 we have already discussed that in a first order approximation the cavity resonance frequency

changes linearly with the mechanical amplitude, $\omega_c(x) = \omega_c - \frac{\partial \omega_c}{\partial x} x$. As already mentioned in Section 4.2, we place the nanobeam in the voltage node of the μ-wave cavity. An equivalent circuit diagram is shown in Figure 4.8. The nanomechanical beam together with the ground plane of the resonator build a capacitance $C_g(x(t))$ between center conductor and ground, which vibrates with the mechanical resonance frequency Ω_m around its equilibrium position $C_g(0) \equiv C_{g,0}$. We approximate this capacitance as a plate capacitance, yielding

$$C_g(x(t)) \approx \varepsilon_0 \varepsilon_r A \frac{1}{d - x(t)} \approx C_{g,0} + \frac{\partial C_g}{\partial x} x(t) \ . \tag{4.7}$$

Here, d is the gap between nanobeam and ground plane and ε_r is the effective dielectric constant, which we will set to one since no dielectric is present in the volume between ground and nanobeam. We have neglected any inhomogeneous contributions to the capacitance and evaluated $C_g(x(t))$ for small mechanical displacements. The derivative is given by $\partial C_g / \partial x = C_{g,0}/d$. The area A is defined by the length L and height h_{Nb} of the beam's superconducting layer, $A = L \cdot h_{Nb}$.

The plate capacitor is connected parallel to the overall capacitance of the microwave cavity. Since the capacitance mediating the coupling to the feed line is small compared to the overall capacitance in the CPW structure, we will neglect it in this discussion and approximate $C + C_{ext} \approx C$. For small displacements, we can approximate the eigenfrequency of the microwave cavity to

$$\omega_c(x) = \frac{2\pi}{4\sqrt{L(C + C_g(x))}} \approx \omega_c \left(1 - \frac{C_g(x)}{2C}\right) \tag{4.8}$$

With this, we can estimate the electromechanical coupling to [69]

$$G = -\frac{\partial \omega_c}{\partial x} = \frac{\omega_c}{2C} \frac{\partial C_g}{\partial x} = \frac{2Z\omega_c^2}{2\pi} \frac{\partial C_g}{\partial x} \ , \tag{4.9}$$

where we have used $Z = \sqrt{L/C}$. Equation (4.9) allows us to estimate the coupling using the known impedance $Z = 50\,\Omega$ and $\omega_c/2\pi = 6.070\,\text{GHz}$. With a coupling distance of $d \approx 200\,\text{nm}$ and a niobium film thickness of $h_{Nb} = 130\,\text{nm}$, we estimate $C_g = 0.34\,\text{fF}$ and $\partial C_g/\partial x = 1.72\,\text{nF/m}$. With these values, we calculate $G/2\pi = 6.36\,\text{kHz/nm}$, what is a factor of six lower than the experimentally determined coupling in Section 5.2.2 of $G/2\pi = 36.3\,\text{kHz/nm}$. We account the difference to the fact, that we have simplified the capacitance between beam and ground plane, neglecting the considerable stray capacitance and ignoring losses due to the silicon nitride layer under the niobium. With Equation (4.9), we calculate the coupling capacitance following from the experimental value of G to $C_g = 1,97\,\text{fF}$. We will use this value in further discussions, as it is more accurate than the estimated one.

4.5   Characterization of the nanobeam

For the purpose of this thesis, we now review the nanomechanical oscillator coupled to the microwave cavity. As we discuss in more detail in Section 5.1, any opto-/electromechanical device allows to study of the mechanical mode without disturbing its dynamics due to backaction effects. In this section, we thus ignore the parameters of the microwave resonator and focus on the nanobeam's intrinsic properties.
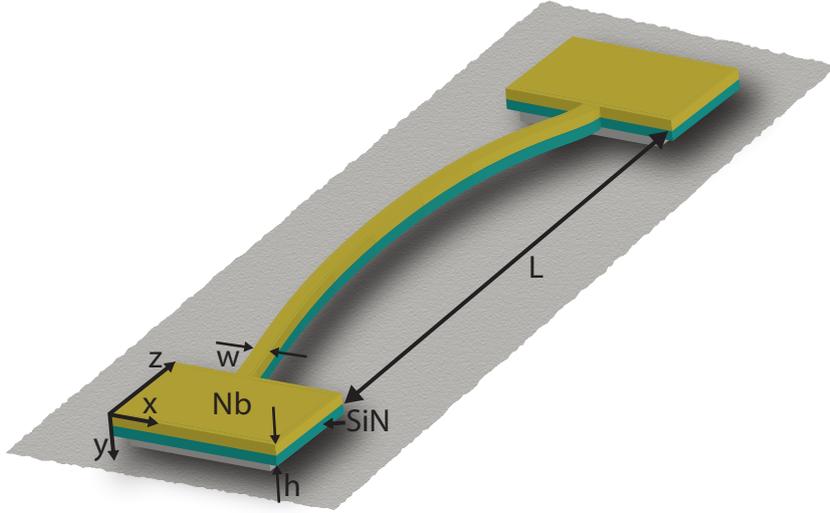
Figure 4.9: Schematic of the nanobeam analyzed in this work. The niobium layer is shown in yellow, the silicon nitride in green, the silicon substrate in grey. The oscillation in x direction is shown schematically and highly exaggerated.

First, we present the equations to describe the mechanical vibration, showing that it is sufficient to focus on the center of mass amplitude with an effective mass. Afterwards we analyze the thermal behavior at low temperatures of the two main parameters defining the mechanical motion; the mechanical eigenfrequency $\Omega_{\mathrm{m}}(T)$ and the mechanical linewidth $\Gamma_{\mathrm{m}}(T)$. In the last part of this section we study mechanical motion beyond Hook's regime, where the effective potential is no longer parabolic but contains higher order terms. In particular, we discuss the so-called Duffing regime. We show, that this regime is useful to extract intrinsic mechanical parameters, otherwise not easily accessible in mechanical oscillators built from combinations of different material systems.

4.5.1   Description of a tensile stressed doubly clamped beam

In the following, we briefly present the necessary equations to describe the vibration of a mechanical doubly clamped beam. Here, we show that it is sufficient to restrict the discussion of a vibrating nanobeam to its center of mass amplitude and we state the connection between mechanical resonance frequency and the material parameters.

The derivation and solution of these equations is commonly found in textbooks about continuous mechanics and Euler-Bernoulli beam theory, for example in Ref. [211]. Here, we present only the main results of these considerations. For a discussion within the context of nanomechanics see [212] and the references therein.

The dynamics of a one-dimensional, vibrating, undamped (nano-)beam extending along the z-axis and vibrating in x-direction (see Figure 4.9) is covered by the Euler-Bernoulli equation [211]

$$\frac{\partial^4 \widetilde{x}(t,z)}{\partial z^4} = -\frac{\rho A}{E I_x} \cdot \frac{\partial^2 \widetilde{x}(t,z)}{\partial t^2} \ , \tag{4.10}$$

with the mass density ρ, the cross-section $A = wt$, the Young's modulus E and the moment of inertia in x-direction $I_x = Aw^2/12$. Note, that the damping of the vibration is ignored to keep the discussion as simple as possible. The nanobeam in this work has a high aspect ratio between beam length and width or hight of more than 10^2. This justifies the

approximation as an one-dimensional beam. To solve Equation (4.10), one separates the spatial and time dependency $\widetilde{x}(t,z) = x(t) \cdot X(z)$. We get two differential equations, one for the center of mass motion $x(t)$ and one for the modal shape $X(z)$,

$$\ddot{x}(t) + \Omega_\mathrm{m}^2 x(t) = 0 \,, \tag{4.11}$$

$$\frac{\partial^4 X(z)}{\partial z^4} - \frac{\Omega_\mathrm{m}^2}{c_t} X(z) = 0 \,. \tag{4.12}$$

Here, we have introduced $c_t = \rho A / E I_x = 12\rho / E w^2$. Equation (4.11) shows that the center of mass motion $x(t)$ follows the equation of motion of an harmonic oscillator. In experiments we will only analyze $x(t)$, while the spatial mode shape is not directly accessible.

When solving Equation (4.12), the eigenfrequency follows from numerically solving a transcendent equation, given by the boundary conditions of the structure and the system parameters [211]. For a doubly clamped beam, the eigenfrequency of the fundamental mode Ω_m in x-direction is given by [212]:

$$\Omega_\mathrm{m} = 2\pi C_1 \frac{w}{L^2} \sqrt{E} \rho \,. \tag{4.13}$$

The constant C_1 follows from solution of the transcendent equation, w is the beam width and L its length. For highly tensile stressed beams, the eigenfrequency can be shown [176, 211] to modify to:

$$\Omega_\mathrm{m} = \frac{\pi^2}{L^2} \sqrt{\frac{EI}{\rho} \left(1 + \frac{\sigma L^2}{EI_x \pi^2}\right)} \approx \frac{\pi}{L} \sqrt{\frac{\sigma}{\rho}} \,, \tag{4.14}$$

Here, σ is the stress present in the structure, ρ its density. We expect the highly stressed silicon nitride layer to dominate the resonance frequency of the nanobeam used in this work. The stress of silicon nitride on a silicon layer is specified to $\sigma_\mathrm{SiN} \approx 800\,\mathrm{MPa}$ at room temperature. At lower temperatures, we expect this value to increase due to the higher thermal expansion coefficient of silicon nitride compared to silicon (see table A.1). For the density, we take the weighted average of the two layer's density. The density of silicon nitride is $\rho_\mathrm{SiN} = 3000\,\mathrm{kg/m^3}$ [213], the density of niobium is $\rho_\mathrm{Nb} = 8570\,\mathrm{kg/m^3}$, resulting in an effective density of $\rho_\mathrm{eff} = (\rho_\mathrm{SiN} t_\mathrm{SiN} + \rho_\mathrm{Nb} t_\mathrm{Nb})/t = 6620.5\,\mathrm{kg/m^3}$. We estimate the mechanical frequency to $\Omega_\mathrm{m}^\mathrm{calc}/2\pi \approx 2.90\,\mathrm{MHz}$. Experimentally, we observe a mechanical resonance of $\Omega_\mathrm{m}/2\pi \approx 1.45\,\mathrm{MHz}$ at temperatures around $200\,\mathrm{mK}$. For details on the measurement of the mechanical eigenfrequency, see Section 4.5.2, where the mechanical eigenfrequency is studied as a function of temperature. The experimental value of Ω_m implies that the niobium layer is stressed compressively, reducing the overall stress present in the nanobeam. Plugging the measured value of Ω_m into Equation (4.14), we get an effective stress of $\sigma_\mathrm{eff} = 199\,\mathrm{MPa}$. Comparing this to the initial value of the stressed silicon nitride layer of $\sigma_\mathrm{SiN} \approx 800\,\mathrm{MPa}$, corroborates that the compressive stress of the niobium[2] significantly reduces the strain. In Section 4.5.3, we additionally estimate the effective Young's modulus of the nanobeam, completing the set of relevant system parameters.

The center of mass motion is sufficient to capture the dynamical behavior of a beam's amplitude. To accurately describe further parameters, like the energy, one has to consider that only a fraction of the whole beam mass contributes to the center of mass motion. To account for this, an effective mass is introduced. It depends on the structure and

---

[2]The exact value is unknown, but the compressive stress in superconductive DC-sputtered Nb thin films is well studied [214].

boundary conditions of the beam [212]. For a doubly clamped beam, the effective mass is given by $m_{\text{eff}} = 0.73\,m$, with $m = \rho A L$. With the effective density, we estimate $m_{\text{eff}} \approx 7 \times 10^{-15}\,\text{kg} = 7\,\text{pg}$.

4.5.2   Temperature dependence of the mechanical mode

Now, we turn the discussion to the characterization of the nanobeam's thermal behavior at low temperatures, giving insight in different loss mechanisms. The changes of Γ_{m} and Ω_{m} with temperature give another degree of freedom to tune the system under investigation for different applications. Additionally, having understood the different contributing mechanisms, we can corroborate the the thermalization of the sample to mixing chamber temperature and even use it as an additional thermometry device [188]. The μ-wave cavity is robust against temperature changes below $1\,\text{K}$, we have not observed any changes in eigenfrequency of dissipation within this temperature. So the signal strength as well as the driving field's frequency remain stable. Electromechanical back-action can be neglected, since we perform all measurements with a weak drive tone at cavity resonance ω_{c}. For more details on this see Section 5.1

Due to the differently stressed layers of the nanobeam and its different mechanical properties, it is difficult to distinguish their specific influence on the vibration of the beam. Nevertheless, we will show that the overall thermal dissipation can be clearly associated with interactions between phonons and two level systems (TLS) present in the nanobeam proving that the combination of amorphous insulators and polycrystalline superconductors in nanobeams show the same thermal behavior as a purely amorphous insulator beam.

We first explain the different loss mechanisms so far identified in nanobeams, discussing their respective relevance in our observation. Then, we present the experimental details, explaining the setup and measurement parameters. The experimental results are finally analysed with respect to the presented theory and compared to the results achieved in similar studies.

Dissipation and eigenfrequency behavior in a nanobeam

First, we add damping to the undamped harmonic oscillator described by Equation (4.11). Damping in harmonic oscillators is treated as viscous damping, what implies the damping force is proportional to the velocity with a damping constant Γ_{m} [211]. Taking a driving force $F_{\text{d}}(t)$ into account, Equation (4.11) modifies to

$$m_{\text{eff}}\ddot{x}(t) + m_{\text{eff}}\Gamma_{\text{m}}\dot{x}(t) + m_{\text{eff}}\Omega_{\text{m}}^2 x(t) = F_{\text{d}}(t). \tag{4.15}$$

The origin of dissipation in mechanical oscillators has inspired various studies during the last decades. Multiple loss mechanisms have been identified and analyzed. We present the most prominent ones and discuss their contribution to our analysis:

The finite viscosity of gases and fluids damp the vibration of mechanical oscillators placed within [146, 147]. All our measurements take place in ultrahigh vacuum, so we can neglect this effect.

Phonon-phonon interaction and so-called thermoelastic losses originate from redistribution of phonons due to different thermal equilibria of the surfaces of bent materials [148–151]. The amplitudes of the vibrations studied here are in the range of nanometers due to the high tensile stressed silicon nitride layer. This amplitude is small compared to

the length and width of the nanobeam (see Section 4.1). The mechanical vibration does not induce bending sufficiently strong to result in high stress gradients. Thus, we can also exclude these effects. The high tensile stress in the nanobeam even reduces the dissipation and leads to very high mechanical quality factors [176–178].

Depending on the thermal expansion of the nanobeam and the underlying substrate, the eigenfrequency and Q-factor will change [69, 152] with decreasing temperature. On a temperature scale below $1\,\mathrm{K}$ we can ignore this effect since the thermal expansion is negligible in this regime.

The anchoring of the nanobeam is the loss mechanism fundamentally limiting the dissipation; acoustic excitations tunnel into the clamps and the underlying substrate [141, 151, 153–159]. Minimizing these losses include free-free clamping[3] of the beam [160] or the manipulation of the substrate at the clamps to prevent the propagation of phonons with the beam's resonance frequency in these areas [78]. Using highly stressed silicon nitride these measures are not necessary, Q-factors up to seven million have been demonstrated with this material at room temperature [144].

Interaction of acoustic excitations with defects in the material or surface due to relaxation processes is very prominent in amorphous and polycrystalline materials. The energy states of these defects relax into the environment, giving these interactions a dissipative nature. Mostly, the defects can be treated as two level systems (TLS) with a broad distribution of the level splitting [143, 215, 216]. The microscopic nature of the TLS is difficult to specify. The temperature dependence of the mechanical linewidth and eigenfrequency is defined by the nature of the interaction between TLS and phonons present in the nanobeam [161–166]. The coupling between acoustic excitations and two level systems is easy to understand. The potential of a TLS is given by an asymmetric double well potential [216]. The periodically changing stress distribution following a mechanical excitation shifts the two wells with respect to each other, bringing the TLS out of their thermodynamic equilibrium; the two systems couple and the TLS relaxation transfers energy to the thermal bath, leading to dissipation. The derivation of the coupling details is complicated. We only present the main results, without deriving the predictions and instead focus on comparison to previous results with nanobeams. More detailed discussions are found within the references [162, 164–166, 215–221].

Depending on the temperature regime, different processes dominate the state transition in the TLS. At temperatures below the transition temperature of a TLS, the state occupation of the TLS is highly unbalanced and most TLS are found in their ground state. Relaxation processes are negligible. In this regime, the most effective mechanism for state transfer is (resonant) absorption of phonons [218]. This effect shows saturation behavior [217].

For higher temperatures up to typically 1 Kelvin [215], the TLS are thermally excited and Raman processes involving tunneling through the barrier of the double well potential become the dominant relaxation processes.

For an even increased temperature, multi-phonon processes and thermally activated relaxation are the most prominent effects.

In metals, the electron cloud couples to TLS as well, leading to relaxation. However, Black *et al.* [219] have shown that this coupling is negligible in superconductors as well as

---

[3]Here, the clamps are placed at amplitude antinodes, respectively and thus ideally do not damp the vibration.

in polycrystalline metals [220].

We measure $\Gamma_{\mathrm{m}}(T)$ and $\Omega_{\mathrm{m}}(T)$ in a temperature window ranging from $30\,\mathrm{mK}$ up to $600\,\mathrm{mK}$. The relevant relaxation process is thus given by tunneling relaxation.

All relaxation processes of TLS presented here show the same logarithmic temperature dependence of the mechanical eigenfrequency [216]:

$$\Delta\Omega_{\mathrm{m}} = \Omega_{\mathrm{m}}(T) - \Omega_{\mathrm{m}}(T_0) = C\Omega_{\mathrm{m}}(T_0)\ln\left(\frac{T}{T_0}\right) . \qquad (4.16)$$

The mechanical resonance frequency is compared to its value at a fixed reference temperature T_0. The dimensionless constant C is defined by $C = D_n\lambda^2/E$, where we have introduced the density of states of the TLS D_n, an interaction constant λ and the Young's modulus E of the material. Extraction of D_n and λ is not possible from our measurements. In Al nanobeams, typical values of C in are in the range of 10^{-4} to 10^{-5} at temperatures in the millikelvin range [165, 166].

In contrast to the eigenfrequency, the temperature dependence of the dissipation due to TLS interaction strongly depends on the type of interaction. At low temperatures where the TLS relaxation results from resonant absorption of an acoustic excitation, the dissipation is monotonously decreasing for increasing temperature following the temperature induced decrease of the TLS relaxation time [218]:

$$\Gamma_{\mathrm{m,res}}(T) \propto \tanh\left(\frac{\hbar\Omega_{\mathrm{m}}}{2k_{\mathrm{B}}T}\right) , \qquad (4.17)$$

As we can see in Figure 4.13 the dissipation increases with temperature. This indicates that the relaxation process discussed above is of no relevance in the temperature window of this work in agreement to our statement above.

In the temperature regime studied here, tunneling relaxation processes are dominant in TLS. The TLS relaxation due to tunneling is induced by changes of the stress inside the system, thus the relaxation depends on the phonon density of states [162, 216]. Studies of the damping of acoustic waves in bulk material [215] reveal a T^3 behavior for the inverse Q-factor [221] and thus the acoustic dissipation ($1/Q = \Gamma_{\mathrm{m}}/\Omega_{\mathrm{m}}$). Seoánez *et al.* [162] predict a square root dependence $Q^{-1} \propto \sqrt{T}$ for doubly clamped nanobeams in this temperature regime and Venkatesan *et al.* [164] experimentally corroborate this in a study of Au nanobeams. They argue that transferring the phonon induced TLS relaxation process from bulk material to nanobeams, one has to take into account that the phonon density of states in the temperature regime below $1\,\mathrm{K}$ has to be considered as one dimensional, since the minimum phonon wavelength is on the order of $100\,\mathrm{nm}$ [222], corresponding to the nanobeam's lateral dimensions. The phonon dispersion in a nanobeam modifies to $\Omega_{\mathrm{m}} \propto k^2$ [222], where we have introduced the wavevector k that is inversely proportional to the wavelength.

However, for a highly stressed nanobeam, the mechanical eigenfrequency and thus the phonon dispersion follow the inverse length $1/L$ as stated in equation (4.14). The phonon spectrum becomes linear, $\Omega_{\mathrm{m}} \propto k$. The corresponding phonon density of states is constant in this case and one can show that this results in a TLS relaxation with linear temperature dependency [215].
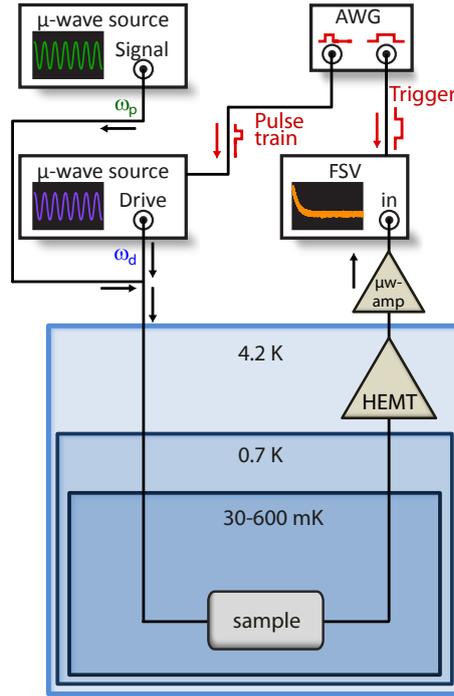
Figure 4.10: Schematic setup to measure the mechanical amplitude's ring down. A drive tone is applied to the blue sideband at $\omega_d = \omega_c + \Omega_m$ and drives the mechanical mode by the resulting beat between the drive and the probe field at cavity resonance ω_c. The Stokes sideband of the probe field is recorded with a spectrum analyzer in time domain, showing the mechanical decay to amplitudes corresponding to the thermal Brownian motion.

Experimental details

To analyze the thermal dissipation of the mechanical mode in our electromechanical system, we perform two sets of experiments:

First we measure the mechanical eigenfrequency as a function of temperature with the same setup shown in Section 5.2. A weak drive tone at cavity resonance minimizes electromechanical back-action onto the nanobeam. As shown in Section 5.2 the mechanical displacement spectrum translates into the phase and amplitude spectrum of the cavity. We record the phase spectrum around the mechanical resonance with a homodyne detection scheme, providing exact values of the mechanical resonance frequency. In contrast to the frequency noise calibration in Section 5.2, the measurements are performed in cryostat No.2, where we can precisely adjust the temperature. With the knowledge of the mechanical eigenfrequency, we perform a ring down measurement to extract the mechanical linewidth Γ_m.

For this purpose, we drive the mechanical motion with a beating force, resulting from interference between a blue detuned drive field at the mechanical sideband $\omega_d \approx \omega_c + \Omega_m$ and a probe field at the cavity eigenfrequency $\omega_p \approx \omega_c$ as schematically shown in Figure 4.10. When switching off the drive field, the electromechanical backaction drops to zero; the mechanical high amplitude motion relaxes to its thermodynamic equilibrium amplitude with a decay rate $\tau(T) = 2/\Gamma_m(T)$ (the theoretical details for this conclusion are derived in Section 7.2). The probe field generates sidebands proportional to the mechanical amplitude. The decay of the red sideband at frequencies of $\omega_c - \Omega_m$ is recorded with a
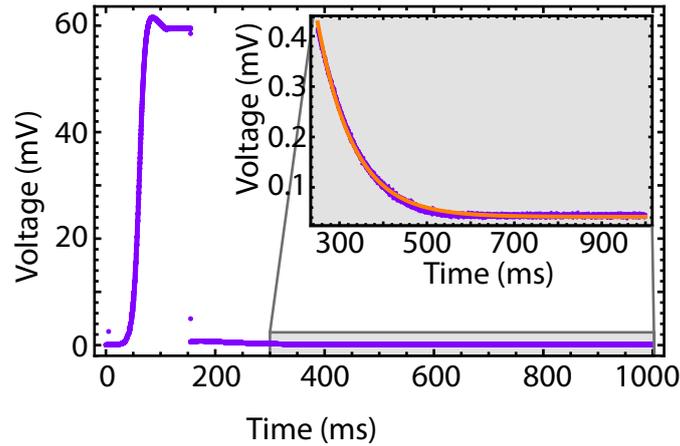
Figure 4.11: Complete time trace of the mechanical motion. The displacement amplitude rings up due to the blue detuned driving field. Upon switching off the field the amplitude decays to its thermal equilibrium amplitude. The inset shows the mechanical ring down including a fit to the data.

spectrum analyzer in time domain after passing an amplifier chain. An arbitrary wave form generator shapes the rectangular drive pulses and triggers the measurement.

Figure 4.11 shows a typical time trace including the ring up of the mechanical amplitude. The inset shows the decay of the sideband amplitude including an exponential fit to the data (orange curve).

Experimental study of Γ_{m} and Ω_{m} with temperature

Figure 4.12 shows the recorded change of eigenfrequency extracted from the homodyne temperature sweep. The red line is a fit to equation 4.16 with a reference temperature $T_0 = 32\,\mathrm{mK}$[4]. From the fit we extract $C \approx 3 \times 10^{-6}$, which is more than one magnitude smaller than reported in Al nanobeams [165, 166]. We attribute the smaller value to the higher tensile stress in our nanobeams. The Young's modulus E in the definition of C has to be replaced by the stress modulus σ, similar to the modification of the eigenfrequency in highly stressed beams (see equation (4.14)). Sulkko *et al.* [166] report on changes in C when changing a DC gate voltage, stressing their Al nanobeams but attribute this to a change in the materials dielectric constant. Further experiments are necessary to clarify the stress dependence of C and to give insight into the TLS density of states and λ, possibly clarifying the microscopic nature of the TLS. The good agreement between theory and results show that the nanobeam and thus the sample thermalizes well with the mixing chamber in the cryostat even down to temperatures of $30\,\mathrm{mK}$.

From the ring down measurements we extract a linear temperature dependence of mechanical dissipation, $\Gamma_{\mathrm{m}} = AT + \Gamma_0$ with $A \approx 2\pi \times 37\,\mathrm{Hz/K}$ as shown in Figure 4.13. Our observations corroborate the findings of Hoehne *et al.* [165] and Sulkko *et al.* [166]. The constant A extracted from our measurements is indeed one order of magnitude smaller than reported by Sulkko *et al.*. Again, we attribute this outcome to the higher tensile stress in our nanobeam, leading to a weaker TLS-phonon coupling (the stress in the Al beams studied by Sulkko *et al.* originates solely from the different thermal expansion

---

[4]Changing the reference temperature T_0 and $\Omega_{\mathrm{m}}(T_0)$ accordingly gives similar results.
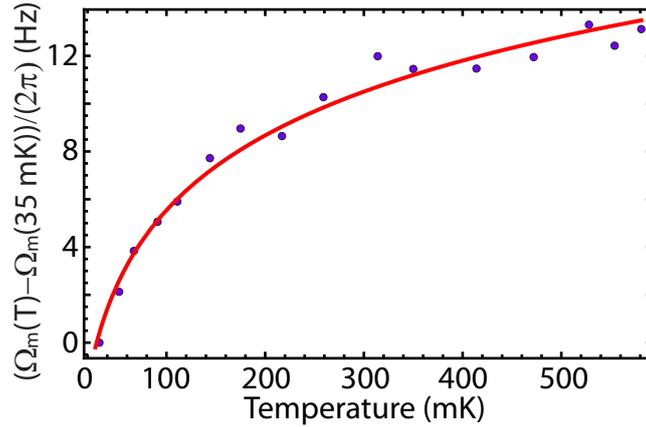
Figure 4.12: Mechanical eigenfrequency change plotted against temperature. The eigenfrequency at a temperature of $T = 32\,\mathrm{mK}$ is chosen as reference point. The red line is a fit of Equation (4.16) to the data showing the logarithmic temperature dependence and proving that the mechanical mode thermalizes well with the mixing chamber.
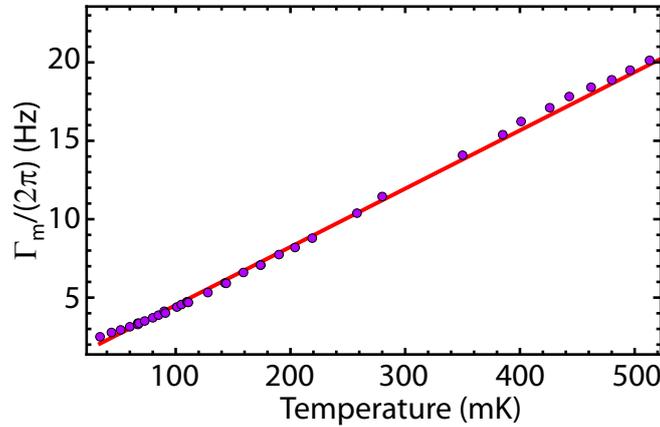
Figure 4.13: The extracted mechanical linewidth as function of temperature. The red line is a linear fit to the data.

coefficients, while the nanobeam studied here is highly stressed even at room temperature). At the lowest temperature of $32\,\mathrm{mK}$, we extract $\Gamma_{\mathrm{m}} = 2\pi \times 2.59\,\mathrm{Hz}$ corresponding to $Q_{\mathrm{m}} = 5.60 \times 10^5$. The data at the lowest temperatures indicate the onset of saturation of the mechanical dissipation. This cannot be clarified here, since measurements at even lower temperatures are difficult to realize.

Concluding, we understand the mechanisms of thermal behavior of mechanical eigenfrequency and dissipation. The data agree to previous considerations and measurements when adjusting the underlying theory to a highly stressed beam and the following phonon density of states. This corroborates that the main dissipation mechanism in our system at millikelvin temperatures originates from coupling of phonons two TLS. Although the nanobeam has a double layer structure consisting out of an amorphous insulator and a polycrystalline superconducting layer the temperature dependence of Ω_{m} and Γ_{m} is covered by the theory of amorphous insulators. This dramatically simplifies the study of double-layered nanobeams by assuming one amorphous insulator layer with effective stress, density and Young's modulus following from both layers' material parameters.

The good agreement between the data and theory of the mechanical eigenfrequency

as a function of temperature that is supposed to be valid over an even wider temperature range presents an onchip thermometry device [188]. We can thus identify temperature changes due to high driving fields or bad thermalization of the sample.

One way to reduce the dissipation is to reduce the number of TLS. Thermal annealing of the sample before measurement is one way to achieve this [220]. Optimization of the mechanical mode in an optomechanical/electromechanical system is still a crucial task. Recently, several groups started to explore this systematically, taking the known loss channels into account [73, 78, 111, 223].

Finally, we want to mention the coupling of TLS to other solid state base circuitries has been reported and analyzed. In microwave resonators, TLS lead to additional $1/f$-noise due to dipole coupling to the electric field [224]. The dipole coupling between TLS in the insulating tunnel barrier and qubits leads to dephasing and decoherence [225, 226]. In these systems, the coupling between qubit and TLS can be so strong, that single TLS even have served as a memory for qubit states [227] or become entangled to a qubit [228].

4.5.3   Duffing nonlinearity of a doubly clamped nanobeam

One of the most prominent nonlinear oscillation regime in doubly clamped nanobeams is the Duffing regime [212]. For amplitudes exceeding a system dependent critical amplitude, the model of an damped harmonic oscillator defined in Equation (4.15) is not sufficient to cover the physical phenomena. To extend the model, one includes higher order terms of the restoring force, leading to anharmonic effects. In the case of a doubly clamped beam the physical background is that the stiffness of the material as function of the amplitude exceeding the critical one cannot be described by a harmonic potential anymore. Thus the approximation of a linear restoring force (Hooks law) does not cover the dynamics [211]. We have to deal with a nonlinear system resulting in much richer nonlinear dynamics.

The most prominent feature of a Duffing oscillator is the establishment of bifurcation for amplitudes beyond the critical one. This phenomenon can be exploited as a detector sensitive to very weak system disturbance. Qualitative and quantitative data of the onset of the Duffing regime offers ultimately improved control over the system under duty. For future applications, aiming for operation within this regime or for operation in the harmonic regime at high amplitudes, this is of essential interest.

In the following paragraphs, we briefly review the most important aspects of a Duffing oscillator and extract the effective Young's modulus of our sandwich structured nanobeam from the analysis of it's operation in the Duffing regime.

The harmonically driven Duffing oscillator

To account for the nonlinear behavior of the oscillator, the potential has to be extended by terms going beyond the quadratic term $m_{\text{eff}}\Omega_{\text{m}}^2 x^2/2$. In an expansion of a symmetric potential (as is the case for doubly clamped nanobeams) around its minimum all terms with odd parity are zero. This implies that the next relevant term is proportional to x^4, leading to the additional restoring force term αx^3 in the differential equation of the oscillator. The constant α is the so-called Duffing parameter and characterizes the nonlinear force dependence on the mechanical displacement. The full differential equation of a Duffing

oscillator thus reads

$$m_{\text{eff}}\ddot{x}(t) + m_{\text{eff}}\Gamma_{\text{m}}\dot{x}(t) + m_{\text{eff}}\Omega_{\text{m}}^2 x(t) + \alpha x^3(t) = K\cos(\omega t) \ . \tag{4.18}$$

We have here assumed a harmonic driving force with frequency ω and amplitude K. In electromechanical systems equation (4.18) is valid for a weak probe at the microwave cavity's resonance ($\omega_{\text{p}} = \omega_{\text{c}}$), a configuration without back-action on the mechanical mode as derived in Section 5.1. An overview of the most relevant phenomena of a Duffing oscillator are presented in Ref. [229]. Our aim is to determine the effective Young's modulus of the nanobeam. For this purpose, it is sufficient to analyze the amplitude of the mechanical oscillation as a function of drive frequency, including the shift in eigenfrequency, as discussed further below. We focus on the experimental extraction of the Duffing parameter α and the onset of nonlinear behavior, i.e. the critical amplitude x_{crit}.

The left side of Figure 4.14 shows a typical amplitude spectrum of a Duffing oscillator with a drive sufficiently strong to generate amplitudes exceeding x_{crit}. We see that the frequency spectrum becomes tilted. If $\alpha > 0$ ($\alpha < 0$), the nonlinearity hardens (weakens) the beam, the eigenfrequency shifts to higher (lower) frequency values. For tensile stressed doubly clamped nanobeams the increase in tension for large displacements usually leads to hardening of the beam in contrast to nanocantilevers [152]. Therefore, we restrict the discussion to the case $\alpha > 0$ as shown in Figure 4.14. The red curve of the left side of Figure 4.14 shows the amplitude spectrum of a frequency upsweep. At the point B_{up} a jump in the amplitude is clearly visible. This is the upper branch of the Duffing oscillator. The lower branch can be observed with a frequency downsweep, with a jump in amplitude at B_{down}, where the amplitude spectrum has a vertical slope. These two points indicate a hysteretic amplitude behavior what implies that the observed amplitude depends on the history of the drive. The hysteretic behavior mathematically occures from the existence of three amplitude solutions within a frequency window defined by B_{up} and B_{down}. The blue line in the left part of Figure 4.14 indicates the third, metastable amplitude solution, which is not experimentally accessible and always lies between the low and the high amplitude solution [152]. The eigenfrequency $\Omega_{\text{max}}(x_{0,\text{max}})$ can only be accessed by a frequency upsweep.

Equation (4.18) cannot be solved analytically, usually the Duffing oscillator is treated by numerical or by approximative methods. Using secular pertubation theory one can show that the amplitude response of the system follows [229]

$$x_0^2 = \frac{(K/2)^2}{(m_{\text{eff}}\Omega_{\text{m}}(\Omega - \Omega_{\text{m}}) - \frac{3}{8}\alpha x_0^2)^2 + (\frac{1}{2}m_{\text{eff}}\Gamma_{\text{m}}\Omega_{\text{m}}^2)^2} \ , \tag{4.19}$$

under the assumption that the mechanical displacement can be approximated as an harmonic oscillation plus higher order terms (which we will neglect in our discussion) $x(t) \approx x_0\cos(\omega t + \phi) + \mathcal{O}(\omega^2)$. Substitution of x_0 with the dimensionless amplitude $a = \sqrt{\alpha/(m_{\text{eff}}\Gamma_{\text{m}}\Omega_{\text{m}})}x_0$, Ω with the dimensionless drive frequency $\tilde{\Omega} = (\Omega - \Omega_{\text{m}})/\Omega_{\text{m}}$ and K with the dimensionless force amplitude $k = K\sqrt{\alpha/m_{\text{eff}}^3}/\Gamma_{\text{m}}^3$, Equation (4.19) reduces to

$$a^2 = \frac{k^2}{(2\tilde{\Omega} - \frac{3}{4}a^2)^2 + 1} \ , \tag{4.20}$$

We calculate the maximum by differentiating this equation and solving $d\tilde{\Omega}/da^2 = 0$ and find that the dimensionless resonance frequency $\tilde{\Omega}_{\text{max}} = (\Omega_{\text{max}} - \Omega_{\text{m}})/\Omega_{\text{m}}$ (see Figure 4.14)
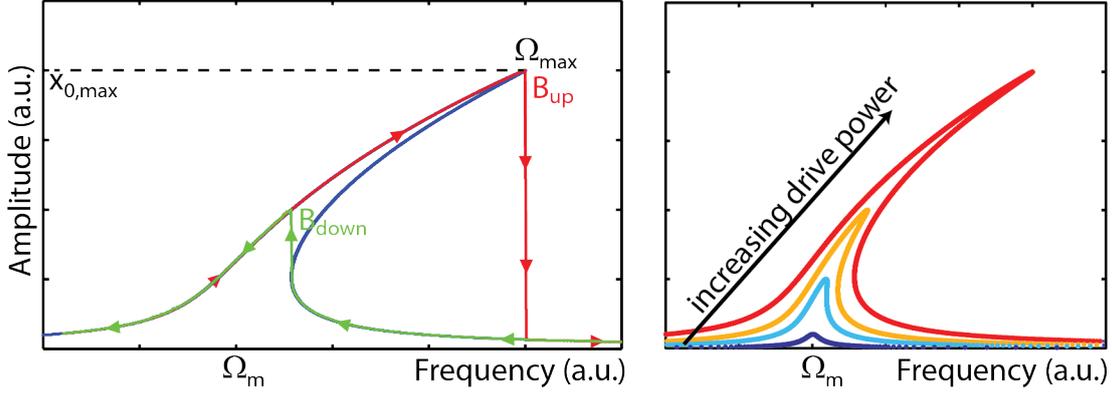
Figure 4.14: On the left hand side, a simulated amplitude spectrum of a Duffing oscillator with $\alpha > 0$ (blue curve), showing the hysteresis of the amplitude when performing an up (red curve) or down sweep (green curve) of the drive frequency, respectively. The inflection points B_{up} and B_{down}, at which the corresponding curve makes a jump, show the bifurcation between up- and down-sweep. The blue line shows the metastable branch, not accessible in experiments. The shifted eigenfrequency $\Omega_{\mathrm{max}}(x_{0,\mathrm{max}})$ can be estimated in an up-sweep. Right hand side: The behavior of the Duffing oscillator for increasing drive powers, showing the increase of the bistable region with increasing drive (from blue to red).

depends quadratically on the peak amplitude a_{max}, $\tilde{\Omega}_{\mathrm{max}} = 3/8a_{\mathrm{max}}^2$, or in terms of the original parameters

$$\Omega_{\mathrm{max}} = \Omega_{\mathrm{m}} + \frac{3\alpha}{8m_{\mathrm{eff}}\Omega_{\mathrm{m}}}x_{0\mathrm{max}}^2 \ . \tag{4.21}$$

This relation is called the backbone of the Duffing resonator connecting the resonance peaks for different driving amplitudes.

The critical amplitude is the amplitude where the two bifurcation points B_{up} and B_{down}, defining the hysteresis between frequency up and down sweep, merge to a single inflection point. This requires both $d\tilde{\Omega}/da^2 = 0$ and $d^2\tilde{\Omega}/(da^2)^2 = 0$. Solving these two equations gives

$$a_{\mathrm{crit}}^2 = (4/3)^{3/2} \ . \tag{4.22}$$

The knowledge of the critical dimensionless amplitude a_{crit} and the possibility to extract α enables us to calculate the critical amplitude x_{crit}, according to our previous definition of the dimensionless amplitude a,

$$x_{\mathrm{crit}} = \sqrt{\frac{a_{\mathrm{crit}}^2 m_{\mathrm{eff}}\Gamma_{\mathrm{m}}\Omega_{\mathrm{m}}}{\alpha}} \ . \tag{4.23}$$

Experimentally this implies, that we can calculate α from Equation (4.21) if we know the displacement spectral density. Equation (4.23) allows then to extract the critical amplitude.

Unterreithmeier *et al.* presented a relation between Duffing parameter, eigenfrequency and material properties of a nanobeam [170], which allows to estimate the effective Young's modulus of the nanobeam, the last relevant system parameter to characterize the mechanical oscillation. One obtains

$$\Omega_{\mathrm{m}} = \frac{\pi}{L}\sqrt{\frac{\sigma}{\rho}} \ , \tag{4.24}$$

$$\alpha = m_{\mathrm{eff}}\pi^4\frac{E + \frac{3}{2}\sigma}{4L^4\rho} \ . \tag{4.25}$$
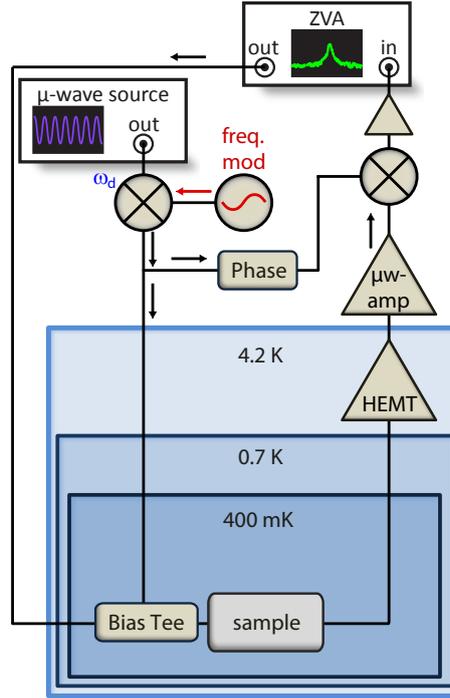
Figure 4.15: Schematic of the setup used to estimate the Duffing parameter. We use the same homodyne setup as before for the determination of the electromechanical coupling constant. The pump field's frequency corresponds to the μ-wave cavity eigenfrequency, to not disturb the mechanical motion. Additionally an AC driving field is combined with the pump field employing a ZVA network analyzer.

where E is Young's modulus, σ the tensile stress, ρ the density and L is the length of the beam structure. The derivation of these equations is achieved by exploiting Euler's beam theory. To estimate the effective Young's modulus, we define an effective density of the beam and use the stress estimated in our system in Section 4.5.1.

Accessing the Duffing parameter

The measurement of the critical amplitude to estimate the Duffing parameter was performed in the dilution fridge No.1 at a temperature of approximately 400 mK. A schemtatic of the setup is shown in Figure 4.15. The setup is the identical homodyne setup with calibrated cable lengths as in Section 5.2, but the spectrum analyzer is replaced by a ZVA vector network analyzer to drive the mechanical motion of the beam. This is accomplished by combining the AC output of the network analyzer with the probe tone generated by the microwave source at the mixing chamber using a cold bias tee. The probe tone is set to the cavity eigenfrequency $\omega_p = \omega_c$ and is fixed to a power of -83 dBm to minimize electromechanical back-action on the nanobeam. It is frequency modulated with $(\Omega_{\text{mod}} - \Omega_{\text{m}})/2\pi = -50$ Hz using a modulation depth of 100 kHz to calibrate the mechanical amplitude. After transmission through the sample, followed by an amplifier chain, the tone is down converted to a DC-signal using an IQ-mixer and part of the probe tone as reference. The phase quadrature is fed into the input of the network analyzer. Hereby the frequency modulation experiences the same transduction as the mechanical motion (see Section 5.2 and Ref. [230] for more details) allowing for calibration of the mechanical
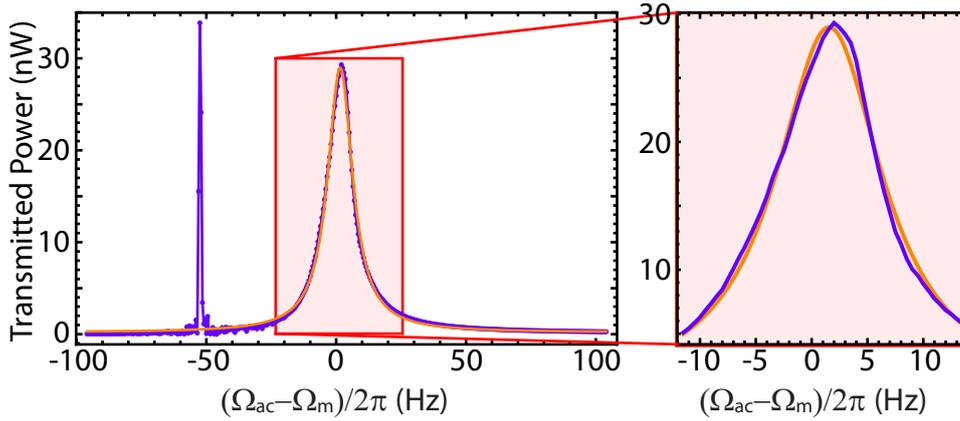
Figure 4.16: The spectrum of the nanobeam including the calibration peak for a probe power of $-91\,\mathrm{dBm}$. The orange curve is a Lorentzian fit to the spectrum. On the right we zoom to the mechanical response. The spectrum does not agree to a Lorentzian lineshape, clearly indicating the onset of the Duffing response.

displacement spectrum.

A typical power spectrum as function of the drive frequency Ω_{ac} including the calibration peak resulting from the frequency modulation is shown in Figure 4.16 and a zoom of the mechanical resonance including a Lorentzian fit to emphasize the onset of nonlinearity is shown on the right. Increasing the AC drive power of the network analyzer, we clearly observe nonlinear behavior of the nanobeam. Figure 4.17 shows the detected mechanical displacement spectrum for different AC drive powers of a frequency up sweep (due to technical reasons we cannot perform down sweeps). The lowest, blue curve, corresponding to a drive power of $-100\,\mathrm{dBm}$ shows Lorentzian behavior. The remaining curves are recorded with increasing drive power in $1\,\mathrm{dB}$ steps, starting at drive a power of $-95\,\mathrm{dBm}$ and clearly show the expected evolution of a Duffing resonator. The dotted light blue line is a fit of the backbone curve following Equation (4.21). It yields a Duffing parameter of $\alpha = 1.99 \times 10^{11}\,\mathrm{N/m^3}$. Note, that Equation (4.21) does not require knowledge on the driving force used in the experiment. The resulting critical amplitude is $x_{crit} = 2.57\,\mathrm{nm}$.

Using Equation (4.25) and $\sigma_{eff} = 199\,\mathrm{MPa}$, we obtain for our structure an effective Young's modulus of $E_{eff} = 140\,\mathrm{GPa}$. This value is in good agreement to the estimated Young's modulus $E_{calc} = (E_{SiN}A_{SiN} + E_{Nb}A_{Nb})/A_{tot} = 173\,\mathrm{GPa}$, where $E_{SiN} = 300\,\mathrm{GPa}$ and $E_{Nb} = 105\,\mathrm{GPa}$ are the Young's moduli of silicon nitride and Nb respectively. A_{SiN}, A_{Nb} and A_{tot} are the profiles of the single layers and the total profile of the beam respectively. The difference between E_{eff} and E_{calc} can be attributed to the change of the Young's modulus while processing the single layers. Unterreithmeier *et al.* [170] observed a reduction of the Young's modulus in silicon nitride thin films from $300\,\mathrm{GPa}$ to $100\,\mathrm{GPa}$. We assume E_{eff} to represent the more accurate value, since we cannot estimate the difference of the initial Young's moduli for the processed sample compared to the original ones.

We have shown, that the nanomechanical resonator of our electromechanical system exhibits a Duffing like behavior for high direct driving amplitudes, a feature well known and studied in NEMS and MEMS systems. The analysis of the backbone curve allows to extract the Duffing parameter $\alpha = 1.99 \times 10^{11}\,\mathrm{N/m^3}$ and the critical displacement amplitude $x_{crit} = 2.57\,\mathrm{nm}$ of the nanobeam. Thereby we determine the effective Young's
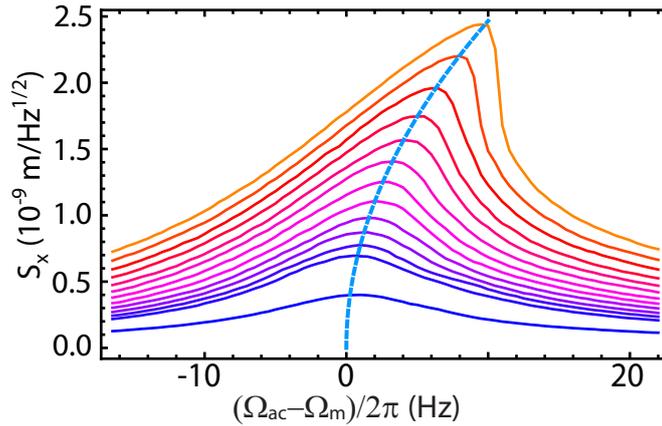
Figure 4.17: The mechanical displacement spectrum of the nanobeam for increasing driving powers. The blue curve corresponds to the lowest driving power of $-100\,\mathrm{dBm}$, the second blue curve to a drive power of $-95\,\mathrm{dBm}$. The drive power increases in $1\,\mathrm{dB}$ steps up to the orange curve with a driving power of $-84\,\mathrm{dBm}$. The dotted light blue line is the backbone curve of the system obtained by fitting equation 4.21 to the maximum amplitudes.

modulus of the sandwich structure.

4.6 Summary and discussion

In this chapter we present the most important sample parameters and discussed the production steps used to fabricate the sample consisting of a niobium CPW $\lambda/4$ microwave cavity capacitively coupled to a $\mathrm{Nb/Si_3N_4}$ bilayer nanobeam, placed in the cavities voltage antinode.

The microwave cavity is shows a resonance frequency of $\omega_c/2\pi = 6.070\,\mathrm{GHz}$, an external decay rate of $\kappa_{ex}/2\pi = 339\,\mathrm{kHz}$ and an overall cavity linewidth of $\kappa/2\pi = 759\,\mathrm{kHz}$. We calculate the electromechanical coupling to $G/2\pi = 6.36\,\mathrm{kHz/nm}$ from the sample geometry. This is a factor of six lower than the experimentally determined coupling (see Section 5.2.2). We attribute the difference to the simplification of treating the coupling capacitance as a plate capacitance, neglecting all inhomogeneities contributing to the capacitance.

The sandwich structured nanobeam, made out of a highly stress silicon nitride film and a niobium thin film shows an eigenfrequency of $\Omega_m/2\pi = 1.45\,\mathrm{MHz}$ and a mechanical decay rate of $\Gamma_m/2\pi = 2.59\,\mathrm{Hz}$ at $32\,\mathrm{mK}$, estimated by ring down measurements and corresponding to a Q-factor of $Q_m = 5.60 \times 10^5$. By comparing the mechanical resonance frequency to theory we estimate the stress in our structure to $\sigma_{eff} = 199\,\mathrm{MPa}$. Our observations show that the damping is temperature dependent and can be attributed to the coupling of acoustic excitations to two level systems, a phenomenon observed in most amorphous solid state systems. We furthermore find that the double layer structure, consisting of an amorphous insulator and a polycrystalline superconductor, behaves as an effective amorphous single layer structure, corroborating the temperature dependence of the damping.

The well-defined behavior of the mechanical resonance frequency enables the use of the mechanical oscillator as a thermometer. Precise measurement of the mechanical resonance frequency allows thus for testing the thermalization of the mechanical mode with

temperature. We observe a good thermalization of the sample down to $30\,\mathrm{mK}$.

Further analysis of the damping under the influence of artificial white noise could clarify the origin of the two level systems allowing to minimize their influence. White noise does not heat the structure but drives the mechanical motion as well as TLS transitions. This could shed new light onto the physical background of the TLS.

In this chapter we also present a detailed analysis of the nonlinear response of the nanobeam in the Duffing regime. We determine in this context the Duffing parameter to $\alpha = 1.99 \times 10^{11}\,\mathrm{N/m^3}$ and a critical displacement amplitude of $x_\mathrm{crit} = 2.57\,\mathrm{nm}$. This allows to calculate the effective Young's modulus of the structure to $E_\mathrm{eff} = 140\,\mathrm{GPa}$, in good agreement to theoretical estimation based on the individual material components.

The spectroscopic analysis of the mechanical eigenfrequency and the Duffing parameter are thus an important tool to characterize the system parameters of mechanical oscillators fabricated from more than one layer. These systems open the avenue to exploit the favorable parameters of each material system or to study the influence of more complex layers, like ferro- or ferrimagnetic systems. In Section 6.3 we show that we can even map the Duffing nonlinearity into the microwave regime, bringing applications like an electromechanical detector of qubit states into reach.

5

Single tone experiments

Systems employing a parametric coupling between an optical and a mechanical mode have been studies intensively over the last years. Here, the holy grail of was to cool the mechanical mode into the ground-state and still be able to resolve its motion, what was achieved only recently [78, 113]. Limitations, imposed by system parameters or the measurement setup were studied extensively theoretically [103, 105–108, 231–234] and experimentally in various systems, where we have to distinguish precise position measurement [46, 48, 235, 236], active feedback cooling (cold damping) [45, 62, 63, 237, 238] and radiation pressure cooling [47, 76, 100–102, 109, 110, 239–241]. The latter lead to observations of low mechanical excitation numbers [32, 75, 78, 111, 113]. Limitations include the necessity to operate in the resolved sideband regime where the mechanical frequency exceeds the optical decay rate, amplitude and phase noise of the light sources and noise from amplifying the signal. Schemes to study these limitations and to achieve ground-state cooling of the mechanical oscillator involve one drive tone used to manipulate and to read out the system.

We review these basic features of opto/electromechancial systems in this section to get insight in the underlying physical phenomena. For illustration purpose, we discuss optomechanical features on a Fabry-Perot cavity with one moveable mirror (see Figure 5.1). All results achieved are perfectly valid for other opto-/electromechanical systems, as for the electromechanical system we study in this work. We present the optomechancial Hamiltonian and derive the most prominent features including linewidth broadening/narrowing, the optical spring effect and sideband cooling/amplification of the mechanical mode. We also show how to extract the optomechanical vacuum coupling and hereby calibrate the attenuation of the microwave input lines of the experimental setup. We estimate the optomechanical vacuum coupling to $g_0/2\pi = 1.26\,\mathrm{Hz}$ and experimentally validate the optomechanical influence on the mechanical linewidth and the optical spring effect. Further, we show cooling of the mechanical mode to an average occupation of $\bar{n}_\mathrm{m} \approx 13$. Analysis of our measurement reveals a position measurement uncertainty a factor 100 away from the Heisenberg limit of $\sqrt{2}\hbar$ for an optimally red detuned drive tone.
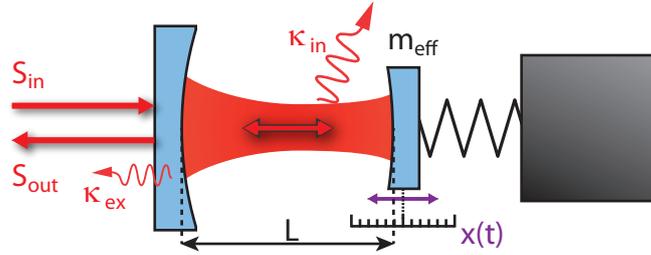
Figure 5.1: Scheme of a generic optomechanical system, showing a Fabry-Perot cavity with one mirror free to vibrate.

5.1 Electromechanical features

5.1.1 Electromechanical interaction

In our discussion of the fundamental electromechanical features, we partly follow the more detailed derivation given by Schliesser [242].

Considering a Fabry-Perot cavity in which one mirror is free to move, the cavity resonance condition is a function of the displacement $x(t)$ with the frequency of the mechanical motion Ω_m. For small mechanical amplitudes, the coupling between cavity resonance frequency and mechancical displacement is linear with the coupling constant $G = \partial \widetilde{\omega}_\mathrm{c}/\partial x$. The coupling between the two modes $G = -\widetilde{\omega}_\mathrm{c}/L$, is defined by the geometric boundary conditions, in the case of a Fabry-Perot cavity with length L and resonance frequency $\widetilde{\omega}_\mathrm{c}$. For the electromechanical system we study in this work (see Chapter 4 for details), the coupling follows from change of the overall capacitance C due to the mechanical motion. That is, $G = (\partial C_\mathrm{g}/\partial x)2Z\widetilde{\omega}_\mathrm{c}^2/2\pi$ as discussed in more detail in Section 4.4, for a schematic of the system we point the reader to Figure 4.8. To compare different opto-/electromechanical systems, it is advantageous to define the electromechanical vacuum coupling $g_0 = G/x_\mathrm{zpf}$, where $x_\mathrm{zpf} = \sqrt{\hbar/2m_\mathrm{eff}\Omega_\mathrm{m}}$ is the root-mean-square amplitude of the mechanical zero point fluctuations. The vacuum coupling g_0 allows for comparison of opto- and electromechanical systems working in different frequency regimes. A second advantage of this definition for the vacuum coupling lies in the freedom to define or rescale the displacement x, without affecting g_0 [230].

Neglecting the back-action on the mechanical mode, the mechanical motion leads to the formation of Stokes and anti-Stokes sidebands around a monochromatic drive tone driving the cavity. As discussed in more detail in Section 6.4, even higher order sidebands become observable for sufficiently high mechanical amplitudes due to the modulation of the intra-cavity field.

Classical analysis

To get insight into the effects in optomechanical systems we consider the mutual coupling of optical and mechanical degrees of freedom. The optical mode influences the motion of the mechanical oscillator by radiation pressure. The back-action force F_rp acting on the vibrating mirror is proportional to the average number of intra-cavity photons $\bar{n}_\mathrm{c}$, transferring their momentum onto the movable mirror. In total

$$F_\mathrm{rp} = \frac{\bar{n}_\mathrm{c}\hbar\widetilde{\omega}_\mathrm{c}}{L} = -\hbar G\bar{n}_\mathrm{c} \; . \tag{5.1}$$

For a cavity with linewidth κ and a mechanical mode with linewidth Γ_{m}, eigenfrequency Ω_{m} and effective mass m_{eff}, the following equation of motion describes the physics of the complete system. Note, that the differential equations are written in a frame rotating with the laser frequency ω_{d} as derived with coupled mode theory [243],

$$\dot{a}(t) = \left(i(\bar{\Delta} - Gx(t)) - \kappa/2\right) a(t) + \sqrt{\frac{\kappa_{\mathrm{ex}}}{2}} s_{\mathrm{in}}(t) \, , \tag{5.2}$$

$$\ddot{x}(t) + \Gamma_{\mathrm{m}}\dot{x}(t) + \Omega_{\mathrm{m}}^2 x(t) = \frac{F_{\mathrm{rp}}}{m_{\mathrm{eff}}} = -\hbar G \frac{|a(t)|^2}{m_{\mathrm{eff}}} \, . \tag{5.3}$$

These two coupled equations describe a driven optical cavity, parametrically coupled to the mechanical displacement via $-Gx(t)$ and a mechanical harmonic oscillator coupled to the photons inside the cavity via the radiation pressure force F_{rp}. We have introduced the field amplitude $a(t)$ and normalize it to the photon flux in the cavity, $|a(t)|^2 = n_{\mathrm{c}}(t)$. Furthermore, $\bar{\Delta} = \omega_{\mathrm{d}} - \widetilde{\omega}_{\mathrm{c}}$ is the detuning of the driving field from cavity resonance. To analyze these coupled linear differential equations we look for static solutions $\bar{a}$, $\bar{x}$ and dynamical ones $\delta a(t)$, $\delta x(t)$. The full solution is given by a superposition of both, $a(t) = \bar{a} + \delta a(t)$ and $x(t) = \bar{x} + \delta x(t)$, where we demand the dynamical part to be small compared to the static one. For a constant drive amplitude $\bar{s}_{\mathrm{in}}$ the static solution where all time derivatives vanish is given by

$$\bar{a} = \frac{\sqrt{\kappa_{\mathrm{ex}}/2}}{-i(\bar{\Delta} - G\bar{x}) + \frac{\kappa}{2}} \bar{s}_{\mathrm{in}} \text{ and} \tag{5.4}$$

$$\bar{x} = -\frac{\hbar G \bar{a}^2}{m_{\mathrm{eff}}\Omega_{\mathrm{m}}^2} \, . \tag{5.5}$$

Here, we have assumed the phase of the drive field to be adjusted in a way that $\bar{a}$ becomes real, what is easily achieved in experiments. The dynamic response modulates both degrees of freedom around this set of static solutions. We restrict ourselves to a small fluctuating force $\delta F(t)$ arising from various noise contributions, acting on the dynamic parts of the mechanical mode. Entering the full expressions $a(t) = \bar{a} + \delta a(t)$ and $x(t) = \bar{x} + \delta x(t)$ into equations (5.2) and (5.3), introducing the equilibrium detuning $\Delta = \omega_{\mathrm{d}} - (\widetilde{\omega}_{\mathrm{c}} + G\bar{x}) \equiv \omega_{\mathrm{d}} - \omega_{\mathrm{c}}$[1] and neglecting higher order terms in $\delta a(t)$ and $\delta x(t)$, these equations modify to

$$\dot{\delta a}(t) = (i\Delta - \kappa/2)\delta a(t) - iG\bar{a}\delta x(t) \text{ and} \tag{5.6}$$

$$\ddot{\delta x}(t) + \Gamma_{\mathrm{m}}\dot{\delta x}(t) + \Omega_{\mathrm{m}}^2 \delta x(t) = -\frac{\hbar G\bar{a}}{m_{\mathrm{eff}}}(\delta a(t) + \delta a^*(t)) + \delta F(t) \, . \tag{5.7}$$

This set of equations is most easily accessed in frequency domain. Performing a Fourier transformation with $f(\Omega) = \int_{-\infty}^{\infty} dt f(t)\exp(i\Omega t)$ and exploiting $\delta a^*(\Omega) = (\delta a(-\Omega))^*$, we find:

$$(-i(\Delta + \Omega) + \kappa/2)\delta a(\Omega) = -iG\bar{a}\delta x(\Omega) \, , \tag{5.8}$$

$$(+i(\Delta - \Omega) + \kappa/2)\delta a^*(\Omega) = +iG\bar{a}\delta x(\Omega) \, , \tag{5.9}$$

$$(\Omega_{\mathrm{m}}^2 - \Omega^2 - i\Gamma_{\mathrm{m}}\Omega)\delta x(\Omega) = -\frac{\hbar G\bar{a}}{m_{\mathrm{eff}}}(\delta a(\Omega) + \delta a^*(\Omega)) + \frac{\delta F(\Omega)}{m_{\mathrm{eff}}} \, . \tag{5.10}$$

---

[1]The term $G\bar{x}$ is very small in our system, so $\omega_{\mathrm{c}} \approx \widetilde{\omega}_{\mathrm{c}}$.

Here, Equations (5.8) and (5.9) correspond to the Stokes and anti-Stokes sideband for a non-zero displacement $\delta x(\Omega)$ at frequency Ω:

$$\delta a(\Omega) = \frac{-iG\bar{a}}{-i(\Delta + \Omega) + \kappa/2}\delta x(\Omega)\,, \tag{5.11}$$

$$\delta a^*(\Omega) = \frac{+iG\bar{a}}{+i(\Delta - \Omega) + \kappa/2}\delta x(\Omega)\,. \tag{5.12}$$

Since the mechanical amplitude is maximal at $\Omega = \Omega_{\mathrm{m}}$, the sidebands are centered around $\omega_{\mathrm{c}} \pm \Omega_{\mathrm{m}}$. The modulation of the intra-cavity field gives rise to an oscillating force that acts on the mechanical mode

$$
\begin{aligned}
\delta F_{\mathrm{rp}}(\Omega) = &-\hbar G\bar{a}(\delta a(\Omega) + \delta a^*(\Omega)) \\
= &-\hbar G^2 \bar{n}_{\mathrm{c}}\left(\frac{\Delta + \Omega}{(\Delta + \Omega)^2 + (\kappa/2)^2} + \frac{\Delta - \Omega}{(\Delta - \Omega)^2 + (\kappa/2)^2}\right)\delta x(\Omega) \\
&+ i\hbar G^2 \bar{n}_{\mathrm{c}}\left(\frac{\kappa/2}{(\Delta + \Omega)^2 + (\kappa/2)^2} - \frac{\kappa/2}{(\Delta - \Omega)^2 + (\kappa/2)^2}\right)\delta x(\Omega)\,. \tag{5.13}
\end{aligned}
$$

The additional force due to radiation pressure shows dynamical back-action [244] on the mechanical degree of freedom. The coupling to the radiation field also modifies the response of the mechanical mode to an external force $\delta F(\Omega)$. Substituting the expression (5.13) into (5.10) and sorting the real and complex terms, we can write

$$\delta x(\Omega) = \chi_{\mathrm{eff}}(\Omega)\delta F(\Omega)\,. \tag{5.14}$$

The effective susceptibility $\chi_{\mathrm{eff}}(\Omega)$ accounts for the dynamical back-action by modifying the mechanical damping and spring constant:

$$\chi_{\mathrm{eff}}(\Omega)^{-1} = m_{\mathrm{eff}}\left(-\Omega^2 + \left(\Omega_{\mathrm{m}}^2 + \frac{k_{\mathrm{ba}}(\Omega)}{m_{\mathrm{eff}}}\right) - i[\Gamma_{\mathrm{m}} + \Gamma_{\mathrm{ba}}(\Omega)]\Omega\right) \tag{5.15}$$

compared to the undisturbed mechanical susceptibility

$$\chi_{\mathrm{m}}(\Omega)^{-1} = m_{\mathrm{eff}}\left(-\Omega^2 + \Omega_{\mathrm{m}}^2 - i\Gamma_{\mathrm{m}}\Omega\right)\,, \tag{5.16}$$

the effect of the dynamical back-action is clearly visible. Both the mechanical damping and the spring constant are modified by a term $\Gamma_{\mathrm{ba}}(\Omega)$ and $k_{\mathrm{ba}}(\Omega)/m_{\mathrm{eff}}$, respectively, arising from the fluctuating contribution to the radiation pressure. Explicitly, the modification of the mechanical damping and spring constant are given by:

$$\Gamma_{\mathrm{ba}} = \frac{\hbar G^2 \bar{n}_{\mathrm{c}}}{m_{\mathrm{eff}}\Omega}\left(\frac{\kappa/2}{(\Delta + \Omega)^2 + (\kappa/2)^2} - \frac{\kappa/2}{(\Delta - \Omega)^2 + (\kappa/2)^2}\right)\,, \tag{5.17}$$

$$k_{\mathrm{ba}} = \hbar G^2 \bar{n}_{\mathrm{c}}\left(\frac{\Delta + \Omega}{(\Delta + \Omega)^2 + (\kappa/2)^2} + \frac{\Delta - \Omega}{(\Delta - \Omega)^2 + (\kappa/2)^2}\right)\,. \tag{5.18}$$

The change of the eigenfrequency by photons is known as optical spring effect, to our knowledge first observed in a massive 1.5 t niobium antenna used for gravitational wave detection [53]. Importantly, the mechanical mode still follows the dynamics of a damped harmonic oscillator, with the natural damping and eigenfrequency replaced by effective

ones [62, 100, 102]. For frequencies close to the mechanical resonance, we can approximate $\Omega \approx \Omega_\mathrm{m}$. Under these conditions

$$\Gamma_\mathrm{eff} \approx \Gamma_\mathrm{m} + 2g_0^2 \bar{n}_\mathrm{c} \left(\frac{\kappa/2}{(\Delta + \Omega_\mathrm{m})^2 + (\kappa/2)^2} - \frac{\kappa/2}{(\Delta - \Omega_\mathrm{m})^2 + (\kappa/2)^2} \right) , \tag{5.19}$$

$$\Omega_\mathrm{eff} \approx \Omega_\mathrm{m} + g_0^2 \bar{n}_\mathrm{c} \left(\frac{\Delta + \Omega_\mathrm{m}}{(\Delta + \Omega_\mathrm{m})^2 + (\kappa/2)^2} + \frac{\Delta - \Omega_\mathrm{m}}{(\Delta - \Omega_\mathrm{m})^2 + (\kappa/2)^2} \right) , \tag{5.20}$$

where we have used that the effect of the optical spring is small compared to Ω_m. The mechanical linewidth experiences the strongest changes for $\Delta = \pm\Omega_\mathrm{m}$. For a red detuned drive tone with respect to the cavity resonance the mechanical linewidth increases. Further below, we show that this corresponds to cooling of the mechanical mode. In contrast, for a blue detuned drive tone the effective linewidth can become zero. In this regime, the mechanical oscillator starts performing self-sustaining oscillations [52, 53, 65, 94]. For a drive field with $\omega_\mathrm{d} = \omega_\mathrm{c}$, the mechanical properties are not disturbed. This configuration can be used to study the intrinsic parameters of the mechanical vibration and provides easy access to the opto-/electromechanical coupling.

Quantum cavity electromechanics

The identical system can be analyzed within the framework of quantum mechanics. For this purpose, we write down the corresponding Hamiltonian introduced by Law [198] and further studied in Refs. [103, 104],

$$\hat{H} = \hbar\widetilde{\omega}_\mathrm{c} \left(\hat{n}_\mathrm{c} + \frac{1}{2} \right) + \hbar\Omega_\mathrm{m} \left(\hat{n}_\mathrm{m} + \frac{1}{2} \right) + \hbar G \hat{n}_\mathrm{c} \hat{x} + \hat{H}_\mathrm{d} . \tag{5.21}$$

Here, $\hat{n}_\mathrm{c} = \hat{a}^\dagger \hat{a}$ and $\hat{n}_\mathrm{m} = \hat{b}^\dagger \hat{b} = \frac{1}{2}[\frac{m_\mathrm{eff}\Omega_\mathrm{m}}{\hbar}\hat{x}^2 + \frac{\hat{p}^2}{m_\mathrm{eff}\Omega_\mathrm{m}\hbar}]$ are the intra-cavity (photon) and mechanical (phonon) excitation number operators. The photon and phonon creation (annihilation) operators are given by $\hat{a}^\dagger$ ($\hat{a}$) and $\hat{b}^\dagger$ ($\hat{b}$), respectively. The operator $\hat{x} = x_\mathrm{zpf}(\hat{b}^\dagger + \hat{b})$ is the mechanical displacement operator and $\hat{p}$ the corresponding mechanical momentum. The term

$$\hat{H}_\mathrm{d} = i\hbar\sqrt{\frac{\kappa_\mathrm{ex}}{2}} \left(\bar{s}_\mathrm{in}\hat{a}^\dagger e^{-i\omega_\mathrm{d}t} - \bar{s}_\mathrm{in}\hat{a}e^{+i\omega_\mathrm{d}t} \right) \tag{5.22}$$

represents the external drive fields. The drive amplitude $\bar{s}_\mathrm{in}$ is normalized to the phonon flux resulting from the drive field's intensity $|\bar{s}_\mathrm{in}|^2 = P_\mathrm{d}/\hbar\omega_\mathrm{d}$. The interaction Hamiltonian $\hat{H}_\mathrm{int} = \hbar G \hat{n}_\mathrm{c} \hat{x}$ is a consequence of the integration of $-F_\mathrm{rp}d\hat{x}$.

By introducing damping for the optical and mechanical degrees of freedom and noise terms due to fluctuations, we derive the Quantum Langevin equations in a frame rotating with ω_d first presented in Ref. [245].

$$\frac{d}{dt}\hat{a}(t) = \left(+i\bar{\Delta} - \frac{\kappa}{2} \right) \hat{a}(t) - iG\hat{x}(t)\hat{a}(t) + \sqrt{\frac{\kappa_\mathrm{ex}}{2}}(\bar{s}_\mathrm{in} + \delta\hat{s}_\mathrm{in}(t)) + \sqrt{\frac{\kappa}{2}}\delta\hat{s}_\mathrm{vac}(t) , \tag{5.23}$$

$$\frac{d}{dt}\hat{x}(t) = \frac{\hat{p}(t)}{m_\mathrm{eff}} , \tag{5.24}$$

$$\frac{d}{dt}\hat{p}(t) = -m_\mathrm{eff}\Omega_\mathrm{m}^2\hat{x}(t) - \hbar G\hat{a}^\dagger(t)\hat{a}(t) - \Gamma_\mathrm{m}\hat{p}(t) + \delta\hat{F}_\mathrm{th}(t) . \tag{5.25}$$

The noise term $\delta\hat{s}_\mathrm{in}(t)$ accounts for fluctuations of the drive field, while $\delta\hat{s}_\mathrm{vac}(t)$ contains the non vanishing vacuum noise contributions (and can be extended to include all other

non vanishing noise contributions as well). To account for the Brownian motion of the mechanical oscillator, we introduced thermal fluctuations $\delta\hat{F}_{\text{th}}(t)$. We also assume that the cavity has zero thermal excitations, which is justified since the temperature regime we consider is sufficiently low, $\hbar\omega_{\text{d}} < k_{\text{B}}T$. Ref. [246] shows that the following commutation relation applies

$$\left[\delta s_i(t), \delta s_i^\dagger(t')\right] = \delta(t - t') \tag{5.26}$$

with the following correlator

$$\langle \delta s_i(t)\delta s_i^\dagger(t')\rangle = \delta(t - t') \ . \tag{5.27}$$

The thermal correlator accounting for Brownian motion of the mechanical mode is [245]

$$\langle \delta\hat{F}_{\text{th}}(t)\delta\hat{F}_{\text{th}}(t')\rangle = \hbar m_{\text{eff}}\Gamma_{\text{m}}\int \frac{d\Omega}{2\pi}\left(\coth\left(\frac{\hbar\Omega}{2k_{\text{B}}T}\right) + 1\right)e^{-i\Omega(t-t')} \ . \tag{5.28}$$

Solving the Langevin equations (5.23)–(5.24) is performed as in the classical case; a static solution $\bar{a}$ and $\bar{x}$ is split from the dynamical part $\delta\hat{a}(t)$ and $\delta\hat{x}(t)$. The static solutions are again given by equations (5.4) and (5.5). For a strong coherent drive field $\bar{a} \gg 1$, we can derive a linearized version of the initial differential equations, which we then transform into Fourier space. This gives analogous to the derivation before:

$$(-i(\Delta + \Omega) + \kappa/2)\delta\hat{a}(\Omega) = -iG\bar{a}\delta\hat{x}(\Omega) + \sqrt{\frac{\kappa_{\text{ex}}}{2}}\delta\hat{s}_{\text{in}}(\Omega) + \sqrt{\frac{\kappa}{2}}\delta\hat{s}_{\text{vac}}(\Omega)\,, \tag{5.29}$$

$$(+i(\Delta - \Omega) + \kappa/2)\delta\hat{a}^\dagger(\Omega) = +iG\bar{a}\delta\hat{x}(\Omega) + \sqrt{\frac{\kappa_{\text{ex}}}{2}}\delta\hat{s}_{\text{in}}^\dagger(\Omega) + \sqrt{\frac{\kappa}{2}}\delta\hat{s}_{\text{vac}}^\dagger(\Omega)\,, \tag{5.30}$$

$$(\Omega_{\text{m}}^2 - \Omega^2 - i\Gamma_{\text{m}}\Omega)\delta\hat{x}(\Omega) = -\frac{\hbar G\bar{a}}{m_{\text{eff}}}(\delta\hat{a}(\Omega) + \delta\hat{a}^\dagger(\Omega)) + \frac{\delta\hat{F}_{\text{th}}(\Omega)}{m_{\text{eff}}} \ . \tag{5.31}$$

According to the the Wiener-Khinchin [232] theorem the Fourier transformation of the noise correlators define the corresponding spectral noise densities[2]

$$S_{\text{ss}} \equiv \langle \delta s_i(\Omega)\delta s_i^\dagger(\Omega')\rangle = 2\pi\delta(\Omega - \Omega') \tag{5.32}$$

and the thermal noise contribution gives

$$S_{\text{FF}}^{\text{th}} \equiv \langle \delta\hat{F}_{\text{th}}(\Omega)\delta\hat{F}_{\text{th}}(\Omega')\rangle = \delta(\Omega - \Omega')\hbar m_{\text{eff}}\Gamma_{\text{m}}\left[\coth\left(\frac{\hbar\Omega}{2k_{\text{B}}T}\right) + 1\right]$$

$$\approx 4k_{\text{B}}Tm_{\text{eff}}\Gamma_{\text{m}} \ . \tag{5.33}$$

To derive the last term we have approximated $\hbar\Omega_{\text{m}} \ll k_{\text{B}}T$ and used the first order approximation $\cot(x + 1) \approx 1/x$. In an actual measurement, one wants to extract physical information from within the cavity resulting from interaction with an input field. This is realized by analysis of the field leaking out of the system. The connection between the fluctuations entering the cavity and the fluctuations leaving it can be derived by standard input-output theory [232, 246] to

$$\delta s_{out}(\Omega) = \delta s_{in}(\Omega) - \sqrt{\frac{\kappa_{\text{ex}}}{2}}\delta\hat{a}(\Omega) \tag{5.34}$$

---

[2]We mark a spectral density by $S_{\text{ii}}(\Omega)$, where "i" is the observable, the units are [(unit of i)^2/Hz]. The square root of S_{ii} is denoted by S_{i}.

These equations cover most phenomena in opto-/electromechanical systems. The introduction of static and dynamic solution leads to another interesting observation. We can factorize $\hat{H}_{\text{int}}$ by replacing $\hat{a} = \bar{a} + \delta\hat{a}$ and obtain a linearized interaction Hamiltonian [106]

$$\hat{H}_{\text{int}} \approx \hbar g_0 \bar{a} (\delta\hat{a} + \delta\hat{a}^\dagger)(\hat{b} + \hat{b}^\dagger)$$
$$= \hbar g_0 \bar{a} (\delta\hat{a}\hat{b} + \delta\hat{a}^\dagger\hat{b}^\dagger) + \hbar g_0 \bar{a} (\delta\hat{a}\hat{b}^\dagger + \delta\hat{a}^\dagger\hat{b}) , \qquad (5.35)$$

where we have neglected higher order terms. The shift of the cavity resonance due to the static mechanical displacement has been already taken into account here.

The first term is a two mode squeezer type interaction Hamiltonian (or parametric amplifer Hamiltonian) [247] and describes the transfer of energy from the optical to the mechanical mode or vice versa and joint excitations of both degrees of freedom. This term dominates for a drive tone blue detuned with respect to the cavity $\Delta > 0$. In this configuration generation of entanglement is possible or alternatively, the system operates as an parametric amplifier, as demonstrated recently in an electromechanical system [120].

The second term is a beam splitter type Hamiltonian, describing the transfer of excitations. This term dominates for a drive tone red detuned with respect to the cavity $\Delta < 0$. In this configuration quantum state transfer between optical and mechanical mode can be achieved [37]. This was in the focus during the last years as it attracted the possibility of cooling of the mechanical mode as we discuss in more detail in the next section.

Furthermore, a drive tone at cavity resonance $\Delta = 0$ has the same contribution of both terms leading to a quantum non-demolition (QND) type interaction Hamiltonian [44] commuting with the optical amplitude quadrature. Here, the mechanical mode is probed without being disturbed by the measurement. This agrees with the conclusion from semi-classical considerations stated in equations (5.19) and (5.20), that this configuration leaves Γ_{m} and Ω_{m} unchanged; i.e. no dynamical back-action is present.

Cooling and amplification of the mechanical mode

As discussed above, a red or blue detuned driving field leads to cooling or amplification of the mechanical mode. To discuss these effect we first define the mode temperature of an oscillation. The fluctuation dissipation theorem [232] allows to approximate the displacement spectral density of mechanical fluctuations for a vibrational mode in contact with a thermal bath at temperature T for high mechanical occupation $\bar{n}_{\text{m}} \approx k_{\text{B}} T / \hbar\Omega_{\text{m}} \gg 1$ as[3] [248]:

$$S_{\text{xx}}(\Omega) = |\chi_{\text{m}}(\Omega)|^2 S_{\text{FF}}^{\text{th}}(\Omega) \approx \frac{1}{2m_{\text{eff}}} \cdot \frac{2\Gamma_{\text{m}} k_{\text{B}} T}{(\Omega^2 - \Omega_{\text{m}}^2)^2 + \Gamma_{\text{m}}^2 \Omega^2} , \qquad (5.36)$$

with the Boltzmann constant k_{B}, intrinsic mechanical linewidth Γ_{m}, the mechanical eigenfrequency Ω_{m} and the effective mass of the mechanical mode m_{eff}. For high Q oscillators, we can simplify this to a Lorentzian:

$$S_{\text{xx}}(\Omega) \approx \frac{k_{\text{B}} T}{2m_{\text{eff}} \Omega_{\text{m}}^2} \cdot \frac{\Gamma_{\text{m}}}{(\Omega - \Omega_{\text{m}})^2 + \left(\frac{\Gamma_{\text{m}}}{2}\right)^2} , \qquad (5.37)$$

The mean squared amplitude of the resonator can be calculated from the mechanical displacement spectrum to

$$\langle \delta x^2 \rangle = \int_0^{+\infty} \frac{d\Omega}{2\pi} 2 S_{\text{xx}}(\Omega) \approx \frac{k_{\text{B}} T}{m_{\text{eff}} \Omega_{\text{m}}^2} . \qquad (5.38)$$

---

[3]Here we use single sided spectra.
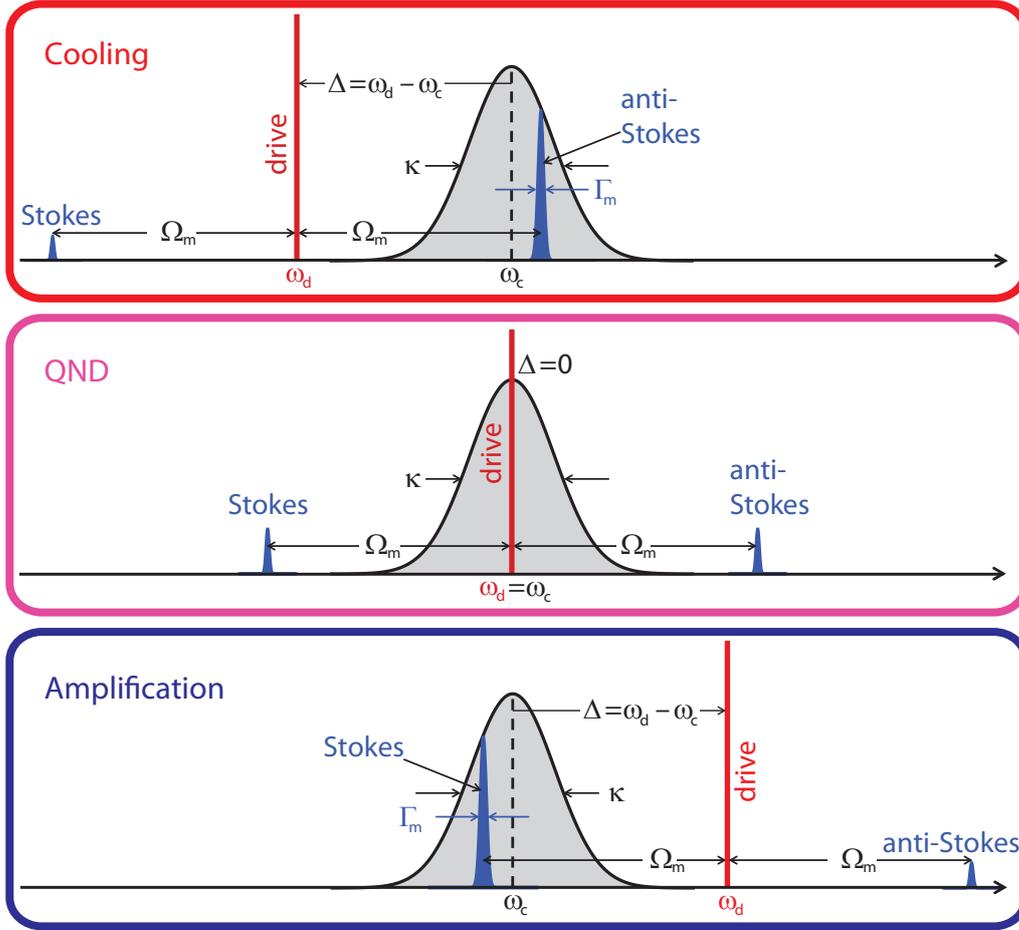
Figure 5.2: Schematic of the sideband distribution in an electromechanical system for different detunings of the drive tone with respect to the cavity resonance. The Stokes sideband is suppressed when the drive is red detuned (red box). This leads to a transfer of energy from the mechanical mode to the optical one to account for the higher energy of the photons scattered into the anti-Stokes sideband. For a blue detuned drive tone (blue box), the situation is reverse, the suppression of the anti-Stokes sideband leads to energy transfer to the mechanics. The sidebands are symmetric in the case of zero detuning (as long as $\hbar\Omega_\mathrm{m} \ll k_\mathrm{B}T$), the mechanical motion experiences no back-action from the photons inside the cavity (pink box).

With this result, we can assign a temperature to the mechanical mode

$$T_\mathrm{m} = \frac{m_\mathrm{eff}\Omega_\mathrm{m}^2}{k_\mathrm{B}}\langle\delta x^2\rangle \ . \tag{5.39}$$

If the mechanical resonator is thermalized with the environment the mode temperature corresponds to the bath temperature, $T_\mathrm{m} = T$. Applying a drive field changes the mechanical properties according to Equation (5.15) due to dynamical back-action. The thermal Langevin force resulting from the coupling to the thermal bath remains unchanged. We get

$$\langle\delta x^2\rangle = \int_0^{+\infty} \frac{d\Omega}{2\pi} 2 \left|\chi_\mathrm{eff}(\Omega)\right|^2 S_\mathrm{FF}^\mathrm{th}(\Omega) \approx \frac{k_\mathrm{B}T}{m_\mathrm{eff}\Omega_\mathrm{m}^2} \cdot \frac{\Gamma_\mathrm{m}}{\Gamma_\mathrm{eff}} \ . \tag{5.40}$$

The mode temperature changes due to the dynamical back-action

$$T_\mathrm{m} = \frac{\Gamma_\mathrm{m}}{\Gamma_\mathrm{m} + \Gamma_\mathrm{ba}}T \ . \tag{5.41}$$

We identify Γ_{ba} as the cooling or amplification rate depending on the sign of the detuning Δ. The change of the mode temperature is a consequence of coupling the mechanical oscillator not only to a thermal bath but to a photonic field disturbing the initial equilibrium position. The laser field either introduces additional dissipation leading to a new thermodynamic equilibrium with a lower temperature or drives the mechanical motion by constantly transferring energy leading to a higher mode temperature. The heating effect is not to be confused with thermal effects like photothermal pressure resulting from bolometric absorption of a photon studied in Ref. [249].

Figure 5.2 gives a second intuitive approach to understand cooling, heating and monitoring of the mechanical mode. As mentioned before, the coupling of the lightfield to a mechanical oscillator inside a cavity generates sidebands. Depending on the detuning of the drive field with respect to the cavity resonance, the relative weight of the Stokes and anti-Stokes scattered photons changes; the cavity acts as a filter. For a drive frequency on the red sideband ($\Delta < 0$), the Stokes sideband is suppressed (red box in Figure 5.2). To upconvert photons to the anti-Stokes sideband phonons are extracted from the mechanical resonator. This transfer of energy from the mechanical to the optical mode leads to cooling of the former. A drive tone on the blue sideband ($\Delta > 0$) reversed this effect. Here, the anti-Stokes sideband is suppressed by the cavity, the photons are down-converted into a photon with the anti-Stokes frequency and a phonon each, effectively amplifying the mechanical motion (blue box in Figure 5.2). A drive tone at the cavity resonance ($\Delta = 0$) populates both sidebands equally, leaving the mechanical mode unchanged, even in the case of quantized mechanical motion. This quantum non-demolition configuration allows for high sensitive monitoring of the mechanical vibration (pink box in Figure 5.2). The schematics in Figure 5.2 already show that the suppression of one sideband is the most effective for a system in the resolved sideband regime.

Electromechanical cooling in the limit of resolved sidebands

So far we have not imposed any additional assumptions on the electromechanical system. Here, we discuss the situation for a system in the resolved sideband regime, meaning the mechanical frequency is higher than the optical decoherence rate, $\Omega_m > \kappa$) [239]. This requirement is fulfilled in most present opto- and electromechanical systems. Up till now we have also neglected the noise contributions introduced in Equation (5.23). Even if we eliminate all technical noise contributions, the always present quantum noise of a coherent drive source limits the electromechanical cooling. This quantum shot noise provides a fluctuating force competing the dynamical back-action [103,104]. We analyze the fundamental cooling limits for an opto-/electromechanical system in the resolved sideband regime.

Sideband cooling in electromechanical systems in this respect is similar to laser cooling of atoms or ions [250]. In these systems, mechanical vibrations occur from traps forming an harmonic potential, that also defines the frequency of the vibrations. An additional laser drives electronic transitions. A Doppler shift due to the movement of the atom induces a coupling between the electric and the mechanical degree of freedom. Absorbed and emitted photons change in turn the momentum of the atom. A properly detuned laser with respect to the optical transition favors absorption of photons that counter the mechanical movement and thus infers cooling of the mechanical mode. The photon emitted after such a process absorbs energy from the mechanical mode, reducing the number of
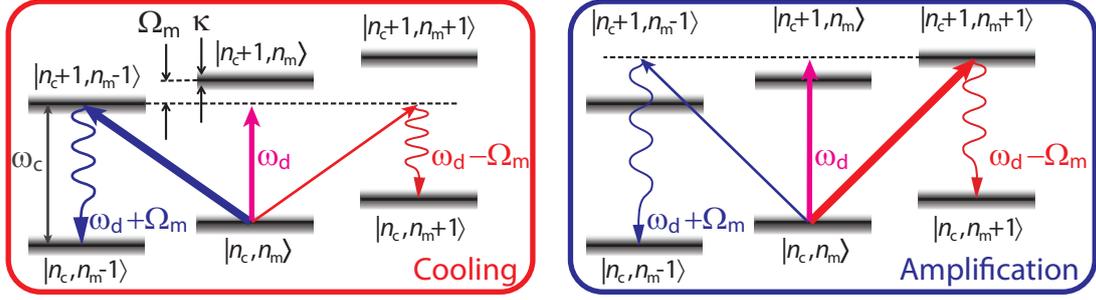
Figure 5.3: Schematic level scheme of electromechanical cooling (left, red box) and amplification
(right, blue box). The electromechanical states are product states of mechanical and optical
excitations. For a drive tone tuned to the red sideband ($\Delta = -\Omega_m$), the red Stokes scattered
sideband (red arrow) is suppressed since it is highly off resonant. The anti-Stokes sideband
(blue arrow) is driven by absorption of a mechanical excitation. For a blue detuned drive field,
the situation is opposite; the Stokes sideband is driven by down conversion into a photon and
a phonon, while the anti-Stokes sideband is suppressed.

acoustic excitations. Cooling down to the mechanical quantum ground-state with energy
$\hbar\Omega_m/2$ is possible in this configuration, provided $\Omega_m \gg \kappa$ [251, 252]. A transfer of this
scheme to opto-/electromechanical systems helps to understand cooling in the resolved
sideband regime as shown in Figure 5.3.

In this scheme the electromechanical states are simplified as product states $|n_c, n_m\rangle$,
characterized by n_c cavity excitations and n_m mechanical excitations. The electromechanical coupling is neglected. Here, a pure cavity excitation is represented by the vertical
grey arrow in the left of Figure 5.3. In contrast, if the drive field is set to $\omega_d \simeq \omega_c - \Omega_m$
(optimal red detuning, red box in Figure 5.3), it is represented by the diagonal blue arrow,
indicating a resonant driving from up-conversion by absorbtion of a phonon. Here, only
the transition from $|n_c, n_m\rangle$ to $|n_c + 1, n_m - 1\rangle$ is driven resonantly. In this picture, the
blue vertical oscillating arrow symbolizes the anti-Stokes sideband and the red vertical
oscillating arrow the Stokes sideband. The latter is not resonant, it is suppressed due to
the absence of fund states in this configuration. The number of phonons is thus reduced
in this configuration, the mechanical mode is cooled. In the case of blue detuning (blue
box in Figure 5.3), the situation is reversed. By down-converting the drive field into a mechanical excitation and a photon with frequency ω_c, the Stokes line is driven resonantly,
dominating all transitions. The mechanical mode gains phonons and is thus amplified.

This scheme gives indeed no insight to the fundamental limit on the minimum occupation when cooling a mechanical resonator in an opto-/electromechanical system. From
the quantum Langevin equations (5.23)–(5.25), we can derive the radiation pressure force
including the various noise terms:

$$
\begin{aligned}
\delta F_{\mathrm{rp}} = {}& -i\hbar G^2 \bar{n}_c \delta\hat{x}(\Omega) \left(\frac{1}{-i(\Delta + \Omega) + \kappa/2} - \frac{1}{+i(\Delta - \Omega) + \kappa/2} \right) \\
& - \hbar G \sqrt{\bar{n}_c} \frac{\sqrt{\frac{\kappa_{\mathrm{ex}}}{2}} \delta\hat{s}_{\mathrm{in}}(\Omega)) + \sqrt{\frac{\kappa}{2}} \delta\hat{s}_{\mathrm{vac}}(\Omega)}{-i(\Delta + \Omega) + \kappa/2} \\
& - \hbar G \sqrt{\bar{n}_c} \frac{\sqrt{\frac{\kappa_{\mathrm{ex}}}{2}} \delta\hat{s}^{\dagger}_{\mathrm{in}}(\Omega)) + \sqrt{\frac{\kappa}{2}} \delta\hat{s}^{\dagger}_{\mathrm{vac}}(\Omega)}{+i(\Delta - \Omega) + \kappa/2} \ .
\end{aligned}
\tag{5.42}
$$

The first line corresponds to the dynamical back-action (see Equation (5.13)) we already
obtained in the semiclassical discussion. It is covered by replacing the mechanical suscepti-

bility with χ_{eff}, see Equation (5.15). The second and third line cover quantum back-action due to fluctuations of the intra cavity photon number. The spectrum of the force resulting from quantum fluctuations can be calculated using the known fluctuation spectra (Equation (5.32)) to

$$S_{\mathrm{FF}}^{\mathrm{qba}} = \frac{\hbar^2}{2x_{\mathrm{zpf}}^2} \left(\frac{g_0^2 \bar{n}_{\mathrm{c}} \kappa}{(\Delta + \Omega)^2 + (\kappa/2)^2} + \frac{g_0^2 \bar{n}_{\mathrm{c}} \kappa}{(\Delta - \Omega)^2 + (\kappa/2)^2} \right) . \tag{5.43}$$

Further, we introduce the rates A^+ and A^-, corresponding to the rate of Stokes and anti-Stokes scattering events, respectively. They describe the annihilation (A^-) and creation (A^+) of a phonon, in analogy to the definition of rates in laser cooling and read

$$A^{\pm} = \frac{g_0^2 \bar{n}_{\mathrm{c}} \kappa}{(\Delta \mp \Omega)^2 + (\kappa/2)^2} . \tag{5.44}$$

As before we can calculate the effective phonon population by integrating the mechanical displacement fluctuations (Equation (5.38)). Here, we assume $G \ll \kappa$ to prevent normal mode splitting leading to hybridization of mechanical and optical mode [105, 112]. Genes *et al.* [106] have shown that the following holds

$$\langle \delta x^2 \rangle = \int \frac{d\Omega}{2\pi} 2 \, |\chi_{\mathrm{eff}}(\Omega)|^2 \left(S_{\mathrm{FF}}^{\mathrm{th}}(\Omega) + S_{\mathrm{FF}}^{\mathrm{qba}}(\Omega) \right)$$

$$= \frac{1}{\Gamma_{\mathrm{eff}}} \left(\frac{k_{\mathrm{B}} T \Gamma_{\mathrm{m}}}{m_{\mathrm{eff}} \Omega_{\mathrm{m}}^2} + \frac{\hbar}{m_{\mathrm{eff}} \Omega_{\mathrm{m}}} (A^- + A^+) \right) . \tag{5.45}$$

Using $\Gamma_{\mathrm{eff}}(\Omega = \Omega_{\mathrm{m}}) = A^- - A^+$ [106] and assuming a significant cooling rate where the Stokes and anti-Stokes rates differ strongly (see Figure 5.2), i.e. $A^- \gg A^+ \gg \Gamma_{\mathrm{m}}$, the mean mechanical occupation is

$$\bar{n}_{\mathrm{m}} = \langle n_{\mathrm{m}} \rangle \approx \frac{\Gamma_{\mathrm{m}}}{\Gamma_{\mathrm{eff}}} \cdot \frac{k_{\mathrm{B}} T}{\hbar \Omega_{\mathrm{m}}} + \frac{A^+}{A^- - A^+} \approx \frac{\Gamma_{\mathrm{m}}}{\Gamma_{\mathrm{eff}}} \cdot \frac{k_{\mathrm{B}} T}{\hbar \Omega_{\mathrm{m}}} + \frac{A^+}{A^-} . \tag{5.46}$$

Even for high cooling powers where $\Gamma_{\mathrm{eff}} \gg \Gamma_{\mathrm{m}}$, the average phonon number has a well defined minimum. The connection between mechanical excitation number and temperature allows to revisit the thermal force fluctuations acting on the mechanical oscillator defined in Equation (5.33). We ignore the small contribution A^+/A^- and obtain the generalized result for the complete thermal force spectrum leading to the reduced mechanical excitation [111]:

$$S_{\mathrm{FF}}^{\mathrm{ba}} = 4\hbar\Omega_{\mathrm{m}} m_{\mathrm{eff}} \Gamma_{\mathrm{eff}} (\bar{n}_{\mathrm{m}} + 1/2) . \tag{5.47}$$

The factor $1/2$ arises from the vacuum phonon energy. This result shows that it is sufficient to know the energy of the mechanical excitation number and the broadened linewidth to estimate the back-action force spectral density.

Two limits of the minimum phonon occupation following from Equation (5.46) are of interest:

In the unresolved sideband regime ($\Omega_{\mathrm{m}} \ll \kappa$), we get

$$\bar{n}_{\mathrm{m}}^{\mathrm{min}} \approx \frac{\kappa}{4\Omega_{\mathrm{m}}} \gg 1 . \tag{5.48}$$

In the resolved sideband regime ($\Omega_{\mathrm{m}} \gg \kappa$), we get

$$\bar{n}_{\mathrm{m}}^{\mathrm{min}} \approx \frac{\kappa^2}{16\Omega_{\mathrm{m}}^2} \ll 1 . \tag{5.49}$$
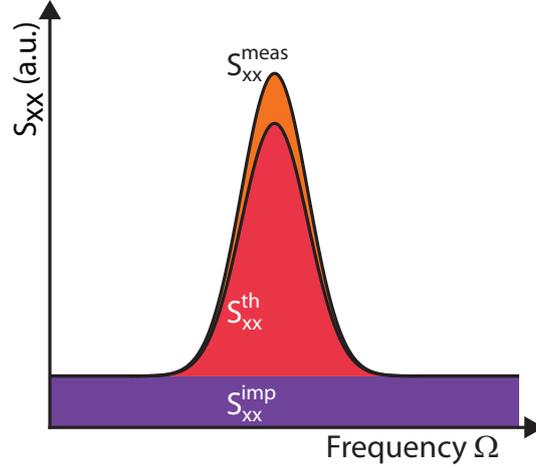
Figure 5.4: Schematic of a mechanical oscillator's displacement spectrum indicating the different noise contributions. The red colored area indicates the displacement due to coupling to the internal bath including back-action effects. Fluctuating forces acting on the mechanical resonator result in the orange shaped area effectively increasing the mechanical occupation. The purple background attributes additional noise contributions limiting the signal to noise ratio.

To reach the mechanical groundstate $\bar{n}_\mathrm{m} \approx 0$, being in the resolved sideband regime is a necessary condition. This theoretical limit is the lower bound for the number of mechanical excitations when cooling the mechanical mode of an opto-/electromechanical system. In an actual experiment several technical conditions limit the achievable phonon occupation to a higher number.

5.1.2 Limits in cooling and displacement sensing

Cooling of the mechanical motion into the ground state requires a temperature below $T = \hbar\Omega_\mathrm{m}/k_\mathrm{B}$. For mechanical resonance frequencies in the MHz-regime this corresponds to temperatures far below the millikelvin regime, not accessible with conventional dilution refrigerator systems with a base temperature of typically $10\,\mathrm{mK}$.

The phonon occupation in thermal equilibrium is $\bar{n}_\mathrm{m}^\mathrm{th} \approx k_\mathrm{B}T/\hbar\Omega_\mathrm{m} \gg 0$. For optomechanical cooling, Marquardt *et al.* [103] have shown the more stringent condition for high initial occupation that the mechanical eigenfrequency has to exceed the thermal decoherence rate $\Omega_\mathrm{m} > \Gamma_\mathrm{m}\bar{n}_\mathrm{m}^\mathrm{th}$ while Dobrinth *et al.* [105] have shown that this is true for the cavity decay rate as well, $\kappa > \Gamma_\mathrm{m}\bar{n}_\mathrm{m}^\mathrm{th}$. The latter implies that the photon flux into and out of the cavity has to exceed the mechanical thermal repopulation rate. This ensures that we can extract energy from the vibrational mode sufficiently fast to prevent thermal repopulation.

An actual measurement of $S_\mathrm{xx}^\mathrm{meas}(\Omega)$ contains contributions from different noise sources. Gernerally we can write [232]

$$S_\mathrm{xx}^\mathrm{meas}(\Omega) = S_\mathrm{xx}(\Omega) + S_\mathrm{xx}^\mathrm{imp}(\omega) \ . \tag{5.50}$$

The measurements imprecision $S_\mathrm{xx}^\mathrm{imp}(\omega)$ is a direct measure of the detection efficiency, influencing the visibility of the position measurement (purple area in Figure 5.4). It limits also the detectable minimum phonon occupation. Contributions to the background noise arise

from different effects. In our setup (as in most setups in the microwave regime) the limiting contribution to the imprecision noise is the HEMT amplifier (see Section 3) adding noise to any amplified signal resulting from its finite noise temperature [69, 110]. The imprecision noise is inversely proportional to the drive power, $S_{\mathrm{xx}}^{\mathrm{imp}} \propto 1/P_{\mathrm{d}}$; the amplifier adds a constant, power independent noise contribution to the signal. This limit can be overcome in the microwave regime with Josephson parametric amplifiers [48]. They parametrically amplify one quadrature with an efficiency close to the quantum limit [253]. The imprecision background can also be associated with an imprecision in phonon occupation [113]

$$\bar{n}_{\mathrm{m}}^{\mathrm{imp}} = \frac{m_{\mathrm{eff}}\Omega_{\mathrm{m}}\Gamma_{\mathrm{eff}}}{4\hbar} S_{\mathrm{xx}}^{\mathrm{imp}} \ . \tag{5.51}$$

Fluctuations also dynamically interact with the mechanical mode, thus modifying the displacement spectrum $S_{\mathrm{xx}} = S_{\mathrm{xx}}^{\mathrm{th}} + S_{\mathrm{xx}}^{\mathrm{ba}}$ (orange area in Figure 5.4)[4]. As we have seen above, photon shot noise of a coherent light source limits the thermal occupation [47]. Only recently direct observation of quantum shot noise was reported in the optical domain in a Fabry-Perot cavity incorporating a vibrating membrane [241]. In the microwave regime, a second limit is amplitude and phase noise of the microwave source, leading to a finite photon occupancy [105]. Additional photons in the cavity present an additional back-action force dynamically interacting with the mechanical mode, leading to an increased phonon population. Rocheleau *et. al* even observe an out of phase coupling between mechanical mode and phase noise generated phonons leading to effects like noise squashing [110].

For experiments in the optical domain photons have a much higher energy compared to the microwave regime. Thus it is easier to suppress (thermal) noise from the light source [107], while single photon detectors allow for nearly noiseless amplification. The fluctuations in the source become relevant for experiments aiming for phononic occupations near the ground state, where high drive powers increase the noise whereas the low mechanical occupation allows for direct observation of additional phonons [110, 113].

The observation of the mechanical motion discussed so far is a weak measurement, implying that the signal is integrated over time in contrast to an instantaneous, strong, projective measurement [232]. This results from the weak coupling between optical and mechanical mode and has the advantage that the vibrational state is not affected by the measurement itself. To quantify a weak position measurement, it is useful to compare the imprecision $S_{\mathrm{xx}}^{\mathrm{imp}}$, defining the measurement background and thus the resolution to the standard quantum limit (SQL) of the mechanical mode, given by [46]

$$S_{\mathrm{xx}}^{\mathrm{SQL}}(\Omega_{\mathrm{m}}) = \frac{\hbar}{m_{\mathrm{eff}}\Omega_{\mathrm{m}}\Gamma_{\mathrm{m}}} \ . \tag{5.52}$$

For the mechanical excitation number approaching zero, the displacement spectrum approaches $S_{\mathrm{xx}}^{\mathrm{SQL}}$ corresponding to half of the quantum mechanical zero point fluctuation amplitude x_{zpf} of the mechanical oscillator [49, 50, 244]. The SQL should not be confused with the Heisenberg uncertainty principle. Any position measurement is limited by the SQL, but the imprecision noise $S_{\mathrm{xx}}^{\mathrm{imp}}$ can become smaller than $S_{\mathrm{xx}}^{\mathrm{SQL}}$ [48, 49]. The limit of a weak position measurement is easy to understand in terms of the measurement: As long as no single quadrature measurement squeezes the state of the mechanical motion, a measurement introduces at least one half quantum of noise by back-action on the mechanical

---

[4]Note, that here $S_{\mathrm{xx}}^{\mathrm{th}}$ also contains effects due to dynamical back-action

oscillator [232, 244]. The uncertainty principle reads

$$\sqrt{S_{\text{xx}}^{\text{imp}} S_{\text{FF}}^{\text{ba}}} \geq \hbar \ . \tag{5.53}$$

The equality is valid for a quantum limited measurement. We can use Equation (5.53) to estimate how far the actual measurement is away from a quantum limited measurement. Note, that the Heisenberg uncertainty principle has been expressed in terms of single sided spectra, thus the factor $1/2$ usually expected on the right hand side is missing in Equation (5.53). The back-action force spectral density $S_{\text{FF}}^{\text{ba}}$ responsible for the additional mechanical back-action can be expressed in terms of a mechanical displacement spectrum, $S_{\text{xx}}^{\text{ba}} = |\chi_{\text{eff}}|^2 S_{\text{FF}}^{\text{ba}}$. Thus, above formulation of the uncertainty principle is only valid in for a drive tone at the cavity's resonance. A tone with zero detuning $\Delta = 0$ allows for highest measurement precision, while for a red detuned drive, it weakens to $\sqrt{S_{\text{xx}}^{\text{imp}} S_{\text{FF}}^{\text{ba}}} \geq \sqrt{2}\hbar$ [47, 232].

The limit of position measurements imposed by the SQL is only valid in weak position measurements. Schemes only measuring one mechanical quadrature by stroboscopic measurements or amplitude modulation of the drive tone circumvent this limit [254]. A first step towards this kind of position measurement is presented in [255] in a system similar to ours. Instead of performing a weak, continuous position measurement with long averaging times of a moderate drive tone, Vanner *et al.* propose [128] and experimentally validate [129] a measurement scheme involving high intensity pulses much shorter than one mechanical oscillation period, capable to reconstruct the mechanical Wigner density. This scheme operates in the unresolved sideband regime ($\Omega_{\text{m}} \ll \kappa$).

5.1.3 Connection between different spectra

In this section, we discuss the relation between the experimentally accessible parameters like microwave voltage or power spectra to the displacement and force spectral densities. These values depend strongly on technical parameters, like the exact wiring of the experiment or the amplitude of the drive power. To calculate the mechanical displacement spectrum $S_{\text{xx}}(\Omega)$ we have to estimate the transduction of mechanical motion into intra cavity phase ($S_{\phi\phi}(\Omega)$) or frequency fluctuations ($S_{\omega\omega}(\Omega)$).

A mechanical displacement x changes the cavity resonance frequency $\widetilde{\omega}_{\text{c}}$ in first order linearly to $\omega_{\text{c}} = \widetilde{\omega}_{\text{c}} - Gx$. This leads to a connection of displacement spectrum and resonance frequency spectrum:

$$S_{\omega\omega}(\Omega) = G^2 S_{\text{xx}}(\Omega) \approx g_0^2 \frac{k_{\text{B}}T}{\hbar\Omega_{\text{m}}} \cdot \frac{\Gamma_{\text{m}}}{(\Omega - \Omega_{\text{m}})^2 + \left(\frac{\Gamma_{\text{m}}}{2}\right)^2} \ , \tag{5.54}$$

where we have used Equation (5.37) in the second part of the expression. Integrating over the frequency fluctuations spectral density gives

$$\langle \delta\omega_{\text{c}}^2 \rangle = \int_0^\infty 2S_{\omega\omega}(\Omega) \frac{d\Omega}{2\pi} = \frac{1}{2} S_{\omega\omega}(\Omega_{\text{m}})\Gamma_{\text{m}} = 2g_0^2 \bar{n}_{\text{m}} \ . \tag{5.55}$$

From Equation (5.55) we see, that to estimate the vacuum coupling g_0, it is sufficient to know the average frequency displacement and the number of acoustic excitations of the

vibrational mode. A fluctuation of the cavity resonance frequency also implies a fluctuation of the intra-cavity phase ϕ according to

$$S_{\phi\phi}(\Omega) = \frac{1}{\Omega^2} S_{\omega\omega}(\Omega) \,, \tag{5.56}$$

for small frequency fluctuations. Therefore it is synonymous to measure the phase fluctuations or the resonance frequency fluctuations of the cavity. Both eventually allow to calculate the displacement spectrum via Equation (5.54).

In this work, we use a homodyne detection scheme to record the phase spectrum as a function of frequency. The recorded signal is detected by a spectrum analyzer, recording the power spectral density S_{PP}. Thus, we have to connect the power spectrum at the detector to the phase or frequency fluctuations of the cavity:

$$S_{\mathrm{PP}}(\Omega) = K(\Omega) S_{\phi\phi}(\Omega) = \frac{K(\Omega)}{\Omega^2} S_{\omega\omega}(\Omega) \approx \frac{K(\Omega)}{\Omega_{\mathrm{m}}^2} S_{\omega\omega}(\Omega) \,. \tag{5.57}$$

To exploit this relation we need absolute knowledge of the transfer function $K(\Omega)$. The calculation of the transfer function takes into account the actual detection scheme and the exact wiring including attenuation and amplification in the current system. The function $K(\Omega)$ can be determined experimentally by applying a known frequency of phase modulation at all frequencies of interest creating a reference for the signal and repeating the measurement for all relevant frequencies. On the theoretical side one can calculate the transfer function by considering the measurement conditions, i.e. the attenuation (Att), the amplification (Amp) and the transduction of the signal (for example, in the case of homodyne detection, we have to consider the down conversion of the signal).

For a quantitative understanding of $K(\Omega)$, we present two special cases assuming homodyne detection (the complete expression for homodyne and direct amplitude detection is found in reference [230]). For this approach, we have to know the signal power at the mixer P_{Sig} and the power applied to the local oscillator P_{LO}. In an experiment, the input lines leading to the sample are heavily attenuated (Att) to suppress thermal noise and the output lines are amplified (Amp). To get a correct expression for the transfer function K, it is mandatory to know these two parameters precisely to calculate $P_{\mathrm{Sig}} = \mathrm{Att} \times \mathrm{Amp} \times P_{\mathrm{d}}$ from the drive power P_{d}. Note, that we ignore the influence on the signal by the cavity and include this into the rest of the expression below.

Considering a drive tone at zero detuning, $\Delta = \omega_{\mathrm{c}} - \omega_{\mathrm{d}} = 0$, we find

$$K(\Omega) = \frac{16\Omega^2 \kappa_{\mathrm{ex}}^2/\kappa^2}{\Omega^2 + (\kappa/2)^2} P_{\mathrm{Sig}} P_{\mathrm{LO}} \,. \tag{5.58}$$

Second, we consider a pump tone at optimum detuning, i.e. at the red or blue mechanical sideband of the cavity ($\Delta = \pm\Omega_{\mathrm{m}}$), for a system in the resolved sideband regime $\Omega_{\mathrm{m}} > \kappa$. Here,

$$K(\pm\Omega_{\mathrm{m}}) \approx 4\frac{\kappa_{\mathrm{ex}}^2}{\kappa^2}\left(1 + \frac{\kappa^2(16\kappa_{\mathrm{ex}}/\kappa - 13)}{16\Omega_{\mathrm{m}}^2}\right) P_{\mathrm{Sig}} P_{\mathrm{LO}} \,. \tag{5.59}$$

In many experimental situations the mechanical spectral density is recorded in close vincinity to Ω_{m}, the transduction function $K(\Omega)$ is almost constant over the range of frequencies considered in such an experiment, $K(\Omega) \approx K(\Omega_{\mathrm{m}}) \approx K(\Omega_{\mathrm{mod}})$. Importantly, to access the mechanical linewidth or eigenfrequency, it is sufficient to record $S_{\mathrm{PP}}(\Omega)$ without transforming the outcome into a displacement spectrum, since all translations are linear.

5.2 Frequency noise calibration

Different methods exist to determine the electromechanical coupling: In electromechanical systems where temperature is an experimental degree of freedom, one can make use of Equation (5.55) and analyze the mechanical displacement spectrum as a function of temperature [69,255–257]. This has also been demonstrated in the optical domain [78]. A precise knowledge of the transfer function $K(\Omega)$ is also sufficient to experimentally estimate the vacuum coupling. This results from the fact that the effective electromechanical coupling $g = g_0\sqrt{\bar{n}_c}$ is easily accessible in experiments (see the measurement of the electromechanical linewidth broadening in Section 6.1) and that knowledge of the transfer function implies a calibrated setup. The calibration of the damping and thus the power reaching the sample is very demanding in experiments involving dilution fridges and the same is true for the exact amplification of the output lines, since one cannot separate the attenuation and amplification by experimental means. The measurement of g_0 is thus a very effective method to calibrate the attenuation in an experimental setup, also providing a value for the transfer function at the particular frequency of the measurement.

The idea behind frequency noise calibration is to send a well defined signal to the sample. The signal undergoes the same phase shift inside the μ-wave cavity as phase fluctuation due to the mechanical motion. As shown below, this allows to cancel the cavity response function and to calculate the electromechanical vacuum coupling [230].

An experimental realization is to apply a well defined frequency modulation to the microwave source tone used as reference and test signal of the homodyne detection. Gorodetsky *et al.* [230] show that for this detection type, as well as for direct amplitude detection, the applied phase modulation undergoes the same transduction. It follows

$$S_{\mathrm{PP}}(\Omega) = K(\Omega)S_{\varphi\varphi}(\Omega) \ . \tag{5.60}$$

The spectral phase density $S_{\varphi\varphi}(\Omega)$ of the frequency modulated tone obeys exactly the same transformation rules as the phase spectral density $S_{\phi\phi}(\Omega)$ of the electromechanical system when converted into a power spectral density $S_{\mathrm{PP}}(\Omega)$ at the detector.

A monochromatic phase modulation of the input field ($E \propto \exp\left(i\varphi_0\cos(\Omega_{\mathrm{mod}}t)\right)$) is in the ideal case a superposition of two δ-peaks in frequency domain. Taking into account that most analyzers only show single sided spectra and the signal is convoluted with the inverse detection bandwidth (called ENBW in the following), the detected spectrum can be approximated by [230]

$$S_{\mathrm{PP}}^{\mathrm{meas}}(\Omega_{\mathrm{mod}}) \approx \frac{\varphi_0^2}{2} \cdot \frac{K(\Omega_{\mathrm{mod}})}{\mathrm{ENBW}} \ , \tag{5.61}$$

where we know all parameters except $K(\Omega_{\mathrm{mod}})$. Around the mechanical resonance, the transfer function only varies slowly [230]. A frequency modulation close to the mechanical resonance frequency ($\Omega_{\mathrm{mod}} \approx \Omega_{\mathrm{m}}$) undergoes almost the same transformation, it is justified to assume $K(\Omega) \approx K(\Omega_{\mathrm{m}}) \approx K(\Omega_{\mathrm{mod}})$. This allows to replace $K(\Omega)$ in Equation (5.57) by using (5.61). Plugging Equation (5.54) into (5.57) evaluates the electromechanical vacuum coupling to

$$g_0^2 \approx \frac{1}{2\bar{n}_{\mathrm{m}}} \cdot \frac{\varphi_0^2\Omega_{\mathrm{mod}}^2}{2} \cdot \frac{S_{\mathrm{PP}}^{\mathrm{meas}}(\Omega_{\mathrm{m}})\,\Gamma_{\mathrm{m}}/4}{S_{\mathrm{PP}}^{\mathrm{meas}}(\Omega_{\mathrm{mod}})\,\mathrm{ENBW}} \ . \tag{5.62}$$

For a known g_0, we can express the mechanical displacement spectral density in terms of $S_{\mathrm{PP}}^{\mathrm{meas}}$:
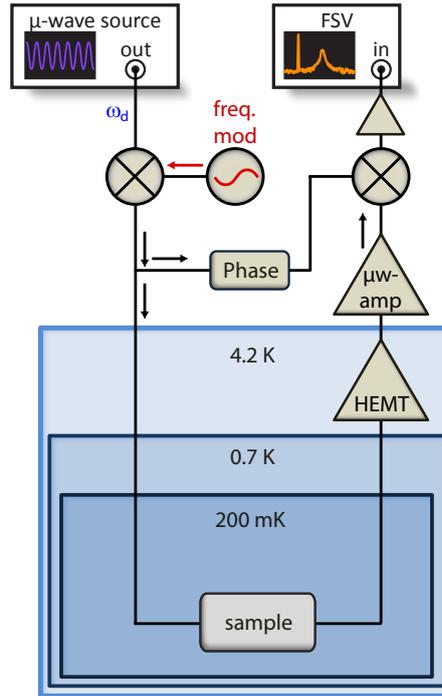
Figure 5.5: Schematic of the setup to estimate the Duffing parameter. We use a homodyne setup to detect the mechanical motion. The pump field's frequency is set to the μ-wave cavity eigenfrequency, to minimize back-action on the mechanical motion. The frequency modulation is applied before splitting up the signal for the homodyne detection. This is necessary to cancel contributions from the modulation when the signal is not affected by transduction through a cavity.

$$S_{\mathrm{xx}}^{\mathrm{meas}}(\Omega) \approx \frac{\varphi_0^2 \Omega_{\mathrm{mod}}^2}{2g_0^2/x_{\mathrm{zpf}}^2} \cdot \frac{S_{\mathrm{PP}}^{\mathrm{meas}}(\Omega)}{S_{\mathrm{PP}}^{\mathrm{meas}}(\Omega_{\mathrm{mod}})\,\mathrm{ENBW}} \,. \tag{5.63}$$

5.2.1 Setup

To determine the electromechanical vacuum coupling, we operate the sample in fridge No.1 at a temperature of approximately $200\,\mathrm{mK}$. We measure in a homodyne detection scheme with a drive at the cavity eigenfrequency ω_{c}.

A schematic of the setup is presented in Figure 5.5. A Rhode&Schwarz SMF microwave source provides the drive and reference tone by splitting its output with a power divider. The drive tone is attenuated and fed to the sample. After passing an amplifier chain, an IQ-mixer in homodyne configuration downconverts the microwave signal to DC. This signal is analyzed with a Rhode&Schwarz FSV9 spectrum analyzer which records the power spectral density around the mechanical resonance frequency Ω_{m}. We apply frequency modulation with a frequency $\Omega_{\mathrm{mod}}/2\pi = \Omega_{\mathrm{m}}/2\pi - 50\,\mathrm{Hz}$ and a modulation depth of $\Omega_{\mathrm{mod}}/2\pi = 80\,\mathrm{Hz}$ (equivalent to a phase modulation with a modulation index $\varphi_0 = \Omega_{\mathrm{md}}/\Omega_{\mathrm{mod}} \approx 5.5\times10^{-5}$). Note, that the frequency modulation is applied before splitting up the microwave tone into drive tone and reference tone for the homodyne detection.

The frequency modulation spectrum undergoes the same transduction as the mechanical displacement spectral density. For the measurement, only these components are of relevance as discussed above. On the other hand, the drive tone carries the frequency
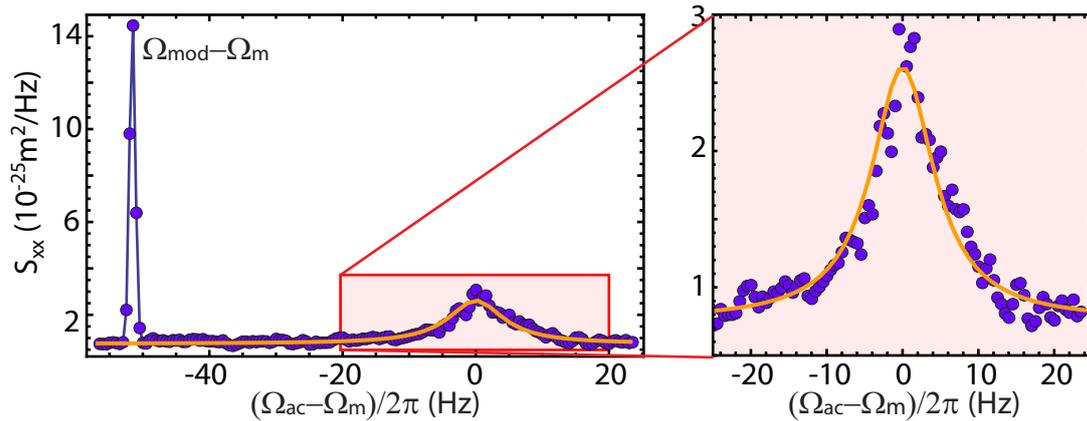
Figure 5.6: Mechanical displacement spectrum to determine g_0 for a drive power of $P_d = -73.5\,\text{dBm}$. The left peak results from the frequency modulation of the input source. The zoomed part shows the mechanical peak including a fit of a Lorentzian to the data (orange line).

modulation as well to the spectrum analyzer, thus creating an additional signal at the modulation frequency. To neutralize these contributions, we adjust the cable length of the reference signal line. We optimize the electric length of the reference line by replacing the IQ-mixer with a power divider to combine both arms and then sweeping the frequency of the microwave source while monitoring the resulting interference signal with a microwave diode and an oscilloscope. When the electrical lengths of both arms are equal, the resulting signal shows no frequency dependence and the microwave drive tone is completely eliminated including the contributions from frequency modulation by adjustment of the reference phase. We verify this by performing a homodyne detection at frequencies away from the cavity eigenfrequency. At a detuning of $\omega_c \pm 2\pi \times 10\,\text{MHz}$, the frequency modulation signal is suppressed by more than $30\,\text{dB}$. This ensures that the reference peak visible in Figure 5.6 stems from transduction through the cavity. All measurements are performed with the sample characterized in Section 3.

5.2.2   Measurement of the electromechanical vacuum coupling

To determine g_0, we measure the mechanical displacement spectrum with three different drive powers ($P_d = -69.5, -73.5$ and $-79.5\,\text{dBm}$) at cavity resonance, $\omega_d = \omega_c$. We can exclude back-action of the light field onto the mechanical mode and thus monitor the Brownian motion of the nanobeam.

Figure 5.6 shows a measured spectrum, obtained with the drive at the cavity eigenfrequency. We show the spectrum in terms of a displacement spectrum according to Equation 5.63. The mechanical Brownian motion centered around $\Omega_{ac} - \Omega_m = 0$ is clearly distinguishable from the calibration peak. The zoom shows the mechanical displacement. From these measurements we obtain $g_0/2\pi = 1.26\,\text{Hz}$, giving $G = g_0/x_{zp}/2\pi = 36.3\,\text{kHz/nm}$. This value is approximately a factor of six higher than $G/2\pi = 6.36\,\text{kHz/nm}$ extracted in Section 4.4 by geometric considerations, where we have simplified the electric field between ground and nanobeam and ignored inhomogeneities contributing to the capacitance. By measuring the linewidth broadening in electromechanically induced transparency we obtain $g = g_0\sqrt{\bar{n}_c}$ as a function of drive power (see Section 6.1 for details). Together with
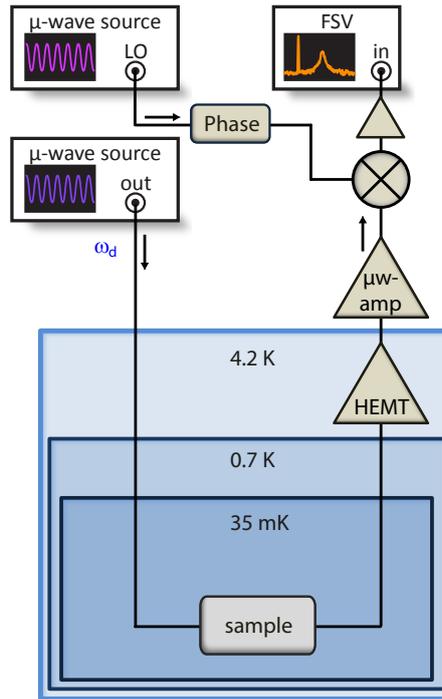
Figure 5.7: Schematic setup to record the mechanical displacement as a function of drive frequency and power. Two microwave sources provide local oscillator and signal line of the homodyne detection, respectively. The signal is fed into the cryostat via heavily attenuated coaxial cables, passes the sample and is combined at an IQ-mixer with the phase adjusted local oscillator signal after passing an amplifier chain. The resulting signal is collected in a frequency window centered around Ω_m.

the measured g_0, we then calculate the mean intra-cavity photon number $\bar{n}_c$ as function of applied drive power. This allows to extract the damping in our system to $65.5 \pm 0.5\,\mathrm{dB}$. A similar measurement in fridge No.2, reproduces the known value of g_0 and allows to estimate a damping of $62 \pm 0.5\,\mathrm{dB}$.

5.3 Experimental demonstration of electromechanical features

With the determination of the electromechanical vacuum coupling and the accompanying calibration of the attenuation of the input line, we experimentally examine the predictions made in Section 5.1.

5.3.1 Homodyne setup to manipulate drive power

A drawback of the setup presented in Section 5.2, is the inability to tune the drive power with high accuracy. The measurements presented in this section are performed in dilution fridge No.2 at a temperature of $35\,\mathrm{mK}$. The mechanical displacement is recorded with a homodyne detection scheme as schematically shown in Figure 5.7. To adjust the drive power precisely, we use two phase locked Rhode&Schwarz SMF microwave sources. One source serves as local oscillator with a fixed output power of $10\,\mathrm{dBm}$. The second source provides the drive field, which is fed into the cryostat and combined with the local oscillator

field at an IQ-Mixer after successively passing the sample and an amplifier chain. A phase shifter in the local oscillator line is used to nullify the phase shift between signal and local oscillator. Similar to the setup presented in Section 5.2, the length of the cable guiding the local oscillator signal is adjusted to have the same electrical length as the signal line, including the fridge wiring. The downconverted signal is amplified by $10\,\mathrm{dB}$ and recorded with a Rhode&Schwarz FSV spectrum analyzer in a narrow frequency window, centered around the mechanical resonance frequency. All measurements are performed with the sample characterized in Section 3.

5.3.2   Linewidth broadening and optical spring effect

First we study the electromechanical linewidth broadening and and the shift of the mechanical eigenfrequency due to the mechanical spring effect. The drive tone's frequency is swept from $\Delta/2\pi = -3\,\mathrm{MHz}$ to $\Delta/2\pi = 2.4\,\mathrm{MHz}$. The local oscillator's frequency is swept correspondingly. To keep the intra-cavity photon number constant, we change the drive power with every frequency step. The drive power follows the condition

$$P_\mathrm{d} = \left(\frac{1}{\hbar\omega_\mathrm{d}} \cdot \frac{\kappa_\mathrm{ex}/2}{(\kappa/2)^2 + \Delta^2} \right)^{-1} \bar{n}_\mathrm{c} \; . \tag{5.64}$$

Figure 5.8 shows the mechanical linewidth $\Gamma_\mathrm{eff}(\Delta)$ (top) and eigenfrequency shift $\Delta\Omega_\mathrm{m}(\Delta) = \Omega_\mathrm{m}(\Delta) - \Omega_\mathrm{m}(0)$ (bottom) extracted from the recorded corresponding displacement spectra as a function of the drive detuning Δ. This allows to compare the experimental values to the theory, given in Equations (5.19) and (5.20). Hereby, we set the average intra-cavity photon number to $\bar{n}_\mathrm{c} \approx 9.24 \times 10^5$. The orange line in the top of Figure 5.8 is a fit of Equation (5.19) to the data (purple points). The only fit parameters are the initial mechanical linewidth Γ_m and the cavity resonance frequency ω_d. As expected, the electromechanical linewidth broadening peaks around $\Delta = -\Omega_\mathrm{m}$, corroborating that the optimum detuning corresponds to the mechanical resonance frequency. For a blue detuned drive tone, Γ_eff dips at $\Delta = \Omega_\mathrm{m}$, approaching 0. This implies that the mechanical mode becomes undamped and enters the self-oscillation regime [93]. As easily verified from Equation (5.19), the parametric oscillation regime broadens with increasing drive power. Thus self-oscillation is observable even for detunings in a frequency window centered around Ω_m.

Comparing the fitted initial linewidth of $\Gamma_\mathrm{m}/2\pi = 5\,\mathrm{Hz}$, with the linewidth extracted from ring down measurements at the same temperature (see Section 4.5.2), we see that the initial mechanical linewidth has twice the expected value. Comparing the linewidth fit of Equation (5.19) with the experimentally extracted linewidths in this measurement we see they overlap well, even at $\Delta = 0$. This is the case, because we chose the intra-cavity photon number sufficiently low to exclude back-action. So we attribute the difference in the homodyne detected linewidth to a systematic measurement error, resulting from slow frequency fluctuations present in the system at low temperatures. The measurement time for every single sweep of approximately $5\,\mathrm{min}$ due to the average count of 150 in combination with these fluctuation lead to a broadened observed linewidth. The origin of the fluctuations remains unclear and is presently object of further research. Different groups observe similar yet unidentified fluctuations at temperatures below $150\,\mathrm{mK}$ [69, 110]. Regal *et al.* [69] attribute the resulting fluctuating beam temperature to a loss of the coupling between the nanobeam and the thermal bath, what we exclude from the
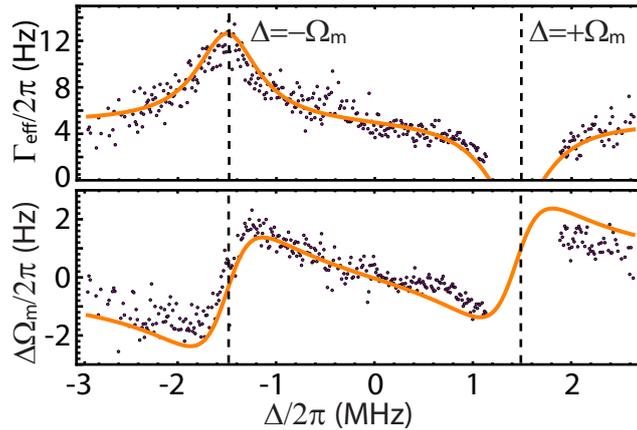
Figure 5.8: Electromechanical linewidth broadening (top) and shift of the mechanical eigenfrequency (bottom) as a function of detuning. The purple points are obtained by Lorentzian fits to the recorded power spectra monitoring the mechanical displacement. The orange curves are fits to the data.

measurements in Section 4.5.2. Teufel *et al.* [113] show that these fluctuations are not due to phase noise of the microwave source. Recently, Fong *et al.* [175] have studied the frequency and amplitude noise in high Q silicon nitride beams, proposing that the fluctuations origin are thermally activated defect states with a broad spectrum of elastic dipole reorientation time. They suggest that this mostly influences high Q devices. Their study provides the starting point for further research.

The optical spring effect observed in this work is small compared to the mechanical resonance frequency, $\Delta\Omega_{\mathrm{m}}(\Delta)/\Omega_{\mathrm{m}}(0) < 1.4 \times 10^{-6}$ as shown at the bottom of Figure 5.8. The orange line is a plot of Equation (5.20), using the fit parameters obtained from the linewidth fit. Data and theory agree well. At optimum red and blue detuning $\Delta = \pm\Omega_{\mathrm{m}}$ no frequency shift is observed. This allows for precise alignment of the optimum detuning when the cavity resonance ω_{c} is exactly known. The lack of points in a region around $\Delta = \Omega_{\mathrm{m}}$ stems from the strong frequency shift (several kHz) of the mechanical mode entering the parametric oscillation regime. Our data agrees well with measurements of a similar system made by Teufel *et al.* [240].

We repeated the measurement shown here for a higher intra-cavity photon number of $\bar{n}_{\mathrm{c}} \approx 1.46 \times 10^6$, showing the same behavior and corroborating above fit parameters.

5.3.3 Electromechanical cooling

Next we tune the drive tone to the red sideband ($\Delta = -\Omega_{\mathrm{m}}$) and measure the mechanical displacement spectrum as a function $\bar{n}_{\mathrm{c}}$, still at a temperature of $35\,\mathrm{mK}$. In Figure 5.9a we have plotted the power spectral density $S_{\mathrm{PP}}(\Omega)$ recorded around the mechanical resonance frequency for four different intra-cavity photon numbers $\bar{n}_{\mathrm{c}} \approx 0.15 \times 10^6$ (red data), 0.41×10^6 (pink data), 1.30×10^6 (purple data) and 4.11×10^6 (blue data). The solid lines are Lorentzian fits to the data. To quantify the cooling we transform the data into displacement spectra using $S_{\mathrm{xx}}^{\mathrm{meas}}(\Omega) = \frac{\Omega_{\mathrm{m}}^2 g_0^2}{x_{\mathrm{zpf}}^2 K(\Omega_{\mathrm{m}})} S_{\mathrm{PP}}(\Omega)$ with $K(\Omega_{\mathrm{m}})$ from Equation (5.59). Hereby, we can translate the experimentally obtained spectra displayed in Figure 5.9a to the displacement spectra shown in panel b. For this calculation we need in addition to the attenuation of the input the net amplification of the output line. Here, we take advantage
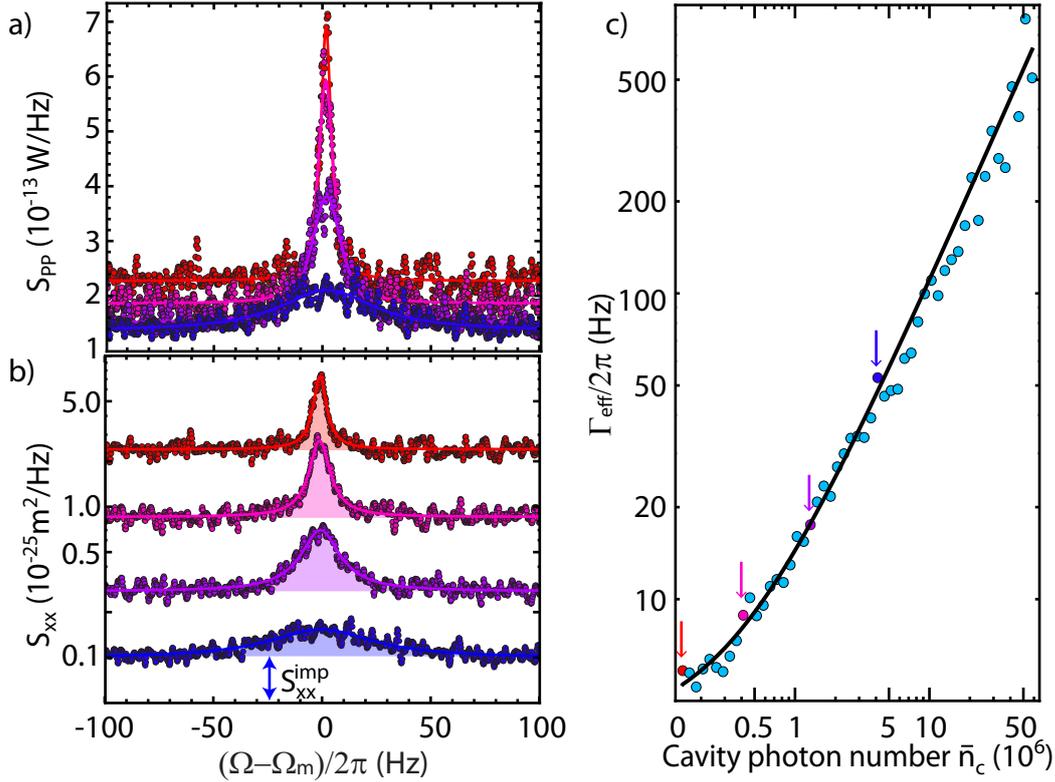
Figure 5.9: Measurement of the electromechanical linewidth broadening. a) shows four recorded power spectra for increasing drive power from red to blue. The corresponding displacement spectra are plotted in b) on a logarithmic scale. Note, that no offsets are used to seperate the data. The solid lines are Lorentzian fits to the data. The imprecision noise S_{xx}^{imp} for the blue curve is indicated by the blue arrow The extracted effective mechanical linewidths are plotted in c), where the colored arrows indicate the corresponding curve in a) and b). The solid black line is a fit to the data.

from the fact that the power spectral density allows to measure the effective linewidth Γ_{eff} of the mechanical displacement as a function of average intra-cavity photon number as shown in Figure 5.9c (light blue dots). We use this to extract the effective temperature $T_{eff} = T \cdot \Gamma_m / \Gamma_{eff}$ for low photon numbers where we can ignore fluctuations. Then we estimate the natural linewidth to $\Gamma_m / 2\pi \approx 3.8\,\mathrm{Hz}$ by fitting the mechanical linewidth to the photon number using $\Gamma_{eff} = \Gamma_m + 4g_0^2 \bar{n}_c / \kappa$ (black curve in Figure 5.9c). This expression results from Equation (5.19) at optimum detuning. Now, we compare the amplitude of one of the recorded peaks (red curve in Figure 5.9a) with the expected peak amplitude of the mechanical displacement $S_{xx}^{meas}(\Omega_m, \Gamma_{eff}) = k_B T_{eff} / m_{eff} \Omega_m^2$ following from Equation (5.36) and replacement of χ_m with χ_{eff}. Knowing all factors except the amplification, we can calculate the amplification to $34\,\mathrm{dB}$, where we have assumed $P_{LO} = 10\,\mathrm{dB}$. This agrees well with the expected amplification taking cable losses into account[5].

When transforming the data into displacement spectra, we noticed an unexpected additional absorption in the output line showing a weak power dependence proportional to $(P_d)^{0.2}$ (see appendix A.3 for more details and discussion), that we had to correct

---

[5]The microwave amplifiers add a total amplification of $70\,\mathrm{dB}$, the output cabling has a higher damping of approx. $30\,\mathrm{dB}$, resulting from the additional components compared to the input wiring and the IQ-mixer has a conversion loss of approx. $6\,\mathrm{dB}$.
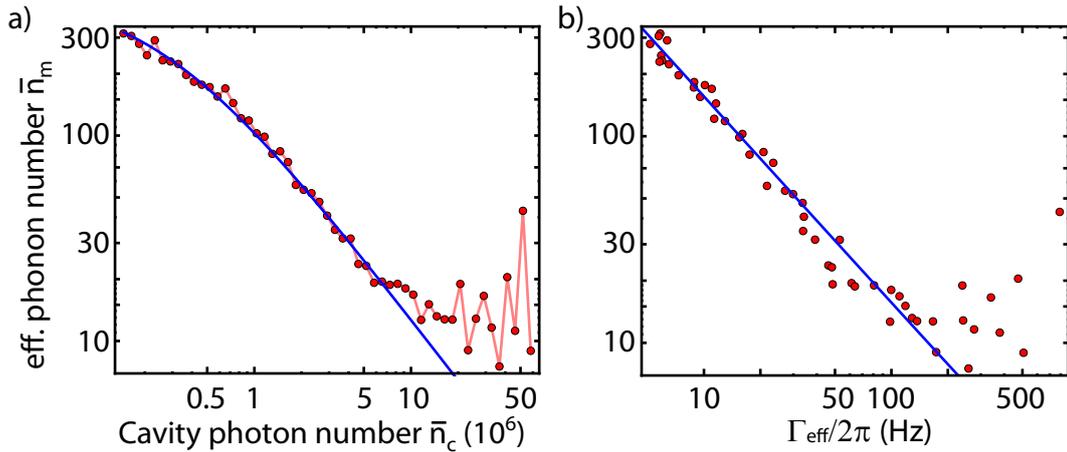
Figure 5.10: Mechanical excitation number $\bar{n}_\mathrm{m}$ plotted versus a) the intra-cavity photon number and b) the extracted mechanical linewidth Γ_eff. The red dots are the experimental data, the blue line is a fit to the data. The light red line in a) connects the data for better visibility.

the data for. Its precise origin is unknown, we attribute this effect to either one of the amplifiers, the IQ-mixer or the circulator chain.

The calibrated displacement spectrum $S_\mathrm{xx}^\mathrm{meas}(\Omega)$ is plotted on a logarithmic scale in Figure 5.9b for the same intra-cavity photon number as the power spectral density in Figure 5.9a. The solid lines are Lorentzian fits to the data according to Equation 5.36. Note that we have not artificially offset the data. Using this representation, it is clearly visible, that the area under the Lorentzian is decreasing with increasing drive photon number.

To quantify the decrease we calculate the area $\langle \delta x^2 \rangle$ under every recorded displacement spectrum excluding the background $S_\mathrm{xx}^\mathrm{imp}$, shown in Figure 5.4. We can transform the area under the curve (colored areas in Figure 5.9c) into a mean mechanical excitation number $\bar{n}_\mathrm{m}$ according to $\bar{n}_\mathrm{m} = \langle \delta x^2 \rangle m_\mathrm{eff} \Omega_\mathrm{m}/\hbar$. Plotting the extracted phonon number against $\bar{n}_\mathrm{c}$ and against the extracted effective linewidth Γ_eff (Figure 5.10a and b, respectively) shows a clear decrease of the mechanical occupation up to an intra-cavity photon number $\bar{n}_\mathrm{c} \approx 1 \times 10^7$ and the corresponding linewidth of $\Gamma_\mathrm{eff}/2\pi \approx 100\,\mathrm{Hz}$. Here, the initial mechanical linewidth is the only fit parameter, giving $\Gamma_\mathrm{m}/2\pi \approx 2.2\,\mathrm{Hz}$ for the fitting $\bar{n}_\mathrm{m}$ versus $\bar{n}_\mathrm{c}$ and $\Gamma_\mathrm{m}/2\pi \approx 3.3\,\mathrm{Hz}$ versus Γ_eff. We attribute the difference to measurement noise leading to scattering of the extracted values of Γ_eff.

The initial occupation is given by the thermal equilibrium with the environment, $\bar{n}_\mathrm{m} = k_\mathrm{B}T/\hbar\Omega_\mathrm{m} \approx 497$. As we can see from Figure 5.10, the electromechanical back action changes the occupation at the lowest photon number $\bar{n}_\mathrm{c} \approx 0.15 \times 10^6$ to $\bar{n}_\mathrm{m} \approx 314$, yielding an effective mode temperature of $T_\mathrm{eff} \approx 22\,\mathrm{mK}$. The lowest occupation we record before the values of $\bar{n}_\mathrm{m}$ become unreliable is $\bar{n}_\mathrm{m} \approx 13$ ($T_\mathrm{eff} \approx 0.9\,\mathrm{mK}$) for $\bar{n}_\mathrm{c} \approx 1.16 \times 10^7$.

Fitting the data to the model prediction given by Equation (5.46) (blue lines in Figure 5.10) reveals excellent agreement between experiment and theory up to an intra-cavity photon number $\bar{n}_\mathrm{c} \approx 7 \times 10^6$ and the corresponding linewidth of $\Gamma_\mathrm{eff}/2\pi \approx 100\,\mathrm{Hz}$. For higher drives, the cooling rate starts to saturate until the measured phonon number becomes unreliable. The latter has technical reasons as exemplary shown in Figure 5.11 displaying the recorded mechanical displacement spectrum for a drive photon number of $\bar{n}_\mathrm{c} \approx 3.67 \times 10^7$: The effective linewidth approaches the measurement window and the
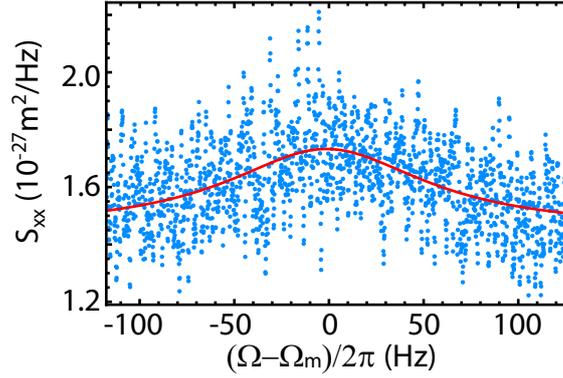
Figure 5.11: Mechanical displacement spectrum (light blue points) and the fit of a Lorentzian to the data for a high drive photon number of $\bar{n}_c \approx 3.67 \times 10^7$. The decrease of the signal to noise ratio compared to Figure 5.9 and the mechanical linewidth approaching the detection window is clearly visible.

signal to noise ratio approaches one. To overcome these limitations we have to increase the detection window and increase the number of averages. Still, we expect saturation to set in before cooling to a mechanical occupation below one. Phase noise of the microwave source increases with increasing drive power. Thus, with increasing drive power, the cavity is populated with photons generated by noise as shown in Ref. [110]. Here, the authors show that a finite population $\bar{n}'_c$ of the cavity due to noise or thermal excitation leads to an increased measured phonon number of $\bar{n}_{eff} = \bar{n}_m + 2\bar{n}'_c$ and eventually to noise squashing. Additional microwave filters help to suppress the noise [202,255]. For the microwave power regime of the measurements presented here, we do not attribute heating of the sample to increase the mechanical population. All measured temperatures were below $200\,\text{mK}$, the effective temperature of a single photon with the cavity frequency. Quantum back-action is also negligible in the regime discussed here, since the microwave source is not quantum limited and thus other noise contributions dominate.

To benchmark our measurement it is instructive to compare the measurement imprecision with the SQL. Figure 5.12 shows that S_{xx}^{imp} is proportional to $1/\bar{n}_c$ (orange line). Here, we have ignored the values where $\bar{n}_c \geq 2 \times 10^7$, since we approach the experimental noise level in this case. The imprecision noise shows a weaker power dependency already at a moderate drive photon numbers of $\bar{n}_c \geq 4 \times 10^6$, in agreement to the fact that the fundamental noise limit is given by the HEMT amplifier. The decrease of the imprecision noise with increasing intra-cavity photon number agrees with the above conclusion that quantum back-action is not relevant but other mechanisms like phase noise of the microwave source dominate. As shown recently in Ref [241] quantum backaction noise increases with the drive power. We record a measurement imprecision of down to $S_{xx}^{imp} \approx 3.8 \times 10^{-27}\ \text{m}^2/\text{Hz}$, corresponding to $\bar{n}_m^{imp} \approx 260$. Increasing the number of averages should improve this result. Comparing the minimal value of the imprecision noise with the SQL, we find $S_{xx}^{imp} \approx 35 \cdot S_{xx}^{SQL}$, showing that we are not able to resolve single phonon occupation.

To assess the measurement precision in terms of the Heisenberg uncertainty principle, we have to estimate the force fluctuations S_{FF}^{ba} acting on the nanobeam. A conservative approach is to assume that the measurement outcome is purely due to dynamical back-action noise, implying that we assume $S_{FF}^{ba} = S_{FF}^{th}$. From Equation (5.47), we obtain
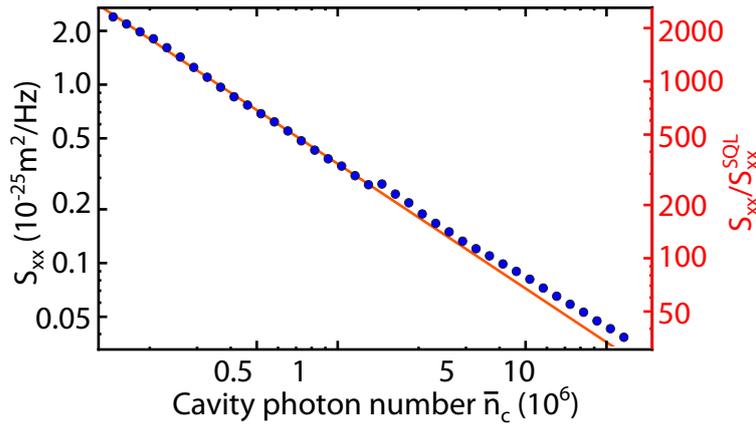
Figure 5.12: Imprecision noise in terms of displacement spectral density (left, black scale) and multiples of S_{xx}^{SQL} (right, red scale) versus intra-cavity photon number. The orange line represents a $1/\bar{n}_c$ dependence.

$S_{FF}^{th} = 4\hbar\Omega_m m_{eff}\Gamma_{eff}(\bar{n}_m + 1/2) \approx 1.6 \times 10^{-37} \text{ N}^2/\text{Hz}$ for $\bar{n}_m \approx 13$. The measurement uncertainty achieved in this measurement is thus $\sqrt{S_{xx}^{imp}S_{FF}^{ba}} \approx 234\hbar$ placing us a factor of 165 above the minimum uncertainty of $\sqrt{2}\hbar$ as discussed in Section 5.1.2. We emphasize that this value mainly results from the high imprecision noise present in our system, which we can easily minimize in future experiments by integrating a high-Q microwave filter (for example a sapphire filter [258]) into the setup. A less conservative approximation excludes the Langevin force spectral density arising from the thermal bath [111], i.e. we take into account the low temperature of the sample in the experiment and set $S_{FF}^{ba} = S_{FF}^{th} - S_{FF}^{cryo}$. Following Equation (5.33), the cryogenic environment contributes with $S_{FF}^{cryo} = 4m_{eff}k_B T_{cryo}\Gamma_m(T_{cryo}) \approx 1.0 \times 10^{-37} \text{ N}^2/\text{Hz}$. The resulting uncertainty is $\sqrt{S_{xx}^{imp}(S_{FF}^{th} - S_{FF}^{cryo})} \approx 100\sqrt{2}\hbar$.

5.3.4 Discussion

In this chapter we have presented the theoretical framework to describe most of the basic electromechanical phenomena. We have discussed electromechanical linewidth broadening and the optical spring effect as well as electromechanical cooling of the mechanical mode. The interpretation of measurement results in terms of mechanical displacement spectra and the necessary calibration of the measurement have been explained including a simple way to calibrate the input attenuation while simultaneously assigning the electromechanical vacuum coupling g_0. Frequency noise calibration reveals for our specific device $g_0/2\pi = 1.26\,\text{Hz}$, completing the system characterization. The analysis of the linewidth broadening in two-tone experiments (see Section 6.1) allows together with the estimated value of g_0 to quantify the attenuation in fridge No.1 (No.2) to 65.5 dB (62 dB). Changing the fabrication technique to minimize the gap between nanobeam and ground, for example by involving a focused ion beam [166] can easily increase the coupling by about one order of magnitude [120]. Our device geometry thus combines sufficiently strong coupling to demonstrate ground state cooling with access to higher modes of the microwave cavity. This is a clear advantage over electromechanical systems with a lumped element microwave resonator [80, 120].

With measurements of the mechanical displacement spectrum as a function of drive tone detuning we demonstrate the before discussed electromechanical linewidth broadening and the optical spring effect.

By applying an optimally red detuned driving tone, we observe cooling of the mechanical mode to a mean occupation of $\bar{n}_{\mathrm{m}} \approx 13$ mechanical quanta in excellent agreement to theory, corroborating that the vacuum coupling is sufficiently high to enable ground-state cooling as demonstrated in the microwave regime [113] and in the optical domain with photonic crystal structures [78]. To reach a mechanical occupation below one, we need to suppress noise in the microwave sources by integrating a microwave filter and to include a Josephson parametric amplifier in our setup [48, 253]. This will also improve the measurement imprecision of currently $S_{\mathrm{xx}}^{\mathrm{imp}} \approx 35 \cdot S_{\mathrm{xx}}^{\mathrm{SQL}} \approx 3.8 \times 10^{-27} \ \mathrm{m}^2/\mathrm{Hz}$ to a value close to the SQL. We estimate the measurement uncertainty to $\sqrt{S_{\mathrm{xx}}^{\mathrm{imp}}(S_{\mathrm{FF}}^{\mathrm{ba}} - S_{\mathrm{FF}}^{\mathrm{th}})} \approx 100\sqrt{2}\hbar$, much higher than achieved in a setup using a parametric amplifier [113].

Chapter 6

Two-tone experiments

Spectroscopy of cavity electromechanical systems incorporating multiple "optical" fields offers access to a new class of phenomena. Recently, studies of (static) two-tone configurations have been in the focus of research [80, 82, 87, 115, 116, 120, 241]. One effect of a two-tone configuration is electromechanically induced transparency (EMIT)[1], incorporating a red detuned drive field and a probe field around the cavity's resonance. Here, the drive and the probe tone destructively interfere inside a photonic cavity due to electromechanical interaction with a mechanical oscillator, leading to a transmission window whose width can be varied by the drive's intensity. Moreover, normal mode splitting occurs for a coupling rate exceeding the decay rate of the cavity due to hybridization of "optical" and mechanical modes. This is a prerequisite for state transfer between cavity photons and mechanical excitations. EMIT presents the route to introduce group delays in pulsed radiation in the GHz regime, as well as being a milestone towards storing information in the mechanical mode of such a system. Practical applications include tunable bandpass filters and electromechanical switching as discussed in Section 7.2. The analogue of EMIT for a blue detuned drive tone is electromechanically induced absorption (EMIA) [82, 116]. The interference effect in this case leads to an increased absorption in a narrow frequency band defined by the (electromechanically narrowed) mechanical loss rate.

Both EMIT and EMIA are key requirements for protocols to manipulate and control electromagnetic signals [80, 115, 116, 120]. These, in turn, are prerequisites for the realization of tools e.g. for the conditioning of microwave signals working on the quantum level. To this end, experiments on the red-detuned sideband can become limited by the linewidth of the mechanical resonator, which is broadened by the opto- or electromechanical damping. On the other hand, experiments on the blue-detuned sideband are not restricted by this effect. Here, the filter function can become even sharper due to electromechanical linewidth narrowing.

In this Chapter we analyze configurations employing two-tone spectroscopy. A strong drive tone is applied to the system while the transmission is monitored with a weak probe tone centered in close vicinity to the Stokes or anti-Stokes sideband of the drive. After a phenomenological explanation of these findings, we derive a theoretical framework necessary to discuss both interference effects, EMIT and EMIA. We present a detailed study of EMIT, showing the amplitude dependence and transparency window behavior as a function

---

[1]For experiments in the optical domain, this effect is also-called "OMIT".

of the drive power at optimum detuning and in the situation where the latter restriction is relaxed. We present a comparison between the model and the data, showing where the approximations lead to significant changes between prediction and measurement.

A detailed analysis of EMIA is presented in the following. In particular, we focus on the depth of the absorption feature and its linewidth. We demonstrate that for increasing drive power the effect changes from an absorption window in the probe transmission to a window where additional probe photons leak out of the cavity and discuss the agreement of this feature to the model. Further, we show that as a consequence double dip structures manifest themselves as a function of drive detuning for sufficiently high drive powers.

Turning back to EMIT configuration, we extend the theoretical model to include non-linear mechanical oscillations and corroborate the predictions by mapping the nanobeam's Duffing nonlinearity, studied in Section 4.5.3 into the microwave regime [87].

We close this chapter by focusing on the cavity transmission for a system in EMIA configuration. We operate the system in a regime, where the electromechanical linewidth narrowing leads to phonon lasing (phasing) of the mechanical mode [93]. The high amplitude mechanical motion generates sidebands in the cavity transmission spectrum and gives rise to a shift of the cavity's resonance frequency. We extend the coupling between optical and mechanical mode beyond the linearized model of electromechanical coupling to explain the Kerr like shift.

6.1   Electromechanically induced transparency

6.1.1   Qualitative discussion

Cavity electromechanical systems incorporating a parametrical coupling which links the position of a mechanical oscillator to the photon number of an electromagnetic resonator can be described by the Hamiltonian defined in Equation (5.21):

$$\hat{H} = \hbar\widetilde{\omega}_c \left(\hat{n}_c + \frac{1}{2} \right) + \hbar\Omega_m \left(\hat{n}_m + \frac{1}{2} \right) + \hbar G \hat{n}_c \hat{x} + \hat{H}_d \ . \tag{6.1}$$

To access the interference effect EMIT, the system is exposed to a strong drive tone on the red sideband with drive tone detuning $\Delta = \omega_d - \omega_c \simeq -\Omega_m$. A second, weaker tone is injected into the system to probe the modified cavity resonance at the frequency $\omega_p = \omega_d + \Omega$ (Figure 6.1). The simultaneous presence of the drive and the probe tone result in a radiation pressure force oscillating at $\Omega = \omega_p - \omega_d$. If this difference frequency, referred to as probe detuning, matches the mechanical resonance frequency, $\Omega \simeq \Omega_m$, a coherent oscillation of the mechanical system is induced. Consequently, Stokes and anti-Stokes fields (blue-shaded areas in Figure 6.1) build up at $\omega_d \pm \Omega_m$ around the strong driving field. The microwave resonator acts as a narrow-band filter for these fields. If the system is in the resolved-sideband regime, $\Omega_m > \kappa$, the Stokes line at $\omega_d - \Omega_m < \omega_c$ is strongly suppressed because it is off-resonant with the cavity ($\omega_d - \Omega_m \approx \omega_c - 2\Omega_m \ll \kappa$), whereas the anti-Stokes line at $\omega_d + \Omega_m \simeq \omega_c$ is enhanced (see Section 5.1.1 for more details). Moreover, since the anti-Stokes scattered field is degenerate with the probe field sent to the cavity, it allows for destructive interference of the two fields supressing the build-up of the intra-cavity probe field. This can be viewed as a self-interference between two different excitation pathways. The resulting decreased feeding ("transparency") of
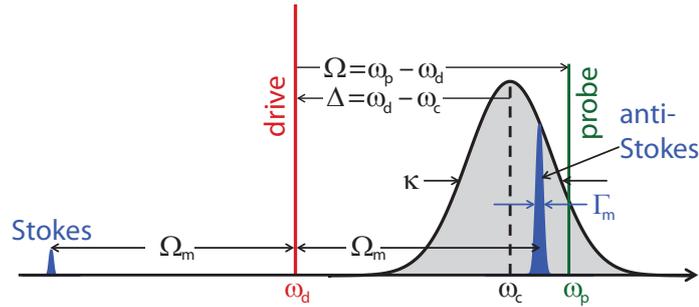
Figure 6.1: Schematic diagram explaining the various frequencies: driving tone frequency ω_d (red line), probe tone frequency ω_p (green line), cavity resonant frequency ω_c (black line), drive tone detuning $\Delta = \omega_\mathrm{d} - \omega_\mathrm{c}$, probe tone detuning $\Omega = \omega_\mathrm{p} - \omega_\mathrm{d}$. Varying Δ shifts the drive tone with respect to the cavity resonance (grey-shaded area). Since the anti-Stokes line (blue shaded area) is fixed to the drive tone at $\omega_\mathrm{d} + \Omega_\mathrm{m}$, the variation of Δ also shifts the anti-Stokes line with respect to the cavity resonance. Varying Ω at constant Δ shifts the probe tone with respect to the cavity resonance and the anti-Stokes line.

probe photons into the cavity manifests itself as a enhanced cavity transmission up to unity compared to the feed line. Depending on the frequency of the electromagnetic field, this effect is referred to as electromechanically or optomechanically induced transparency (EMIT or OMIT) [115, 116], the electromechanical analog of electromagnetically induced transmission (EIT) [118, 259]. For a detailed comparison between OMIT and EIT we point the reader to Weis et al. [115].

Another way of visualizing the effect of EMIT is the use of the level scheme shown in Figure 6.2. In this scheme the electromechanical states are simplified by product states $|n_\mathrm{c}, n_\mathrm{m}\rangle$ characterized by n_c cavity excitations (photons) and n_m mechanical excitations (phonons). Here, a pure cavity excitation would be represented by a vertical arrow increasing only the number photons in the cavity. In contrast, if the drive field is set to $\omega_\mathrm{d} \simeq \omega_\mathrm{c} - \Omega_\mathrm{m}$ (optimal red detuning), it increases the photon number but decreases the phonon number by one and hence is represented by a diagonal red arrow. The photons of the drive field are up-converted by consumption of a mechanical phonon and scatter into the anti-Stokes line at $\omega_\mathrm{d} + \Omega_\mathrm{m}$, matching approximately the cavity resonant frequency ω_c. Since probe and drive tone are coherent with respect to each other[2], the up-converted drive field can interfere with the weak probe field, indicated by the vertical green arrow. In the case that the drive field is not optimally detuned from the cavity resonance ($\Delta = \omega_\mathrm{d} - \omega_\mathrm{c} \neq -\Omega_\mathrm{m}$), virtual levels are involved which are represented by the dashed lines in Fig. 6.2. Also in this situation the up-conversion of the drive field photons generates photons of frequency $\omega_\mathrm{d} + \Omega_\mathrm{m} = \omega_\mathrm{p} \neq \omega_\mathrm{c}$, that is, photons of the same frequency as the probe field, again allowing for destructive interference with the probe field sent to the cavity. Depending on the relative power of the probe and the drive field, the interference can lead to a partial or full extinction of the probe field inside the cavity, what is detected as enhanced cavity transmission in experiments.

---

[2]Note that for EMIT the mutual coherence of probe and drive needs to be reciprocal of the transmission window.
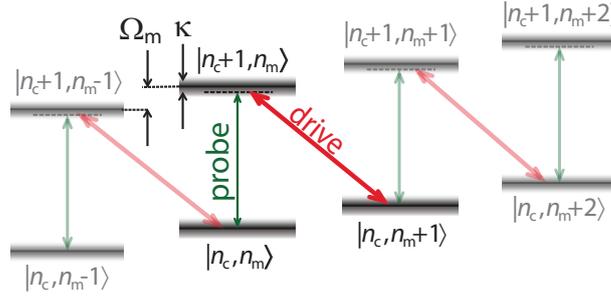
Figure 6.2: Level diagram describing the physics of the electromechanical system: The red detuned drive tone at frequency ω_d (red arrow) induces a transition from a state $|n_\mathrm{c}, n_\mathrm{m} + 1\rangle$ characterized by n_c cavity excitations (photons) and $n_\mathrm{m} + 1$ mechanical excitations (phonons) to a state $|n_\mathrm{c}+1, n_\mathrm{m}\rangle$, that is, it adds one excitation to the cavity and decreases one mechanical oscillator exitation. The cavity photons generated in this up-conversion process are degenerate with the near-resonant probe field at frequency $\omega_\mathrm{p} = \omega_\mathrm{d} + \Omega_\mathrm{m}$ (green arrow), resulting in a constructive interference effect. The dashed lines indicate virtual levels, indicating that the drive field is not optimally red-detuned from the cavity resonance ($\Omega = \Omega_\mathrm{m} \neq \Delta$).

6.1.2   Quantitative analysis

To analyze the effect of EMIT quantitatively as a function of drive power and the detunings Δ and Ω, we have to solve the full Hamiltonian (6.1). We will see, that the probe power transmission spectrum in the resolved sideband regime is given by

$$|t|^2 = \left| 1 - \frac{\kappa_\mathrm{ex}/2}{-i(\Delta + \Omega) + \kappa/2 + \frac{g_0^2 \bar{n}_\mathrm{c}}{-i(\Omega - \Omega_\mathrm{m}) + \Gamma_\mathrm{m}/2}} \right|^2 . \tag{6.2}$$

Following the derivation in reference [115] and [87], we can rewrite the Hamiltonian in a way first described by Law [198]:

$$\hat{H} = \hat{H}_{\mu\mathrm{w}} + \hat{H}_\mathrm{mech} + \hat{H}_\mathrm{int} + \hat{H}_\mathrm{d}, \tag{6.3}$$

$$\hat{H}_{\mu\mathrm{w}} = \hbar\widetilde{\omega}_\mathrm{c} \left(\hat{a}^\dagger \hat{a} + \frac{1}{2} \right) , \tag{6.4}$$

$$\hat{H}_\mathrm{mech} = \frac{\hat{p}^2}{2m_\mathrm{eff}} + \frac{1}{2} m_\mathrm{eff} \Omega_\mathrm{m}^2 \hat{x}^2 , \tag{6.5}$$

$$\hat{H}_\mathrm{int} = \hbar G \hat{x} \hat{a}^\dagger \hat{a} , \tag{6.6}$$

$$\hat{H}_\mathrm{d} = i\hbar \sqrt{\frac{\kappa_\mathrm{ex}}{2}} (s_\mathrm{in}(t)\hat{a}^\dagger - s_\mathrm{in}^*(t)\hat{a}) . \tag{6.7}$$

We have introduced the momentum operator of the mechanical mode $\hat{p}$, the external loss rate $\kappa_\mathrm{ex}/2\pi$ of the μ-wave cavity into the feed line and the complex driving amplitude $s_\mathrm{in}(t)$, normalized to $|s_\mathrm{in}(t)|^2$ is the photon flux at the cavity input. We will now derive the linearized Langevin Equations [56], where we define the driving amplitude as $s_\mathrm{in}(t) = (\bar{s}_\mathrm{in} + \delta s_\mathrm{in}(t))e^{-i\omega_\mathrm{d}t}$. We identify $\bar{s}_\mathrm{in}$ as the driving field and here $\delta s_\mathrm{in}(t) = s_\mathrm{p}e^{-i(\omega_\mathrm{p} - \omega_\mathrm{d})t}$ as the probe field (we will neglect noise contributions in this discussion). By introducing the total electromagnetic loss rate as the sum of external loss rate and intrinsic dissipation rate, $\kappa/2\pi = (\kappa_\mathrm{ex} + \kappa_\mathrm{in})/2\pi$ and the mechanical loss rate $\Gamma_\mathrm{m}/2\pi$ we obtain in a frame

rotating with $\bar{\Delta} = \omega_{\rm d} - \widetilde{\omega}_{\rm c}$, where $\widetilde{\omega}_{\rm c}$ indicates the undisturbed cavity eigenfrequency.

$$\frac{d}{dt}\hat{a}(t) = \left(+i\bar{\Delta} - \frac{\kappa}{2}\right)\hat{a}(t) - iG\hat{x}(t)\hat{a}(t) + \sqrt{\frac{\kappa_{\rm ex}}{2}}s_{\rm in}(t), \tag{6.8}$$

$$\frac{d}{dt}\hat{x}(t) = \frac{\hat{p}(t)}{m_{\rm eff}}, \tag{6.9}$$

$$\frac{d}{dt}\hat{p}(t) = -m_{\rm eff}\Omega_{\rm m}^2\hat{x}(t) - \hbar G\hat{a}^\dagger(t)\hat{a}(t) - \Gamma_{\rm m}\hat{p}(t). \tag{6.10}$$

We first define steady state solutions, whose time derivatives are all zero. The self consistent steady state solutions for the intra-cavity field $\bar{a}$ and the mechanical displacement $\bar{x}$ read

$$\bar{a} = \frac{\sqrt{\kappa_{\rm ex}/2}}{-i(\bar{\Delta} - G\bar{x}) + \frac{\kappa}{2}}\bar{s}_{\rm in}, \tag{6.11}$$

$$\bar{x} = -\frac{\hbar G\bar{a}^2}{m_{\rm eff}\Omega_{\rm m}^2}. \tag{6.12}$$

The solution of the Langevin Equations (6.8)-(6.10) is the sum of the steady state solution and a dynamic part, $\hat{a}(t) = \bar{a} + \delta\hat{a}(t)$, $\hat{x}(t) = \bar{x} + \delta\hat{x}(t)$. Here, $\delta\hat{x}(t)$ is hermitian. Implicitly we have chosen the phase of the cavity as a reference, thus $\bar{a}$ has a real and positive value and $\bar{a}^2$ represents the average intra-cavity photon number $\bar{a}^2 = \bar{n}_{\rm c} = \langle\hat{n}_{\rm c}\rangle \propto \bar{s}_{\rm in}^2 \cdot \kappa_{\rm ex}/2$. Finally we define $\Delta = \bar{\Delta} - G\bar{x}$ as the corrected detuning, due to the static shift of the microwave cavity $\omega_{\rm c} = \widetilde{\omega}_{\rm c} + G\bar{x}$. Replacing those values we get

$$\frac{d}{dt}\delta\hat{a}(t) = \left(i\Delta - \frac{\kappa}{2}\right)\delta\hat{a}(t) - iG(\bar{a} + \delta\hat{a}(t))\delta\hat{x}(t) + \sqrt{\frac{\kappa_{\rm ex}}{2}}\delta s_{\rm in}(t), \tag{6.13}$$

$$\frac{d^2}{dt^2}\delta\hat{x}(t) + \Gamma_{\rm m}\frac{d}{dt}\delta\hat{x}(t) + \Omega_{\rm m}^2\delta\hat{x}(t) = -\frac{\hbar G}{m_{\rm eff}}\bar{a}(\delta\hat{a}(t) + \delta\hat{a}^\dagger(t)). \tag{6.14}$$

For the interference effects, the drive field is much stronger than the probe field ($\bar{a} \gg \delta\hat{a}$), what allows us to neglect higher order terms in $\delta\hat{a}$ and $\delta\hat{a}^\dagger$ in the derivation of above equations. Both drive and probe field are classical coherent fields, thus we can identify all operators $\hat{y}(t)$ with their expectation values $y(t) \equiv \langle\hat{y}(t)\rangle$. This also implies $\langle\hat{y}^\dagger(t)\rangle \equiv y^*(t)$. To solve the Equations (6.13) and (6.14), we switch to a frame rotating with $\Omega = \omega_{\rm p} - \omega_{\rm d}$ and employ the following ansatz

$$\delta a(t) = A^- e^{-i\Omega t} + A^+ e^{+i\Omega t}, \tag{6.15}$$

$$\delta a^*(t) = (A^+)^* e^{-i\Omega t} + (A^-)^* e^{+i\Omega t}, \tag{6.16}$$

$$\delta x(t) = X e^{-i\Omega t} + X^* e^{+i\Omega t}. \tag{6.17}$$

These equations can be separated according to their rotation terms. We are interested in the the probe field's transmission at $\omega_{\rm p} = \omega_{\rm d} + \Omega$, so we have to look for a solution rotating with $e^{-i\Omega t}$. This implies that we need a solution of A^- to describe $\delta a(t)$ and thus the probe tone transmission. Three equations contribute:

$$\left(-i(\Omega + \Delta) + \frac{\kappa}{2}\right)A^- = -iG\bar{a}X + \sqrt{\frac{\kappa_{\rm ex}}{2}}s_{\rm p}, \tag{6.18}$$

$$\left(i(\Omega - \Delta) + \frac{\kappa}{2}\right)A^+ = -iG\bar{a}X^*, \tag{6.19}$$

$$(\Omega_{\rm m}^2 - \Omega^2 - i\Gamma_{\rm m}\Omega)X = -\frac{\hbar G\bar{a}}{m_{\rm eff}}(A^- + (A^+)^*). \tag{6.20}$$

The solution of A^- reads

$$A^- = \frac{1 + if(\Omega)}{-i(\Delta + \Omega) + \kappa/2 + 2\Delta f(\Omega)} \sqrt{\frac{\kappa_{\text{ex}}}{2}} s_{\text{p}}, \tag{6.21}$$

with

$$f(\Omega) = \hbar G^2 \bar{n}_{\text{c}} \frac{\chi_{\text{m}}(\Omega)}{i(\Delta - \Omega) + \kappa/2}. \tag{6.22}$$

Here, we have introduced the susceptibility $\chi_{\text{m}}(\Omega)$ of the mechanical mode according to Equation (5.16),

$$\chi_{\text{m}}(\Omega)^{-1} = m_{\text{eff}}(\Omega_{\text{m}}^2 - \Omega^2 - i\Omega\Gamma_{\text{m}}). \tag{6.23}$$

Please note that this solution describes EMIT as well as EMIA. In the case of EMIA, when making an ansatz according to Equations (6.15)-(6.17) we only have to consider that the rotating wave approximation changes sign, since the drive field is on the blue sideband and the solution of interest is A^+ that has the same frequency as s_{p}. This leads to the same ansatz as in Equations (6.15)-(6.17) and to the same Equations of motion (6.18)-(6.20), but with the roles of A^- and A^+ exchanged. So this equation is valid for $\Delta < 0$ and $\Omega > 0$ (what is the setting for EMIT), as well as for $\Delta > 0$ and $\Omega < 0$, putting the system in an EMIA configuration. We use input-output theory [117, 246] to obtain the output fields:

$$s_{\text{out}}(t) = s_{\text{in}}(t) - \sqrt{\frac{\kappa_{\text{ex}}}{2}} a(t)$$
$$= \left(\bar{s}_{\text{in}} - \sqrt{\frac{\kappa_{\text{ex}}}{2}} \bar{a}\right) e^{-i\omega_{\text{d}}t} + \left(s_{\text{p}} - \sqrt{\frac{\kappa_{\text{ex}}}{2}} A^-\right) e^{-i(\omega_{\text{d}}+\Omega)t} - \sqrt{\frac{\kappa_{\text{ex}}}{2}} A^+ e^{-i(\omega_{\text{d}}-\Omega)t}. \tag{6.24}$$

The transmission of the probe field collects the terms rotating with $\omega_{\text{p}} = \omega_{\text{d}} + \Omega$. The transmission, normalized to the input thus reads $t = (s_{\text{p}} - \sqrt{\frac{\kappa_{\text{ex}}}{2}} A^-)/s_{\text{p}}$. The transmitted power spectrum, normalized to the input is given by

$$|t|^2 = \left| 1 - \frac{\kappa_{\text{ex}}}{2} \frac{1 + if(\Omega)}{-i(\Delta + \Omega) + \kappa/2 + 2\Delta f(\Omega)} \right|^2. \tag{6.25}$$

Most opto- and electromechanical systems operate in the resolved sideband regime, where the mechanical frequency exceeds the cavity linewidth ($\Omega_{\text{m}} > \kappa$). Figure 6.1 shows schematically such a configuration. The Stokes sideband is far off the cavity resonance (anti-Stokes for EMIA configuration) and will be strongly suppressed due to the cavity filter function. So we can neglect the off resonant sideband in our calculation, i.e. $A^+ = 0$.

Additionally, we linearize the mechanical susceptibility for a drive field on the red sideband ($\Delta < 0$) and a probe tone not too far from optimum detuning[3],

$$\chi_{\text{m}}(\Omega)^{-1} \approx m_{\text{eff}}\Omega_{\text{m}}(2(\Omega - \Omega_{\text{m}}) - i\Gamma_{\text{m}}). \tag{6.26}$$

Plugging these assumptions into Equation (6.21) and replacing $G = g_0/x_{\text{zpf}}$ with $x_{\text{zpf}} = \sqrt{\hbar/2m_{\text{eff}}\Omega_{\text{m}}}$, the intra-cavity field simplifies to

$$A^- = \frac{\sqrt{\kappa_{\text{ex}}/2}\, s_{\text{p}}}{-i(\Delta + \Omega) + \kappa/2 + \frac{g_0^2 \bar{n}_{\text{c}}}{-i(\Omega-\Omega_{\text{m}})+\Gamma_{\text{m}}/2}}, \tag{6.27}$$

---

[3]in the case of EMIA, the approximation of χ_{m} looks different. This is the origin of the difference in the formulas (6.2) and (6.37) describing the transmission spectra of EMIT and EMIA in the resolved sideband regime, respectively.
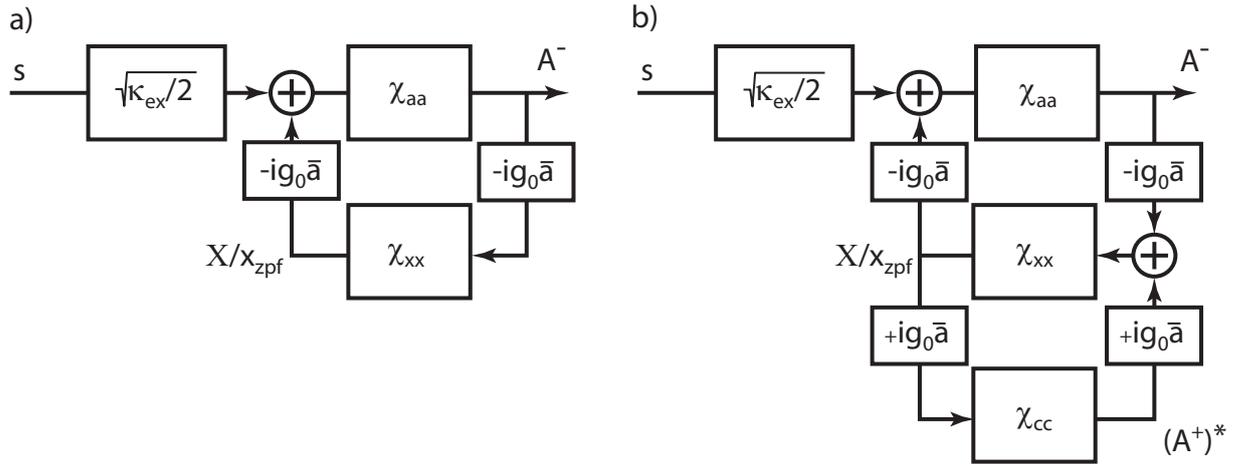
Figure 6.3: Feedback diagramm of EMIT and EMIA. a) shows the simplified diagram if the system is in the resolved sideband regime described by Equation (6.32). A probe field sent to the cavity receives a feedback gain from the mechanical mode due to the electromechanical coupling. The frequency degeneracy of probe field and scattered drive field physically realize the summing nodes. b) shows the full spectrum according to Equation (6.32), taking the feedback between mechanical mode and off-resonant sideband into account.

and the transmitted power spectrum behaves according to Equation (6.2), as stated above.

A different interpretation for the intra-cavity field is achieved by introducing the bare cavity susceptibilities and redefining the mechanical susceptibility in Equations (6.13)-(6.14) [87]. The linearity of these differential equations allows to define a term – the susceptibility χ_{yy} – describing the modification of the corresponding mode y to a force F acting on it. The equation of motion takes then the form $y = \chi_{yy}F$, analogous to Equation (5.14). We identify the susceptibilities in Equations (6.13)-(6.14) to

$$\chi_{aa}(\Omega)^{-1} = \frac{\kappa}{2} - i(\Omega + \Delta) , \tag{6.28}$$

$$\chi_{cc}(\Omega)^{-1} = \chi_{aa}^*(-\Omega) = \frac{\kappa}{2} - i(\Omega - \Delta) , \tag{6.29}$$

$$\chi_{xx}(\Omega)^{-1} = \frac{\Gamma_{m}}{2} - i(\Omega - \Omega_{m}) . \tag{6.30}$$

Here, $\chi_{aa}(\Omega)$ describes the response of a simple μ-wave resonator to a probe field, $\chi_{cc}(\Omega)$ the response of the complex conjugate field and $\chi_{xx}(\Omega)$ describes the linearized response of a high Q mechanical oscillator. In contrast to the previous definition of $\chi_{m}(\Omega)$, we have renormalized the mechanical susceptibility, $\chi_{xx}(\Omega) = m_{eff}\Omega_{m}\chi_{m}(\Omega)$, accounting to the fact that we write the solution in terms of g_0, containing these quantities. Rewriting Equation (6.21) with those susceptibilities gives

$$A^- = \frac{\chi_{aa}(1 - g_0^2 \bar{n}_c \chi_{xx}\chi_{cc})}{1 + g_0^2 \bar{n}_c \chi_{xx}(\chi_{aa} - \chi_{cc})}\sqrt{\frac{\kappa_{ex}}{2}}s_p . \tag{6.31}$$

In the resolved sideband regime ($\Omega_{m} > \kappa$), the intra-cavity field simplifies from Equation (6.27) to

$$A^- = \frac{\chi_{aa}}{1 + g_0^2 \bar{n}_c \chi_{xx}\chi_{aa}}\sqrt{\frac{\kappa_{ex}}{2}}s_p . \tag{6.32}$$
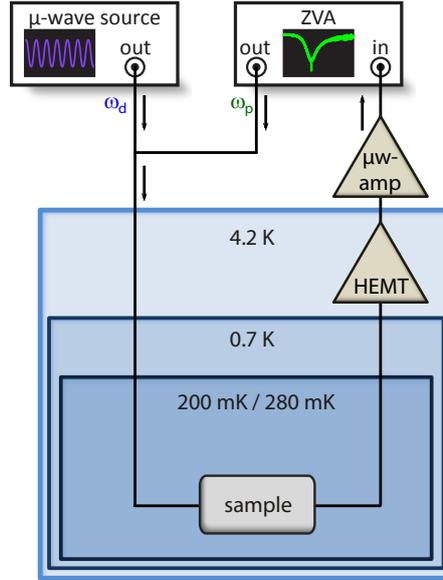
Figure 6.4: Schematic setup to experimentally investigate EMIT and EMIA. A μ-wave source
provides the driving field and is combined at roomtemperature with the output of a vector
network analyzer, providing the probe field. The combined fields are fed to the sample and
analyzed with the vector network analyzer after passing the sample and an amplifier chain.

By introducing susceptibilities for the cavity and mechanical mode respectively, we can
interpret EMIT/EMIA in terms of a feedback diagram, shown in Figure 6.3. In the
resolved sideband regime (Figure 6.3a), the probe field $\sqrt{\frac{\kappa_{\mathrm{ex}}}{2}}s_{\mathrm{p}}$ entering the cavity adds
up at the summing node with the intra-cavity field, which is multiplied with the feedback
gain from the mechanical mode. The electromechanical coupling rate defines the feedback
gain $(-ig_0\bar{a})\chi_{\mathrm{xx}}(-ig_0\bar{a})$. The sum of those two fields interacts again with the cavity (via
χ_{aa}) and result in A^- at the diagram output. The frequency degeneracy of probe field and
scattered drive field physically realizes the summing nodes. For the full diagram, taking
both sidebands into account (Figure 6.3b), we consider the interaction of the mechanical
mode with the off-resonant sideband, visualized by the additional feedback node.

6.1.3 Setup

As depicted in Figure 6.4, the experiments are performed in dilution refrigerator No.1 at
a temperature of $T \approx 200\,\mathrm{mK}$, far below the critical temperature of Nb ($T_{\mathrm{c}} = 9.2\,\mathrm{K}$). The
microwave excitation and detection circuitry consists of a Rohde&Schwarz SMF microwave
source, used to generate the strong red- or blue-detuned drive tone at $\omega_{\mathrm{d}} = \omega_{\mathrm{c}} + \Delta$, while
the weak probe field centered around $\omega_{\mathrm{d}} \pm \Omega_{\mathrm{m}}$ stems from a Rohde&Schwarz ZVA network
analyzer. The latter allows for phase sensitive detection of the the microwave signal after
interacting with the device under investigation. For the two-tone experiments, the two
microwave signals are combined at room temperature and then sent to the electromechan-
ical hybrid via coaxial cables. Several attenuators at the various temperature stages are
used for the reduction of thermal noise and thermalization of the microwave cables. After
passing the device under test, the transmitted signal is amplified using a cryogenic low-
noise HEMT amplifier anchored at $4.2\,\mathrm{K}$ and a room-temperature microwave amplifier.
The HEMT amplifier is isolated from the sample output by a circulator anchored at $0.7\,\mathrm{K}$.
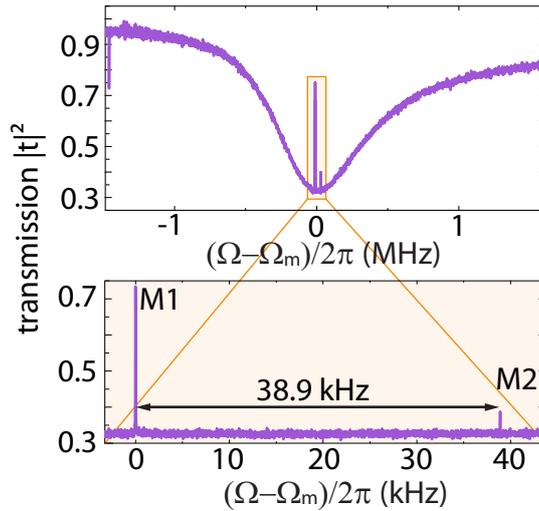
Figure 6.5: Full spectrum of the eletromechanical sample in EMIT configuration. Inside of the μ-wave resonance, two mechanical resonances are visible. We identify them with in-plane ("M1") and out-of-plane mode ("M2") of the nanobeam. The spectrum was recorded with an optimally red detuned drive tone with respect to peak M1 and a power of $P_d = 891\,\mathrm{pW}$. The probe tone is swept over the cavity resonance with a probe power of $28\,\mathrm{fW}$. A zoom of the two mechanical peaks, separated by $38.9\,\mathrm{kHz}$ is shown in the lower window.

To compensate the effect of the attenuators and amplifiers, we normalize the transmitted signal with respect to the transmitted signal away from the cavity resonance. For details of the cryogenic wiring we refer to Chapter 3.

6.1.4 Experimental results

We start our analysis by sweeping the probe frequency over the full μ-wave cavity and simultaneously applying a driving tone around optimum detuning $\Delta = -\Omega_m$. The probe power is kept constant in all EMIT experiments to $P_p = 28\,\mathrm{fW}$ ($-105.5\,\mathrm{dBm}$), the drive power here is $P_d = 891\,\mathrm{pW}$ ($-60.5\,\mathrm{dBm}$). We observe two peaks in the cavity resonance, showing two induced transmission features ("M1" and "M2" in Figure 6.5), separated by $\Delta\Omega/2\pi = 38.9\,\mathrm{kHz}$. The two resonances are more than one thousand mechanical linewidths apart and we do not observe any interaction or overlapping in all our experiments, since the optical spring effect in our system is only on a scale of Hz (see Section 5.3.2). We tried as well frequency tuning by applying an additional DC voltage up to $5\,\mathrm{V}$, without showing any observable effect on the eigenfrequencies. We assume the left peak ("M1") in Figure 6.5 to be the in-plane mode of our nanobeam and the right peak to be the out-of-plane mode ("M2")[4]. All numbers we have given so far refer to the left peak ("M1"). This is the resonance that we usually analyze except differently mentioned.

Analyzing both peaks at optimum detuning, we see that with increasing probe power the obsereved mechanical linewidths $\Gamma_{\mathrm{eff},i}$ broaden (see Figure 6.6a). This is caused by the fact that we have to consider the mechanical mode as dressed mechanical state due to the electromechanical coupling. The resulting state is effectively a phonon-photon polariton.

---

[4]We cannot fully exclude that these two modes are indeed coupled resonances or different superpositions of a more complex modal distribution, including for example torsional modes occurring due to the double layer structure of the nanobeam. To exclude this, further investigation of the higher harmonics is ongoing.

The nonvanishing photonic nature results in a finite coupling of the mechanical mode to the photonic loss channel at a rate $C\Gamma_\mathrm{m}$ [116], where we have introduced the electromechanical cooperativity $C = 4g^2/\kappa\Gamma_\mathrm{m} = 4g_0^2\bar{n}_\mathrm{c}/\kappa\Gamma_\mathrm{m}$ [112]. The effective electromechanical coupling scales linearly with the average number of intra-cavity photons which is related to the applied driving power by

$$\bar{n}_\mathrm{c} = \frac{P_\mathrm{d}}{\hbar\omega_\mathrm{d}} \, \frac{\kappa_\mathrm{ex}/2}{(\kappa/2)^2 + \Delta^2} \; . \tag{6.33}$$

The effective broadening of the mechanical linewidth due to electromechanical interaction with an optical mode is captured by Equation (5.19) as discussed in Section 5.1. At optimum detuning Γ_eff becomes maximal and Equation (5.19) reduces to

$$\Gamma_\mathrm{eff} = \Gamma_\mathrm{m}(1 + C) = \Gamma_\mathrm{m} + \frac{4g^2}{\kappa} \; , \tag{6.34}$$

agreeing with what we expect from the above discussion. The electromechanical manipulation of the mechanical mode results from the strong drive field. Since The influence of the probe tone is negligible, the effective linewidth follows Equation (5.19) for all detunings Δ. First we turn to the in-plane mode "M1". An analysis in terms of the effective linewidth extracted from the data displayed in Figure 6.6a by a Lorentzian fit leads to the data shown in panel b (red filled circles). We extract the intrinsic mechanical linewidth Γ_m and the effective coupling rate g from a linear fit of Equation (6.34). We find $\Gamma_\mathrm{m}/2\pi = 7.7\,\mathrm{Hz}$ in agreement to the measured value around $200\,\mathrm{mK}$ by ring down experiments as discussed in Section 4.5.2. We extract a maximum electromechanical coupling of $g_\mathrm{max}/2\pi = 20.6\,\mathrm{kHz}$ for a mean drive photon number of $\bar{n}_\mathrm{c} = 2.7 \times 10^8$ resulting in a maximum cooperativity of $C = 294$. The maximum coupling exceeds the thermal decoherence rate of the phonons at $30\,\mathrm{mK}$ of $\bar{n}_\mathrm{m}\Gamma_\mathrm{m}/2\pi \approx 1.18\,\mathrm{kHz}$. Thus we overcome the main obstacle in reaching the regime of quantum coherent manipulation ($g \gg \{\bar{n}_\mathrm{m}\Gamma_\mathrm{m}, \kappa\}$) [75]. Together with the electromechanical vacuum coupling of $g_0/2\pi = 1.26\,\mathrm{Hz}$ measured by frequency noise calibration (see Section 5.2.2), we can access the attenuation of the input microwave line connecting the sample with the measurement apparatus. We estimate the damping of the feedline to $65.5\,\mathrm{dB}$.

Now, we turn the discussion to the out-of-plane mode "M2". Extraction of the effective linewidth results in the blue filled circles displayed in Figure 6.6b. The same procedure as above gives an intrinsic linewidth of $\Gamma_\mathrm{m,op}/2\pi = 13.4\,\mathrm{Hz}$ and a maximum cooperativity of $C_\mathrm{op} = 16$. With the known mean intra-cavity photon number $\bar{n}_\mathrm{c}$, calculated from Equation (6.33) using the attenuation of the input line, we determine the electromechanical vacuum coupling to $g_\mathrm{0,op}/2\pi = 0.39\,\mathrm{Hz}$ using Equation (6.34). The out-of-plane mode couples a factor of three weaker to the light field than "M1". This becomes clear, when considering that an ideal out-of-plane motion of the nanobeam changes the capacitance at $2\Omega_\mathrm{m,op}$ due to symmetry arguments. However, the double layer structure of the nanobeam leads to an asymmetric amplitude distribution. Thus, we expect the periodic change in capacitance to have a contribution at the eigenfrequency $\Omega_\mathrm{m,op}$, coupling weaker than the in-plane mode. To quantify the asymmetry of the out-of-plane motion, optical measurements of this mode are ongoing. In the following we will focus on the in-plane mode "M1", as its higher coupling allows for an easier implementation of the experimental requirements needed for the study of theoretical predictions based on high cooperativity. Next, we discuss the amplitude of the transparency peak for increasing number of drive photons. We
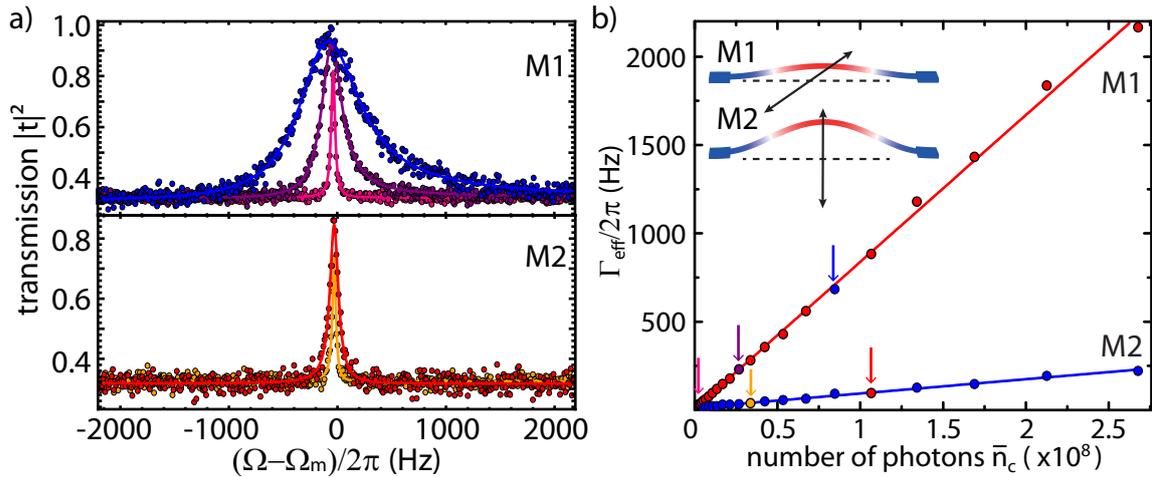
Figure 6.6: a) Probe power transmission spectra of the two resonances for different driving powers. The upper curves correspond to the in-plane mode "M1" (pink: $\bar{n}_c \approx 4.24 \times 10^6$, purple: $\bar{n}_c \approx 2.68 \times 10^7$, blue: $\bar{n}_c \approx 8.47 \times 10^7$) the lower to the out-of-plane mode "M2" (orange: $\bar{n}_c \approx 3.37 \times 10^7$, red: $\bar{n}_c \approx 1.07 \times 10^8$). The solid lines are Lorentzian fits to the data. b) The effective linewidths Γ_{eff} of the two mechanical modes plotted against the number of drive photons. The solid lines are linear fits to Equation (6.34). The differently colored points correspond to the linewidths of the curves with the same color in a).

have to mention, that we do not detect a transmission window of unity. This becomes most evident, when looking the transmission curve shown in Figure 6.5. We see that the microwave cavity has a dispersive shift, resulting from interference with waves traveling along the ground plane and is a well known feature. This shift of the phase reference is well understood and incorporated in our fitting routines as discussed in Appendix A.5. Yet, the maximum transmission in the narrow transparency window is obtained by the line connecting the left and right background of the cavity spectrum, taken at cavity resonance. This gives a maximum power transmission of $|t_0|^2 \approx 0.9$. In Figure 6.7 the height of the transmission peak is plotted against the average number of drive photons $\bar{n}_c$. For a low number of drive photons ($\bar{n}_c < 5 \times 10^6$), we see that the transparency window still approaches its maximum value until it saturates at an approximate photon number of $\bar{n}_c = 2 \times 10^7$. For optimum detuning, the power transmission defined in Equation (6.2) at the mechanical resonance simplifies to

$$|t_0|^2 = \left| \frac{1 - \kappa_{\text{ex}}/\kappa + C}{1 + C} \right|^2 . \tag{6.35}$$

The solid line in Figure 6.7 is a plot of this equation using the parameters as discussed above. Evidently, there is good agreement between experiment and theory.

To validate the full linewidth model on the red sideband, stated in Equation (5.19), we determine Γ_{eff} for various detunings Δ, while keeping the drive power P_d constant. Figure 6.8 shows three sweeps with different drive powers ($P_d = 890\,\text{pW}$, $2.8\,\text{nW}$ and $4.5\,\text{nW}$, respectively). The probe power was fixed at $P_p = 28\,\text{fW}$. The detuning $\Delta/2\pi$ is swept over a range from $-2.5\,\text{MHz}$ to $0\,\text{Hz}$. As expected we observe the strongest linewidth broadening for high drive powers and the maximum broadening occurs at optimum detuning. The reduction of the effective linewidth towards its intrinsic value for a detuning away from the mechanical resonance ($\Delta/2\pi \to -2.5\,\text{MHz}$ and $\Delta/2\pi \to 0\,\text{Hz}$) comes from
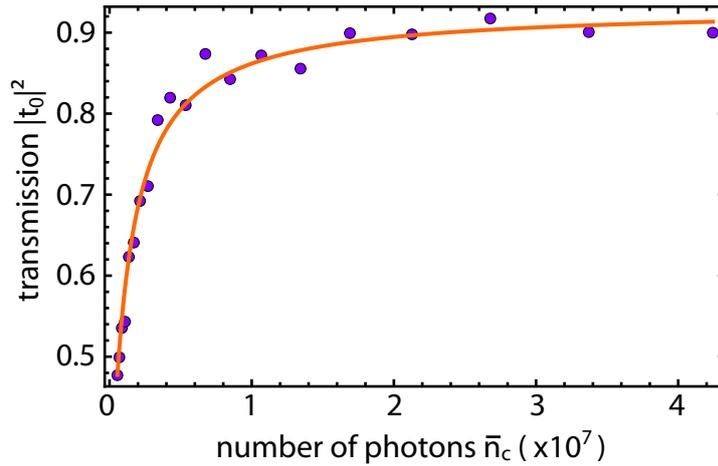
Figure 6.7: Transmission of the in plane mode plotted versus the number of drive photons. The solid line is a plot of Equation (6.35) using the measured parameters of κ, κ_{ex}, g_0 and Γ_{m}. Only the fact that the amplitude of the transmission does not reach unity was used as a fit parameter. See the text for more details.

the reduced electromechanical coupling efficiency due to the reduction of the ratio between anti-Stokes and Stokes sideband. The saddle point results from the varying average intra-cavity photon number $\bar{n}_{\mathrm{c}}$ for different detunings Δ: A smaller detuning implies that the drive tone is closer to the cavity resonance, allowing more drive photons to enter the cavity. This results in a higher effective electromechanical coupling $g = g_0\sqrt{\bar{n}_{\mathrm{c}}}$. The resulting effective linewidth Γ_{eff} is higher than for a sweep with constant photon number $\bar{n}_{\mathrm{c}}$ and modulated by the filter function of the μ-wave cavity. The orange lines in Figure 6.8 are fits to Equation (5.19), taking the varying photon number $\bar{n}_{\mathrm{c}}(\Delta)$ into account using Equation (6.33). The data show good agreement with theory, corroborating the above discussion that the linewidth broadening occurs from electromechanical interaction of the mechanical mode with the driving field and is described by assuming a single tone configuration neglecting the probe tone. To conclude the discussion of EMIT we take a look at the two models we have derived so far: The full model, predicting the transmission according to Equation (6.25) and the model for a system in the resolved sideband regime given in Equation (6.2). In above discussion we have already shown that both models predict the same results at optimum detuning for a system in the resolved sideband limit. An interesting question is how long the approximations made in those two models lead to an adequate description of the observed physical phenomena. We briefly recall the assumptions we made, when we evaluated the theoretical model. First, we treat the Hamiltionian in a frame rotating with Δ. This assumption does not reduce the accuracy of the description, there is no evidence that counter-rotating terms with a frequency of $-\Delta$ will occur. Second, we analyze the system in terms of a steady state and time dependent solution. This is a valid assumption, the Langevin equations are linear, the superposition principle we implicitly assume is valid. Third, we apply a rotating wave equation in Ω, only counting the terms directly contributing to the interference with the probe tone. This assumption is only valid, as long as we can ignore a contribution of the off resonant sideband, because it is strongly suppressed by the cavity filter function. When the drive tone is closer to the microwave resonance than the cavity linewidth, $|\Delta| \approx \kappa$, this is no longer the case. If the drive tone moves closer to the microwave resonance, $|\Delta| < \kappa$, we expect that the
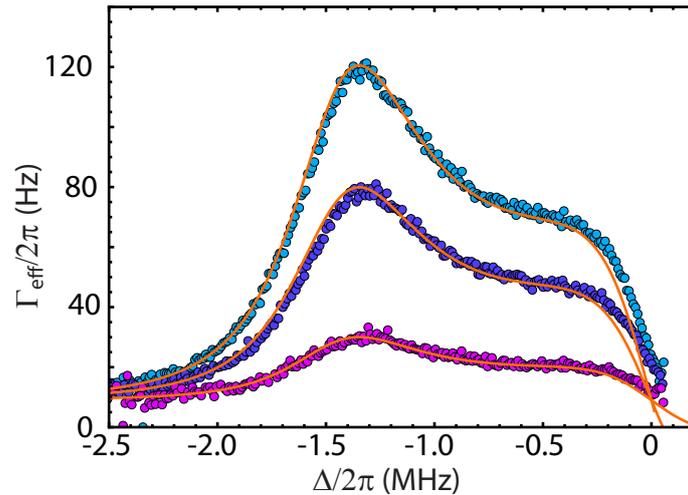
Figure 6.8: Effective linewidth plotted versus the detuning for three different drive powers. The solid lines are fits to the expected effected linewidth behavior given in Equation (5.19), taking into account the varying drive photon number $\bar{n}_c$ (pink: $P_d = 890\,\mathrm{pW}$, dark blue: $P_d = 2.8\,\mathrm{nW}$, light blue: $P_d = 4.5\,\mathrm{pW}$).

contribution of the counter rotating terms can no longer be neglected and we expect to see a difference between theory and experiment. This is shown in Figure 6.9. The plots show color-coded representations of the probe power transmission $|t|^2$ as a function of the normalized drive detuning Δ/Ω_m and the probe tone detuning $\Omega - \Omega_m$ away from the anti-Stokes line. In Figure 6.9a we have plotted the theoretical prediction, given by the full EMIT theory in Equation (6.25). The corresponding experimental data are shown in Figure 6.9b. The resolved sideband limit defined by Equation (6.2) is shown in Figure 6.9c and is discussed further below. For the simulations, we assume the same sample parameters as given in the experiment. We use a constant drive power of $P_d = 4.5\,\mathrm{nW}$ taking the varying intra-cavity photon number $\bar{n}_c$ into account (see Equation (6.33)). For relative detunings outside the cavity linewidth (with the parameters used in Figure 6.9: $\Delta/\Omega_m > 0.5$, since $\kappa \approx 0.5\,\Omega_m$), we see that the full model and the experiment agree well (curves a and b in Figure 6.9). But for Δ/Ω_m approaching 0, significant discrepancies between data and theory prediction are observed. The dispersive shift in the experiment towards lower mechanical frequency (the blue colored area in panel b shifts "downwards" for $\Delta/\Omega_m \to 0$) is not captured by Equation (6.25). The difference between theory and experiment is even worse if we compare the experiment with the resolved sideband theory (see Equation (6.2)). The latter ignores even on-resonant contributions from the complex conjugate of the Stokes sideband. For large relative detunings, this assumption gives good results. However, as expected the approximation breaks down earlier than the full model, namely for $\Delta/\Omega_m < 0.75$. We see that both descriptions of EMIT give good results for a broad range around optimum detuning. But as soon as we cannot ignore the off-resonant sideband, the theory shows flaws. This becomes important, when extending two-tone experiments to samples incorporating two or more cavities, where by design, both sidebands could be amplified.
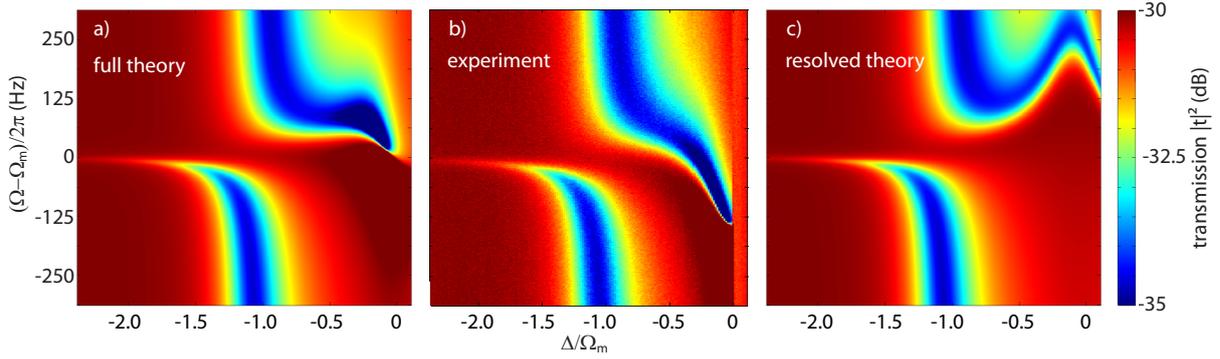
Figure 6.9: Comparison of full EMIT theory and resolved sideband theory with experimental data. The plots are color-coded represantations of the probe power transmission $|t|^2$ as a function of the normalized drive detuning $\Delta/\Omega_{\mathrm{m}}$ and the probe tone detuning $\Omega - \Omega_{\mathrm{m}}$ away from the anti-Stokes line. a) shows the results of a simulation incorporating the sample parameters of the full EMIT theory, b) the experimentally obtained data, c) shows the same as a) but calculated with the resolved sideband theory.

6.1.5 Conclusion

In this section we have presented a detailed analysis of EMIT. We have developed the theoretic model to describe induced transparency effects and discussed the agreement to the experimental data. Two mechanical modes were analysed, the more prominent one shows a broadened linewidth of $\Gamma_{\mathrm{eff}}/2\pi = 2.16\,\mathrm{kHz}$ for an average drive photon number of $\bar{n}_{\mathrm{c}} = 2.7 \times 10^8$, compared to the intrinsic linewidth of $\Gamma_{\mathrm{m}}/2\pi = 7.7\,\mathrm{Hz}$. The former corresponds to a cooperativity of $C = 294$ (electromechanical coupling of $g/2\pi = 20.6\,\mathrm{kHz}$). Thus, the coupling exceeds the mechanical thermal decoherence rate at $30\,\mathrm{mK}$ of $\bar{n}_{\mathrm{m}}\Gamma_{\mathrm{m}}/2\pi \approx 1.18\,\mathrm{kHz}$, overcoming the main obstacle in reaching the strong coupling regime, where quantum coherent manipulations become possible ($g \gg \{\bar{n}_{\mathrm{m}}\Gamma_{\mathrm{m}}, \kappa\}$) [75]. The fit of the electromechanical linewidth broadening allows for estimation of the damping of the input microwave line, giving an attenuation of $65.5\,\mathrm{dB}$. The second mode has a twice as large linewidth $\Gamma_{\mathrm{m,op}}/2\pi = 13.4\,\mathrm{Hz}$ and a weaker coupling $g_{0,\mathrm{op}}/2\pi = 0.39\,\mathrm{Hz}$. The linewidth behavior is in excellent agreement with theory as a function of the drive power as well as the drive frequency. We do not observe normal mode splitting [80], since the relatively low vacuum coupling requires even higher drive photon numbers. This is a technical problem, the Nb μ-wave cavity allows for sufficiently high photon numbers.

We also have analyzed EMIT as a function of the detuning of the drive field with respect to the cavity, corroborating that the effective mechanical linewidth is determined by electromechanical linewidth broadening due to the strong drive field. We have compared the derived expressions with the data, showing that the approximations lead to significant changes between prediction and measurement for a $\Delta > \kappa$.

The strong dispersion due to EMIT allows for generating group delays at frequencies of the mechanical transmission feature, the highest delays are predicted at optimum detuning. We will analyse this effect in the next chapter. Observation of EMIT is also a prerequisite for electromechanical state swapping between electromagnetic and mechanical mode.
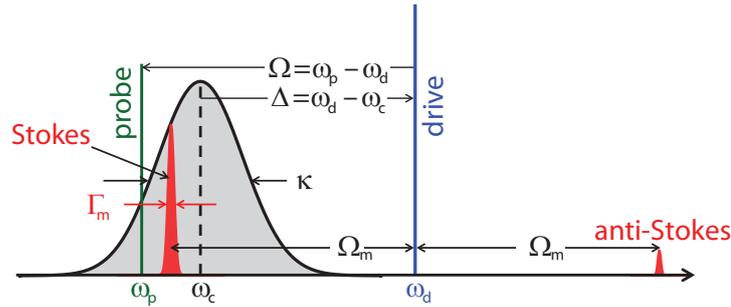
Figure 6.10: Schematic diagram explaining the various frequencies: driving tone frequency ω_d (blue line), probe tone frequency ω_p (green line), cavity resonant frequency ω_c (black line), drive tone detuning $\Delta = \omega_d - \omega_c$, probe tone detuning $\Omega = \omega_p - \omega_d$. Varying Δ shifts the drive tone with respect to the cavity resonance (grey-shaded area). Since the Stokes line (red shaded area) is fixed to the drive tone at $\omega_d - \Omega_m$, the variation of Δ also shifts the Stokes line with respect to the cavity resonance. Varying Ω at constant Δ shifts the probe tone with respect to the cavity resonance and the Stokes line. Figure from Ref. [82].

6.2 Electromechanically induced absorption

6.2.1 Qualitative discussion

In the following, we discuss the case of blue-detuning ($\Delta \simeq +\Omega_m$). As discussed in the following, this situation leads to an interference effect similar to EMIT, but with two differences: First, the interference effect between drive and probe field is phase shifted by about π, leading to constructive instead of destructive interference as in the case of EMIT. Second, the frequency window decreases with increasing drive power due to electromechanical linewidth narrowing resulting from the blue detuned driving field, in contrast to the increasing transparency window in case of EMIT.

Similar to EMIT, a strong drive tone at ω_d is applied to the system, but here, it is close to the upper motional sideband of the cavity, while a second, much weaker tone probes the modified cavity resonance at frequency $\omega_p = \omega_d + \Omega$ schematically shown in Figure 6.10. The simultaneous presence of the drive and the probe tone result again in a radiation pressure force oscillating at $\Omega = \omega_p - \omega_d$. If this difference frequency is close to the mechanical resonance frequency, $\Omega \simeq -\Omega_m$, a coherent oscillation of the mechanical system is induced. As a consequence of this oscillation, Stokes and anti-Stokes fields (red-shaded areas in Figure 6.10) build up at $\omega_d \pm \Omega_m$ around the strong driving field. And again, the microwave resonator acts as a narrow-band filter for these fields. If the system is in the resolved-sideband regime, $\Omega_m > \kappa$, the anti-Stokes line at $\omega_d + \Omega_m > \omega_c$ is strongly suppressed because it is off-resonant with the cavity, whereas the Stokes line at $\omega_d - \Omega_m \simeq \omega_c$ is enhanced. Moreover, since the Stokes scattered field is degenerate with the probe field sent to the cavity, it allows for constructive interference of the two fields enhancing the build-up of the intra-cavity probe field. This can be viewed as a self-interference between two different excitation pathways. The resulting increased feeding ("absorption") of probe photons into the cavity manifests itself as a reduced cavity transmission. Depending on the frequency of the electromagnetic field, this effect is referred to as electromechanically or optomechanically induced absorption (EMIA or OMIA) [116], the electromechanical analog of electromagnetically induced absorption (EIA) [119]. At even higher drive field power, the system switches from EMIA to parametric amplification
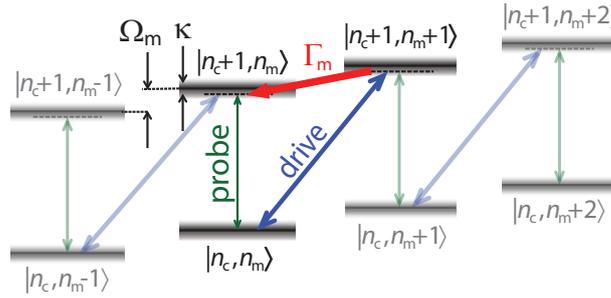
Figure 6.11: Level diagram describing the physics of the electromechanical system: The blue detuned drive tone at frequency ω_d (blue arrow) induces a transition from a state $|n_c, n_m\rangle$ characterized by n_c cavity excitations (photons) and n_m mechanical excitations (phonons) to a state $|n_c + 1, n_m + 1\rangle$, that is, it adds one excitation both to the cavity and the mechanical oscillator. The cavity photons generated in this down-conversion process are degenerate with the near-resonant probe field at frequency $\omega_p = \omega_d - \Omega_m$ (green arrow), resulting in a constructive interference effect. The dashed lines indicate virtual levels, indicating that the drive field is not optimally blue-detuned from the cavity resonance ($\Omega = \Omega_m \neq \Delta$). Figure from Ref. [82].

[120], resulting in electromagnetic signal amplification, and eventually phonon-lasing. In the picture of parametric amplification, the electromechanical system can be viewed as a parametric amplifier strongly pumped at ω_d and amplifying the weak input signal at ω_p. This amplification is detected as an enhanced cavity transmission.

The effect of EMIA can also be visualized in the same level scheme describing EMIT, see Figure 6.11. Here, a pure cavity excitation would be represented by a vertical arrow increasing only the number photons in the cavity. In contrast to EMIT, we consider the case where the drive field is set to $\omega_d \simeq \omega_c + \Omega_m$ (optimal blue detuning), so it increases both the photon and the phonon number by one and hence is represented by a diagonal arrow with opposite direction compared to the EMIT case in Figure 6.2. The photons of the drive field are down-converted and scatter into the Stokes line at $\omega_d - \Omega_m$, matching approximately the cavity resonant frequency ω_c. Since probe and drive tone are coherent with respect to each other[5], they can interfere with the weak probe field, indicated by the vertical green arrow. Virtual levels, involved when the drive tone is not optimally detuned ($\Delta = \omega_d - \omega_c \neq \Omega_m$) are again represented by the dashed lines in Fig. 6.11. In this situation the down-conversion of the drive field photons generates photons of frequency $\omega_d - \Omega_m = \omega_p \neq \omega_c$, corresponding to the probe field's frequency. Again, the resulting field interferes constructively with the probe field sent to the cavity. Depending on the relative power of the probe and the drive field, the interference can lead to a partial or full extinction of the probe field outside the cavity, what is detected as a reduced cavity transmission (enhanced absorption) in experiments.

6.2.2   Quantitative analysis

For a quantitative analysis of the absorption as a function of the drive power and the detunings Δ and Ω, we follow the same derivation presented in the case of EMIT. As

---

[5]Note that also for EMIA the mutual coherence of probe and drive needs to be reciprocal of the absorption window. Due to the small absorption linewidth this is a stronger condition than in the case of EMIT

already discussed in the derivation of EMIT, Equation (6.25) remains valid in the case of blue detuning. When considering an electromechanical system in the resolved sideband regime ($\Omega_\mathrm{m} > \kappa$)for blue detuning, Equation (6.26) modifies to

$$\chi_\mathrm{m}(\Omega)^{-1} \approx m_\mathrm{eff}\Omega_\mathrm{m}(2(\Omega + \Omega_\mathrm{m}) + i\Gamma_\mathrm{m}) \ , \tag{6.36}$$

since the probe detuning is negative, $\Omega \approx -\Omega_\mathrm{m}$ in contrast to EMIT, where $\Omega \approx \Omega_\mathrm{m}$.

For convenience, we briefly summarize the steps, leading to the transmission spectrum in the resolved sideband regime: Again, we include both the drive and probe fields as well as the losses in the electromagnetic and mechanical resonator. The weak probe field allows for a linearization of the system's dynamics around the steady-state values $\bar{n}_\mathrm{c} = \langle \hat{n}_\mathrm{c} \rangle$ and $\bar{x} = \langle \hat{x} \rangle$, where the former is the average number of photons inside the cavity and the latter the average displacement of the mechanical mode. Solving the resulting Langevin equations for the intra-cavity field in a frame rotating with Δ and calculating the transmission spectrum of the probe field using input-output theory [115–117, 246], yields the following expression for the probe power transmission for a system in the resolved sideband regime,

$$|t|^2 = \left| 1 - \frac{\kappa_\mathrm{ex}/2}{-i(\Delta + \Omega) + \kappa/2 + \frac{g_0^2 \bar{n}_\mathrm{c}}{i(\Omega + \Omega_\mathrm{m}) - \Gamma_\mathrm{m}/2}} \right|^2 \ . \tag{6.37}$$

Here, $g = g_0\sqrt{\bar{n}_\mathrm{c}}$ is the field-enhanced electromechanical coupling rate, $\Gamma_\mathrm{m}/2\pi$ the loss rate of the mechanical oscillator, and $\kappa/2\pi = (\kappa_\mathrm{ex} + \kappa_\mathrm{in})/2\pi$ the total loss rate of the cavity taking into account both internal losses due to dissipative effects and external losses due to the finite coupling to the feedline. In deriving Equation (6.37), the strong suppression of the anti-Stokes field due to the filter function of the electromagnetic resonator has been taken into account. We also note that the transmission spectrum is completely analogous to that obtained for EIA. However, in contrast to atomic systems the coupling strength between the electromagnetic and mechanical mode can be easily varied over a wide range by changing the average photon number $\bar{n}_\mathrm{c}$ inside the cavity.

6.2.3   Experimental results

The setup used to analyze EMIA is exactly the same as presented above, the only difference is a slightly increased temperature of $T \approx 280\,\mathrm{mK}$.

In the following, we discuss the experimental results of the two-tone spectroscopy experiments performed of our electromechanical system. Figure 6.12 shows two typical probe power transmission spectra obtained by plotting $|t|^2$ versus the probe tone detuning $\Omega + \Omega_\mathrm{m}$ for a constant drive power of $P_\mathrm{d} = 264\,\mathrm{pW}$ (purple) and $P_\mathrm{d} = 365\,\mathrm{pW}$ (pink) applied at $\omega_\mathrm{d} = \omega_\mathrm{c} + \Omega_\mathrm{m}$, that is at optimum drive tone detuning $\Delta = \Omega_\mathrm{m}$. The spectra have been recorded for a probe tone power of $2.4\,\mathrm{fW}$ ($-116.5\,\mathrm{dBm}$), one order of magnitude lower than in the case of EMIT to avoid nonlinear effects due to the reduced linewidth Γ_eff (see Figure 6.17). At $\Omega = -\Omega_\mathrm{m}$, a narrow absorption dip (peak) is observed in addition to the bare cavity absorption. Note that the much broader absorption curve of the cavity as shown in Figure 6.5 is not seen due to the small frequency window of the spectrum. Evidently, the very narrow absorption dip (peak) has a reduced mechanical linewidth of $\Gamma_\mathrm{eff}/2\pi = 5.1\,\mathrm{Hz}$ ($2.1\,\mathrm{Hz}$), which is significantly less than the intrinsic linewidth $\Gamma_\mathrm{m}/2\pi = 11\,\mathrm{Hz}$ of the mechanical oscillator at a temperature of $280\,\mathrm{mK}$. The reason is that
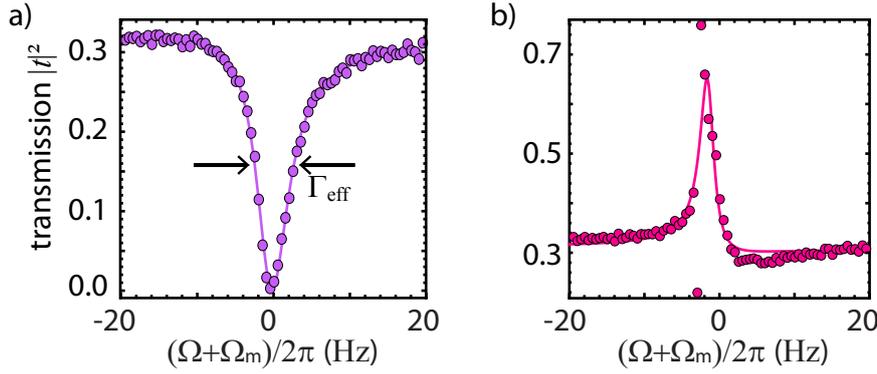
Figure 6.12: In a, the probe power transmission $|t|^2$ is plotted versus the probe tone detuning $\Omega + \Omega_{\mathrm{m}}$ for a constant drive power of $264\,\mathrm{pW}$, showing the typical EMIA dip at $\Omega = -\Omega_{\mathrm{m}}$. In b, the probe power transmission $|t|^2$ is plotted versus the probe tone detuning $\Omega + \Omega_{\mathrm{m}}$ for a constant drive power of $356\,\mathrm{pW}$, showing the typical EMIA peak at $\Omega = -\Omega_{\mathrm{m}}$. The symbols represent the measured data, the solid line is obtained by fitting the data by a damped harmonic oscillator spectrum. The fitting process yields $|t_0|^2$ at $\Omega = -\Omega_{\mathrm{m}}$ for a particular drive power. These values represent the data points in the $|t_0|^2$ versus P_{d} dependence (see Figures 6.14 and 6.13). Figure from Ref. [82].

due to electromechanical coupling the dressed mechanical mode, which is now effectively a phonon-photon polariton, has acquired a finite photonic nature, thereby coupling the mechanical mode to the photonic loss channels at a rate $C\Gamma_{\mathrm{m}}$. The additional photonic loss channel causes an electromechanical linewidth narrowing which scales linearly with the average number of drive photons given in Equation (6.33) and hence with the drive power P_{d}. Since part of the losses of the mechanical system now occur via the photonic channel – in contrast to the electromechancial linewidth broadening in EMIT – a reduced mechanical linewidth is obtained [115, 240]. For arbitrary detunings and given photon number, the mechanical linewidth is given by Equation (5.19), for optimum blue detuning where Γ_{eff} becomes minimal it reduces to

$$\Gamma_{\mathrm{eff}} = \Gamma_{\mathrm{m}}(1 - C). \tag{6.38}$$

Note that as expected, the dependence of the effective linewidth on the cooperativity has opposite sign compared to EMIT (see Equation (6.34). The cooperativity can easily be accessed in experiments, since it is directly proportional to the drive power. In Figures 6.14 and 6.13, the drive power and cooperativity are shown on the bottom and top scale, respectively. The reduction of the linewidth at optimum detuning is shown in Figure 6.13. The data are obtained by extracting the linewidth by a Lorentzian fit of the EMIA feature. The purple and pink point represents the linewidth of the datasets, presented in Figure 6.12.

In Figure 6.14, the peak probe power transmission $|t_0|^2$ is plotted versus the drive power. It is given by the extremum of the mechanical dip feature shown in Figure 6.12, which is determined by fitting the data by a damped harmonic oscillator spectrum, corresponding to a Lorentzian. The peak probe power transmission decreases with increasing drive power from about 0.3 for the bare cavity minimum ($P_{\mathrm{d}} = 0$) to a minimum value of $|t_0|^2 = 0.0046$ for a drive power of $P_{\mathrm{d}} = 270\,\mathrm{pW}$. This corresponds to an additional absorption of $18.3\,\mathrm{dB}$ with respect to the bare microwave cavity background and $23.4\,\mathrm{dB}$ with respect to unity transmission. Increasing the drive power further, $|t_0|^2$ increases again
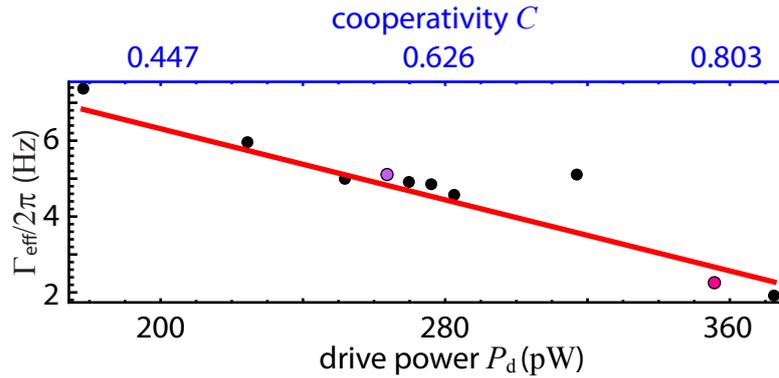
Figure 6.13: Measured linewidth Γ_{eff} at optimum drive tone detuning $\Delta = \Omega_{\text{m}}$ as a function of the drive power P_{d}. The red line is a fit of the data to Equation (6.38).

and exceeds the initial value of the bare cavity, $|t_0|^2 (P_{\text{d}} = 0) \simeq 0.3$, at higher drive powers. In other words, the transmission reduction ("absorption") turns into a transmission enhancement ("emission"). At drive powers above 380 fW, $|t_0|^2 > 1$, i.e. it even exceeds the undisturbed transmission of the feedline. At this power level we are entering the regime of parametric amplification, which has been studied recently by Massel *et al.* [120]. Finally, when the drive power is increased even further, the beam starts to perform self-oscillations at $P_{\text{d}} \simeq 390$ pW. Here, the electromechanical linewidth narrowing induced by the driving field cancels the internal losses of the mechanical system, leading to a regime of zero damping (i.e. parametric instability) and resulting in self-oscillations of the system. This nonlinear regime is beyond the scope of this work and warrants a more detailed study.

An important feature of EMIA is the fact that without additional adjustments the variation of the drive power by a factor of about two leads to a variation of the probe power transmission of almost three orders of magnitude. Qualitatively, the functional dependence of $|t_0|^2$ on the drive power can be understood in terms of the interference of the probe tone and the part of the drive tone, which is down-converted and coherently scattered into the cavity due to phonon generation. If the drive power is low enough, the number of down-converted drive photons is smaller than the number of probe photons sent to the cavity. Therefore, the stimulated absorption of probe photons by the cavity caused by constructive interference with the scattered drive photons is only partial. Note that the physics is completely analogous to EMIT, where destructive interference of the probe and drive tone results in stimulated emission of the cavity, causing an enhanced probe power transmission. With increasing drive power, the absorption dip deepens and minimum transmission is obtained if the number of down-converted drive photons becomes equal to the number of probe photons. With further increasing drive power the number of down-converted drive photons exceeds the number of probe photons, resulting in an increase of the probe power transmission above the level of the bare cavity. That is, the absorption dip in the transmission spectrum changes sign and turns into a transmission peak. We point to the fact that the appearance of a peak in the transmission signal should not be mistaken for an induced transparency effect in the sense of EMIT. At even larger drive power, the power transmission exceeds unity due to parametric amplification of the probe tone by the electromechanical system, which can be considered as a heavily pumped parametric amplifier.
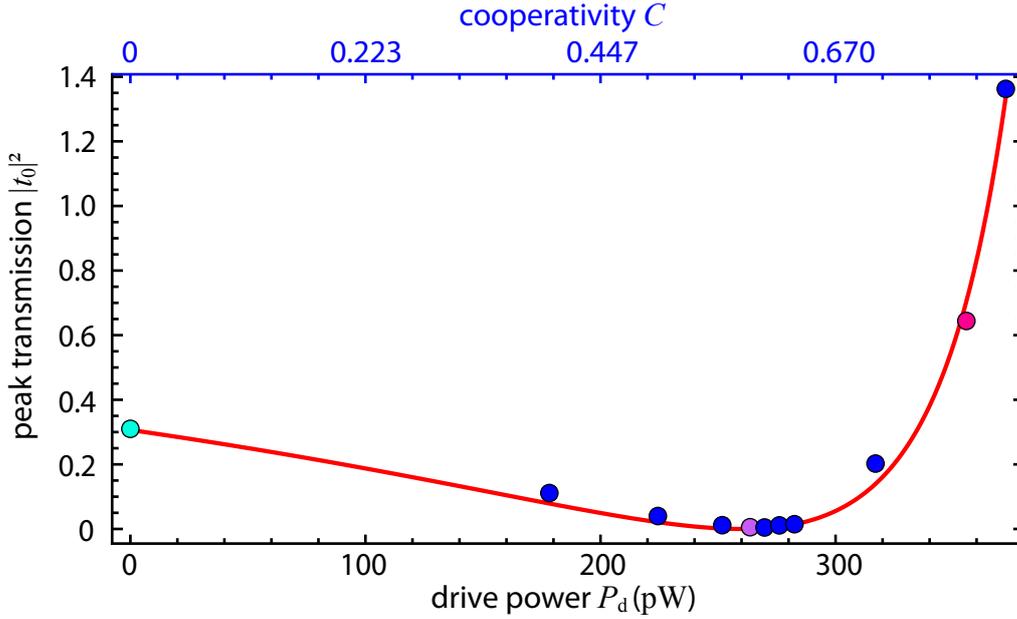
Figure 6.14: Measured peak probe power transmission $|t_0|^2$ at optimum drive tone detuning $\Delta = \Omega_m$ as a function of the drive power P_d. The green data point shows the power transmission of the bare cavity without a drive tone. The red line is a fit of the data to Equation (6.39). Figure from Ref. [82].

A quantitative analysis of the measured probe power transmission shown in Figure 6.14 can be made by Equation (6.37), which can be rewritten for optimal drive tone detuning $\Delta = \Omega_m$ and $\Omega = -\Omega_m$ as

$$|t_0|^2 = \left| \frac{1 - (\kappa_{ex}/\kappa) - C}{1 - C} \right|^2 . \tag{6.39}$$

The red solid line in Figure 6.14 shows a fit of this expression to the data. Evidently, the measured data can be well described in a quantitative way. We replace $\bar{n}_c$ in $C = 4g_0^2 \bar{n}_c/\kappa \Gamma_m$ by Equation (6.33) and use g_0 as a fit parameter to test the model. The fit yields $g_0/2\pi = 1.22\,\text{Hz}$, close to the expected value of $g_0/2\pi = 1.26\,\text{Hz}$ obtained in Section 5.2.2, showing good agreement between data and the derived model. The data analysis in terms of Equation (6.39) is valuable in two respects. On the one hand, it allows for a quantitative explanation of the drive power dependence of the probe transmission. On the other hand, fitting the data by Equation (6.39) yields the cooperativity C, which ranges from 0.38 to 0.80 for the studied drive power range. These values show that the studied system is on the edge to the strong coupling regime. However, self-oscillation sets in before reaching this regime.

Up to now, we have only discussed the case of optimal drive tone detuning $\Delta = \Omega_m$. In the following this analysis is extended to the case of arbitrary detunings $\Delta \neq \Omega_m$. Figure 6.15a shows a two-dimensional color-coded representation of the probe power transmission $|t|^2$ around the Stokes line as a function of the drive detuning $\Delta = \omega_p - \omega_c$, while keeping the probe tone window centered around $\omega_p = \omega_d - \Omega_m$ (equivalent to $\Omega = -\Omega_m$). That is, the frequency window of the probe tone has a constant detuning from the drive tone, thereby probing the same frequency window around the Stokes line (see red-shaded area in Figure 6.10). The variation of the drive tone detuning Δ means that the Stokes line and the related probe frequency window are shifted with respect to the
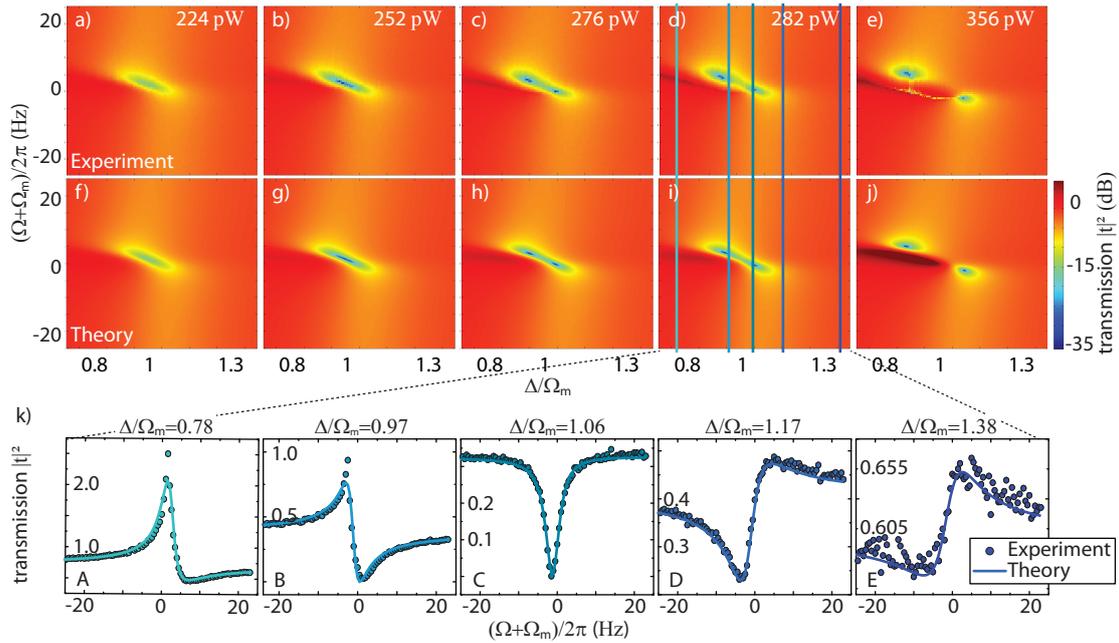
Figure 6.15: a)-e) Color-coded representation of the probe power transmission $|t|^2$ as a function of the normalized drive tone detuning $\Delta/\Omega_{\mathrm{m}}$ and the probe tone detuning $\Omega + \Omega_m$ away from the Stokes line. The constant drive field power, which is increasing from a) to e), is indicated in the upper right corner of each experimental dataset. f)-j) Model fits to the data. k) Vertical line scans along the probe tone frequency axis for various fixed values of the drive detuning $\Delta/\Omega_{\mathrm{m}}$ at a constant drive power of 282 pW. The symbols represent the data, the solid lines are model fits to the data according to Equation (6.37). Figure from Ref. [82].

cavity resonance (see grey-shaded area in Figure 6.10). The probe and drive powers are adjusted to 2.4 fW and 224 pW, respectively. By the two-dimensional spectroscopy shown in Figure 6.15a, we obtain complete information on the probe power transmission. We first discuss the variation of $|t|^2$ along the drive tone detuning $\Delta/\Omega_{\mathrm{m}}$ (horizontal axis) at $\Omega + \Omega_{\mathrm{m}} = 0$. At a relative drive tone detuning $\Delta/\Omega_{\mathrm{m}} = 1$ (optimal detuning), we find the absorption feature already discussed above. When the drive detuning is not optimal, $\Delta/\Omega_{\mathrm{m}} \neq 1$, we observe that the absorption feature decreases and becomes vanishingly small when moving away from optimal drive detuning. This is obvious, since we are shifting the Stokes line out of the resonance window of the microwave cavity, which acts as a narrow-band filter of width κ schematically shown in Figure 6.10. Outside this window the absorption feature is strongly suppressed. We note that $\kappa/\Omega_{\mathrm{m}} \simeq 0.5$, in good agreement with the width of the absorption feature along the $\Delta/\Omega_{\mathrm{m}}$ axis. The panels in Figure 6.15a–e show the transmission feature for increasing drive power. The absorption at optimal detuning increases until it reaches the largest value at a drive power of 252 pW (see Figure 6.15c). For even higher drive power, the transmission at optimal detuning increases again, as already discussed in the context of Figure 6.14.

We next discuss the structure of the absorption feature along the probe tone detuning $\Omega + \Omega_{\mathrm{m}}$ (vertical axis). For optimal drive tone detuning, $\Delta/\Omega_{\mathrm{m}} = 1$, the same probe power transmission curve as already shown in Figure 6.12 is obtained. However, when moving away from optimal drive tone detuning, $\Delta/\Omega_{\mathrm{m}} \neq 1$, we observe that the absorption feature changes its shape. This becomes most obvious in Figure 6.15k, where we have plotted the probe power transmission as a function of the probe tone detuning (vertical
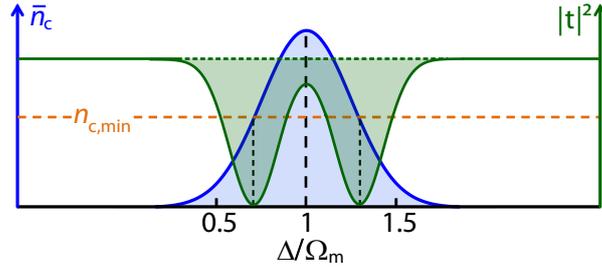
Figure 6.16: Schematic diagram showing the variation of the average cavity photon number $\bar{n}_c$ (blue) and the resulting probe power transmission $|t|^2$ (olive) as a function of the drive tone detuning Δ/Ω_m at constant applied drive tone power. The photon number $\bar{n}_c$ is assumed to vary as the cavity transmission. Minima in the probe power transmission are obtained for $\bar{n}_c(\Delta/\Omega_m) = \bar{n}_{c,min}$, resulting in the characteristic double dip structure observed in the experiment. Figure from Ref. [82].

line scans) for several fixed values of the drive detuning Δ/Ω_m marked by the vertical lines in Figures 6.15d and i. The observed behavior can be attributed to the CPW resonator, whose envelope can be considered as a dispersive background. For $\Delta/\Omega_m = 1.06$, the Stokes line and probe frequency window is positioned close to the center of the cavity resonance. In this case the phase shift between the probe and cavity field is about $\pi/2$, whereas it changes towards 0 and π upon moving away from optimal drive detuning $\Delta/\Omega_m = 1$, i.e. when shifting the Stokes line and the probe window out of the center of the cavity resonance. This results in transmission curves resembling the imaginary and real part of the susceptibility of a damped harmonic oscillator for the probe frequency window positioned close to and left/right from the resonance, respectively. The data shown in Figure 6.15k can be well approximated by a Lorentzian in a dispersive environment.

We also observe that the single transmission dip around $\Delta/\Omega_m = 1$ and $\Omega + \Omega_m = 0$ splits into two along the drive frequency detuning on increasing the drive power. This behavior is not a signature of the normal mode splitting [105, 260], setting in when the coupling strength $g = g_0\sqrt{\bar{n}_c}$ becomes comparable to the cavity loss rate κ. However, for our system, $g \ll \kappa$ even for the largest driving powers. The double dip feature results from the effect that the number of down-converted drive photons varies with the drive tone detuning Δ/Ω_m due to the filtering function of the cavity as sketched in Figure 6.16. Since the minimum transmission is achieved for a specific cavity photon number $\bar{n}_{c,min}$ and increases both for smaller and larger values, two dips in the probe power transmission are obtained at those drive detunings where $\bar{n}_c(\Delta/\Omega_m) = \bar{n}_{c,min}$. Finally, for the highest drive power of 356 pW (see Figure 6.15e) we find additional sharp features forming a line of very narrow dips. They can be attributed to the transition to the nonlinear Duffing regime [87].

To analyze the absorption more quantitatively, one has to compare the experimental results with Equation (6.37). Figures 6.15f–j show the probe power transmission $|t|^2$ obtained according to this equation. Evidently, the results of the model calculation agree well with the experimental data, apart from the onset of nonlinear features for high driving power. Additionally, Figure 6.15k displays vertical line scans along the probe tone frequency axis for a drive power of 141 pW. Fitting the data yields $\Omega_{m,fit}/2\pi = 1.45$ MHz and $g_{0,fit}/2\pi = 1.29$ Hz, corroborating the values given above.

By fitting the data obtained in Figure 6.15 to a Lorentzian in a dispersive environment,
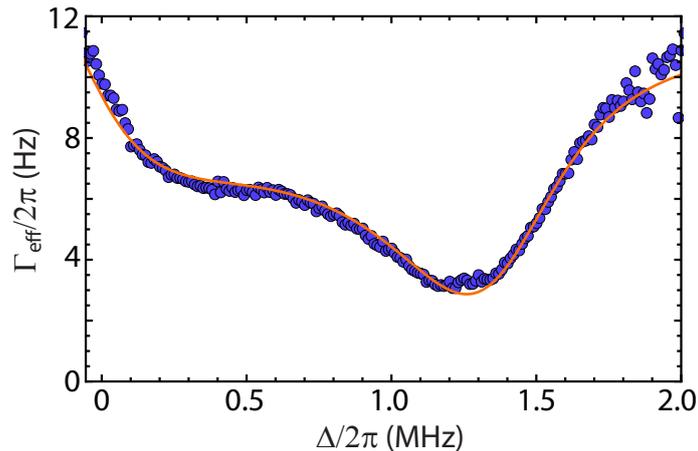
Figure 6.17: Measured linewidth Γ_{eff} at a fixed drive power of $P_{\mathrm{d}} = -282\,\mathrm{pW}$ for varying detuning Δ. The orange line is a fit of the data to eq. (5.19), where we have taken the variation of the average intra-cavity photon number with the detuning into account.

we obtain the effective mechanical linewidth Γ_{eff} as a function of the detuning frequency Δ. The data shown in Figure 6.17 shows the outcome of $\Gamma_{\mathrm{eff}}(\Delta)$ for a detuning sweep with a constant drive power of $P_{\mathrm{d}} = 282\,\mathrm{pW}$. The orange line is a fit of the data to Equation (5.19) including the variation of $\bar{n}_{\mathrm{c}}$. Evidently, there is excellent agreement between experiment and theory. The linewidth behavior is exactly what one would expect with no exact knowledge of the formula. At optimum detuning Γ_{eff} is expected to have a minimum and to increase towards the undisturbed mechanical linewidth Γ_{m} when $\Delta \to 0$ or $\Delta \gg \Omega_{\mathrm{m}}$. The increasing intra-cavity number $\bar{n}_{\mathrm{c}}$ when Δ is swept from Ω_{m} to 0 leads to a smaller effective linewidth since the electromechanical coupling g constantly increases.

6.2.4 Conclusion

In conclusion, we have performed a detailed two-tone spectroscopy analysis of electrome-chanically induced absorption (EMIA) in a hybrid system consisting of a superconducting microwave resonator coupled to a nanomechanical beam as function of the drive power. In two-dimensional spectroscopy experiments the probe power transmission has been mea-sured both as a function of the drive and probe tone detuning for a wide range of drive tone powers. We find good quantitative agreement between the measured transmission spectra and model calculations based on the Hamiltonian formulation of a generic elec-tromechanical system. For optimal drive tone detuning we show that the absorption of microwave signals at cavity resonance can be adjusted by more than $25\,\mathrm{dB}$ on varying the power of the drive tone by a factor of two. A minimum normalized power transmission of 0.0046 has been demonstrated in a very narrow absorption window of $\Delta\omega/2\pi = 5\,\mathrm{Hz}$ at $\omega = 6\,\mathrm{GHz}$, resulting from line narrowing in the dressed mechanical system. Even nar-rower band pass filters have be achieved at larger drive powers, however with increased probe power transmission. Our results clearly demonstrate that the studied electrome-chanical system can be applied to filter out extreme narrow frequency bands ($\sim \mathrm{Hz}$) of the much wider frequency band ($\sim \mathrm{MHz}$) defined by the linewidth of the microwave cavity. The amount of absorption as well as the filtering frequency is tunable around the cavity resonance over about $1\,\mathrm{MHz}$ by adjusting the power and frequency of the drive field.

Another possible application of the nanomechanical system is the nonlinear manipulation of light fields down to the quantum level by introducing a group advance or delay to weak microwave pulses centered around the cavity resonance [87]. This capability results, similar to the case of EMIT, from the rapid phase dispersion originating from EMIA. In contrast to EMIT, for EMIA the change from absorptive to transmissive behavior allows both for advancing and delaying microwave signals.

At high drive power we observed parametric amplification of the weak probe tone, that is, microwave amplification with a nanomechanical resonator. However, due to the low mechanical loss rate of the nanomechanical beam ($\Gamma_m/2\pi = 11\,\mathrm{Hz}$) the drive power range for parametric amplification is very narrow, since the beam rapidly starts to perform self-oscillations and eventually shows phonon lasing. Experiments exploring this regime are in progress.

6.3 Mapping the Duffing nonlinearity into microwave regime

In section 4.5.3, we have studied the Duffing nonlinearity of the nanomechanical displacement and used the Duffing parameter to characterize the effective material parameters of the double layer sandwich structure of the nanobeam. Here, we show that the nonlinear displacement spectrum can directly be mapped into the microwave regime by exploiting electromechanically induced transparency (EMIT). Implementing a nonlinearity in a μ-wave resonator allows to create an bifurcation amplifier or detector. Recently, this has been realized electrically by placing a Josephson junction in a μ-wave resonator [261]. As we will see, the nonlinearity occurs not only for direct drive of the mechanical mode but also from the beating force resulting from the simultaneous presence of a drive and a probe field.

The linear Langevin Equations (6.8)–(6.10) describing EMIT defined in Section 6.1 do not capture the nonlinear oscillation of the mechanical mode. To grasp the full wealth of the system we introduce the Duffing parameter α, defined in Section 4.5.3 to Equation (6.10). The remaining two Langevin equations stay unchanged. The set of equations modifies to

$$\frac{d}{dt}\hat{a}(t) = \left(+i\bar{\Delta} - \frac{\kappa}{2}\right)\hat{a}(t) - iG\hat{x}(t)\hat{a}(t) + \sqrt{\frac{\kappa_{\mathrm{ex}}}{2}}s_{\mathrm{in}}(t), \tag{6.40}$$

$$\frac{d}{dt}\hat{x}(t) = \frac{\hat{p}(t)}{m_{\mathrm{eff}}}, \tag{6.41}$$

$$\frac{d}{dt}\hat{p}(t) = -m_{\mathrm{eff}}\Omega_m^2\hat{x}(t) - \hbar G\hat{a}^\dagger(t)\hat{a}(t) - \Gamma_m\hat{p}(t) - \alpha\hat{x}^3(t). \tag{6.42}$$

As before, we can first determine the steady state solutions, whose time derivatives are all zero. The self-consistent steady state solutions for the intra-cavity field and the mechanical displacement read

$$\bar{a} = \frac{\sqrt{\kappa_{\mathrm{ex}}/2}}{-i(\bar{\Delta} - G\bar{x}) + \frac{\kappa}{2}}\bar{s}_{\mathrm{in}}, \tag{6.43}$$

$$m_{\mathrm{eff}}\Omega_m^2\bar{x} + \alpha\bar{x}^3 + \hbar G\bar{a}^2 = 0. \tag{6.44}$$

Again, the solution of the modified Langevin Equations (6.40)–(6.42) is the sum of the steady state solution and a dynamic part, $\hat{a}(t) = \bar{a} + \delta\hat{a}(t)$, $\hat{x}(t) = \bar{x} + \delta\hat{x}(t)$, where $\delta\hat{x}(t)$ is hermitian. The presence of drive and probe fields is captured by $s_{\mathrm{in}}(t) = (\bar{s}_{\mathrm{in}} +$

$\delta s_{\mathrm{in}}(t))e^{-i\omega_{\mathrm{d}}t}$, where the latter term in the brackets represents the probe field. Implicitly we have chosen the phase of the cavity as a reference, thus $\bar{a}$ has a real and positive value and $\bar{a}^2$ represents the average intra cavity photon number $\bar{n}_{\mathrm{c}} \propto \kappa_{\mathrm{ex}}/2\bar{s}_{\mathrm{in}}^2$. Finally we define $\Delta = \bar{\Delta} - G\bar{x}$ as the corrected detuning. Replacing those values we get

$$\frac{d}{dt}\delta\hat{a}(t) = \left(i(\Delta - \frac{\kappa}{2}\right)\delta\hat{a}(t) - iG(\bar{a}+\delta\hat{a}(t))\delta\hat{x}(t) + \sqrt{\frac{\kappa_{\mathrm{ex}}}{2}}\delta s_{\mathrm{in}}(t), \tag{6.45}$$

$$\frac{d^2}{dt^2}\delta\hat{x}(t) + \Gamma_{\mathrm{m}}\frac{d}{dt}\delta\hat{x}(t) + \Omega_{\mathrm{m}}^2\delta\hat{x}(t) = -\frac{\hbar G}{m_{\mathrm{eff}}}\bar{a}(\delta\hat{a}(t) + \delta\hat{a}^\dagger(t))$$
$$-\frac{\alpha}{m_{\mathrm{eff}}}(\bar{x}^3 + \delta\hat{x}^3(t) + 3\bar{x}^2\delta\hat{x}(t) + 3\bar{x}\delta\hat{x}^2(t)). \tag{6.46}$$

The drive field is to be much stronger than the probe field ($\delta\hat{a} \ll \bar{a}$), what allows us to neglect higher order terms in $\delta\hat{a}$ and $\delta\hat{a}^\dagger$. We use the same rotating frame $\Omega = \omega_{\mathrm{p}} - \omega_{\mathrm{d}}$ and the same ansatz to solve the linear Langevin equations as before in Equations (6.15)–(6.15) and sort the relevant terms $\propto e^{-i\Omega t}$, where we have replaced $\delta s_{\mathrm{in}}(t) = s_{\mathrm{p}}e^{-i\Omega t}$. Under these modifications, Equations (6.15)–(6.17) modify to

$$A^- \left(-i(\Omega + \Delta) + \frac{\kappa}{2}\right) = -iG\bar{a}X + \sqrt{\frac{\kappa_{\mathrm{ex}}}{2}}s_{\mathrm{p}}, \tag{6.47}$$

$$A^+ \left(i(\Omega - \Delta) + \frac{\kappa}{2}\right) = -iG\bar{a}X^*, \tag{6.48}$$

$$(\Omega_{\mathrm{m}}^2 - \Omega^2 - i\Gamma_{\mathrm{m}}\Omega)X = -\frac{\hbar G}{m_{\mathrm{eff}}}(A^- + (A^+)^*) - 3\alpha(\bar{x}^2 X + |X|^2 X). \tag{6.49}$$

As highlighted in Section 6.1, A^+ is negligible in the resolved sideband regime ($\Omega_{\mathrm{m}} \gg \kappa$), which we will assume here. We define $A \equiv A^-$ and set $A^+ = 0$. Further, we require a large mechanical quality factor $\Omega_{\mathrm{m}}/\Gamma_{\mathrm{m}} \gg \bar{a}/A$. This assumption ensures that the dynamical resonant response of the mechanical oscillator $X \propto \bar{a}A$ exceeds the static displacement $\bar{x} \propto \bar{a}^2$, what agrees with our findings. With these requirements, we can neglect $\bar{x}^2 X$ in Equation (6.49). With $G = g_0/x_{\mathrm{zpf}}$, we end up with the following set of coupled mode equations:

$$A \left(-i(\Omega + \Delta) + \frac{\kappa}{2}\right) = -i\frac{g_0\bar{a}}{x_{\mathrm{zpf}}}X + \sqrt{\frac{\kappa_{\mathrm{ex}}}{2}}s_{\mathrm{p}}, \tag{6.50}$$

$$(\Omega_{\mathrm{m}}^2 - \Omega^2 - i\Gamma_{\mathrm{m}}\Omega)X + 3\alpha |X|^2 X = -\frac{\hbar g_0 A}{m_{\mathrm{eff}}x_{\mathrm{zpf}}}. \tag{6.51}$$

This set of differential equations in no longer analytically solvable. But comparison of Equation (6.51) with Equation (6.20) reveals, that the Duffing nonlinearity is mapped into the probe field's response. Note that we have not introduced susceptibilities as in the discussion of EMIT due to the nonlinear response of the mechanical oscillator.

For a simple harmonically driven damped Duffing oscillator, as treated in Section 4.5.3, the nonlinearity becomes more pronounced for increasing driving field. In the case of EMIT, there exists no direct drive. Still the drive and probe field both contribute linearly via $\bar{a}$ and A respectively to the driving force term on the right hand side of Equation (6.51). Physically, this contribution results from the beat frequency due to the interference of those two fields. Naively, one could expect to observe nonlinear mechanical motion when ramping up the drive power. This is not the case, since the linewidth broadening depends quadratically on the driving field ($\Gamma_{\mathrm{eff}} = \Gamma_{\mathrm{m}}(1 + C) \propto 1 + P_{\mathrm{d}} \propto 1 + \bar{s}^2$) showing a
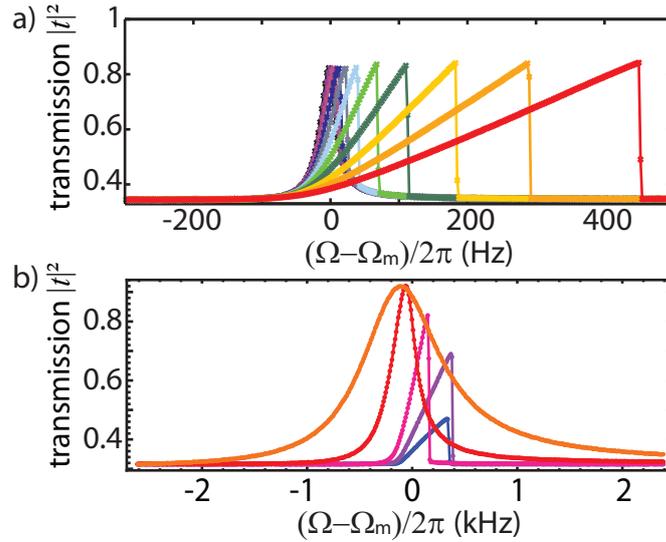
Figure 6.18: Transmission of the probe tone versus probe detuning. a) shows the mapping of the Duffing nonlinearity of the nanobeam into the microwave regime for different probe powers. The drive tone is kept constant at optimum red detuning, the probe power increases from black over purple and green to red. The nonlinear behavior is first visible for a probe power of $-100\,\mathrm{dBm}$ (light purple curve). The curve was adapted from reference [87]. b) For a given constant probe power, the Duffing nonlinearity can be overcome by increasing the drive power, still at optimum detuning. As a consequence the electromechanical linewidth broadening dominates the nonlinear terms.

stronger drive field dependence than the force driving the mechanical amplitude ($F_{\mathrm{rp}} \propto \bar{s}$). To induce nonlinear behavior it is crucial for the resulting driving force to overcome the damping, what can easily be understood by looking at the denominator of Equation (4.19):

$$x_0^2 = \frac{(K/2)^2}{(m_{\mathrm{eff}}\Omega_{\mathrm{m}}(\Omega - \Omega_{\mathrm{m}}) - \frac{3}{8}\alpha x_0^2)^2 + (\frac{1}{2}m_{\mathrm{eff}}\Gamma_{\mathrm{m}}\Omega_{\mathrm{m}}^2)^2} \qquad (6.52)$$

Thus only for increasing probe power one can overcome the transition from linear to nonlinear behavior with an electromechanical system in EMIT configuration. However, finding a closed expression relating the onset of bifurcation to the ratio of damping versus nonlinearity remains challenging and was not realized within the scope of this work.

The increasing bifurcation behavior is shown in Figure 6.18a for optimum detuning ($\Delta = -\Omega_{\mathrm{m}}$), where the probe power is increased from $-99\,\mathrm{dBm}$ (black curve) to -79 dBm (red curve) in 2 dB steps. The drive power is $-64\,\mathrm{dBm}$. Still, for any given probe power one can increase the drive power to a point, where the nonlinearity is fully suppressed, due to the electromechanical linewidth broadening as shown in Figure 6.18b for a constant probe power of $-79\,\mathrm{dBm}$ and drive powers of -73 (blue),-68 (purple),-61 (pink),-53 (red) and $-48\,\mathrm{dBm}$ (orange), respectively. The electromechanical damping starts to dominate at $-61\,\mathrm{dBm}$. Note, that although we clearly observe the bifurcation in amplitude, the Duffing parameter cannot be extracted by these measurements since we do not access information about the mechanical amplitude in this measurement.

In summary, in this section we presented the mapping of a Duffing type nonlinearity as discussed in Section 4.5.3 into the μ-wave regime exploiting the nonlinearity of the mechanical mode of an electromechanical system. The theoretical analysis supports our findings concerning the influence of probe and drive field, respectively.

6.4 Cavity sideband generation detected with two-tone spectroscopy

In this section we discuss the effect of high amplitude mechanical motion on the cavity. We exploit the linewidth narrowing of a system in EMIA configuration to access the phonon lasing regime. The mechanical motion is undamped and driven by the beat between drive and probe tone.

The occurrence of sidebands was mentioned already earlier in Section 5.1. Yet, direct observation remains challenging for a mechanical oscillator undergoing Brownian motion. In contrast, if the nanobeam is exited to high amplitude motion, the sidebands become accessible. This effect was to our knowledge first observed in optical microtorroids [64, 239]. We derive the theoretical model showing the connection between depth of the cavity sidebands and mechanical amplitude.

Fitting the model to the data reveals mechanical amplitudes exceeding $50\,\mathrm{nm}$. Additionally we observe a Kerr like shift of the cavity eigenfrequency up to $\kappa/2$ to lower frequencies, not covered by the theoretical treatment, where linear electromechanical coupling was assumed. Considering different orders of approximation of the full coupling between "optical" and mechanical mode fails to explain this shift. We consider the full expression of the coupling and show that the resulting frequency shift (using the parameters derived in Section 4.4) agrees to the data. This provides clear evidence that the shift of the microwave resonance results indeed from the high mechanical oscillation amplitude.

6.4.1 Theory

Following the derivation presented in Ref. [239], we show in the following that the normalized power transmission spectrum of a tone swept over the cavity resonance is given by

$$|t|^2 = 1 - \frac{\kappa_{\mathrm{ex}}}{2}(\kappa - \frac{\kappa_{\mathrm{ex}}}{2}) \sum_{n=-\infty}^{\infty} \frac{J_n(Gx_0/\Omega_{\mathrm{m}})^2}{(\kappa/2)^2 + (\Delta + n\Omega_{\mathrm{m}})^2} \ , \tag{6.53}$$

where J_n are Bessels functions of order n and Δ is the detuning between cavity resonance and probe tone $\Delta = \omega_{\mathrm{p}} - \omega_{\mathrm{c}}$.

To describe the sidebands occurring due to the high mechanical amplitude, we will neglect the backaction of the electromagnetic mode onto the mechanical oscillator. We assume that the oscillator motion can be approximated by a harmonic oscillation as

$$x(t) \approx x_0 \sin(\Omega_{\mathrm{m}} t) \ . \tag{6.54}$$

We are not interested in the interference effect responsible for EMIA, so we ignore the strong driving field and only analyze the response of the probing field $s_{\mathrm{in}}(t) = s_{\mathrm{in}} e^{i\omega_{\mathrm{p}} t}$. The modified Langevin Equation (6.8) reads

$$\frac{d}{dt}\hat{a}(t) = \left(-i\omega_{\mathrm{c}} - \frac{\kappa}{2}\right)\hat{a}(t) - iG\hat{x}(t)\hat{a}(t) + \sqrt{\frac{\kappa_{\mathrm{ex}}}{2}}s_{\mathrm{in}}e^{-i\omega_{\mathrm{p}} t} \ . \tag{6.55}$$

To solve this equation, we need a solution $a_{\mathrm{h}}(t)$ to the homogenous part and a particular solution $a_{\mathrm{p}}(t)$ to the full equation. The general solution is the sum of those two, $a(t) = a_{\mathrm{h}}(t) + a_{\mathrm{p}}(t)$. The solution to the homogenous part follows from integration and reads

$$a_{\mathrm{h}}(t) = A_0 \exp\left(\left(-i\omega_{\mathrm{c}} - \frac{\kappa}{2}\right)t - i\frac{Gx_0}{\Omega_{\mathrm{m}}}\cos(\Omega_{\mathrm{m}} t)\right) \ . \tag{6.56}$$

The amplitude A_0 depends on the boundary conditions of the system. A particular solution can be found by trying $a_{\mathrm{p}}(t) = A(t)a_{\mathrm{h}}(t)$. $A(t)$ has then to fulfill

$$\frac{d}{dt}A(t) = \sqrt{\frac{\kappa_{\mathrm{ex}}}{2}} s_{\mathrm{in}} \exp\left(\left(i(\omega_{\mathrm{c}} - \omega_{\mathrm{p}}) + \frac{\kappa}{2}\right)t + i\frac{Gx_0}{\Omega_{\mathrm{m}}}\cos(\Omega_{\mathrm{m}}t)\right) . \tag{6.57}$$

We further define the modulation index

$$\beta \equiv \frac{Gx_0}{\Omega_{\mathrm{m}}} , \tag{6.58}$$

what simplifies the expansion of the cosine into Bessel functions to

$$\exp(i\beta\cos(\Omega_{\mathrm{m}}t)) = \sum_{n=-\infty}^{\infty} i^n J_n(\beta)\exp(-in\Omega_{\mathrm{m}}t) . \tag{6.59}$$

Now, we can integrate Equation (6.57). The result for the particular solution is (replacing $\omega_{\mathrm{p}} - \omega_{\mathrm{c}} = \Delta$):

$$a_{\mathrm{p}}(t) = \sqrt{\frac{\kappa_{\mathrm{ex}}}{2}} s_{\mathrm{in}} \sum_{n=-\infty}^{\infty} \frac{i^n J_n(\beta)}{\kappa/2 - i(\Delta + n\Omega_{\mathrm{m}})} \exp(-i(\omega_{\mathrm{p}} + n\Omega_{\mathrm{m}})t - i\beta\cos(\Omega_{\mathrm{m}}t)) . \tag{6.60}$$

For times $t > 2/\kappa$, $a_{\mathrm{h}}(t)$ becomes negligible, the steady state solution is $a(t) = a_{\mathrm{p}}(t)$. Using input-output theory (stated in Equation (6.24)), the transmission amplitude reads $t(t) = s_{\mathrm{in}}(t) - \sqrt{\frac{\kappa_{\mathrm{ex}}}{2}}a(t)$. Looking at the power spectrum, we can use the following relation to simplify the expression as described by Schliesser et al in Ref. [239]:

$$|x - y|^2 = |x|^2 - 2\mathrm{Re}(x^*y) + |y|^2 , \tag{6.61}$$

for two complex numbers x and y. The second term on the right hand side reads in our case

$$-2\mathrm{Re}\left(s_{\mathrm{in}}^*\exp(i\omega_{\mathrm{p}}t)\sqrt{\frac{\kappa_{\mathrm{ex}}}{2}}a_{\mathrm{p}}(t)\right) = -2|s_{\mathrm{in}}|^2\frac{\kappa_{\mathrm{ex}}}{2}\mathrm{Re}\left(\sum_{n,m}\frac{i^{n-m}J_n(\beta)J_m(\beta)e^{-i(n-m)\Omega_{\mathrm{m}}t}}{\kappa/2 - i(\Delta + n\Omega_{\mathrm{m}})}\right) . \tag{6.62}$$

The sum over n and m results from replacing the last term $\exp(-i\beta\cos(\Omega_{\mathrm{m}}t))$ in $a_{\mathrm{p}}(t)$ by Bessel functions. The term reads

$$\left|\sqrt{\frac{\kappa_{\mathrm{ex}}}{2}}a_{\mathrm{p}}(t)\right|^2 = |s_{\mathrm{in}}|^2\left(\frac{\kappa_{\mathrm{ex}}}{2}\right)^2\left|\sum_{n,m}\frac{i^{n-m}J_n(\beta)J_m(\beta)e^{-i(n-m)\Omega_{\mathrm{m}}t}}{(\kappa/2 - i(\Delta + n\Omega_{\mathrm{m}}))(\kappa/2 + i(\Delta + m\Omega_{\mathrm{m}}))}\right|^2 . \tag{6.63}$$

Only the components with $m = n$ in Equation (6.62) and Equation (6.63) contribute to the signal we detect with a network analyzer. Considering this, the normalized transmitted power spectrum reduces to Equation (6.53). Sweeping the probe frequency, we observe sidebands at frequencies $n \cdot \Omega_{\mathrm{m}}$ away from the cavity resonance. Their width is determined by the cavity linewidth κ. For a given optomechanical coupling rate G, the mechanical amplitude x_0 determines the shape of the dips. The higher the mechanical amplitude, the deeper the sidebands become and the more sidebands can be distinguished.
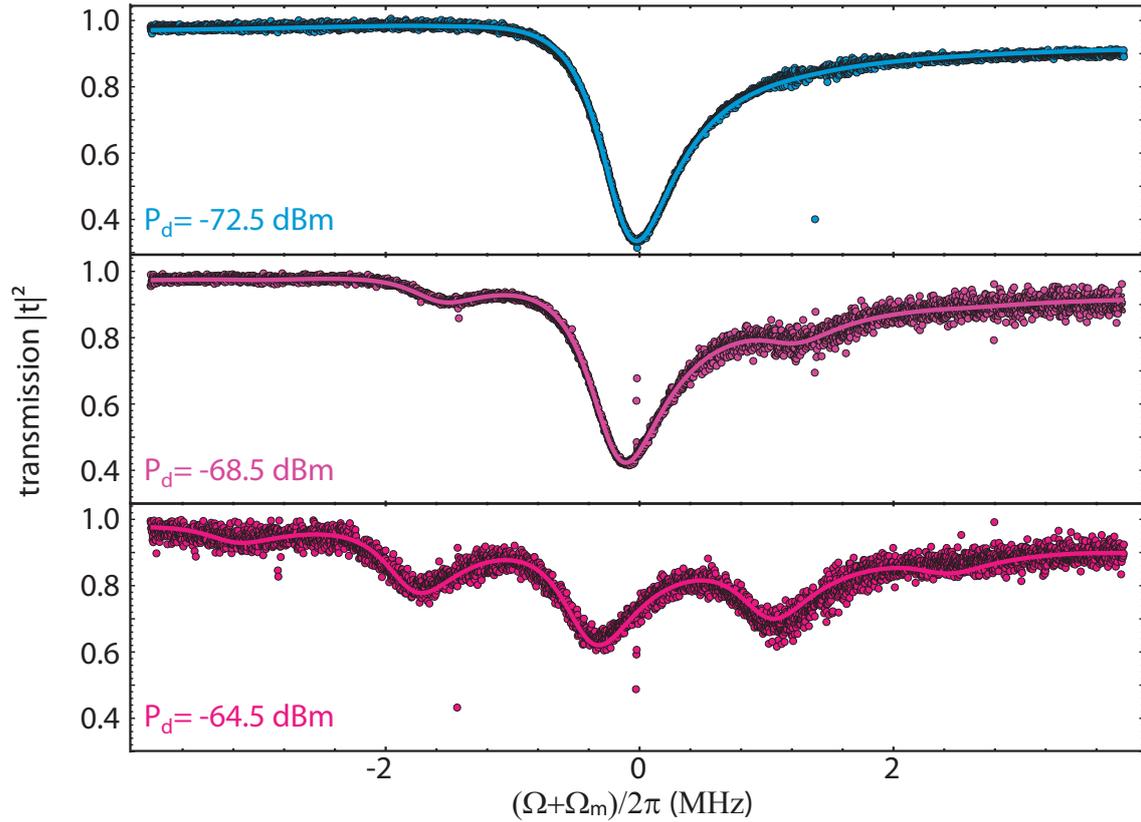
Figure 6.19: Transmitted power spectrum of the probe tone around the resonant frequency of the microwave cavity for three different optimally blue detuned drive tones. The power increases from top to bottom. The corresponding mean intra-cavity photon numbers from top to bottom are $\bar{n}_\mathrm{c} \approx 0.50 \times 10^6, 1.06 \times 10^6$ and 1.97×10^6 respectively. Sidebands at integer multiples of Ω_m occur from the high amplitude mechanical motion. The eigenfrequency shift of the main mode is not understood yet.

6.4.2 Observation of high amplitude mechanical motion

The measurements were performed with the same setup as the EMIT/EMIA measurements discussed before (see Figure 6.4) at a temperature of $T \approx 100\,\mathrm{mK}$. Figure 6.19 shows a probe frequency sweep for three increasing drive powers from top to bottom at a detuning $\Delta \approx \Omega_\mathrm{m}$ from the initial cavity resonance. The solid lines are fits to the data using Equation (6.53). For relatively low drive photon numbers, the cavity shows the undisturbed absorption spectrum as in the case of EMIA. Please note, that the measurement bandwidth is set to $100\,\mathrm{Hz}$, too high to observe the EMIA dip properly. For increasing drive photon number, we observe two sidebands at $\pm\Omega_\mathrm{m}$ with respect to the cavity resonance (Figure 6.19b). These dips become more pronounced if we increase the drive photon number even further, and we even observe weak sidebands at $\pm 2\Omega_\mathrm{m}$. The decrease of the main peak follows Equation (6.53). Qualitatively speaking, it occurs due to scattering of photons into the sidebands, leading to a reduced number of photons at optimum resonance.

By fitting the data we can extract the mechanical amplitude x_0 as shown in the top part of Figure 6.20a. The purple points show a sweep from high to low drive power, the light blue ones a sweep in the opposite direction. As expected, for low photon numbers $\bar{n}_\mathrm{c} < 0.64 \times 10^6$ the mechanical amplitude is low, the mechanical damping still dominates
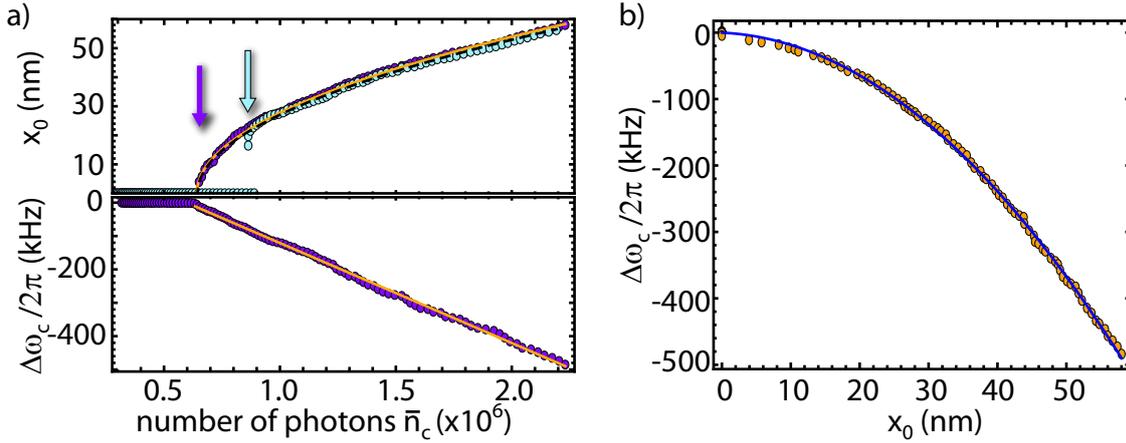
Figure 6.20: a) shows the mechanical oscillation amplitude (top) and eigenfrequency shift (bottom) of the μ-wave cavity plotted against the average intra-cavity drive photon number. The orange lines are a square root (top) and a linear fit (bottom) to the data. The light blue points in the top Figure show a sweep for increasing photon number, the purple points for a decreasing one. The hysteresis of the threshold for self-oscillation is clearly visible (indicated by the purple and light blue arrows). b) shows the parabolic dependence of the cavity shift on the mechanical displacement amplitude. The blue curve is a quadratic fit to the data.

the electromechanical linewidth reduction stated in Equation (6.38). When ramping up the drive power, we observe a sudden jump of the mechanical amplitude at $\bar{n}_c \approx 0.89 \times 10^6$. This is the threshold to self-oscillations of the mechanical mode, where the mechanical motion becomes undamped due to the electromechanical linewidth narrowing resulting from the blue detunded drive field. Comparing the data for increasing and decreasing drive power, we observe hysteretic behavior in the sense that the large mechanical amplitude prevails for decreasing drive power. This behavior indicates that the nanobeam is in a coherent state, an effect called phasing (phonon amplification by stimulated emission of radiation) due to the analog behavior of optical lasers and is a well known phenomenon in opto/-electromechanical systems [52, 260]. The amplitude follows the force acting on the mechanical mode, showing a square root dependence to the average drive photons number. The orange curve is a fit of a square root function to the down-sweep, the black dashed curve is a fit to the up-sweep ignoring the low amplitude data. Both curves describe the data (except from the threshold) very well and have reasonable overlap. We can drive the mechanical motion to amplitudes above $50\,\text{nm}$, corresponding to one fourth of the gap between nanobeam and ground without damaging the beam.

Coming back to the microwave spectrum, we observe a shift of the center frequency towards lower frequencies, an observation that is not covered by the presented theory. The bottom of Figure 6.20a plots the difference $\Delta\omega_c = \omega_{\text{measured}} - \omega_c$ against the drive photon number $\bar{n}_c$, including a linear fit to the data. We observe a shift up to $500\,\text{kHz}$, more than $\kappa/2$. Up to $\bar{n}_c \approx 0.64 \times 10^6$, no shift is visible, strongly suggesting that it results from the electromechanical coupling to the mechanical mode and the high amplitude mechanical oscillation. We find that the cavity eigenfrequency depends linearly on the drive photon number. This can be interpreted as a mechanically mediated Kerr nonlinearity, since the average intra-cavity photon number $\bar{n}_c$ is proportional to P_d. Additionally to the fact that the frequency shift follows the mechanical amplitude, we do not see a shift of the cavity resonance for a drive tone applied to the red sideband as done in Section 6.1, corroborating

that the observed shift is mediated by the mechanical motion. Plotting $\Delta\omega_c$ against x_0 reveals a parabolic dependency, as shown in Figure 6.20b.

The static shift of $\omega_c = \widetilde{\omega}_c + G\bar{x}$ stated in Section 5.1 is not responsible for this behavior. Even for high amplitudes, the shift of the steady state equilibrium position is only dependent on the intra-cavity photon number. On the red sideband, we do not observe a shift of ω_c even for photon numbers exceeding 10^8, what is two orders of magnitude higher than the maximum photonic excitation number in this measurement.

In the modeling of the mechanical sidebands, we have approximated the coupling to be linear in the mechanical amplitude. However, for high mechanical amplitudes, this approximation is no longer valid. The sinusoidal mechanical vibration introduces a pondermotive force effectively shifting the mechanical resonance. To cover this behavior, in a first step we take the full square-root into account (in contrast to Section 4.4, where we consider a first order approximation). The cavity resonance, expressed as a function of mechanical amplitude x_0 then reads

$$\omega_c(x_0) = \left\langle \frac{\omega_c(x_0 \approx 0)}{\sqrt{1 + \frac{1}{C}\left(C_{g,0} + \frac{\partial C_g}{\partial x}x_0 \sin(\Omega_m t)\right)}} \right\rangle . \tag{6.64}$$

Here, the brackets denote the time average over one mechanical oscillation. Note, that we still have evaluated the coupling capacitance to first order. Furthermore, we keep the approximation of a plate capacitor and describe the mechanical motion by its center of mass motion and which is assumed to be sinusoidal. Evaluation of above expression reveals a shift of ω_c to higher values for increasing amplitudes, clearly in contrast to our observations.

In the next step, we include the complete (but still simplified) expression of the coupling capacitance. The approximation

$$\left(C_{g,0} + \frac{\partial C_g}{\partial x}x_0 \sin(\Omega_m t)\right) \tag{6.65}$$

is replaced by

$$\frac{C_g \cdot d}{d + x_0 \sin(\Omega_m t)} \tag{6.66}$$

according to Equation (4.7) and Equation (6.64) modifies to

$$\omega_c(x_0) = \left\langle \frac{\omega_c(x_0 \approx 0)}{\sqrt{1 + \frac{1}{C}\frac{C_g \cdot d}{d + x_0 \sin(\Omega_m t)}}} \right\rangle . \tag{6.67}$$

We numerically calculate the time average over this expression using $\Omega_m/2\pi = 1.45\,\text{MHz}$, $d = 200\,\text{nm}$, $C = 2\pi/4Z\omega_c = 830\,\text{fF}$ and the coupling capacitance extracted from the measured G, $C_g = 1,97\,\text{fF}$ (see Section 4.4 for more details). The values reproduce the Kerr like shift of the cavity resonance observed in the experiment. The square-root dependence on the mechanical amplitude and the linear shift of the cavity resonance as a function of drive photons $\bar{n}_c$ (see Figure 6.20a) implies that the resonance frequency changes quadratically with amplitude. We assume an effective coupling $\widetilde{g}$ between the cavity resonance frequency and the mechanical amplitude. Then, fitting the function $\omega_c = \omega_c(0) - \widetilde{g}x_0^2$ to the numerically extracted eigenfrequency shift gives $\widetilde{g}/2\pi = 88\,\text{Hz/nm}^2$. This corroborates

the value obtained by fitting the experimental data to a parabolic dependence, yielding $\widetilde{g}/2\pi = 146\,\mathrm{Hz/nm}^2$. This is the only case in which the linear approximation of the coupling between "optical" and mechanical mode does not describe the experiment in the scope of the thesis. The mechanical amplitudes we extract from the data with the simplified model describe the cavity shift properly, suggesting that the linear approximation is valid to describe the sideband behavior. Within this thesis, only the shift of the cavity resonant frequency is not covered by electromechanical theory.

In conclusion, we succeeded to drive the mechanical motion to high mechanical amplitudes using the force from the beat between drive and probe. The mechanical motion leads to sidebands in the cavity transmission with a spacing of the mechanical resonance frequency. We extract the mechanical amplitude by fitting the derived model to the data showing values above 50 nm. The high amplitude mechanical motion leads to a Kerr like shift of the cavity resonance to lower frequencies by more than half its linewidth. This observation is not covered by the approximation of linear coupling assumed within the model of electromechanics. Considering the full expression in Equation (6.67), connecting the cavity eigenfrequency and mechanical amplitude explains the observed behavior. This demonstrated, that even for high mechanical amplitudes, electromechanical theory covers most of the observed phenomena correctly, corroborating the validity of this theoretical approach.

6.5   Summary and discussion

In this chapter we have studied an electromechanical system in a two-tone configuration. We have presented the theory to understand two-tone experiments with a strong drive tone and a weak probe tone in close vicinity to the drive's Stokes and anti-Stokes sideband.

We have in detail studied EMIT. In particular, we developed the theoretical model to describe induced transparency effects and corroborated the theory with experimental data. In our experiment, two mechanical modes were analyzed. For the one with stronger coupling we observed a maximum linewidth broadening of $\Gamma_\mathrm{eff}/2\pi = 2.16\,\mathrm{kHz}$ for an average drive photon number of $\bar{n}_\mathrm{c} = 2.7 \times 10^8$, compared to the intrinsic linewidth of $\Gamma_\mathrm{m}/2\pi = 7.7\,\mathrm{Hz}$ at a temperature of approximately $200\,\mathrm{mK}$. The former corresponds to an effective electromechanical coupling of $g/2\pi = 20.6\,\mathrm{kHz}$, implying a cooperativity of $C = 294$. Hence, we overcome a critical obstacle in reaching the quantum coherent coupling regime ($g \gg \{\bar{n}_\mathrm{m}\Gamma_\mathrm{m}, \kappa\}$) [75] by exceeding the mechanical decoherence rate at $30\,\mathrm{mK}$ of $\bar{n}_\mathrm{m}\Gamma_\mathrm{m}/2\pi \approx 1.18\,\mathrm{kHz}$. To observe normal mode splitting [80, 112], we have to modify the setup to allow for higher powers or increase the electromechanical coupling by about a factor of 10, what can be achieved with current fabrication technology [120]. Together with the low thermal decoherence rate of $\Gamma_\mathrm{m}\bar{n}_\mathrm{m}/2\pi \approx 1.29\,\mathrm{kHz}$ observed at temperatures of $32\,\mathrm{mK}$ (see Section 4.5.2), an increased coupling promises access to the quantum coherent coupling regime [75] thus allowing for coherent state transfer from the "optical" to the mechanical mode.

With the measurement of g_0 in Section 5.2.2, the electromechanical linewidth broadening allows to estimate the damping of the input microwave line, giving an attenuation of $65.5\,\mathrm{dB}$.

Characterization of the second mode reveals a broader linewidth of $\Gamma_\mathrm{m,op}/2\pi = 13.4\,\mathrm{Hz}$ and a weaker coupling to the microwave cavity, $g_\mathrm{0,op}/2\pi = 0.39\,\mathrm{Hz}$.

We also have performed a systematic study of the mechanical linewidth as function of the detuning of the drive field with respect to the cavity. Our results show that the electromechanical linewidth broadening depends on both power and frequency of the drive field. We have compared the derived expressions describing the EMIT feature with the data for a drive frequency sweep up to $\Delta = 0$. Our results clearly show that the approximations made in the theoretical modelling lead to significant changes between prediction and measurement for a $\Delta > \kappa$.

The strong dispersion due to EMIT allows for generating group delays at frequencies of the mechanical transmission feature, the highest delays are predicted at optimum detuning. We will analyse this effect in the next chapter. Observation of EMIT is also a prerequisite for electromechanical state swapping between electromagnetic and mechanical mode.

Further, we have analyzed the counterpart of EMIT for a blue detuned drive tone, EMIA. In two-dimensional spectroscopy experiments we have measured the probe power transmission as a function of the drive and probe tone detuning for a wide range of drive tone powers. For optimal detuning of the drive tone we show that the absorption of microwave signals at cavity resonance can be varied by more than 25 dB on adjusting the power of the drive tone by a factor of two. We demonstrate a minimum normalized power transmission of 0.0046 in a very narrow absorption window of $\Delta\omega/2\pi = 5$ Hz at $\omega/2\pi = 6$ GHz, resulting from line narrowing in the dressed mechanical system. Even narrower band pass filters have been achieved at larger drive powers, however with increased probe power transmission. Our results clearly demonstrate that the studied electromechanical system can be applied to filter out extreme narrow frequency bands ($\sim$ Hz) of the much wider frequency band ($\sim$ MHz) defined by the linewidth of the microwave cavity. The amount of absorption as well as the filtering frequency are tunable around the cavity resonance over about 1 MHz by adjusting the power and frequency of the drive field.

At high drive power we observed parametric amplification of the weak probe tone. However, due to the low mechanical loss rate of the nanomechanical beam ($\Gamma_m/2\pi = 11$ Hz) the drive power range for parametric amplification is very narrow, the beam rapidly starts to perform self-oscillations and eventually shows phonon lasing. Experiments exploring this regime are in progress.

The increase of the probe power in an EMIT configuration leads to nonlinear oscillations of the nanobeam. In contrast to an increase of the drive power, no additional linewidth broadening compensates the increasing force from the beat between drive and probe tone driving the mechanical motion. We have used this effect to experimentally demonstrate mapping of a Duffing type nonlinearity into the μ-wave regime exploiting the nonlinearity of the mechanical oscillator.

To demonstrate the effect of high amplitude mechanical motion on the microwave cavity, we have exploited an EMIA configuration to bring the mechanical oscillator into the phonon "lasing" (phasing) regime, where it performs undamped self-oscillations. We observe sidebands in the cavity transmission separated by the mechanical resonance frequency. We show that we can extract the mechanical amplitude from the depth of the sidebands. The data show amplitude values above 50 nm. Additionally, the high amplitude mechanical motion shifts the cavity resonance to lower frequencies by more than half its linewidth. This is essentially a mechanical Kerr effect. The mechanical amplitude follows the square root of the drive power leading to a shift linearly depending on the number of drive photons. This effect is not covered by the approximation of linear coupling as-

sumed within the model of electromechanics. We consider the full connection between cavity resonance and mechanical amplitude to calculate the observed behavior, showing good agreement to the data. The extracted mechanical amplitude is based on the theory of electromechanics, which does not to include higher order terms. This provides evidence that even for high mechanical amplitudes, electromechanical theory covers most of the observed phenomena correctly.

Chapter 7

Electromechanics in the time domain

After having presented a systematic spectroscopic analysis of the electromechanical system, we now switch to experiments in the time domain. Doing so, we focus on electromechanical systems in the EMIT configuration. The dynamics of multi-tone excitation in electromechanics offer applications ranging from the generation of slow light [87, 116] over (quantum) state transfer between microwave cavity and mechanical oscillator [37, 130, 131] to the connection of systems residing in arbitrary frequency regimes [39–42, 132, 133].

The strong phase shift at the transparency peak in EMIT suggests the generation of slow light, similar to its analog EIT [121–123]. Here, we analyze in detail the delay of probe pulses at the cavity resonance as a function of detuning and drive power for a fixed continuous drive tone at optimum red detuning.

We change the configuration to a continuous probe tone and a pulsed drive tone to analyze the ring up and -down behavior of the mechanical oscillator. We find that the mechanical amplitude rings up according to its electromechanically broadened linewidth for a present pump tone. When switching off the drive, the mechanical amplitude decays to its thermal equilibrium amplitude with its intrinsic linewidth.

We use the fact, that the mechanical oscillation prevails to study the switching dynamics of the probe tone. Counterintuitively the transparency effect's switching dynamics is dominated by the fastest timescale of the system, the cavity decay time and not the slowest one defined by the nanobeam's decay time.

7.1 Slow light in electromechanical systems

The strong phase shift in the frequency domain coming with electromagnetically induced absorbtion (EIT) in atomic clouds [118] gives rise to a decreased group velocity of light passing through the medium [121–123], so-called slow light. For a review of EIT see Ref. [259] and for a comparison of different realizations of slow light see Ref. [262]. Even stopping the light and storing it inside the medium has been demonstrated [263].

The analogy between EIT and EMIT [115] can be extended to the concept of slow light. In this section we derive and experimentally demonstrate the delay of probe pulses in an EMIT configuration with an optimally red detuned drive tone. By analyzing the drive power dependency we show a maximum delay of more than 16 ms close to the predicted maximum value of 19.4 ms for a probe pulse centered exactly around the anti-Stokes
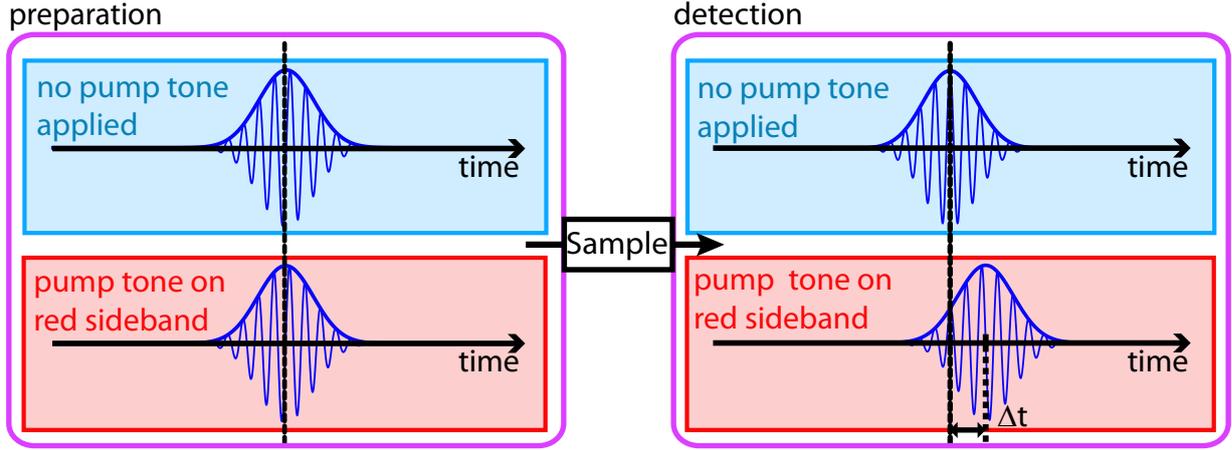
Figure 7.1: Schematic of a group delay. A probe wavepacket travels through a measurement
setup, passing the sample under investigation. If additionally a control field (or driving field
in terms of EMIT) is applied, the envelop of the wavepacket is delayed, i.e. the group velocity
v_g is reduced. The phase velocity v_p of a wavefront remains unchanged.

sideband. For detunings of the probe pulse the achievable maximum delay monotonously
decreases while the cooperativity (and thus the drive power) to achieve this delay in-
creases. Advancing of pulses, i.e. negative group delays are observed for small deviations
of the probe pulse center from the ideal configuration. To take the dispersive shift of the
microwave cavity into account we modify the group delay function and achieve excellent
agreement with theory.

7.1.1   Theoretical details

The group delay of a wavepacket with central frequency Ω_0 is given by [264]

$$\tau_g = -\left.\frac{d\phi(\omega)}{d\omega}\right|_{\Omega_0} , \tag{7.1}$$

where $\phi(\omega)$ is the phase of a transmission spectrum at frequency ω. The relation between
delay and phase is easy to see. Suppose an arbitrary wavepacket at a given coordinate z_0[1],

$$A(\omega, t) = \widetilde{A}(\omega) \exp(-i(\omega t + k(\omega)z_0)) \equiv \widetilde{A}(\omega) \exp(-i(\omega t + \phi(\omega))) . \tag{7.2}$$

Here, $\widetilde{A}(\omega)$ is the envelope function and $k(\omega) = \omega\, n(\omega)/c$ the k-vector defined by the
dispersion relation with the frequency dependent refractive index $n(\omega)$ and the speed of
light c. The wavepacket is now assumed to travel through a medium from $z = 0$ to $z = z_0$
where its group velocity experiences a reduction $v_p = d\omega/dk < c$. The delay compared to
passing the distance in free space reads

$$\tau_g = \frac{z_0}{v_p} - \frac{z_0}{c} = \frac{d}{d\omega}\left(\frac{z_0}{c}(\omega\, n(\omega) - 1)\right) = \frac{dk}{d\omega}z_0 = \frac{d\phi}{d\omega} . \tag{7.3}$$

The constant factor z_0/c defines a global phase that can be adjusted experimentally. The
sharp transparency window in EMIT goes along with a steep phase shift along the peak
induced by the mechanical displacement. Figure 7.2 shows the phase for an optimally

---

[1]without loss of generality, it is sufficient to restrict the discussion to one spatial dimension
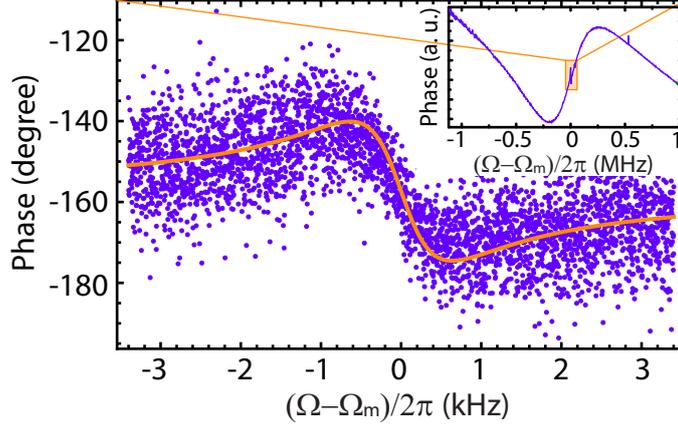
Figure 7.2: Phase spectrum at the transparency window, measured at $35\,\text{mK}$ with a drive power of $-49.5\,\text{dBm}$. The orange line is a fit to Equation 7.4. The inset shows the full phase spectrum of the cavity in EMIT configuration.

red detuned drive tone with a power of $P_{\text{d}} \approx -49.5\,\text{dBm}$ at cavity resonance (purple points), measured in fridge No.2 at $35\,\text{mK}$. The orange curve is a fit to the phase using the approximation given in Equation (7.4), agreeing well with the data. The only fit parameters used are the drive power and a constant phase offset. The inset shows the complete phase spectrum of the mechanical resonance.

To calculate the group delay in the case of EMIT, we expect the group delay to be most prominent at optimum detuning ($\Delta = -\Omega_{\text{m}}$). We will restrict ourselves to this case and allow the probe signal's center frequency to vary slightly from the anti-Stokes sideband ($\Omega \approx \Omega_{\text{m}}$). This allows to simplify the transmitted field for a system in the resolved sideband as discussed in Section 6.1 (see Equation (6.2)) to

$$t(\Omega) = 1 - \frac{\kappa_{\text{ex}}/2}{i(\Delta + \Omega) + \kappa/2 + \frac{g_0^2 \bar{n}_{\text{c}}}{i(\Omega - \Omega_{\text{m}}) + \Gamma_{\text{m}}/2}} \approx 1 - \frac{\kappa_{\text{ex}}/2}{\kappa/2 + \frac{g_0^2 \bar{n}_{\text{c}}}{i(\Omega - \Omega_{\text{m}}) + \Gamma_{\text{m}}/2}} \ . \tag{7.4}$$

The approximation is based on the fact, that the phase of the microwave cavity is almost constant in a wide range around the mechanical resonance. Figure 7.3 shows a comparison of the power and corresponding phase spectrum of the full transmission theory (black) and above approximation (red dotted) for a drive photon number of 1.5×10^7 (cooperativity of $C = 1.1$). The remaining parameters are similar to those of the studied sample. Up to a probe frequency detuning $\delta/2\pi \approx \pm 1\,\text{kHz}$, the curves overlap very well. The phase of the transmitted field is given by

$$\phi(\Omega) = \arctan\left(\frac{\text{Im}\,(t(\Omega))}{\text{Re}\,(t(\Omega))}\right). \tag{7.5}$$

The group delay is then given by

$$\tau_g = -\frac{1}{1 + [\text{Im}\,(t(\Omega))/\,\text{Re}\,(t(\Omega))]^2} \frac{d}{d\Omega}\left(\frac{\text{Im}\,(t(\Omega))}{\text{Re}\,(t(\Omega))}\right) \ . \tag{7.6}$$

After some basic algebra and using the abbreviations $C = 4g^2\bar{n}_{\text{c}}/(\kappa\Gamma_{\text{m}})$, $\delta = \Omega - \Omega_{\text{m}}$ and $\eta_{\text{c}} = \kappa_{\text{ex}}/\kappa$, the group delay is obtained without any further assumptions to [87]

$$\tau_g = -\frac{\frac{2\eta_{\text{c}}}{1 - \eta_c} \cdot \frac{C}{\Gamma_{\text{m}}}}{\left(\frac{2\delta}{\Gamma_{\text{m}}}\right)^2 + (1 + C)^2} \cdot \frac{\left(\frac{2\delta}{\Gamma_{\text{m}}}\right)^2 - \lambda(1 + C)}{\left(\frac{2\delta}{\Gamma_{\text{m}}}\right)^2 + \lambda^2} \ , \tag{7.7}$$
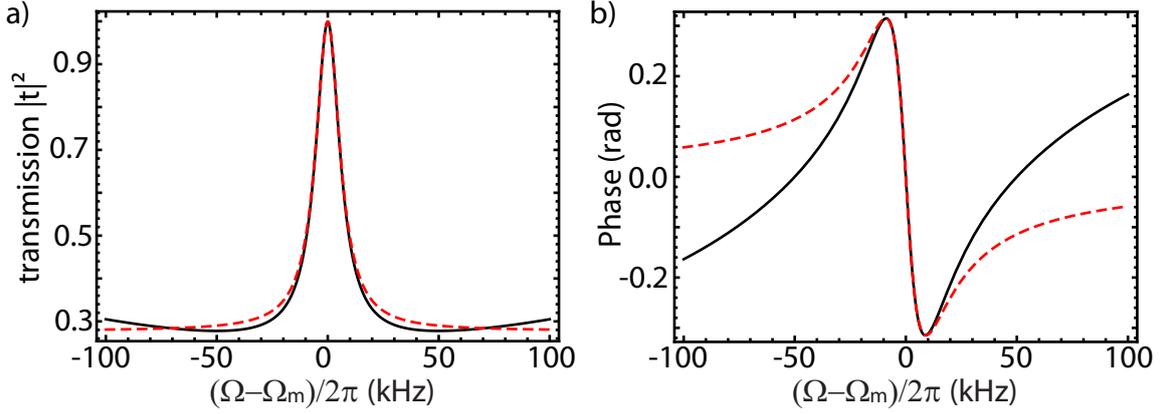
Figure 7.3: Comparison of the full transmission spectrum (black) and the approximation accord-
ing to Equation 7.4 (red dotted) at optimum detuning for a drive photon number of 1.5×10^7
(cooperativity of $C = 1.1$). The other parameters are comparable to those of the studied
sample. a) shows the power spectrum, b) the corresponding phase spectrum.

with $\lambda = 1 + \frac{C}{1-\eta_c}$. For values $|\delta| > \Gamma_m/2$, the group delay can become negative. This
implies, that for an appropriately chosen cooperativity, EMIT can delay wavepackets as
well as advance them by changing the wavepackets centerfrequency on a small scale.

The group delay according to Equation (7.7) is maximal for $\delta = 0$. It is instructive to
analyze the group delay at this point. For $\delta = 0$, Equation (7.7) simplifies to

$$\tau_g = \frac{2\eta_c C}{(1 + C - \eta_c)(1 + C)}\Gamma_m^{-1} . \tag{7.8}$$

A useful value to quantify group delays is the delay-bandwidth product [265], where the
bandwidth is defined as the bandwidth a pulse can have without being distorted by the
system introducing the group delay. This implies that the pulse viewed in frequency space
completely fits into the frequency window where the system under investigation has the
steep phase dispersion. In the case of EMIT, the bandwidth is given by the electromechan-
ically broadened transmission window, $\Delta\Omega_g = \Gamma_m(C + 1)$. The delay-bandwidth product
can be written as

$$\tau_g \cdot \Delta\Omega_g = \frac{2\eta_c C}{1 - \eta_c + C} . \tag{7.9}$$

To increase the product a high cooperativity is favorable, we then can approximate $\tau_g \cdot \Delta\Omega_g \approx
2\eta_c$ [116]. For $\kappa_{ex} \approx \kappa$, meaning that all internal losses are negligible, the product reaches
a value of 2. For $\delta = 0$, the group delay reaches its maximum for $C_{opt} = \sqrt{1 - \eta_c}$ when
$d\tau_g/dC = 0$,

$$\tau_g^{max} = \frac{2(1 - \sqrt{1 - \eta_c})^2}{\eta_c \Gamma_m} , \tag{7.10}$$

To tune the maximum delay, the cavity needs negligible internal losses and the mechanical
mode needs very low dissipation. The coupling to the feedline or detection circuitry is not
a critical parameter, as long as the external losses are dominating the system, $\kappa_{ex} \geq \kappa_{in}$.
For increasing detuning the group delay approaches zero.
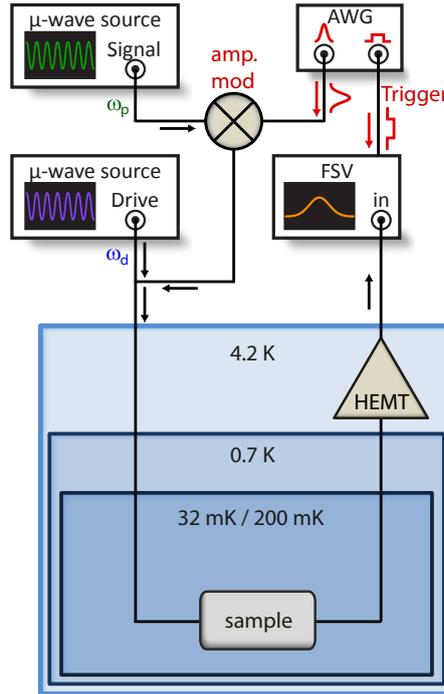
Figure 7.4: Schematic setup to experimentally investigate the group delay in an electromechanical system. A μ-wave source provides the driving field and is combined at room temperature with the output of a second source, providing the probe pulses. The combined fields are fed into the dilution fridge and analyzed with a spectrum analyzer in time domain centered at the probe frequency after passing the sample and an amplifier chain. An arbitrary waveform generator shapes the Gaussian pulses by amplitude modulation and triggers the measurement.

7.1.2 Setup

To demonstrate the group delay in an electromechanical system, we will show data from both dilution fridges. We acquired the data in fridge No.1 at temperature of approximately 200 mK, in fridge No.2 at a temperature of 32 mK. As long as not noted differently, we show data from fridge No.1. The internal and external wiring are similar in both setups, the amplifiers, sources and analyzers are the same, only the damping varies, what is compensated for by postprocessing of the data.

Figure 7.4 shows a schematic of the setup. We use a Rhode&Schwarz SMF microwave source to provide the driving field at the optimum red detuning. A second SMF source generates the probe signal with a centerfrequency close to the μ-wave cavity, i.e. at the anti-Stokes sideband. Both signals are combined with a power splitter and fed to the sample via heavily attenuated coaxial line. After passing a cold HEMT amplifier, a Rhode&Schwarz FSV9 spectrum analyzer in time domain modus detects the signal at the probe frequency. To generate the Gaussian pulses an arbitrary waveform generator (LeCroy ArbStudio 1104D) modulates the amplitude of the probe signal. It also triggers the signal detection.

The sample is the same nanoelectromechanical sample as presented in Section 4.1, consisting of a Nb quarterwave cavity centered at $\omega_c/2\pi = 6.07$ GHz with an external coupling rate of $\kappa_{ex} = 339$ kHz and a total loss rate of $\kappa/2\pi = 759$ kHz. A nanomechanical double layered nanobeam with an eigenfrequency of $\Omega_m/2\pi \approx 1.45$ MHz and a linewidth of $\Gamma_m/2\pi = 12$ Hz at 200 mK ($\Gamma_m/2\pi = 2.5$ Hz at 32 mK) is capacitively coupled to the voltage antinode of the cavity. The electromechanical coupling rate is $g_0/2\pi = 1.26$ Hz.
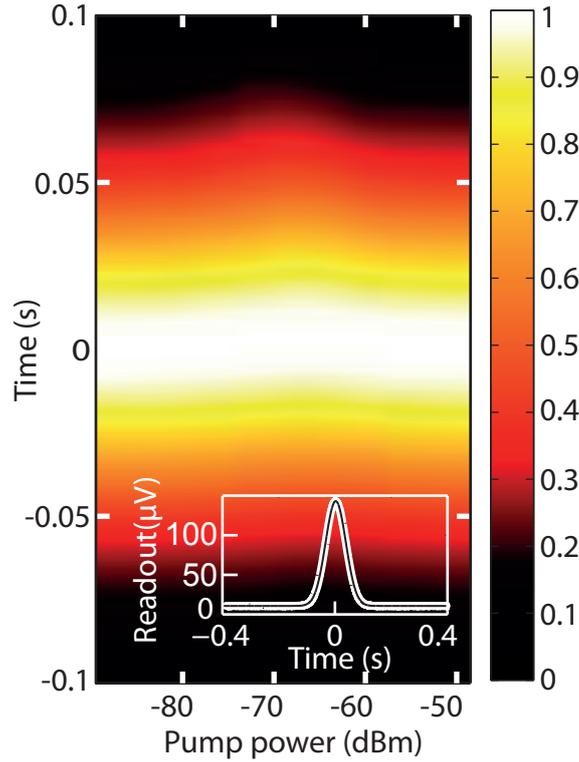
Figure 7.5: Color-coded representation of the Gaussian shaped probe pulses as a function of power on a dB scale and detection time. The group delay is clearly visible at a power of approximately $-65\,\text{dBm}$. The drive field is optimally red detuned, the frequency detuning of the drive field away from cavity resonance is $|\delta|/2\pi = 1.2\,\text{Hz}$ at a power of $P_\text{d} = -104.5\,\text{dBm}$. The inset shows a detected non delayed gaussian pulse. The curve was adapted from Ref. [87].

With these parameters, the optimum cooperativity at zero detuning is $C_\text{opt}(\delta = 0) \approx 0.74$.

7.1.3 Experimental demonstration of group delay

To demonstrate the group delay we apply a driving tone with fixed frequency of $\Delta \approx -\Omega_\text{m}$ and Gaussian shaped probe pulses centered close to the cavity resonance with a fixed weak probe power of $P_\text{d} = -104.5\,\text{dBm}$. To avoid pulse distortion occurring for pulses with a spectral width exceeding the electromechanically broadened transparency peak with $\Gamma_\text{eff} = \Gamma_\text{m}(1 + C)$, we chose the full width half maximum duration to $\Delta t \approx 83\,\text{ms} > 1/\Gamma_\text{m}$ at $200\,\text{mK}$ ($\Delta t \approx 417\,\text{ms} > 1/\Gamma_\text{m}$ at $32\,\text{mK}$). $1/\Gamma_\text{m}$ is the lower limit for a pulse width in time domain to fit into the transparency window for all pump powers. To define the zero delay time $\tau = 0$, a calibration probe pulse propagates through the setup for a pump power weak enough not to create EMIT. Figure 7.5 shows the surface plot of a pump power sweep from -85.5 to $-45.6\,\text{dBm}$. The transmitted pulse is plotted as a function of power on a dB scale and detection time. The probe pulse's center frequency is slightly detuned from the anti-Stokes sideband due to small temperature variations, $|\delta|/2\pi = 1.2\,\text{Hz}$. The group delay is clearly visible and peaks at a power of approximately $-65\,\text{dBm}$. The inset shows the pulse envelope in time domain.

To estimate the group delay, we fit a Gaussian to the pulse in the time domain, analyze the time the peak value is detected and subtract the time at which the calibration peak is detected. In Figure 7.6a, the curve labeled with "1" shows such a fit of the data
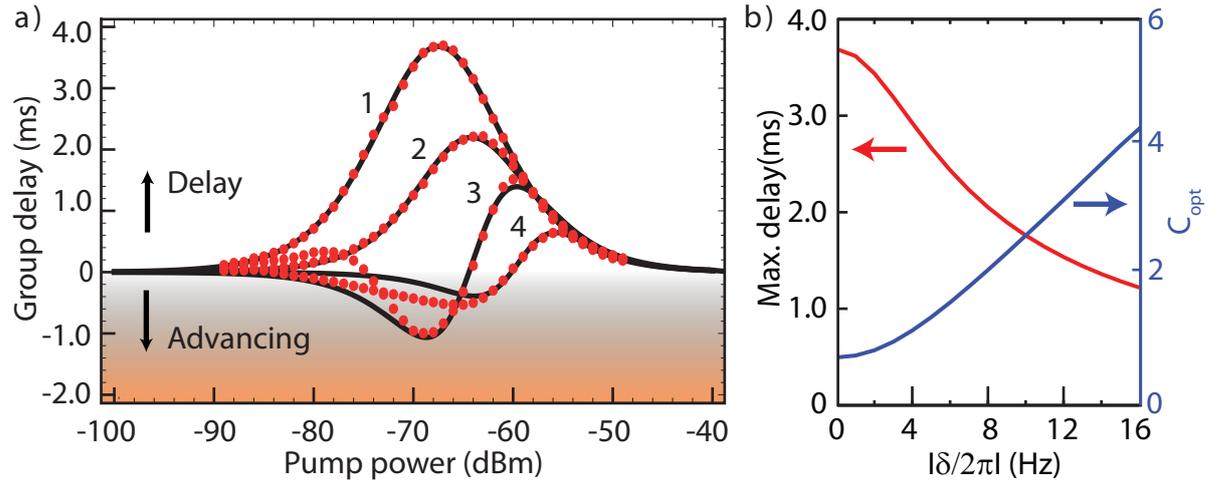
Figure 7.6: a)Fitted group delays versus drive power for a detuning of $|\delta|/2\pi = 1.2\,\mathrm{Hz}$ (set 1), $|\delta|/2\pi = 5.4\,\mathrm{Hz}$ (set 2), $|\delta|/2\pi = 10\,\mathrm{Hz}$ (set 3), $|\delta|/2\pi = 44\,\mathrm{Hz}$ (set 4), respectively. The black curves are fits to the full model given in Equation 7.7. b) Maximum group delay for a given detuning $|\delta|$ (red curve) and the optimum cooperativity C_{opt} (blue curve) the value is achieved for. The curves were adapted from Ref. [87].

presented in Figure 7.5. The remaining datasets show the group delay for a detuning of $|\delta|/2\pi = 5.4\,\mathrm{Hz}$ (set 2), $|\delta|/2\pi = 10\,\mathrm{Hz}$ (set 3), $|\delta|/2\pi = 44\,\mathrm{Hz}$ (set 4), respectively, plotted against the drive power. The black curves are fits of Equation (7.7). The dataset 3 and 4 show clearly a negative group delay as predicted. Curve 1 shows the highest group delay of $\tau_g \approx 3.9\,\mathrm{ms}$, close to the maximally expected value of $\tau_g^{\mathrm{max}} = 4.0\,\mathrm{ms}$.

Figure 7.6a shows that for increasing detuning, the maximum group delay monotonically decreases. In Figure 7.6b these values are extracted from Equation (7.7) (red curve). The optimum cooperativity to reach this value is included as well (blue curve). For increasing detuning the cooperativity to reach the maximum delay increases as well. The accompanying linewidth broadening corrects the strongest phase change towards the center of the pulse. This comes at the cost of a lower maximum delay, since a broadened transparency window has a weaker phase slope in frequency domain.

Studying the group delay as a function of detuning is difficult in cryostat No.1 since we observe temperature fluctuations, leading to frequency fluctuations of the setup on the scale of several Hz. We explored the relation between group delay and detuning δ in fridge No.2 at a temperature of $32\,\mathrm{mK}$. This also reduces the mechanical linewidth (cf. Section 4.5.2) to a value of $\Gamma_{\mathrm{m}}/2\pi \approx 2.5\,\mathrm{Hz}$. Therefore, we expect to observe an increased group delay. Figure 7.7 shows the group delay as a function of detuning at two different pump powers of $P_{\mathrm{d}} = -68\,\mathrm{dBm}$ in a) and $P_{\mathrm{d}} = -72\,\mathrm{dBm}$ in b). These drive powers result in higher cooperativities than $C_{\mathrm{opt}}(\delta = 0)$, $C_{\mathrm{a}} \approx 3.25$ and $C_{\mathrm{b}} \approx 1.29$, respectively, so we do not expect to detect the maximally achievable group delay.

The maximum group delay observed is $\tau_g \approx 16\,\mathrm{ms}$, a factor of 4 higher than in the measurements at higher temperatures and close to the expected maximum delay of $\tau_g^{\mathrm{max}} = 19.4\,\mathrm{ms}$. This corresponds to a group velocity $v_g = 0.3\,\mathrm{m/s}$, when we assume the pulse passes the length of the microwave cavity. The delay corresponds to a cable length of approximately $2000\,\mathrm{km}$.

The group delay decreases for increasing detuning $|\delta| \neq 0$ until it reaches negative values
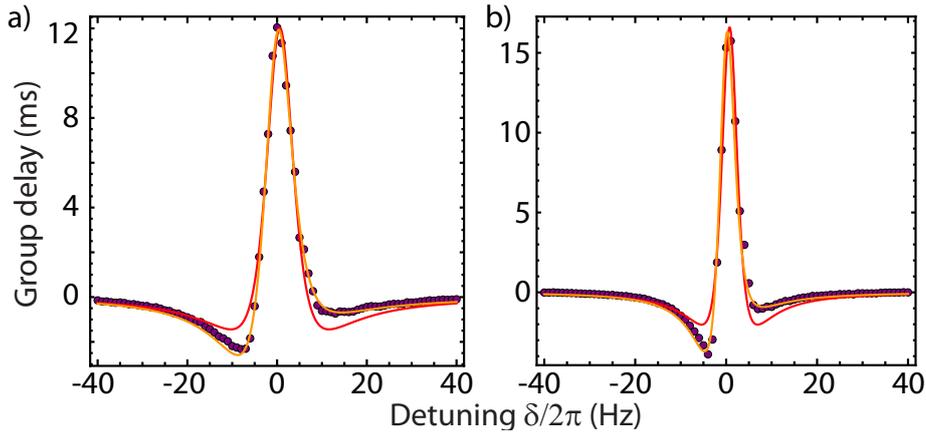
Figure 7.7: Group delay as a function of detuning for two different drive powers measured in
   fridge No.2 at a temperature of 32 mK. The red lines are fits of function (7.7). The orange
   lines represent numerical fits of the phase dispersion of EMIT, where the dispersive shape of
   the microwave cavity has been taken into account. The data in a) were acquired with an drive
   power of $P_{\mathrm{d}} = -68\,\mathrm{dBm}$, the data in b) with drive power of $P_{\mathrm{d}} = -72\,\mathrm{dBm}$.

of down to $-5\,\mathrm{ms}$. On a scale of $|\delta|/2\pi \propto 5\,\mathrm{Hz}$, we can tune the group delay over more
than 20 ms. The red line in Figure 7.7 is a fit to Equation (7.7). The phenomenological
behavior of the group delay is captured by this fit and reproduces the mechanical linewidth
and drive power, we used as fit parameters. Still we see that the fit does not account for
the asymmetry of the wings. The asymmetric behavior originates from the dispersive
shape of the microwave cavity as shown in Figure 6.5. In amplitude-phase space this shift
corresponds to a rotation of a small angle. This effect results from interference of the
detected signal with traveling waves on the ground plane and is commonly observed. We
introduce a small complex term as approximation to a small rotation in Equation (7.4), see
Appendix A.5 for more details. In this case, the outcome cannot be simplified to a simple
expression as before. Fitting the resulting phase dispersion to the data in Figure 7.7 gives
the orange curves. Evidently, the resulting fit parameters agree very well with the ones
from fitting Equation (7.7). The good agreement between data and theory corroborates the
assumption that the dispersive microwave cavity spectrum causes the asymmetric wings.

   In summary, we have evaluated the theoretical background supporting slow light in
electromechanical systems. The data agrees excellently with the theory for both variation
in drive power and detuning. At points where this is not the case, we are able to modify
the theory to adapt additional features. We demonstrate a group delay of up to 16 ms
corresponding to a cable delay of about 2000 km. The theoretical evaluation is valid for
EMIA as well, only Equation (7.4) has to be modified. For cooperativities $C \geq 1 - \eta_{\mathrm{c}}$, the
group delay switches sign at $\delta = 0$ and becomes positive for all values of δ. Due to the
electromechanical linewidth narrowing group delays up to 300 ms should be observable (see
Figure 7.8), still the maximum delay-bandwidth product remains 2. The bandwidth de-
creases proportional to the mechanical linewidth, the huge delays do not give a qualitative
improvement.

   One approach to increase the delay-bandwidth product is to use arrays of systems [266].
This has successfully been realized with photonic crystal cavities, combining up to 500
cavities [267]. Chang *et al.* [125] have proposed a similar scheme using optomechanical
arrays, leading to a group delay that scales with $\Delta\Omega \cdot \tau = \min\{\sqrt{2N\kappa_{\mathrm{ex}}\kappa}, (6\pi N^2)^{1/3}\}$,
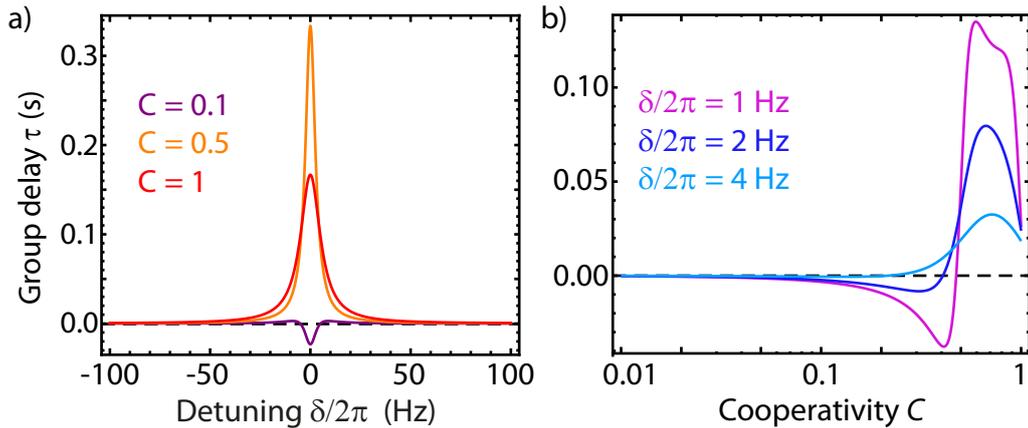
Figure 7.8: Group delay of an electromechanical system in EMIA configuration. a) shows the group delay as a function of detuning for a cooperativity of $C = 0.1$ (purple), $C = 0.5$ (red) and $C = 11$ (orange). The group delay is plotted as a function of cooperativity in b) for various detunings of $\delta/2\pi = 1\,\mathrm{Hz}$ (pink), $\delta/2\pi = 2\,\mathrm{Hz}$ (blue) and $\delta/2\pi = 4\,\mathrm{Hz}$ (light blue). The parameters used in this simulation are the one of the sample under investigation at a temperature of $200\,\mathrm{mK}$. For a cooperativity higher than 1, the mechanical mode starts lasing, not captured by the theory of EMIA.

where N is the number of optomechanical systems. With arrays of this type even storage of light should be possible. Altogether, electromechanical systems are promising elements to delay and even store pulses even in the quantum regime.

7.2   Pulse control

We now turn the discussion to the modulation of the drive field. The effective electromechanical coupling g depends on the average intra-cavity photon number $\bar{n}_\mathrm{c}$, $g = g_0 \sqrt{\bar{n}_\mathrm{c}}$, a pulsed drive field modulates the coupling between optical mode and mechanical oscillator.

In this section we analyze an electromechanical system in EMIT configuration incorporating a pulsed drive field optimally detuned from cavity resonance and a continuous probe tone. We theoretically and experimentally study the ring up and ring down of the mechanical amplitude in presence and absence of the drive tone, respectively. We find that the enhanced electromechanical coupling due to the drive tone leads to a mechanical ring up time scaling with the electromechanically broadened linewidth $t_\mathrm{ru} = 2/\Gamma_\mathrm{eff}$, while on switching off the drive field the mechanical amplitude decays on a much slower timescale with its initial linewidth $t_\mathrm{rd} = 2/\Gamma_\mathrm{m}$.

Further, we demonstrate switching of a transmitted continuous probe tone as function of the power of an optimally red detuned drive tone. We show that the asymmetry of ring up and -down of the mechanical amplitude leads to a switching behavior that is limited by the cavity decay time $1/\kappa$ in contrast to most physical systems that are limited by the system's slowest dynamics, here $1/\Gamma_\mathrm{m}$.

The experiments presented in this section are prerequisites for more complex protocols like the transfer into, storage in and retrieval of mechanical states [37, 131]. A second promising application is the swapping or entanglement of states between otherwise incompatible systems [39–42].
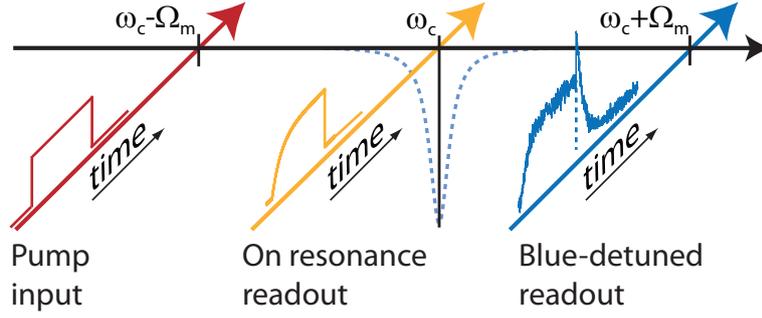
Figure 7.9: Schematic of the pulse scheme to study electromechanical switching. A driving field at optimum red detuning is switched to induce mechanical motion. When switched on, a probing field monitors the ring up of the EMIT feature. Additionally the anti-Stokes sideband of the probing field is detected to analyze the mechanical ring down. The figure is adapted from Ref. [87].

7.2.1 Electromechanical switching

An EMIT configuration is ideal to analyze the switching behavior of electromechanical systems (cf. Figure 7.9). To observe the dynamics of the system, a driving field, tuned to the red sideband induces a resonant force on the mechanical mode due to the beat between drive and probe field described in Section 6.1. Additionally, it induces electromechanical interaction like mechanical linewidth broadening. By pulsing the driving field, dynamical behavior is induced when switching. A probe tone at cavity resonance monitors the dynamical interaction, say the ring up of EMIT. To observe the mechanical motion for a switched off driving field where no induced transparency effect is visible, we also monitor the evolution of the anti-Stokes scattered field of the probe tone.

To understand the switching in an optimally detuned EMIT configuration, we first analyze its dynamics. For this purpose, we start with equations (6.15)–(6.17). To capture the time dependence we allow the amplitudes to become time dependent:

$$\delta a(t) = A^-(t)e^{-i\Omega t} + A^+(t)e^{+i\Omega t} , \tag{7.11}$$

$$\delta a^*(t) = \left(A^+(t)\right)^* e^{-i\Omega t} + \left(A^-(t)\right)^* + e^{+i\Omega t} , \tag{7.12}$$

$$\delta x(t) = X(t)e^{-i\Omega t} + X(t)^* e^{+i\Omega t} . \tag{7.13}$$

The intra-cavity phonon number $\bar{n}_c$ is assumed to be at a constant value, either $\bar{n}_{on}$ or $\bar{n}_{off} \approx 0$ for switched on or switched off driving field, respectively. The same is true for the corresponding field $\bar{a}$ with $\bar{a}^2 = \bar{n}_c$. We plug the above ansatz in Equation (6.13) and (6.14), ignore nonlinear higher order terms and sort after the rotating terms. As in Section 6.1, only the terms with $\exp(-i\Omega t)$ contribute:

$$\frac{d}{dt}A^-(t) + \left(-i(\Omega + \Delta) + \frac{\kappa}{2}\right) A^-(t) = -iG\bar{a}X(t) + \sqrt{\frac{\kappa_{ex}}{2}}s_p , \tag{7.14}$$

$$\frac{d}{dt}A^+(t) + \left(i(\Omega - \Delta) + \frac{\kappa}{2}\right) A^+(t) = -iG\bar{a}X(t)^* , \tag{7.15}$$

$$\frac{d^2}{dt^2}X(t) + \frac{d}{dt}X(t)(\Gamma_m - 2i\Omega) + (\Omega_m^2 - \Omega^2 - i\Gamma_m\Omega)X(t) = -\frac{\hbar G\bar{a}}{m_{eff}} \left(A^-(t) + \left(A^+(t)\right)^*\right) . \tag{7.16}$$

Assuming the resolved sideband regime, we can neglect the Stokes field $A^+(t) = 0$. The low mechanical damping allows to assume a slowly varying mechanical amplitude, on scales much smaller than the mechanical resonance frequency $\Gamma_{\mathrm{m}} \ll \Omega_{\mathrm{m}}$. We can neglect Γ_{m} in the first time derivative for the probe field close to the anti-Stokes field, $\Omega \approx \Omega_{\mathrm{m}}$. We can further ignore $\Omega_{\mathrm{m}}^2 - \Omega^2$. For a close but off resonant probe tone, the latter leads to an oscillatory term in the complete solution with the frequency difference $\exp(-i(\Omega - \Omega_{\mathrm{m}}))$. The slow mechanical modulation function allows to neglect the second order derivative, $d^2 X(t)/dt^2 \ll \Omega \cdot dX(t)/dt$. The above set of equations then reduces to

$$\frac{d}{dt}A^-(t) + \left(-i(\Omega + \Delta) + \frac{\kappa}{2}\right)A^-(t) = -iG\bar{a}X(t) + \sqrt{\frac{\kappa_{\mathrm{ex}}}{2}}s_{\mathrm{p}} , \qquad (7.17)$$

$$-2i\Omega\frac{d}{dt}X(t) - i\Gamma_{\mathrm{m}}\Omega X(t) = -\frac{\hbar G\bar{a}}{m_{\mathrm{eff}}}A^-(t) . \qquad (7.18)$$

The first equation has two solutions, one for switching on the drive field, one for switching it off. The solution for the former reads (for switching on at $t = 0$):

$$A^-(t) = -\sqrt{\frac{\kappa_{\mathrm{ex}}}{2}}\frac{s_{\mathrm{p}}}{i(\Omega + \Delta) - \frac{\kappa}{2}} + \frac{iGX(t)\bar{a}_{\mathrm{on}}}{i(\Omega + \Delta) - \frac{\kappa}{2}}\left(1 - e^{i(\Omega+\Delta)t - \frac{\kappa}{2}t}\right) , \qquad (7.19)$$

and the switching-off dynamics reads for negligible $\bar{a}_{\mathrm{off}}$ (for switching off at $t = 0$).

$$A^-(t) = -\sqrt{\frac{\kappa_{\mathrm{ex}}}{2}}\frac{s_{\mathrm{p}}}{i(\Omega + \Delta) - \frac{\kappa}{2}} + \frac{iGX(t)\bar{a}_{\mathrm{on}}}{i(\Omega + \Delta) - \frac{\kappa}{2}} e^{i(\Omega+\Delta)t - \frac{\kappa}{2}t} , \qquad (7.20)$$

Working at optimum detuning with a probe tone on the anti-Stokes sideband ($\Delta = -\Omega_{\mathrm{m}}$ and $\Omega = \Omega_{\mathrm{m}}$), the complex term in the exponential function is zero. Note, that in this configuration the field rings up/down on a timescale $2/\kappa$. For times exceeding this value the dynamics of the intra-cavity field amplitude is only determined by the dynamics of the mechanical mode (depending on switching on or off, $\bar{a} = \bar{a}_{\mathrm{on}}$ or $\bar{a} = \bar{a}_{\mathrm{off}}$),

$$A^-(t) = \frac{-iGX(t)\bar{a} + \sqrt{\frac{\kappa_{\mathrm{ex}}}{2}}s_{\mathrm{p}}}{\kappa/2} . \qquad (7.21)$$

This solution modifies Equation (7.18) to

$$\frac{d}{dt}X(t) = -\frac{\Gamma_{\mathrm{m}}}{2}\left(1 + C_{\mathrm{on/off}}\right)X(t) - \frac{ig_0\bar{a}x_{\mathrm{zpf}}}{\kappa/2}\sqrt{\frac{\kappa_{\mathrm{ex}}}{2}}s_{\mathrm{p}} , \qquad (7.22)$$

where we have replaced $Gx_{\mathrm{zpf}} = g_0$ and $4g_0^2\bar{n}_{\mathrm{on/off}}/(\Gamma_{\mathrm{m}}\kappa) = C_{\mathrm{on/off}}$.

Switching-on dynamics of the electromechanical system

We assume the driving field to be switched on at $t = 0$. The initial mechanical displacement results from the Brownian motion of the beam, $X(0) \approx 0$. Equation (7.22) then has the solution

$$X(t) = X_{\mathrm{ss}}\left(1 - e^{-\frac{\Gamma_{\mathrm{eff}}}{2}t}\right) , \qquad (7.23)$$

with the steady state amplitude

$$X_{\mathrm{ss}} = -\frac{i4g_0\bar{a}_{\mathrm{on}}x_{\mathrm{zpf}}}{\Gamma_{\mathrm{m}}\kappa}\frac{1}{1 + C_{\mathrm{on}}}\sqrt{\frac{\kappa_{\mathrm{ex}}}{2}}s_{\mathrm{p}} . \qquad (7.24)$$

The mechanical mode rings up to its steady state amplitude at the rate $\Gamma_{\text{eff}}/2 = (1 + C)\Gamma_{\text{m}}/2$. Stepping back to Equation (7.21) and using the solution of $X(t)$, we get

$$A^-(t) = \frac{-i\frac{C_{\text{on}}}{1+C_{\text{on}}}\left(1 - e^{-\frac{\Gamma_{\text{eff}}}{2}t}\right) + \sqrt{\frac{\kappa_{\text{ex}}}{2}}s_{\text{p}}}{\kappa/2} \ . \tag{7.25}$$

We see that the intra-cavity field decays from an initial amplitude, given by the probe field $A^-(0) = \frac{\sqrt{\kappa_{\text{ex}}/2}}{\kappa/2}s_{\text{p}}$ to a steady state amplitude $A_{\text{ss}} = -iC_{\text{on}}/(1 + C_{\text{on}}) + \frac{\sqrt{\kappa_{\text{ex}}/2}}{\kappa/2}s_{\text{p}}$ with a rate $\Gamma_{\text{eff}}/2$. By observing the intra-cavity ring down, which results in the transparency window we have access to the mechanical ring up time. The result of Γ_{eff} is what one would naively expect:

When switching on the driving field, the intra-cavity field $\bar{n}_{\text{c}}$ saturates quickly compared to the mechanical timescales. The mechanical mode experiences electromechanical linewidth broadening before ringing up due to the driving force.

Switching-off dynamics of the electromechanical system

As mentioned above, when switching off the drive field, the intra-cavity photon number $\bar{n}_{\text{off}}$ decays to zero at a rate of $\kappa/2$ in the same way as the corresponding electromechanical coupling $g = g_0\sqrt{\bar{n}_{\text{c}}}$. As a result, the mechanical loss rate relaxes to its initial value, $\Gamma_{\text{eff}} = \Gamma_{\text{m}}$ on the same timescale. However, the mechanical oscillation prevails. With the driving tone switched off, the intracavity field increases to a constant value, given by the present probe field, $A^-(t) \approx \frac{\sqrt{\kappa_{\text{ex}}/2}}{\kappa/2}s_{\text{p}}$, modifying the differential Equation (7.22) to

$$\frac{d}{dt}X(t) = -\frac{\Gamma_{\text{m}}}{2}X(t) - \frac{ig_0\bar{a}x_{\text{zpf}}}{\kappa/2}\sqrt{\frac{\kappa_{\text{ex}}}{2}}s_{\text{p}} \ . \tag{7.26}$$

The constant intra-cavity field amplitude at the probe-frequency does not allow to monitor the mechanical decay. For this purpose, we monitor the anti-Stokes sideband of the probe tone at the frequency $\omega_{\text{c}} + \Omega_{\text{m}}$. The ring down of the mechanical displacement amplitude leads to a proportionally decreasing sideband amplitude. This is due to the parametric coupling; the number of anti-Stokes scattered photons is proportional to the mechanical amplitude multiplied by the cavity filter function at the frequency $\omega_{\text{p}} + \Omega_{\text{m}}$. In principle the proportionality between scattered photons and mechanical displacement amplitude also modifies the probe field at cavity resonance. Yet, the number of scattered photons is very small. For a rough estimate one can compare the depth of the dip in the cavity resonance in Equation (6.53)[2] for $x_0 \approx 0$ and $x_0 \approx 1\,\text{nm}$ (what is already highly exaggerated). The result is of the order of 10^{-4} and can be neglected in our calculations. The assumption of a constant probe field with negligible backation from the mechanical mode in our calculations is justified. Detection of this change is in general possible, however observing the anti-Stokes field (or the Stokes field) gives a higher contrast.

7.2.2 Setup

We study the switching behavior of an electromechanical system in cryostat No.1. We measure a temperature of approximately $100\,\text{mK}$ inside the mixing chamber. The sample

---

[2]To recall, this equation gives the transmission spectrum of a microwave cavity being subject to electromechanical coupling to a sinusoidal, mechanical mode.
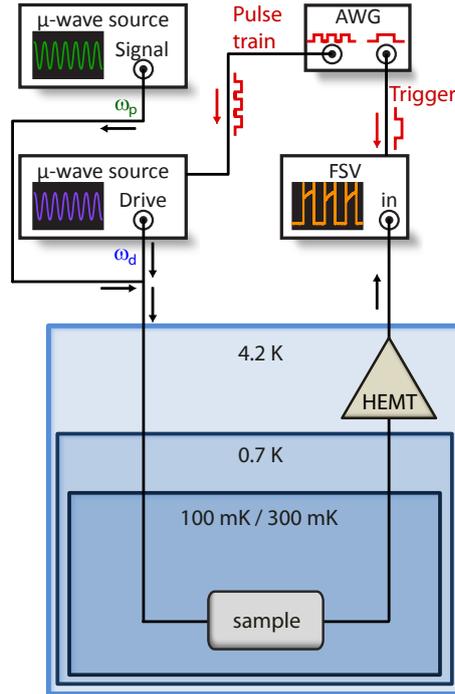
Figure 7.10: Schematic setup to study switching in an electromechanical system. A μ-wave source provides the pulsed driving field and is combined at room temperature with a second source, providing the probe tone. The combined fields are fed into the dilution fridge, passing the sample and an amplifier chain and analyzed with a spectrum analyzer in time domain centered at the probe frequency or the blue sideband of the probe at $\omega = \omega_\mathrm{c} + \Omega_\mathrm{m}$ to study the ring up and ring down behavior, respectively. An arbitrary waveform generator generates rectangular pulses by pulse modulation and triggers the measurement.

is the same one, presented in Section 4.1. Unfortunately, the sample is not well thermalized at this temperature; the mechanical linewidth drifts between $\Gamma_\mathrm{m}/2\pi \approx 5\,\mathrm{Hz}$ and $8\,\mathrm{Hz}$. The latter corresponds to a temperature of $200\,\mathrm{mK}$ (see Figure 4.13). We assume a mechanical linewidth of $\Gamma_\mathrm{m}/2\pi \approx 8\,\mathrm{Hz}$ in the first data set. Due to technical reasons the second set of experiments demonstrating the switching speed are performed at approximately $300\,\mathrm{mK}$. This leads to an increase of the mechanical linewidth from $\Gamma_\mathrm{m}/2\pi \approx 8\,\mathrm{Hz}$ to $\Gamma_\mathrm{m}/2\pi \approx 13\,\mathrm{Hz}$.

A Rhode&Schwarz SMF microwave source provides the pulsed driving field at optimum red detuning, $\Delta = -\Omega_\mathrm{m}$. A second source of the same type creates the continuous probe signal at cavity resonance $\Omega = \Omega_\mathrm{m}$. A power divider combines both signals at room temperature. Heavily attenuated coaxial lines guide the tones to the sample. After passing the sample, a circulator at still temperature ($0.7\,\mathrm{K}$) and an amplifier chain, a Rhode&Schwarz FSV9 spectrum analyzer in time domain configuration detects the signal. To study the ring up, it is centered at the cavity resonance ω_c. To analyze the ring down, the center frequency is set to the anti-Stokes sideband of the probe tone $\omega_\mathrm{c} + \Omega_\mathrm{m}$. A LeCroy ArbStudio 1104D arbitrary waveform generator shapes rectangular drive pulses via pulse modulation and triggers the measurement.
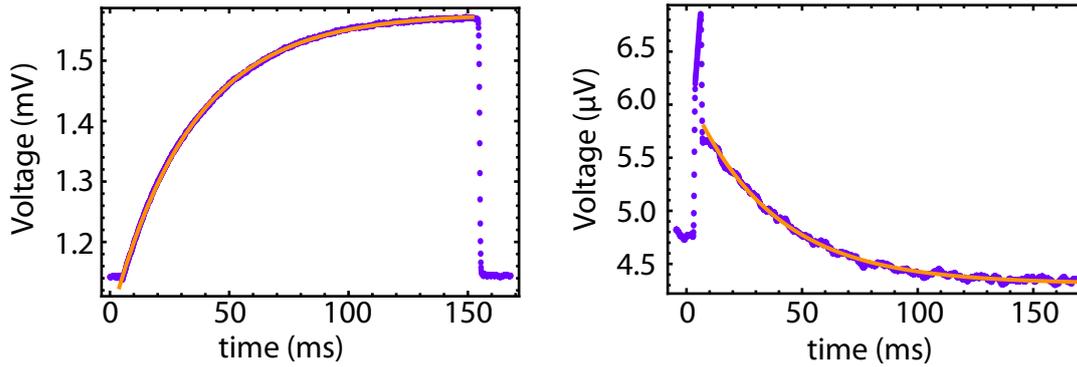
Figure 7.11: a) shows the transmitted probe field amplitude on a voltage scale of a typical ring up measurement, the orange line is an exponential fit to the data. A typical ring down measurement of the transmitted amplitude of the probe tone's blue sideband is shown in b). The solid orange line is a fit to the data. The peak at $t \approx 10\,\text{ms}$ is an artefact from switching off the driving field. The drive power in both curves is $P_\text{d} = -65.5\,\text{dBm}$. Note the different scales of the voltage axis.

7.2.3 Experimental demonstration of mechanical ring up and ring down

We apply drive pulses with 150 ms length to ensure the mechanical mode and thus the intra-cavity field saturates. The driving fields power is swept from $P_\text{d} = -75.5\,\text{dBm}$ to $-55.5\,\text{dBm}$. The probe tone is continuous at a drive power $P_\text{p} = -95.5\,\text{dBm}$. A dataset acquired at $P_\text{d} = -65.5\,\text{dBm}$ is shown in Figure 7.11. From the ring up measurement of the probe tone shown in Figure 7.11a, we extract the rise time of the mechanical displacement amplitude $t_\text{ru} = \frac{1}{\Gamma_\text{eff}/2}$ by fitting Equation (7.25) to the data (orange line). By fitting an exponential decay to the ring down of the blue sideband shown in Figure 7.11b (orange line), we extract the undisturbed mechanical decay time $t_\text{rd} = \frac{\Gamma_\text{m}}{2}$.

The extracted, characteristic rise and decay times are plotted in Figure 7.12. For increasing drive power, the rise time (light blue dots) remains constant and starts decreasing at a $P_\text{d} \approx -69\,\text{dBm}$, down to less than 5 ms. However, this timescale is still long compared to the rise and decay time of the μ-wave cavity, $t_{\mu\text{w}} = 2/\kappa \approx 2\,\mu\text{s}$. We see, that the assumption made in the underlying theory are justified. The orange line is a plot of $t_\text{ru} = ((1 + C)\Gamma_\text{m}/2)^{-1}$ with an initial mechanical linewidth of $\Gamma_\text{m}/2\pi = 8.5\,\text{Hz}$. This corroborates our assumption that the effect occurs due to the electromechanical linewidth broadening. The difference between data and plot occurs due to temperature fluctuations of the sample. On switching off the probe field, no electromechanical coupling to this tone is present. The mechanical mode decays with its natural linewidth. The ring down time (hollow purple dots) stays constant around $2/\Gamma_\text{m} \approx 38\,\text{ms}$ for the whole drive power range.

7.2.4 Demonstration of electromechanical switching

Basing on the ring up and ring down dynamics, we analyze the system under the influence of a pulsed drive tone. A long drive pulse with simultaneously switched on probe field prepares the electromechanical system in its steady state. A series of rectangular shaped drive field pulses with $T_\text{on} = T_\text{off}$ is then sent to the sample while recording the probe tone's transmission. The probe field's amplitude follows the drive pulses modulation on a timescale of the cavity decay rate (see Figure 7.13 for switching times of 10 ms, 1 ms and $100\,\mu\text{s}$). This counterintuitive result proves that switching in an electromechanical system
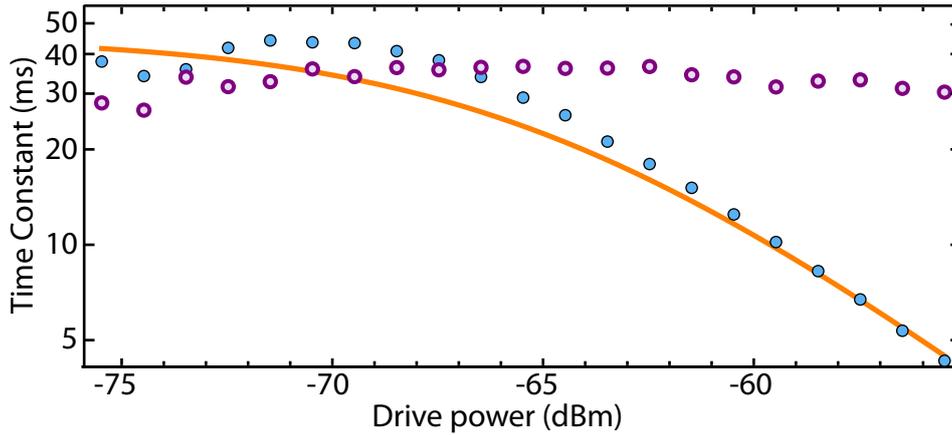
Figure 7.12: Ring up/down time constant versus drive power. The purple dots show the decay time of the anti-Stokes scattered photons of the probe field, when switching off the drive tone. The ring up (light blue dots) time decreases as expected with increasing drive power. The orange line is a plot of the model with an intrinsic mechanical linewidth of $\Gamma_\mathrm{m}/2\pi = 8.5\,\mathrm{Hz}$.

is not limited by it's longest timescale, the mechanical ring down time $2/\Gamma_\mathrm{m}$.

When switching off the drive tone, the mechanical oscillation relaxes to its equilibrium position on this timescale. The black lines in Figure 7.13 show an exponential decay with a linewidth $\Gamma_\mathrm{m}/2\pi \approx 12.7\,\mathrm{Hz}$ with different initial amplitudes. The transmission of the probe field drops on the cavity's characteristic timescale $2/\kappa$. In the on state, the force acting on the mechanical mode results from the beat between drive field and probe field drives it again towards it's steady state value on a faster timescale $2/\Gamma_\mathrm{eff}$. The transmitted probe signal follows the mechanical amplitude (see Equation 7.21). We achieve high contrast, even for multiple pulse series for a switch off time fulfilling $(\kappa/2)^{-1} < T_\mathrm{off} < (1 + C)T_\mathrm{on}$. The minimum time window for switching off scales linearly with the drive power and its absolute minimum is defined by the cavity linewidth. The contrast also increases with increasing drive power resulting from a higher mechanical amplitude, whereas the probe power defines the level of the off state. Fluctuations due to the mechanical motion are negligible as discussed above.

Using probe pulses instead of a continuous probe field will allow for storage of photonic states by converting them into a coherent excitation of the mechanical mode [37, 42, 131]. Another application is the generation of Einstein-Podolsky-Rosen entangled states [126] and the swapping of photonic states from one cavity mode into a second, distinct mode as proposed in Refs. [39–42] and recently demonstrated in two proof of principle experiments [132, 133].

With the low thermal decoherence rate of $\Gamma_\mathrm{m}\bar{n}_\mathrm{m}/2\pi \approx 1.29\,\mathrm{kHz}$ at $32\,\mathrm{mK}$ and the highest measured coupling of $g/2\pi = 20.6\,\mathrm{kHz}$, the system analyzed in this work should allow for the demonstration of these protocols. Improvements of the measurements setup to compensate for the necessary high drive powers are in progress.

7.3   Summary and discussion

In this chapter we have analyzed two dynamical effects in an electromechanical system in an optimally detuned EMIT configuration, namely slow light and switching.
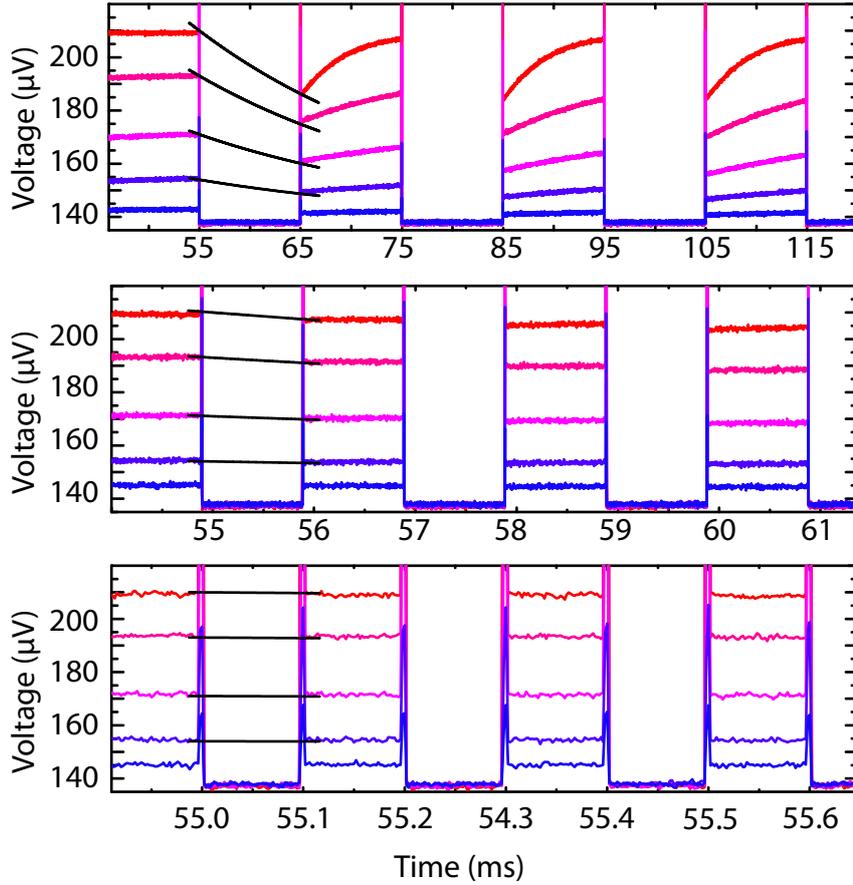
Figure 7.13: Demonstration of the switching dynamics in an electromechanical system for different pulse lengths. From top to bottom, the pulse lengths are 10 ms, 1 ms and 100 μs. The drive powers increases from blue to red, the drive power is $P_\mathrm{d} = -73.5\,\mathrm{dBm}$, $-73.5\,\mathrm{dBm}$, $-69.5\,\mathrm{dBm}$, $-65.5\,\mathrm{dBm}$, $-61.5\,\mathrm{dBm}$ and $-55.5\,\mathrm{dBm}$, respectively. The black lines are exponential decays, describing the mechanical ring down for a linewidth of $\Gamma_\mathrm{m}/2\pi = 12.7\,\mathrm{Hz}$ for the different initial amplitudes.

Slow light in an photonic crystal type optomechanical system was recently demonstrated phenomenologically [116]. In our work, we demonstrate a true delay of probe pulses [87].

We have derived a description of the delay of the group velocity of probe pulses centered close to the cavity resonance as a function of detuning $\delta = \Omega - \Omega_\mathrm{m}$ of the probe pulse and drive power for a continuous drive at $\omega_\mathrm{d} = \omega_\mathrm{c} - \Omega_\mathrm{m}$. We have demonstrated group delays of up to 16 ms showing that the delay decreases for increasing $|\delta|$. The cooperativity and thus the drive power to achieve maximum delay for a given detuning δ increases as well. The maximum achieved delay corresponds to that of a cable of approximately 2000 km or a group velocity of $v_g = 0.3\,\mathrm{m/s}$. We show further that the delay bandwidth product, characterizing the delay in terms of how many pulses fit into a given delay, does not exceed 2 in electromechanical systems.

By careful analysis of slow light as a function of detuning, we show that a detuning exceeding the mechanical linewidth $|\delta| > \Gamma_\mathrm{m}/2$ allows for negative group delays, effectively increasing the group velocity above the speed of light. Note, that this does not violate causality. No information transfer faster than the speed of light takes place, since this

implies discontinuities in the pulse shape in contrast to the smooth pulses studied here.

Integrating the dispersive shift of the cavity into the theory gives excellent agreement to the experimental data, showing that we can tune the group delay over more than 20 ms on variation of the detuning δ about $2\pi \times 5$ Hz.

Similar measurements in an EMIA configuration are expected to allow for observation of delays higher than 300 ms. The electromechanical narrowing of the mechanical linewidth is responsible for the strong dispersion. The experimental study of this huge delay requires much longer pulses, as the delay bandwidth product remains 2.

To qualitatively increase the group delay, i.e. to increase the delay bandwidth product Chang et $al.$ [125] propose the use of optomechanical arrays, similar to other realizations of slow light [266, 267]. With a sufficient large number of optomechanical arrays even the storage of light will be possible, making these systems a good candidate to delay and even store pulses in the quantum regime.

To demonstrate the switching of the transparency effect, we have analyzed the ring up and ring down behavior of the mechanical mode in an EMIT configuration under the presence and absence of the drive field. We show the timescale of the ring up is set by the inverse electromechanically broadened mechanical linewidht $2/\Gamma_{\mathrm{eff}}$ and thus depends on the intensity of the drive field. On switching off the drive field, the driving force due to the beat between drive and probe field vanishes and the mechanical amplitude decays with its intrinsic linewidth to its thermal equilibrium amplitude.

In the next step we have used slow decay of the mechanical excitation to switch the transparency effect on a timescale $(\kappa/2)^{-1} < T_{\mathrm{off}} < (1+C)T_{\mathrm{on}}$. We show that the dynamics of the system is not defined by its slowest dynamics, the mechanical decay time $2/\Gamma_{\mathrm{m}}$ but by the much faster cavity decay time $2/\kappa$.

The temporal control demonstrated in this work is a first step towards more complex protocols to manipulate the state of the mechanical oscillator.

Besides the effects presented in this chapter different dynamical effects have been analyzed in opto-/electromechanical systems employing pulsed schemes. Vanner et $al.$ [128, 129] have studied the reconstruction and manipulation of the Wigner density of a mechanical oscillator. First steps towards coherent state transfer between the optical and the mechanical oscillator have been shown in the optical domain [75, 131] and in the microwave domain [37]. These protocols will in turn allow to transfer states between two cavities operating in different frequency regimes but sharing the mechanical mode proposed in Refs. [39–42] and recently demonstrated in two proof of principle experiments swapping light states between to modes of the same optical cavity [132, 133].

The low thermal decoherence rate of the sample studied in this work of $\Gamma_{\mathrm{m}}\bar{n}_{\mathrm{m}}/2\pi \approx$ 1.29 kHz at 32 mK combined with the highest measured coupling rate of $g/2\pi = 20.6$ kHz is one order of magnitude below the quantum coherent coupling regime [75]. Improvements of the measurement setup to allow for the necessary high drive powers are in progress. On the technological side, increasing the electromechanical coupling by about one order of magnitude is feasible with our production process. So far only classical coherent states have been stored in the mechnical oscillator. Integration of a superconducting qubit into the sample will allow the storage of quantized photonic states in the mechanical mode similar to the work of O'Connell et $al.$ [32], but with higher coherence times. The quantum drum used in their work was limited by a higher decoherence than the qubit, what is no issue in opto-/electromechanically cooled low-frequency mechanical devices.

Chapter 8

Summary and outlook

In this thesis we present the systematic study of a circuit nano-electromechanical hybrid systems consisting of a superconducting microwave resonator and a nanomechanical beam. The study was performed in close collaboration with the group of T. J. Kippenberg at the École Polytechnique Fédérale de Lausanne (EPFL) in Switzerland.

On the experimental side we have set up two low temperature (mK) systems allowing for very sensitive microwave experiments. We demonstrate a high measurement precision, only a factor 100 away from the Heisenberg limit with an imprecision noise of a factor 35 above the standard quantum limit of our device. This is comparable to similar setups without Josephson parametric amplifier used to study electromechanical devices [69, 110, 120, 255].

The particular sample studied in this work is a hybrid system incorporating a niobium CPW microwave cavity, capacitively coupled to a Si_3N_4/Nb double layer nanobeam operating in the resolved sideband regime ($\Omega_m > \kappa$). The nanobeam presents the first implementation of this material system combining the advantages of highly stressed silicon nitride and niobium. This allowed for a high mechanical quality factor of $Q_m = 5.60 \times 10^5$ and a high mechanical frequency of $\Omega_m/2\pi \approx 1.45\,\text{MHz}$ and a temperature of $T = 32\,\text{mK}$. The realization of the nanobeam from the same metallization layer used for the μ-wave cavity reduces losses due to the absence of stray capacitances, which are unavoidable for nanobeams structured by employing an additional superconducting layer [202]. In addition to the ability to access the Duffing regime spectroscopically by driving the nanobeam, the study of the intrinsic mechanical loss channels demonstrates that the electromechanical hybrid systems provide an excellent platform to analyze intrinsic properties of (nano-) mechanical oscillators.

A key parameter of the hybrid system is the electromechanical vacuum coupling. In our quantitative analysis it has been determined to $g_0/2\pi = 1.26\,\text{Hz}$ [87] using frequency noise calibration [230], a technique which is applied for the first time to a system operating in the microwave regime. This technique is complementary to temperature sweeps typically used to calibrate devices and the input wiring. Using it for the study of nanomechanical systems shifts the technological requirements from a variable temperature to the phase (or frequency) modulation of the input field.

To understand the system parameters and to demonstrate the electromechanical behavior, we carefully pre-characterize the electromechanical device and experimentally verify

the most fundamental optomechanical features resulting from dynamical back-action. Using back-action cooling of the mechanical mode from an average occupation of $\bar{n}_m(T = 30\,\mathrm{mK}) \approx 500$ to $\bar{n}_m = 13$, we find excellent agreement of the observed behavior with the theory and establish the limits of mechanical displacement sensing in the current setup. We find that the limiting contributions stem from noise in the microwave source source at high drive power and from noise in the amplifier chain.

The electromechanical hybrid system was systematically studied by spectroscopy experiments in a two-tone configuration. This does not only open the avenue towards the analysis of dynamical effects in electromechanics but also allows for the study of interference effects between a strong driving field and a weak probe field like electromechanically induced transparency (EMIT) and absorption (EMIA) [82]. For the latter, we show that the absorption of microwave signals at cavity resonance can be increased by more than 25 dB on increasing the power of the drive tone by a factor of two. Our results clearly demonstrate that the studied electromechanical system can be used as a tunable notch filter to eliminate extreme narrow frequency bands ($\sim$ Hz) within the much wider frequency band ($\sim$ MHz) defined by the linewidth of the microwave cavity. The analysis of our device in an EMIA configuration at high drive fields explores the limits of the electromechanical theory at high mechanical amplitudes. By comparing the cavity frequency pull towards lower frequencies to the predictions derived based on the assumption of a linearized electromechanical coupling, we find that the mechanically induced Kerr effect is not covered by theory. To understand this effect we extend the model beyond the linear approximation. Regarding the study of the cavity behavior for high mechanical amplitudes, the analysis of the self-oscillation of the mechanical mode is the next logical step. Experiments to study the origins of the hysteresis in the amplitude versus cavity photon number dependence are in preparation.

The study of EMIT as function of detuning and power of a drive field reveals strong dispersion around the transparency window of a probe tone, demonstrating the feasibility of our device to delay and advance the group velocity of a pulsed probe field. This is in close analogy to the generation of slow light in atomic media with EIT [121–123]. Additionally, we overcome the main challenge in the quantum manipulation by achieving a maximum effective electromechanical coupling that exceeds the mechanical thermal decoherence rate at a temperature of $30\,\mathrm{mK}$, $g_{max}/2\pi = 20.6\,\mathrm{kHz} \gg \bar{n}_m \Gamma_m/2\pi \approx 1.18\,\mathrm{kHz}$. Going beyond EMIT, we extend the theory to include nonlinear mechanical contributions and corroborate the model predictions by experimentally mapping the mechanical Duffing regime into the microwave regime. This is a first step towards sensitive electromechanical bifurcation sensors.

The good control of our system in a two-tone configuration, demonstrated by the investigation of EMIT, enables us to demonstrate a true delay of probe pulses [87] up to 16 ms (and an advancement of up to 5 ms), corresponding to the delay induced by an about 2000 km long coaxial cable or an on-chip group velocity of $v_g = 0.3\,\mathrm{m/s}$. This is the first demonstration of slow light in the microwave regime in a circuit electromechanical system. The experimental data agrees excellently with theory derived from the phase dispersion of the transparency window in an EMIT configuration in the resolved sideband regime. From a technical point of view, nano-electromechanical systems offer a promising extension to the quantum tool-box in the microwave regime. Although we only demonstrate the delay of classical pulses, in principal the concepts can be extended to quantized fields. A sample

geometry with improved g_0 to reach the quantum coherent coupling regime [75] together with the powerful progress in generation and detection of single microwave photons [268] may allow the control of the propagation of quantized microwave fields. Thus circuit electromechanical systems offer a promising perspective to synchronize quantized microwave pulses generated by spatially separated systems.

Our time domain measurements of the ring up and ring down behavior of the nanobeam's amplitude in an EMIT configuration reveal that on switching off the drive field the mechanical amplitude decays on a timescale corresponding to its intrinsic linewidth, while the ring up time is correlated to the electromechanical drive power dependent linewidth broadening, reflecting the dynamical electromechanical back-action. We use this asymmetric behavior to demonstrate the counterintuitive fact that electromechanical switching of the transmitted probe field is not limited by the longest timescales in the device – the mechanical ring down – but is limited by the cavity's ring down time [87]. This proof of concept experiment provides the basis for complete storage and retrieval of a microwave quantum state in long-lived mechanical excitations, as recently demonstrated with classical microwave fields [37].

Altogether, the results achieved within the scope of this thesis provide the basis for experiments to test decoherence in macroscopic objects like a nanobeam and to map quantum states between different microwave frequencies, while at the same time offering propagation control over quantized fields.

Beyond the scope of this thesis, the next steps in the direction of a study of decoherence in macroscopic mechanical oscillators is the swapping of a quantum state from a photon to the vibrational mode. Here, three requirements have to be met: First, the mechanical mode needs an occupation close to the quantum mechanical ground state that also needs to be detected efficiently. Second, the system has to operate in the quantum coherent regime, to allow for (nearly) lossless conversion of excitations. Third, a source has to generate microwave quantum states. The first two requirements are met by using a sufficiently strong drive field and samples with improved electromechanical vacuum coupling. Reduction of the gap between nanobeam and ground plane by focused ion beam milling [166] can increase g_0 by about a factor of ten, implying that we can reach the quantum coherent coupling regime with all other parameters within the range of those given in this thesis. First fabrication steps in this direction with our material system look promising[1]. Regarding the experimental techniques, the next modifications of the setup include the integration of a high-Q microwave filter to purify the input microwave fields [202, 258] and the integration of a Josephson parametric amplifier [253] or of a Josephson ring amplifier [269] for (nearly) quantum limited amplification [232]. This will enhance the measurement sensitivity to allow for the detection of a mechanical occupation close to zero due to a highly reduced noise level. At the same time it allows for higher cooling rates and lower mechanical occupations. To meet the third requirement, a superconducting qubit coupled to a microwave cavity may provide a single photon source [268].

Although not studied within this work, CPW microwave cavities support higher modes, all coupling to the displacement of the nanobeam as long as a voltage antinode exists at the nanobeam's position. With the above requirements met, two distinct harmonics of the same microwave cavity in an EMIT configuration may be used to map or frequency convert

---

[1]private communication with M. Pernpeintner

the state of single microwave photons from one of the modes to the second one, providing a (nerly) lossless quantum transducer. This has recently been demonstrated with classical states in the optical domain [132, 133].

The perspectives outlined above and the progress documented in this thesis show that cavity electromechanical hybrid systems as studied here are of great wealth within the field of opto-/electromechanics due to their scalability and the possibility to combine them with other solid state quantum systems operating in the microwave regime.

Appendix A

Appendix

A.1 Table of material parameters

Symbol	Definition	Value and Unit
L	length of the nanobeam	$60\,\mu$m
w	width of the nanobeam	$140\,$nm
h_{SiN}	thickness of the Si_3N_4 layer	$70\,$nm
h_{Nb}	thickness of the Nb layer	$130\,$nm
ρ_{SiN}	density of Si_3N_4	$3000\,$kg/m^3
ρ_{Nb}	density of Nb	$8570\,$kg/m^3
ρ_{eff}	effective density of the nanobeam	$6620.5\,$kg/m^3
m_{eff}	effective mechanical mass	$7\,$pg
E_{SiN}	Young's modulus of Si_3N_4	$300\,$GPa
E_{Nb}	Young's modulus of Nb	$105\,$GPa
E_{calc}	calculated effective Young's modulus of the nanobeam	$173\,$GPa
E_{eff}	measured effective Young's modulus of the nanobeam	$140\,$GPa
σ_{SiN}	tensile stress of the Si_3N_4 layer	$800\,$MPa
σ_{eff}	estimated tensile stress in the nanobeam	$199\,$MPa
α_{Si}	thermal expansion coefficient of Si	$3.0 \times 10^{-6}/^\circ$C
α_{SiN}	thermal expansion coefficient of Si_3N_4	$3.3 \times 10^{-6}/^\circ$C
T_{c}	critical temperature of Nb	$9.2\,$K

A.2 Table of parameters

Symbol	Definition	Value and Unit
$\widetilde{\omega}_{\mathrm{c}}$	μ-wave cavity resonance frequency	$2\pi \times 6.07\,\mathrm{GHz}$
ω_{c}	μ-wave cavity resonance frequency with static shift	$2\pi \times 6.07\,\mathrm{GHz}$
κ	full cavity linewidth	$2\pi \times 759\,\mathrm{kHz}$
κ_{ex}	external cavity linewidth	$2\pi \times 339\,\mathrm{kHz}$
κ_{in}	internal cavity linewidth	$2\pi \times 420\,\mathrm{kHz}$
$\bar{n}_{\mathrm{c}}$	mean intra-cavity photon number	up to 10^9
Ω_{m}	mechanical resonance frequency	$2\pi \times 1.45\,\mathrm{MHz}$
Γ_{m}	mechanical linewidth	$2\pi \times 2.59\,\mathrm{Hz}$
Γ_{eff}	electromech. broadened linewidth	Hz
x_{zpf}	mechanical zero point motion	$30\,\mathrm{fm}$
$\bar{n}_{\mathrm{m}}$	mean mechanical phonon occupation	down to 13
G	electromechanical coupling rate	$2\pi \times 36.3\,\mathrm{kHz/nm}$
g_0	electromechanical vacuum coupling	$2\pi \times 1.26\,\mathrm{Hz}$
ω_{d}	drive field frequency	GHz
ω_{p}	probe field frequency	GHz
Δ	detuning of probe from cavity resonance	mostly $\propto \pm\Omega_{\mathrm{m}}$
T_{c}	critical temperature of niobium	$9.2\,\mathrm{K}$
T_{eff}	effective mode temperature	$10^{-4} - 10^{-2}\,\mathrm{K}$
χ_{m}	mechanical susceptibility	$(\mathrm{kg\,Hz}^2)^{-1}$
χ_{eff}	effective mechanical susceptibility	$(\mathrm{kg\,Hz}^2)^{-1}$
S_{xx}	mechanical displacement spectral density	m^2/Hz
$S_{\varphi\varphi}$	cavity phase spectral density	$\mathrm{rad}^2/\mathrm{Hz}$
$S_{\omega\omega}$	cavity frequency spectral density	$\mathrm{Hz}^2/\mathrm{Hz}$
S_{PP}	detector power spectral density	$\mathrm{W/Hz}$
$S_{\mathrm{xx}}^{\mathrm{SQL}}$	standard quantum limit of mechanical displacement	$\hbar/m_{\mathrm{eff}}\Omega_{\mathrm{m}}\Gamma_{\mathrm{m}}$
α	Duffing parameter of the nanobeam	$1.99 \times 10^{11}\,\mathrm{N/m}^3$

A.3 Power dependent absorption of cryostat No.2

In Section 5.3.3 we demonstrate the cooling of the mechanical occupation to $\bar{n}_{\mathrm{m}} \approx 13$.

In the raw data we observed a faster decrease of the mechanical occupation and the imprecision noise than theory predicts. Figure A.1 shows the raw data of the mechanical occupation in a double logarithmic plot as a function of the intra-cavity photon number and extracted mechanical linewidth. Additionally, we show the imprecision noise as a function of the intra-cavity photon number. The solid lines in purple are plots of the theory according to Equation (5.46):

$$\bar{n}_{\mathrm{m}} = \frac{1}{1 + \frac{4g_0^2 \bar{n}_{\mathrm{c}}}{\Gamma_{\mathrm{m}}\kappa}} \cdot \frac{k_{\mathrm{B}}T}{\hbar\Omega_{\mathrm{m}}} + \frac{\kappa^2}{16\Omega_{\mathrm{m}}^2} = \frac{\Gamma_{\mathrm{m}}}{\Gamma_{\mathrm{eff}}} \cdot \frac{k_{\mathrm{B}}T}{\hbar\Omega_{\mathrm{m}}} + \frac{\kappa^2}{16\Omega_{\mathrm{m}}^2} \ . \tag{A.1}$$

This implies both curves decrease with P_{d}, since both $\bar{n}_{\mathrm{c}}$ and Γ_{eff} are proportional to P_{d}. The orange line for $S_{\mathrm{xx}}^{\mathrm{imp}}$ line is proportional to $1/P_{\mathrm{d}}$ as discussed in Section 5.1.2. Clearly, the data decreases faster than expected. To plot the dotted lines, we introduce an additional power dependency of $(P_{\mathrm{d}})^{0.2}$, meaning that instead of being decrease with
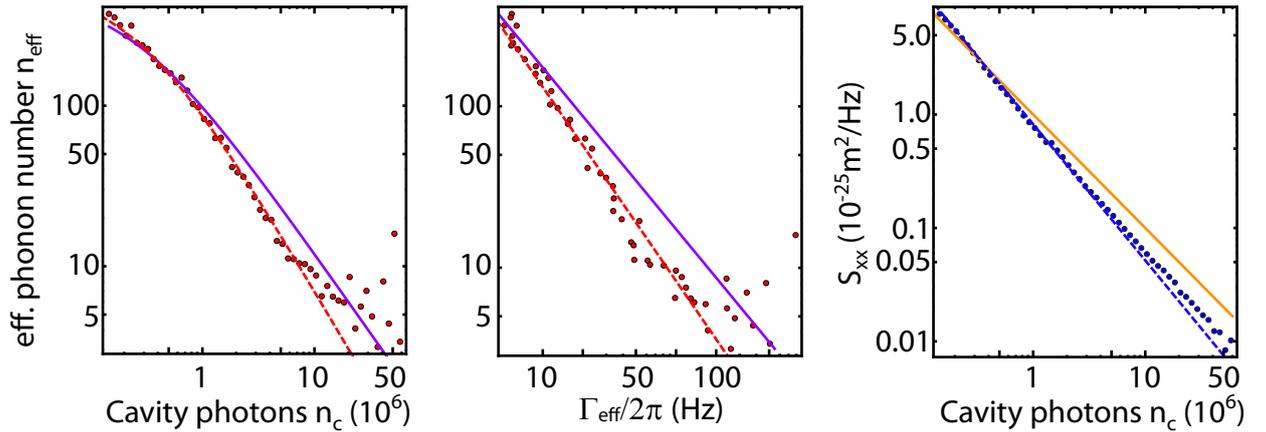
Figure A.1: Raw data of the curves presented in Figure 5.10 and Figure 5.12. A decrease faster than the theory pediction (red line) is clearly visible. Analysis of the data shows an additional decrease proportional $(P_\mathrm{d})^{0.2}$.

P_d as expected, the three data sets decrease with $(P_\mathrm{d})^{1.2} = P_\mathrm{d} \cdot (P_\mathrm{d})^{0.2}$. The curves show good agreement to the data.

We attribute this additional, higher power dependency to a power dependent loss of the cryostat wiring, whose origin is currently unknown and we correct the data to this loss, yielding the curves in Section 5.1.1. Currently we are testing the components of our setup to find the origin of the additional damping.

Above conclusion is based on the following considerations: The increase of Γ_eff is extracted from the data and follows the intra-cavity photon number and thus P_d as expected as shown in Figure 5.9c. Thus, the amplitudes obtained by measuring the mechanical displacement decrease faster for increasing drive power than expected, since only the amplitude and the linewidth of a Lorentzian contribute to its area, needed to exract $\langle \delta x^2 \rangle$ and thus $\bar{n}_\mathrm{m}$.

One option leading to a deviation in the recorded mechanical occupation is a drive tone not optimally detuned from the cavity resonance (either due to a misalignment or a shift of the cavity resonance). This results in a linewidth broadening that is weaker than at optimum detuning, what is easily verified in Figure 5.8 and Equation (5.19). Thus the expected decrease of the mechanical occupation is weaker as a function of drive power, in contradiction to our results.

A second option is additional photonic population of the cavity due to phase noise of the microwave source or heating of the structure. However, this causes an increase of the effective phonon number [110] and agrees to the observations discussed in the main text at high drive powers, but cannot cause above observations.

Further, we can exclude the input wiring. In all experiments performed with this cryostat, the predicted input power agrees well with the measured one. This only leaves the option of an power dependent loss channel in the cryostat output wiring. Note, that due to the results obtained in this thesis, we assume the sample to obey the optomechanical Hamiltonian in above considerations.
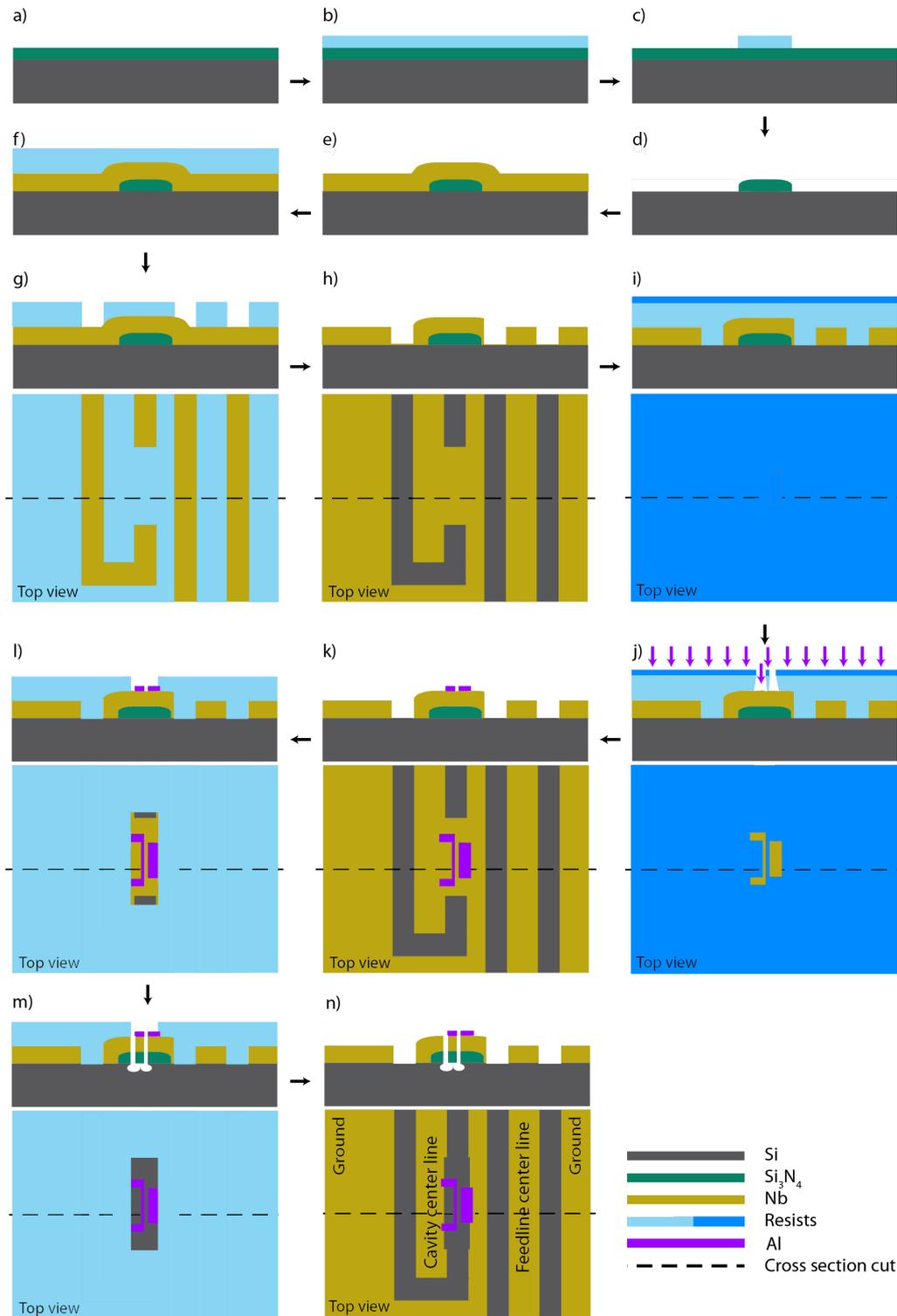
Figure A.2: Schematic of the different fabrication steps of the sample production at the WMI. For details, see the main text.

A.4   Sample production at WMI

The measurements presented in this theses are performed using a sample produced in the group of T. J. Kippenberg at the EPFL in Lausanne (Switzerland). Samples, similar to

the device analyzed in this thesis, were produced as well at the WMI. The main difference is that we produced three layer nanobeams incorporating one additional aluminum layer used as etch mask. Due to the better coupling parameters of the former samples, we preferred those.

For completeness, we present here the production steps of the samples made at the WMI, referring to Figure A.2:

a) A $10 \times 6 \, \text{mm}^2$ silicon substrate coated with a $100 \, \text{nm}$ thick highly tensile stressed silicon nitride layer (deposited by low pressure chemical vapour deposition) is cleaned with aceton and isopropanol.

b) Photoresist AZ 5214E (Microchemicals GmbH) is spincoated onto the sample with $8000 \, \text{rpm}$ resulting in a thickness of approximately $1 \, \mu\text{m}$ and baked on a hotplate at a temperature of $110 \, ^\circ\text{C}$ for $70 \, \text{s}$.

c) With optical lithography using a MJB3 Photomask Aligner from Süss MicroTec and a chrome mask, we remove all resist except at rectangles at the coordinates where the nanobeams will be patterned later:

We expose the resist with UV light outside the rectangulars using an lithography mask (exposure dose: $50 - 60 \, \text{mJ/cm}^2$). The structures are patterned by developing the resist in AZ726 MIF (Microchemicals GmbH) for $60 \, \text{s}$ followed by a rinse in destilled water, washing away the exposed areas.

d) A physical plasma etch in a Oxford 2000 reactive ion etching (RIE) chamber (RF power: $100 \, \text{W}$, ICP power: $50 \, \text{W}$, process pressure: $15 \, \text{mTorr}$, ignited at $30 \, \text{mTorr}$, ratio $\text{SF}_6\text{:Ar:O}_2\text{=50:10:0}$, duration: $60 \, \text{s}$) removes most of the silicon nitride down to a thickness of approx $10 \, \text{nm}$. Hereby, the remaining photoresist protects the Si_3N_4 layer at the later nanobeam position. The removal of the silicon nitride is necessary due to its high absorption of GHz radiation.

After removal of the photoresist with hot acetone followed by an isopropanol rinse, the sample is placed in a buffered oxide etch with AF 87.5/12.5 ($\text{NH}_4\text{F:HF=87.5:12.5}$) for $20 \, \text{min}$ to remove the remaining silicon nitride. This ensures a smooth silicon surface and thins the rectangles to approximately $70 \, \text{nm}$, while smoothing the corners to prevent edge desintegration in of the niobium layer. The etch process is stopped with destilled water followed by an isopropanol rinse.

e) An approx. $100 \, \text{nm}$ thick niobium layer is DC sputtered onto the sample in a high vacuum chamber (background pressure approx. $3 \times 10^{-9} \, \text{mbar}$).

f) The same photoresist as before is spincoated with $8000 \, \text{rpm}$ onto the sample and baked out at $110 \, ^\circ\text{C}$ for $70 \, \text{s}$ on a hotplate.

g) First we remove the resist edge bead to minimize the distance between sample and the chrome mask with the structure in the next step: The edge bead is exposed with a high dose of UV light (approx. $200 \, \text{mJ/cm}^2$) and developed for $60 \, \text{s}$ in AZ726 MIF). Then, the microwave resonators and the feedline are patterned into the photoresist by optical lithography (exposure dose: $50 - 60 \, \text{mJ/cm}^2$) followed by development in AZ726 MIF for $2 \, \text{min}$ followed by a rinse in destilled water. Note, that we leave

a connection between ground and center conductor above the silicon nitride pads to later structure the nanobeams. This is not the case for microwave cavities for precharacterization without a mechanical oscillator.

h) The pattern is transferred into the niobium with a physical RIE process (same parameters as above, duration 90 s. After the transfer, the sample is thoroughly cleaned in hot acetone followed by cleaning in isopropanol.

i) A double layer electron beam (ebeam) resist is spincoated to the sample:

First PMMA 459K A6 (MicroChem) is spincoated with 8000 rpm (thickness approximately 300 nm) and baked out on a hotplate at 175 °C for 10 min, then PMMA 950K A4 (MicroChem) is brought onto the sample with the same parameters (thickness approximately 200 nm). The double layer resist creates an undercut when developed after exposure to allow for lift-off processes.

j) Using ebeam lithography, the nanobeams including the clamps and rectangular pads together forming the coupling capacitances are patterened into the resist (acceleration voltage: 30 kV, dose: $100 - 250\,\mu\mathrm{C/cm^2}$). The clamps overlap with center conductor and the rectangular with the ground plane. The latter is necessary to account for not perfectly reproducible edges of gaps in the CPW structures produced by optical lithography. After development in AR-P 600-56 (Allresist) for 120 s followed by a rinse in isopropanol, an aluminum layer with a thickness of 25 nm serving as etch mask is deposited onto the sample by electron beam evaporation.

k) A lift-off in acetone at a temperature of 70 °C removes all resist and aluminum except at the nanobeam/pad position.

l) To pattern the nanobeams followed by their release, both in one RIE process, the surrounding niobium layer has to be protected. For this purpose we cover the whole sample with photoresist and open windows above the nanobeams in an optical lithography image reversal process (electron lithography would increase the aligment accuracy but the resists are not sufficiently resistant to RIE processes):

Again, the sample is spincoated with AZ 5214E at 8000 rpm and baked for only 50 s at 110 °C on a hotplate. After careful alignment using the same mask as in step c), we expose the resist with UV light outside the rectangulars (exposure dose: approx. $25\,\mathrm{mJ/cm^2}$), then we bake the sample at 130 °C for 2 min. Here the temperature is crucial, for older resists a temperature of 120 °C and the same time gives better results. A flat exposure (exposure dose: $350\,\mathrm{mJ/cm^2}$) of the full sample reverses the resist from a positive to a negative resist. We develop the structures by placing the sample in a mixture of AZ developer:$\mathrm{H_2O}$=1:1 for 160 s (AZ developer does not attack aluminum as most others do) followed by a rinse in destilled water.

m) A physical RIE process (same parameters as above, duration: 150 s) transfers the structure of the Al layer into the niobium and the silicon nitride below. An isotropic low power RIE process (RF power: 5 W, ICP power: 0 W, chamber pressure: 93 mTorr regulated by the hold valve position funciont, ignited at a RF power of 7 W for 30 s, $\mathrm{SF_6}$:Ar:$\mathrm{O_2}$=50:0:0, duration: 30 min) releases the beam. A false colored scanning
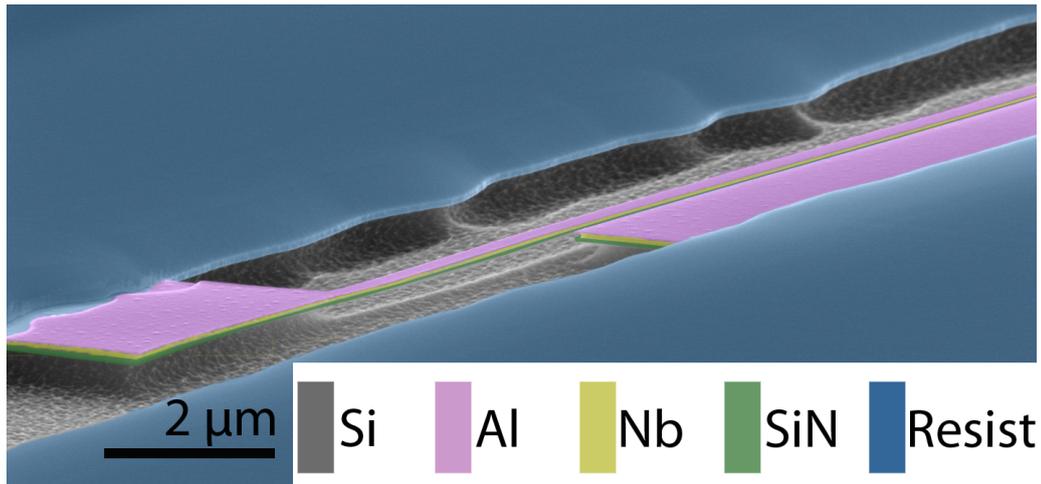
Figure A.3: False colored scanning electron microscope picture of the coupling region of a trilayer nanobeam. Grey represents silicon, pink represents aluminum, yellow represents niobium, green represents silicon nitride and blue represents photoresist to protect the microwave cavity.

electron microscope picture is shown in Figure A.3. Hereby the niobium layer of the nanobeam is slightly attacked as shown in Figure A.3.

n) The remaining photoresist is removed in hot acetone. This is the most critical step, since the nanobeam can stick to the bottom of the opposite patch due to capillary effects.

A false colored scanning electron microscope picture of a beam in a microwave cavity is shown in Figure A.3. The beam has a width of 250 nm, a length of 50 nm and a thickness of approximately 200 nm (70 nm silicon nitride, 100 nm niobium and 30 nm aluminum). The photoresist (indicated in blue) protects the rest of the niobium layer from the reactive ion etch process. The coupling distance between nanobeam and the pad connected to the ground plane is approximately 500 nm wide.

Unfortunately no nanobeams incorporating this three layer structure were precharacterized within the scope of this thesis.

Due to the critical removal of the photoresist in step n), we changed some processing parameters for future structures:

First, we use a 300 nm thick silicon oxide sacrificial layer between silicon substrate and silicon nitride layer. This demands to remove the unwanted silicon nitride completely by a RIE process in step d), since BHF removes silicon oxide with a high etch rate. All steps until m) remain the same. Step m) does not include the isotropic RIE process, only the nanobeam pattern is transferred into the niobium and the silicon nitride. Since the etch time is shorter, a sufficiently thick ebeam resist could replace the photoresist in step l), tests of this are currently performed. After the physical RIE process, the resist is removed with hot acetone. A treatment of the sample in Piranha for 2 min removes the Al mask. To suspend the nanobeam, the sample is placed in BHF for 2 min, removing the silicon oxide under the nanobeam. A further advantage is, that BHF does not affect the niobium. After the release, no additional cleaning steps are necessary, minimizing risks of breaking the beam.
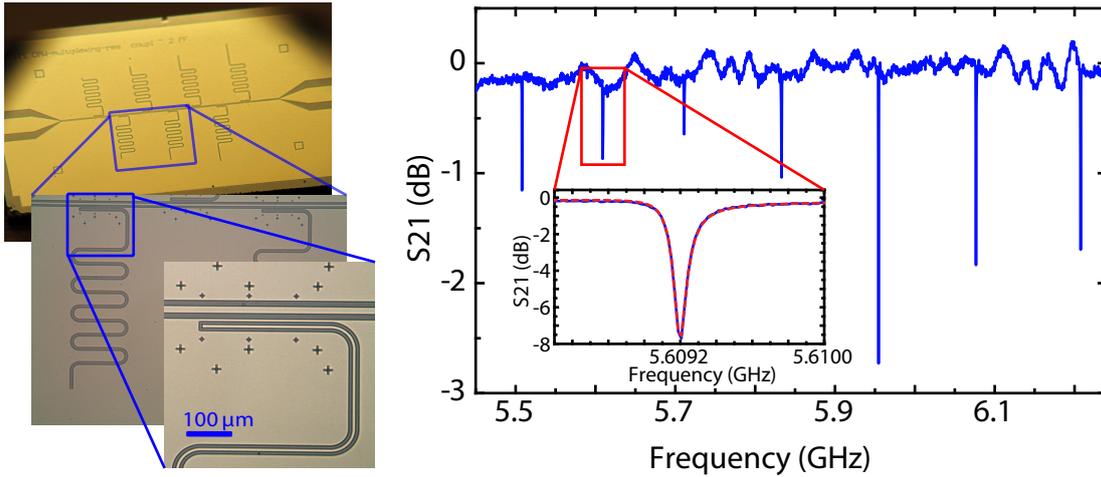
Figure A.4: Microscope pictures of a sample with seven μ-wave cavities, including a zoom to
one cavity and its coupling region is shown on the left. The right side shows a relative power
transmission spectrum of a multiplexed cavity at a temperature of 1.5 K. The inset shows a
zoom to the second cavity spectrum, the red dotted line is a fit to the data.

A.4.1 Multiplexed microwave resonators

We precharacterized multiplexed $\lambda/4$ microwave cavities made by optical lithography with
above parameters (see the left side of Figure A.4 for microscope pictures of one sample)
using an inset placed in pumped liquid helium at temperatures of approximately 1.5 K.
The relative power transmission was recorded with a vector network analyzer. A typical
spectrum for an input power of approximately $-27\,$dBm is shown on the right side of
Figure A.4. The eigenfrequencies are between $2\pi \times 5.5$ and $2\pi \times 6.2\,$GHz. The data is
normalized to the background of the cavity. A fit of Equation 4.5 to the second cavity with
a resonance frequency of $\widetilde{\omega}_c \approx 2\pi \times 5.609\,$GHz is shown in the inset of this Figure. We
measured quality factors up to 75000 at this temperature, making these structures well
suited to operate in an electromechanical configuration.

A.5 Fitting of a dispersive cavity response

In the transmission spectrum of the microwave cavity we observe a dispersive shift as
shown in Figure 4.7 and 6.5. We attribute this shift to interference with microwaves
traveling along the ground plane of the sample due to imperfect connection to ground.
This implies that the physical description of all phenomena is still valid, no extension of
the electromechanical system takes place. Technically, the interference is to first order
approximated by addition of a small, complex value $i\theta$ to the transmission spectrum,

$$t \rightarrow At + i\theta \ . \tag{A.2}$$

The factor A corresponds to an amplitude renormalization with $A^2 < 1$, since we measure
the transmission amplitude normalized to the input power. For example, Equation (4.5)
modifies to:

$$t(\omega) = A\frac{\kappa_{\text{in}}/2 + i(\omega - \widetilde{\omega}_c)}{\kappa/2 + i(\omega - \widetilde{\omega}_c)} + i\theta \ . \tag{A.3}$$

We estimate A by noting that at frequencies ω_{off} far outside the cavity ($|\omega_{\text{off}} - \omega_{\text{c}}| \gg \kappa$) the transmission amplitude is unity. This is true for the non dispersive transmission as well (the transmission spectrum is real far away from cavity resonance), we get $|t|^2 = \text{Re}(t)^2 + \text{Im}(t)^2 = A^2 + \theta^2$.

The dispersive shift is the reason why we do not observe the amplitude of the transmission peak for EMIT to reach unity. When fitting the data according to Equation (6.35), we have to take into account the renormalization A. Note, that fitting the unmodified model to the data gives approximately the same outcome for all fit parameters, showing that it covers the physical phenomena correctly. However, the fit does not agree to the data as well as the modified one (see for example Figure 7.7, where both models are fitted to the data).

Bibliography

[1] Maxwell, J. *Lehrbuch der Electricität und des Magnetismus.* Bd. 2 (J. Springer: Berlin, 1883).

[2] Lebedew, P. Untersuchungen über die Druckkräfte des Lichtes. *Ann. Phys.* **311**, 433–458 (1901).

[3] Nichols, E. F. & Hull, G. F. A Preliminary Communication on the Pressure of Heat and Light Radiation. *Phys. Rev. (Series I)* **13**, 307–320 (1901).

[4] Hänsch, T. & Schawlow, A. Cooling of gases by laser radiation. *Opt. Comm.* **13**, 68–69 (1975).

[5] Wineland, D. J. & Dehmelt, H. Proposed 1014 $\delta\nu/\nu$ laser fluorescence spectroscopy on Tl+ mono-ion oscillator III (side band cooling). *Bull. Am. Phys. Soc.* **20**, 637 (1979).

[6] Meschede, D., Walther, H. & Müller, G. One-Atom Maser. *Phys. Rev. Lett.* **54**, 551–554 (1985).

[7] Thompson, R. J., Rempe, G. & Kimble, H. J. Observation of normal-mode splitting for an atom in an optical cavity. *Phys. Rev. Lett.* **68**, 1132–1135 (1992).

[8] Mabuchi, H. & Doherty, A. C. Cavity Quantum Electrodynamics: Coherence in Context. *Science* **298**, 1372–1377 (2002).

[9] Walther, H., Varcoe, B. T. H., Englert, B.-G. & Becker, T. Cavity quantum electrodynamics. *Rep. Prog. Phys.* **69**, 1325 (2006).

[10] Monroe, C. Quantum information processing with atoms and photons. *Nature* **416**, 238–246 (2002).

[11] Buluta, I., Ashhab, S. & Nori, F. Natural and artificial atoms for quantum computation. *Rep. Prog. Phys.* **74**, 104401 (2011).

[12] Blais, A., Huang, R.-S., Wallraff, A., Girvin, S. M. & Schoelkopf, R. J. Cavity quantum electrodynamics for superconducting electrical circuits: An architecture for quantum computation. *Phys. Rev. A* **69**, 062320–14 (2004).

[13] Wallraff, A., Schuster, D. I., Blais, A., Frunzio, L., Huang, R.-S., Majer, J., Kumar, S., Girvin, S. M. & Schoelkopf, R. J. Strong coupling of a single photon to a superconducting qubit using circuit quantum electrodynamics. *Nature* **431**, 162–167 (2004).

[14] Schoelkopf, R. J. & Girvin, S. M. Wiring up quantum systems. *Nature* **451**, 664–669 (2008).

[15] Clarke, J. & Wilhelm, F. K. Superconducting quantum bits. *Nature* **453**, 1031–1042 (2008).

[16] Niemczyk, T., Deppe, F., Huebl, H., Menzel, E. P., Hocke, F., Schwarz, M. J., Garcia-Ripoll, J. J., Zueco, D., Hummer, T., Solano, E., Marx, A. & Gross, R. Circuit quantum electrodynamics in the ultrastrong-coupling regime. *Nat. Phys.* **6**, 772–776 (2010).

[17] Ladd, T. D., Jelezko, F., Laflamme, R., Nakamura, Y., Monroe, C. & O'Brien, J. L. Quantum computers. *Nature* **464**, 45–53 (2010).

[18] Petersson, K. D., Smith, C. G., Anderson, D., Atkinson, P., Jones, G. A. C. & Ritchie, D. A. Charge and Spin State Readout of a Double Quantum Dot Coupled to a Resonator. *Nano Lett.* **10**, 2789–2793 (2010).

[19] Petersson, K. D., McFaul, L. W., Schroer, M. D., Jung, M., Taylor, J. M., Houck, A. A. & Petta, J. R. Circuit quantum electrodynamics with a spin qubit. *Nature* **490**, 380–383 (2012).

[20] Frey, T., Leek, P. J., Beck, M., Blais, A., Ihn, T., Ensslin, K. & Wallraff, A. Dipole Coupling of a Double Quantum Dot to a Microwave Resonator. *Phys. Rev. Lett.* **108**, 046807 (2012).

[21] Delbecq, M., Bruhat, L., Viennot, J., Datta, S., Cottet, A. & Kontos, T. Photon-mediated interaction between distant quantum dot circuits. *Nat. Commun.* **4**, 1400 (2013).

[22] Schuster, D. I., Sears, A. P., Ginossar, E., DiCarlo, L., Frunzio, L., Morton, J. J. L., Wu, H., Briggs, G. A. D., Buckley, B. B., Awschalom, D. D. & Schoelkopf, R. J. High-Cooperativity Coupling of Electron-Spin Ensembles to Superconducting Cavities. *Phys. Rev. Lett.* **105**, 140501 (2010).

[23] Wu, H., George, R. E., Wesenberg, J. H., Mølmer, K., Schuster, D. I., Schoelkopf, R. J., Itoh, K. M., Ardavan, A., Morton, J. J. L. & Briggs, G. A. D. Storage of Multiple Coherent Microwave Excitations in an Electron Spin Ensemble. *Phys. Rev. Lett.* **105**, 140503 (2010).

[24] Kubo, Y., Ong, F. R., Bertet, P., Vion, D., Jacques, V., Zheng, D., Dréau, A., Roch, J.-F., Auffeves, A., Jelezko, F., Wrachtrup, J., Barthe, M. F., Bergonzo, P. & Esteve, D. Strong Coupling of a Spin Ensemble to a Superconducting Resonator. *Phys. Rev. Lett.* **105**, 140502 (2010).

[25] Amsüss, R., Koller, C., Nöbauer, T., Putz, S., Rotter, S., Sandner, K., Schneider, S., Schramböck, M., Steinhauser, G., Ritsch, H., Schmiedmayer, J. & Majer, J. Cavity QED with Magnetically Coupled Collective Spin States. *Phys. Rev. Lett.* **107**, 060502 (2011).

[26] Bushev, P., Feofanov, A. K., Rotzinger, H., Protopopov, I., Cole, J. H., Wilson, C. M., Fischer, G., Lukashenko, A. & Ustinov, A. V. Ultralow-power spectroscopy of a rare-earth spin ensemble using a superconducting resonator. *Phys. Rev. B* **84**, 060501 (2011).

[27] Huebl, H., Zollitsch, C., Lotze, J., Hocke, F., Greifenstein, M., Marx, A., Gross, R. & Goennenwein, S. T. B. High cooperativity in coupled microwave resonator ferrimagnetic insulator hybrids. *ArXiv:1207.6039* (2012).

[28] Ranjan, V., de Lange, G., Schutjens, R., Debelhoir, T., Groen, J. P., Szombati, D., Thoen, D. J., Klapwijk, T. M., Hanson, R. & DiCarlo, L. Probing Dynamics of an Electron-Spin Ensemble via a Superconducting Resonator. *Phys. Rev. Lett.* **110**, 067004 (2013).

[29] Probst, S., Rotzinger, H., Wünsch, S., Jung, P., Jerger, M., Siegel, M., Ustinov, A. V. & Bushev, P. A. Anisotropic Rare-Earth Spin Ensemble Strongly Coupled to a Superconducting Resonator. *Phys. Rev. Lett.* **110**, 157001 (2013).

[30] Zhu, X., Saito, S., Kemp, A., Kakuyanagi, K., Karimoto, S., Nakano, H., Munro, W. J., Tokura, Y., Everitt, M. S., Nemoto, K., Kasu, M., Mizuochi, N. & Semba, K. Coherent coupling of a superconducting flux qubit to an electron spin ensemble in diamond. *Nature* **478**, 221–224 (2011).

[31] Kubo, Y., Grezes, C., Dewes, A., Umeda, T., Isoya, J., Sumiya, H., Morishita, N., Abe, H., Onoda, S., Ohshima, T., Jacques, V., Dréau, A., Roch, J.-F., Diniz, I., Auffeves, A., Vion, D., Esteve, D. & Bertet, P. Hybrid Quantum Circuit with a Superconducting Qubit Coupled to a Spin Ensemble. *Phys. Rev. Lett.* **107**, 220501 (2011).

[32] O'Connell, A. D., Hofheinz, M., Ansmann, M., Bialczak, R. C., Lenander, M., Lucero, E., Neeley, M., Sank, D., Wang, H., Weides, M., Wenner, J., Martinis, J. M. & Cleland, A. N. Quantum ground state and single-phonon control of a mechanical resonator. *Nature* **464**, 697–703 (2010).

[33] LaHaye, M. D., Suh, J., Echternach, P. M., Schwab, K. C. & Roukes, M. L. Nanomechanical measurements of a superconducting qubit. *Nature* **459**, 960–964 (2009).

[34] Suh, J., LaHaye, M. D., Echternach, P. M., Schwab, K. C. & Roukes, M. L. Parametric Amplification and Back-Action Noise Squeezing by a Qubit-Coupled Nanoresonator. *Nano Lett.* **10**, 3990–3994 (2010).

[35] Etaki, S., Poot, M., Mahboob, I., Onomitsu, K., Yamaguchi, H. & van der Zant, H. S. J. Motion detection of a micromechanical resonator embedded in a d.c. SQUID. *Nat. Phys.* **4**, 785–788 (2008).

[36] Pirkkalainen, J.-M., Cho, S. U., Li, J., Paraoanu, G. S., Hakonen, P. J. & Sillanpää, M. A. Hybrid circuit cavity quantum electrodynamics with a micromechanical resonator. *Nature* **494**, 211–215 (2013).

[37] Palomaki, T. A., Harlow, J. W., Teufel, J. D., Simmonds, R. W. & Lehnert, K. W. Coherent state transfer between itinerant microwave fields and a mechanical oscillator. *Nature* **495**, 210–214 (2013).

[38] Tian, L. & Wang, H. Optical wavelength conversion of quantum states with optomechanics. *Phys. Rev. A* **82**, 053806 (2010).

[39] Regal, C. A. & Lehnert, K. W. From cavity electromechanics to cavity optomechanics. *J. Phys.: Conf. Ser.* **264**, 012025 (2011).

[40] Safavi-Naeini, A. H. & Painter, O. Proposal for an optomechanical traveling wave phonon–photon translator. *N. J. Phys.* **13**, 013017 (2011).

[41] Wang, Y.-D. & Clerk, A. A. Using Interference for High Fidelity Quantum State Transfer in Optomechanics. *Phys. Rev. Lett.* **108**, 153603 (2012).

[42] Tian, L. Adiabatic State Conversion and Pulse Transmission in Optomechanical Systems. *Phys. Rev. Lett.* **108**, 153604 (2012).

[43] Braginsky, V. B., Manukin, A. B. & Y., T. M. Investigation of dissipative pondermotive effects of eletromagnetic radiation. *Sov. Phys. JETP* **31**, 829 (1970).

[44] Braginsky, V. B., Vorontsov, Y. I. & Thorne, K. S. Quantum Nondemolition Measurements. *Science* **209**, 547–557 (1980).

[45] Arcizet, O., Cohadon, P.-F., Briant, T., Pinard, M., Heidmann, A., Mackowski, J.-M., Michel, C., Pinard, L., Francais, O. & Rousseau, L. High-Sensitivity Optical Monitoring of a Micromechanical Resonator with a Quantum-Limited Optomechanical Sensor. *Phys. Rev. Lett.* **97**, 133601 (2006).

[46] Schliesser, A., Anetsberger, G., Rivière, R., Arcizet, O. & Kippenberg, T. J. High-sensitivity monitoring of micromechanical vibration using optical whispering gallery mode resonators. *N. J. Phys.* **10**, 095015–19 (2008).

[47] Schliesser, A., Arcizet, O., Rivière, R., Anetsberger, G. & Kippenberg, T. J. Resolved-sideband cooling and position measurement of a micromechanical oscillator close to the Heisenberg uncertainty limit. *Nat. Phys.* **5**, 509–514 (2009).

[48] Teufel, J., Donner, T., Castellanos-Beltran, M. A., Harlow, J. W. & Lehnert, K. W. Nanomechanical motion measured with an imprecision below that at the standard quantum limit. *Nat. Nano* **4**, 820–823 (2009).

[49] Anetsberger, G., Gavartin, E., Arcizet, O., Unterreithmeier, Q. P., Weig, E. M., Gorodetsky, M. L., Kotthaus, J. P. & Kippenberg, T. J. Measuring nanomechanical motion with an imprecision below the standard quantum limit. *Phys. Rev. A* **82**, 061804 (2010).

[50] Caves, C. M. Quantum-mechanical noise in an interferometer. *Phys. Rev. D* **23**, 1693 (1981).

[51] Cuthbertson, B. D., Tobar, M. E., Ivanov, E. N. & Blair, D. G. Parametric back-action effects in a high-Q cyrogenic sapphire transducer. *Rev. Sci. Instrum.* **67**, 2435–2442 (1996).

[52] Dorsel, A., McCullen, J. D., Meystre, P., Vignes, E. & Walther, H. Optical Bistability and Mirror Confinement Induced by Radiation Pressure. *Phys. Rev. Lett.* **51**, 1550 (1983).

[53] Linthorne, N. P., Veitch, P. J. & Blair, D. G. Interaction of a parametric transducer with a resonant bar gravitational radiation detector. *J. Phys. D: App. Phys.* **23**, 1 (1990).

[54] Jacobs, K., Tombesi, P., Collett, M. J. & Walls, D. F. Quantum-nondemolition measurement of photon number using radiation pressure. *Phys. Rev. A* **49**, 1961–1966 (1994).

[55] Pinard, M., Fabre, C. & Heidmann, A. Quantum-nondemolition measurement of light by a piezoelectric crystal. *Phys. Rev. A* **51**, 2443–2449 (1995).

[56] Fabre, C., Pinard, M., Bourzeix, S., Heidmann, A., Giacobino, E. & Reynaud, S. Quantum-noise reduction using a cavity with a movable mirror. *Phys. Rev. A* **49**, 1337–1343 (1994).

[57] Mancini, S. & Tombesi, P. Quantum noise reduction by radiation pressure. *Phys. Rev. A* **49**, 4055–4065 (1994).

[58] Bose, S., Jacobs, K. & Knight, P. L. Preparation of nonclassical states in cavities with a moving mirror. *Phys. Rev. A* **56**, 4175–4186 (1997).

[59] Mancini, S., Man'ko, V. I. & Tombesi, P. Ponderomotive control of quantum macroscopic coherence. *Phys. Rev. A* **55**, 3042–3050 (1997).

[60] Mancini, S., Vitali, D. & Tombesi, P. Optomechanical Cooling of a Macroscopic Oscillator by Homodyne Feedback. *Phys. Rev. Lett.* **80**, 688–691 (1998).

[61] Cohadon, P. F., Heidmann, A. & Pinard, M. Cooling of a Mirror by Radiation Pressure. *Phys. Rev. Lett.* **83**, 3174–3177 (1999).

[62] Kleckner, D. & Bouwmeester, D. Sub-kelvin optical cooling of a micromechanical resonator. *Nature* **444**, 75–78 (2006).

[63] Poggio, M., Degen, C. L., Mamin, H. J. & Rugar, D. Feedback Cooling of a Cantilever's Fundamental Mode below 5 mK. *Phys. Rev. Lett.* **99**, 017201 (2007).

[64] Carmon, T., Rokhsari, H., Yang, L., Kippenberg, T. J. & Vahala, K. J. Temporal Behavior of Radiation-Pressure-Induced Vibrations of an Optical Microcavity Phonon Mode. *Phys. Rev. Lett.* **94**, 223902 (2005).

[65] Kippenberg, T. J., Rokhsari, H., Carmon, T., Scherer, A. & Vahala, K. J. Analysis of Radiation-Pressure Induced Mechanical Oscillation of an Optical Microcavity. *Phys. Rev. Lett.* **95**, 033901 (2005).

[66] Rokhsari, H., Kippenberg, T., Carmon, T. & Vahala, K. Theoretical and experimental study of radiation pressure-induced mechanical oscillations (parametric instability) in optical microcavities. *IEEE J. Sel. Top. Quant. Electron.* **12**, 96–107 (2006).

[67] Brown, K. R., Britton, J., Epstein, R. J., Chiaverini, J., Leibfried, D. & Wineland, D. J. Passive Cooling of a Micromechanical Oscillator with a Resonant Electric Circuit. *Phys. Rev. Lett.* **99**, 137205 (2007).

[68] Truitt, P. A., Hertzberg, J. B., Huang, C. C., Ekinci, K. L. & Schwab, K. C. Efficient and Sensitive Capacitive Readout of Nanomechanical Resonator Arrays. *Nano Lett.* **7**, 120–126 (2007).

[69] Regal, C. A., Teufel, J. D. & Lehnert, K. W. Measuring nanomechanical motion with a microwave cavity interferometer. *Nat. Phys.* **4**, 555–560 (2008).

[70] Murch, K. W., Moore, K. L., Gupta, S. & Stamper-Kurn, D. M. Observation of quantum-measurement backaction with an ultracold atomic gas. *Nat. Phys.* **4**, 561–564 (2008).

[71] Brennecke, F., Ritter, S., Donner, T. & Esslinger, T. Cavity Optomechanics with a Bose-Einstein Condensate. *Science* **322**, 235–238 (2008).

[72] Aspelmeyer, M., Kippenberg, T. J. & Marquardt, F. Cavity optomechanics. *ArXiv:1303.0733* (2013).

[73] Cole, G. D., Wilson-Rae, I., Werbach, K., Vanner, M. R. & Aspelmeyer, M. Phonon-tunnelling dissipation in mechanical resonators. *Nat. Commun.* **2**, 231 (2011).

[74] Kuhn, A. G., Bahriz, M., Ducloux, O., Chartier, C., Le Traon, O., Briant, T., Cohadon, P.-F., Heidmann, A., Michel, C., Pinard, L. & Flaminio, R. A micropillar for cavity optomechanics. *Appl. Phys. Lett.* **99**, 121103–3 (2011).

[75] Verhagen, E., Deleglise, S., Weis, S., Schliesser, A. & Kippenberg, T. J. Quantum-coherent coupling of a mechanical oscillator to an optical cavity mode. *Nature* **482**, 63–67 (2012).

[76] Park, Y.-S. & Wang, H. Resolved-sideband and cryogenic cooling of an optomechanical resonator. *Nat. Phys.* **5**, 489–493 (2009).

[77] Thompson, J. D., Zwickl, B. M., Jayich, A. M., Marquardt, F., Girvin, S. M. & Harris, J. G. E. Strong dispersive coupling of a high-finesse cavity to a micromechanical membrane. *Nature* **452**, 72–75 (2008).

[78] Chan, J., Mayer Alegre, T. P., Safavi-Naeini, A. H., Hill, J. T., Krause, A., Groblacher, S., Aspelmeyer, M. & Painter, O. Laser cooling of a nanomechanical oscillator into its quantum ground state. *Nature* **478**, 89–92 (2011).

[79] Mahboob, I., Nishiguchi, K., Okamoto, H. & Yamaguchi, H. Phonon-cavity electromechanics. *Nat. Phys.* **8**, 387–392 (2012).

[80] Teufel, J. D., Li, D., Allman, M. S., Cicak, K., Sirois, A. J., Whittaker, J. D. & Simmonds, R. W. Circuit cavity electromechanics in the strong-coupling regime. *Nature* **471**, 204–208 (2011).

[81] Faust, T., Krenn, P., Manus, S., Kotthaus, J. & Weig, E. Microwave cavity-enhanced transduction for plug and play nanomechanics at room temperature. *Nat. Commun.* **3**, 728 (2012).

[82] Hocke, F., Zhou, X., Schliesser, A., Kippenberg, T. J., Huebl, H. & Gross, R. Electromechanically induced absorption in a circuit nano-electromechanical system. *N. J. Phys.* **14**, 123037 (2012).

[83] Strain, K. A. & Shapiro, B. N. Damping and local control of mirror suspensions for laser interferometric gravitational wave detectors. *Rev. Sci. Instrum.* **83**, 044501–9 (2012).

[84] Brooks, D. W. C., Botter, T., Schreppler, S., Purdy, T. P., Brahms, N. & Stamper-Kurn, D. M. Non-classical light generated by quantum-noise-driven cavity optomechanics. *Nature* **488**, 476–480 (2012).

[85] Purdy, T. P., Peterson, R. W., Yu, P.-L. & Regal, C. A. Cavity optomechanics with Si 3 N 4 membranes at cryogenic temperatures. *N. J. Phys.* **14**, 115021 (2012).

[86] Chan, J., Safavi-Naeini, A. H., Hill, J. T., Meenehan, S. & Painter, O. Optimized optomechanical crystal cavity with acoustic radiation shield. *Appl. Phys. Lett.* **101**, 081115–4 (2012).

[87] Zhou, X., Hocke, F., Schliesser, A., Marx, A., Huebl, H., Gross, R. & Kippenberg, T. J. Slowing, advancing and switching of microwave signals using circuit nanoelectromechanics. *Nat. Phys.* **9**, 179–184 (2013).

[88] Kippenberg, T. J. & Vahala, K. J. Cavity Opto-Mechanics. *Opt. Express* **15**, 17172–17205 (2007).

[89] Kippenberg, T. J. & Vahala, K. J. Cavity Optomechanics: Back-Action at the Mesoscale. *Science* **321**, 1172–1176 (2008).

[90] Florian Marquardt, S. M. G. Optomechanics. *Physics* **2**, 40 (2009).

[91] Aspelmeyer, M., Gröblacher, S., Hammerer, K. & Kiesel, N. Quantum optomechanics - throwing a glance [Invited]. *J. Opt. Soc. Am. B* **27**, A189–A197 (2010).

[92] Aspelmeyer, M., Meystre, P. & Schwab, K. Quantum optomechanics. *Phys. Today* **65**, 29–35 (2012).

[93] Braginsky, V., Strigin, S. & Vyatchanin, S. Parametric oscillatory instability in Fabry-Perot interferometer. *Phys. Lett. A* **287**, 331–338 (2001).

[94] Marquardt, F., Harris, J. G. E. & Girvin, S. M. Dynamical Multistability Induced by Radiation Pressure in High-Finesse Micromechanical Optical Cavities. *Phys. Rev. Lett.* **96**, 103901 (2006).

[95] Ludwig, M., Kubala, B. & Marquardt, F. The optomechanical instability in the quantum regime. *N. J. Phys.* **10**, 095013 (2008).

[96] Grudinin, I. S., Lee, H., Painter, O. & Vahala, K. J. Phonon Laser Action in a Tunable Two-Level System. *Phys. Rev. Lett.* **104**, 083901 (2010).

[97] Khurgin, J. B., Pruessner, M. W., Stievater, T. H. & Rabinovich, W. S. Laser-Rate-Equation Description of Optomechanical Oscillators. *Phys. Rev. Lett.* **108**, 223904 (2012).

[98] Suh, J., Shaw, M. D., LeDuc, H. G., Weinstein, A. J. & Schwab, K. C. Thermally Induced Parametric Instability in a Back-Action Evading Measurement of a Micromechanical Quadrature near the Zero-Point Level. *Nano Lett.* **12**, 6260–6265 (2012).

[99] Mahboob, I., Nishiguchi, K., Fujiwara, A. & Yamaguchi, H. Phonon Lasing in an Electromechanical Resonator. *Phys. Rev. Lett.* **110**, 127202 (2013).

[100] Arcizet, O., Cohadon, P.-F., Briant, T., Pinard, M. & Heidmann, A. Radiation-pressure cooling and optomechanical instability of a micromirror. *Nature* **444**, 71–74 (2006).

[101] Gigan, S., Bohm, H. R., Paternostro, M., Blaser, F., Langer, G., Hertzberg, J. B., Schwab, K. C., Bauerle, D., Aspelmeyer, M. & Zeilinger, A. Self-cooling of a micromirror by radiation pressure. *Nature* **444**, 67–70 (2006).

[102] Schliesser, A., Del'Haye, P., Nooshi, N., Vahala, K. J. & Kippenberg, T. J. Radiation Pressure Cooling of a Micromechanical Oscillator Using Dynamical Backaction. *Phys. Rev. Lett.* **97**, 243905 (2006).

[103] Marquardt, F., Chen, J. P., Clerk, A. A. & Girvin, S. M. Quantum Theory of Cavity-Assisted Sideband Cooling of Mechanical Motion. *Phys. Rev. Lett.* **99**, 093902 (2007).

[104] Wilson-Rae, I., Nooshi, N., Zwerger, W. & Kippenberg, T. J. Theory of Ground State Cooling of a Mechanical Oscillator Using Dynamical Backaction. *Phys. Rev. Lett.* **99**, 093901 (2007).

[105] Dobrindt, J. M., Wilson-Rae, I. & Kippenberg, T. J. Parametric Normal-Mode Splitting in Cavity Optomechanics. *Phys. Rev. Lett.* **101**, 263602 (2008).

[106] Genes, C., Vitali, D., Tombesi, P., Gigan, S. & Aspelmeyer, M. Ground-state cooling of a micromechanical oscillator: Comparing cold damping and cavity-assisted cooling schemes. *Phys. Rev. A* **77**, 033804 (2008).

[107] Rabl, P., Genes, C., Hammerer, K. & Aspelmeyer, M. Phase-noise induced limitations on cooling and coherent evolution in optomechanical systems. *Phys. Rev. A* **80**, 063819–10 (2009).

[108] Phelps, G. A. & Meystre, P. Laser phase noise effects on the dynamics of optomechanical resonators. *Phys. Rev. A* **83**, 063838 (2011).

[109] Gröblacher, S., Hertzberg, J. B., Vanner, M. R., Cole, G. D., Gigan, S., Schwab, K. C. & Aspelmeyer, M. Demonstration of an ultracold micro-optomechanical oscillator in a cryogenic cavity. *Nat. Phys.* **5**, 485–488 (2009).

[110] Rocheleau, T., Ndukum, T., Macklin, C., Hertzberg, J. B., Clerk, A. A. & Schwab, K. C. Preparation and detection of a mechanical resonator near the ground state of motion. *Nature* **463**, 72–75 (2010).

[111] Rivière, R., Deléglise, S., Weis, S., Gavartin, E., Arcizet, O., Schliesser, A. & Kippenberg, T. J. Optomechanical sideband cooling of a micromechanical oscillator close to the quantum ground state. *Phys. Rev. A* **83**, 063835–9 (2011).

[112] Gröblacher, S., Hammerer, K., Vanner, M. R. & Aspelmeyer, M. Observation of strong coupling between a micromechanical resonator and an optical cavity field. *Nature* **460**, 724–727 (2009).

[113] Teufel, J. D., Donner, T., Li, D., Harlow, J. W., Allman, M. S., Cicak, K., Sirois, A. J., Whittaker, J. D., Lehnert, K. W. & Simmonds, R. W. Sideband cooling of micromechanical motion to the quantum ground state. *Nature* **475**, 359–363 (2011).

[114] Safavi-Naeini, A. H., Chan, J., Hill, J. T., Alegre, T. P. M., Krause, A. & Painter, O. Observation of Quantum Motion of a Nanomechanical Resonator. *Phys. Rev. Lett.* **108**, 033602 (2012).

[115] Weis, S., Rivière, R., Deléglise, S., Gavartin, E., Arcizet, O., Schliesser, A. & Kippenberg, T. J. Optomechanically Induced Transparency. *Science* **330**, 1520–1523 (2010).

[116] Safavi-Naeini, A. H., Alegre, T. P. M., Chan, J., Eichenfield, M., Winger, M., Lin, Q., Hill, J. T., Chang, D. E. & Painter, O. Electromagnetically induced transparency and slow light with optomechanics. *Nature* **472**, 69–73 (2011).

[117] Agarwal, G. S. & Huang, S. Electromagnetically induced transparency in mechanical effects of light. *Phys. Rev. A* **81**, 041803 (2010).

[118] Boller, K.-J., Imamolu, A. & Harris, S. E. Observation of electromagnetically induced transparency. *Phys. Rev. Lett.* **66**, 2593 (1991).

[119] Lezama, A., Barreiro, S. & Akulshin, A. M. Electromagnetically induced absorption. *Phys. Rev. A* **59**, 4732–4735 (1999).

[120] Massel, F., Heikkilaä, T. T., Pirkkalainen, J.-M., Cho, S. U., Saloniemi, H., Hakonen, P. J. & Sillanpää, M. A. Microwave amplification with nanomechanical resonators. *Nature* **480**, 351–354 (2011).

[121] Hau, L. V., Harris, S. E., Dutton, Z. & Behroozi, C. H. Light speed reduction to 17 metres per second in an ultracold atomic. *Nature* **397**, 594–598 (1999).

[122] Kash, M. M., Sautenkov, V. A., Zibrov, A. S., Hollberg, L., Welch, G. R., Lukin, M. D., Rostovtsev, Y., Fry, E. S. & Scully, M. O. Ultraslow Group Velocity and Enhanced Nonlinear Optical Effects in a Coherently Driven Hot Atomic Gas. *Phys. Rev. Lett.* **82**, 5229–5232 (1999).

[123] Budker, D., Kimball, D. F., Rochester, S. M. & Yashchuk, V. V. Nonlinear Magneto-optics and Reduced Group Velocity of Light in Atomic Vapor with Slow Ground State Relaxation. *Phys. Rev. Lett.* **83**, 1767–1770 (1999).

[124] Liu, C., Dutton, Z., Behroozi, C. H. & Hau, L. V. Observation of coherent optical information storage in an atomic medium using halted light pulses. *Nature* **409**, 490–493 (2001).

[125] Chang, D. E., Safavi-Naeini, A. H., Hafezi, M. & Painter, O. Slowing and stopping light using an optomechanical crystal array. *N. J. Phys.* **13**, 023003 (2011).

[126] Hofer, S. G., Wieczorek, W., Aspelmeyer, M. & Hammerer, K. Quantum entanglement and teleportation in pulsed cavity optomechanics. *Phys. Rev. A* **84**, 052327 (2011).

[127] Machnes, S., Cerrillo, J., Aspelmeyer, M., Wieczorek, W., Plenio, M. B. & Retzker, A. Pulsed Laser Cooling for Cavity Optomechanical Resonators. *Phys. Rev. Lett.* **108**, 153601 (2012).

[128] Vanner, M. R., Pikovski, I., Cole, G. D., Kim, M. S., Brukner, C., Hammerer, K., Milburn, G. J. & Aspelmeyer, M. Pulsed quantum optomechanics. *Proc. Nat. Acad. Sci.* **108**, 16182–16187 (2011).

[129] Vanner, M. R., Hofer, J., Cole, G. D. & Aspelmeyer, M. Experimental Pulsed Quantum Optomechanics. *ArXiv:1211.7036* (2012).

[130] Zhang, J., Peng, K. & Braunstein, S. L. Quantum-state transfer from light to macroscopic oscillators. *Phys. Rev. A* **68**, 013808 (2003).

[131] Fiore, V., Yang, Y., Kuzyk, M. C., Barbour, R., Tian, L. & Wang, H. Storing Optical Information as a Mechanical Excitation in a Silica Optomechanical Resonator. *Phys. Rev. Lett.* **107**, 133601 (2011).

[132] Hill, J. T., Safavi-Naeini, A. H., Chan, J. & Painter, O. Coherent optical wavelength conversion via cavity optomechanics. *Nat. Commun.* **3**, 1196 (2012).

[133] Dong, C., Fiore, V., Kuzyk, M. C. & Wang, H. Optomechanical Dark Mode. *Science* **338**, 1609–1613 (2012).

[134] Poot, M. & van der Zant, H. S. Mechanical systems in the quantum regime. *Phys. Rep.* **511**, 273–335 (2012).

[135] Craighead, H. G. Nanoelectromechanical Systems. *Science* **290**, 1532–1535 (2000).

[136] Blencowe, M. P. Nanoelectromechanical Systems. *Contemp. Phys.* **46**, 249–264 (2005).

[137] Ekinci, K. L. & Roukes, M. L. Nanoelectromechanical systems. *Rev. Sci. Instrum.* **76**, 061101–12 (2005).

[138] Carr, D. W., Evoy, S., Sekaric, L., Craighead, H. G. & Parpia, J. M. Measurement of mechanical resonance and losses in nanometer scale silicon wires. *Appl. Phys. Lett.* **75**, 920–922 (1999).

[139] Sekaric, L., Carr, D. W., Evoy, S., Parpia, J. M. & Craighead, H. G. Nanomechanical resonant structures in silicon nitride: fabrication, operation and dissipation issues. *Sens. Act. A: Phys.* **101**, 215–219 (2002).

[140] Mohanty, P., Harrington, D. A., Ekinci, K. L., Yang, Y. T., Murphy, M. J. & Roukes, M. L. Intrinsic dissipation in high-frequency micromechanical resonators. *Phys. Rev. B* **66**, 085416 (2002).

[141] Photiadis, D. M. & Judge, J. A. Attachment losses of high Q oscillators. *Appl. Phys. Lett.* **85**, 482–484 (2004).

[142] Verbridge, S. S., Shapiro, D. F., Craighead, H. G. & Parpia, J. M. Macroscopic Tuning of Nanomechanics: Substrate Bending for Reversible Control of Frequency and Quality Factor of Nanostring Resonators. *Nano Lett.* **7**, 1728–1735 (2007).

[143] Remus, L. G., Blencowe, M. P. & Tanaka, Y. Damping and decoherence of a nanomechanical resonator due to a few two-level systems. *Phys. Rev. B* **80**, 174103 (2009).

[144] Schmid, S., Jensen, K. D., Nielsen, K. H. & Boisen, A. Damping mechanisms in high-Q micro and nanomechanical string resonators. *Phys. Rev. B* **84**, 165307 (2011).

[145] Karabalin, R. B., Villanueva, L. G., Matheny, M. H., Sader, J. E. & Roukes, M. L. Stress-Induced Variations in the Stiffness of Micro- and Nanocantilever Beams. *Phys. Rev. Lett.* **108**, 236101 (2012).

[146] Verbridge, S. S., Craighead, H. G. & Parpia, J. M. A megahertz nanomechanical resonator with room temperature quality factor over a million. *Appl. Phys. Lett.* **92**, 013112–3 (2008).

[147] Svitelskiy, O., Sauer, V., Liu, N., Cheng, K.-M., Finley, E., Freeman, M. R. & Hiebert, W. K. Pressurized Fluid Damping of Nanoelectromechanical Systems. *Phys. Rev. Lett.* **103**, 244501 (2009).

[148] Zener, C. Internal Friction in Solids. I. Theory of Internal Friction in Reeds. *Phys. Rev.* **52**, 230–235 (1937).

[149] Lifshitz, R. & Roukes, M. L. Thermoelastic damping in micro- and nanomechanical systems. *Phys. Rev. B* **61**, 5600–5609 (2000).

[150] Kiselev, A. A. & Iafrate, G. J. Phonon dynamics and phonon assisted losses in Euler-Bernoulli nanobeams. *Phys. Rev. B* **77**, 205436 (2008).

[151] Wilson-Rae, I. Intrinsic dissipation in nanomechanical resonators due to phonon tunneling. *Phys. Rev. B* **77**, 245418 (2008).

[152] Radons, G., Rumpf, B. & Schuster, H. G. (eds.) *Nonlinear Dynamics of Nanosystems* (WILEY-VCH: Weinheim, 2010).

[153] Cross, M. C. & Lifshitz, R. Elastic wave transmission at an abrupt junction in a thin plate with application to heat transport and vibrations in mesoscopic systems. *Phys. Rev. B* **64**, 085324 (2001).

[154] Mattila, T., Kiihamäki, J., Lamminmäki, T., Jaakkola, O., Rantakari, P., Oja, A., Seppä, H., Kattelus, H. & Tittonen, I. A 12 MHz micromechanical bulk acoustic mode oscillator. *Sens. Act. A: Phys.* **101**, 1–9 (2002).

[155] Park, Y.-H. & Park, K. High-fidelity modeling of MEMS resonators. Part I. Anchor loss mechanisms through substrate. *J. Microelectrom. Syst.* **13**, 238–247 (2004).

[156] Huang, X. M. H., Feng, X. L., Zorman, C. A., Mehregany, M. & Roukes, M. L. VHF, UHF and microwave frequency nanomechanical resonators. *N. J. Phys.* **7**, 247–247 (2005).

[157] Imboden, M., Mohanty, P., Gaidarzhy, A., Rankin, J. & Sheldon, B. W. Scaling of dissipation in megahertz-range micromechanical diamond oscillators. *Appl. Phys. Lett.* **90**, 173502–3 (2007).

[158] Eichenfield, M., Chan, J., Safavi-Naeini, A. H., Vahala, K. J. & Painter, O. Modeling dispersive coupling and losses of localized optical andmechanical modes in optomechanicalcrystals. *Opt. Express* **17**, 20078–20098 (2009).

[159] Suhel, A., Hauer, B. D., Biswas, T. S., Beach, K. S. D. & Davis, J. P. Dissipation mechanisms in thermomechanically driven silicon nitride nanostrings. *Appl. Phys. Lett.* **100**, 173111–5 (2012).

[160] Wang, K., Wong, A.-C. & Nguyen, C.-C. VHF free-free beam high-Q micromechanical resonators. *J. Microelectrom. Syst.* **9**, 347–360 (2000).

[161] Hutchinson, A. B., Truitt, P. A., Schwab, K. C., Sekaric, L., Parpia, J. M., Craighead, H. G. & Butler, J. E. Dissipation in nanocrystalline-diamond nanomechanical resonators. *Appl. Phys. Lett.* **84**, 972–974 (2004).

[162] Seoánez, C., Guinea, F. & Castro Neto, A. H. Surface dissipation in nanoelectromechanical systems: Unified description with the standard tunneling model and effects of metallic electrodes. *Phys. Rev. B* **77**, 125107 (2008).

[163] Imboden, M. & Mohanty, P. Evidence of universality in the dynamical response of micromechanical diamond resonators at millikelvin temperatures. *Phys. Rev. B* **79**, 125424–5 (2009).

[164] Venkatesan, A., Lulla, K. J., Patton, M. J., Armour, A. D., Mellor, C. J. & Owers-Bradley, J. R. Dissipation due to tunneling two-level systems in gold nanomechanical resonators. *Phys. Rev. B* **81**, 073410 (2010).

[165] Hoehne, F., Pashkin, Y. A., Astafiev, O., Faoro, L., Ioffe, L. B., Nakamura, Y. & Tsai, J. S. Damping in high-frequency metallic nanomechanical resonators. *Phys. Rev. B* **81**, 184112 (2010).

[166] Sulkko, J., Sillanpää, M. A., Häkkinen, P., Lechner, L., Helle, M., Fefferman, A., Parpia, J. & Hakonen, P. J. Strong Gate Coupling of High-Q Nanomechanical Resonators. *Nano Lett.* **10**, 4884–4889 (2010).

[167] Kozinsky, I., Postma, H. W. C., Bargatin, I. & Roukes, M. L. Tuning nonlinearity, dynamic range, and frequency of nanomechanical resonators. *Appl. Phys. Lett.* **88**, 253101–3 (2006).

[168] Kozinsky, I., Postma, H. W. C., Kogan, O., Husain, A. & Roukes, M. L. Basins of Attraction of a Nonlinear Nanomechanical Resonator. *Phys. Rev. Lett.* **99**, 207201 (2007).

[169] Karabalin, R. B., Matheny, M. H., Feng, X. L., Defay, E., Le Rhun, G., Marcoux, C., Hentz, S., Andreucci, P. & Roukes, M. L. Piezoelectric nanoelectromechanical resonators based on aluminum nitride thin films. *Appl. Phys. Lett.* **95**, 103111–3 (2009).

[170] Unterreithmeier, Q. P., Manus, S. & Kotthaus, J. P. Coherent detection of nonlinear nanomechanical motion using a stroboscopic downconversion technique. *Appl. Phys. Lett.* **94**, 263104–3 (2009).

[171] Juillard, J., Bonnoit, A., Avignon, E., Hentz, S. & Colinet, E. Large amplitude dynamics of micro-/nanomechanical resonators actuated with electrostatic pulses. *J. Appl. Phys.* **107**, 014907–10 (2010).

[172] Jun, S. C., Moon, S., Kim, W., Cho, J. H., Kang, J. Y., Jung, Y., Yoon, H., Shin, J., Song, I., Choi, J., Choi, J. H., Bae, M. J., Han, I. T., Lee, S. & Kim, J. M. Nonlinear characteristics in radio frequency nanoelectromechanical resonators. *N. J. Phys.* **12**, 043023 (2010).

[173] Unterreithmeier, Q. P., Faust, T. & Kotthaus, J. P. Nonlinear switching dynamics in a nanomechanical resonator. *Phys. Rev. B* **81**, 241405 (2010).

[174] Ilic, B., Krylov, S. & Craighead, H. G. Theoretical and experimental investigation of optically driven nanoelectromechanical oscillators. *J. Appl. Phys.* **107**, 034311–13 (2010).

[175] Fong, K. Y., Pernice, W. H. P. & Tang, H. X. Frequency and phase noise of ultrahigh Q silicon nitride nanomechanical resonators. *Phys. Rev. B* **85**, 161410 (2012).

[176] Verbridge, S. S., Parpia, J. M., Reichenbach, R. B., Bellan, L. M. & Craighead, H. G. High quality factor resonance at room temperature with nanostrings under high tensile stress. *J. Appl. Phys.* **99**, 124304–8 (2006).

[177] Southworth, D. R., Barton, R. A., Verbridge, S. S., Ilic, B., Fefferman, A. D., Craighead, H. G. & Parpia, J. M. Stress and Silicon Nitride: A Crack in the Universal Dissipation of Glasses. *Phys. Rev. Lett.* **102**, 225503 (2009).

[178] Unterreithmeier, Q. P., Faust, T. & Kotthaus, J. P. Damping of Nanomechanical Resonators. *Phys. Rev. Lett.* **105**, 027205 (2010).

[179] Karabalin, R. B., Cross, M. C. & Roukes, M. L. Nonlinear dynamics and chaos in two coupled nanomechanical resonators. *Phys. Rev. B* **79**, 165309–5 (2009).

[180] Almog, R., Zaitsev, S., Shtempluck, O. & Buks, E. Noise Squeezing in a Nanomechanical Duffing Resonator. *Phys. Rev. Lett.* **98**, 078103 (2007).

[181] Szorkovszky, A., Doherty, A. C., Harris, G. I. & Bowen, W. P. Mechanical Squeezing via Parametric Amplification and Weak Measurement. *Phys. Rev. Lett.* **107**, 213603 (2011).

[182] Faust, T., Rieger, J., Seitner, M. J., Krenn, P., Kotthaus, J. P. & Weig, E. M. Nonadiabatic Dynamics of Two Strongly Coupled Nanomechanical Resonator Modes. *Phys. Rev. Lett.* **109**, 037205 (2012).

[183] Westra, H. J. R., Karabacak, D. M., Brongersma, S. H., Crego-Calama, M., van der Zant, H. S. J. & Venstra, W. J. Interactions between directly- and parametrically-driven vibration modes in a micromechanical resonator. *Phys. Rev. B* **84**, 134305 (2011).

[184] Arcizet, O., Jacques, V., Siria, A., Poncharal, P., Vincent, P. & Seidelin, S. A single nitrogen-vacancy defect coupled to a nanomechanical oscillator. *Nat. Phys.* **7**, 879–883 (2011).

[185] Bargatin, I. & Roukes, M. L. Nanomechanical Analog of a Laser: Amplification of Mechanical Oscillations by Stimulated Zeeman Transitions. *Phys. Rev. Lett.* **91**, 138302 (2003).

[186] Mahboob, I. & Yamaguchi, H. Bit storage and bit flip operations in an electromechanical oscillator. *Nat. Nano* **3**, 275–279 (2008).

[187] Bagheri, M., Poot, M., Li, M., Pernice, W. P. H. & Tang, H. X. Dynamic manipulation of nanomechanical resonators in the high-amplitude regime and non-volatile mechanical memory operation. *Nat. Nano* **6**, 726–732 (2011).

[188] Larsen, T., Schmid, S., Grönberg, L., Niskanen, A., Hassel, J., Dohn, S. & A., B. Ultrasensitive string-based temperature sensors. *Appl. Phys. Lett.* **98**, 121901 (2011).

[189] Defoort, M., Lulla, K., Heron, J.-S., Bourgeois, O., Collin, E. & Pistolesi, F. Audio mixing in a tri-port nano-electro-mechanical device. *Appl. Phys. Lett.* **99**, 233107–3 (2011).

[190] Feng, X. L., White, C. J., Hajimiri, A. & Roukes, M. L. A self-sustaining ultrahigh-frequency nanoelectromechanical oscillator. *Nat. Nano* **3**, 342–346 (2008).

[191] Naik, A. K., Hanay, M. S., Hiebert, W. K., Feng, X. L. & Roukes, M. L. Towards single-molecule nanomechanical mass spectrometry. *Nat. Nano* **4**, 445–450 (2009).

[192] Chaste, J., Eichler, A., Moser, J., Ceballos, G., Rurali, R. & Bachtold, A. A nanomechanical mass sensor with yoctogram resolution. *Nat. Nanotech.* **7**, 301–304 (2012).

[193] Hanay, M. S., Kelber, S., Naik, A. K., Chi, D., Hentz, S., Bullard, C. E., Colinet, E., Duraffourg, L. & Roukes, M. L. Single-protein nanomechanical mass spectrometry in real time. *Nat. Nano* **7**, 602–608 (2012).

[194] Masmanidis, S. C., Tang, H. X., Myers, E. B., Li, M., De Greve, K., Vermeulen, G., VanÂ Roy, W. & Roukes, M. L. Nanomechanical Measurement of Magnetostriction and Magnetic Anisotropy in (Ga,Mn)As. *Phys. Rev. Lett.* **95**, 187206 (2005).

[195] Zolfagharkhani, G., Gaidarzhy, A., Degiovanni, P., Kettemann, S., Fulde, P. & Mohanty, P. Nanomechanical detection of itinerant electron spin flip. *Nat. Nano* **3**, 720–723 (2008).

[196] Huber, F., Lang, H. P., Backmann, N., Rimoldi, D. & Gerber, C. Direct detection of a BRAF mutation in total RNA from melanoma cells using cantilever arrays. *Nat. Nano* **8**, 125–129 (2013).

[197] Uhlig, K. $_3$He/$_4$He dilution refrigerator with pulse-tube refrigerator precooling. *Cryogenics* **42**, 73–77 (2002).

[198] Law, C. K. Interaction between a moving mirror and radiation pressure: A Hamiltonian formulation. *Phys. Rev. A* **51**, 2537–2541 (1995).

[199] Pozar, D. M. *Microwave engeneering* (John Wiley & Sons: New York, 1998), 2 edn.

[200] Day, P. K., LeDuc, H. G., Mazin, B. A., Vayonakis, A. & Zmuidzinas, J. A broadband superconducting detector suitable for use in large arrays. *Nature* **425**, 817–821 (2003).

[201] Zhou, X. *Superconducting cavity nanoelectromechanics*. Ph.D. thesis, École Polytechnique Fédérale de Lausanne (2013).

[202] Hertzberg, J. B. *Back-action evading measurements of nanomechanical motion approaching quantum limits*. Ph.D. thesis, University of Maryland (2009).

[203] Williams, K., Gupta, K. & Wasilik, M. Etch rates for micromachining processing-Part II. *J. Microelectromech. Syst.* **12**, 761–778 (2003).

[204] Barends, R., Baselmans, J., Hovenier, J., Gao, J., Yates, S., Klapwijk, T. & Hoevers, H. Niobium and Tantalum High Q Resonators for Photon Detectors. *IEEE Trans. Appl. Supercond* **17**, 263–266 (2007).

[205] Cicak, K., Li, D., Strong, J. A., Allman, M. S., Altomare, F., Sirois, A. J., Whittaker, J. D., Teufel, J. D. & Simmonds, R. W. Low-loss superconducting resonant circuits using vacuum-gap-based microwave components. *Appl. Phys. Lett.* **96**, 093502–3 (2010).

[206] Frunzio, L., Wallraff, A., Schuster, D., Majer, J. & Schoelkopf, R. Fabrication and characterization of superconducting circuit QED devices for quantum computation. *IEEE Trans. Appl. Supercond* **15**, 860–863 (2005).

[207] Megrant, A., Neill, C., Barends, R., Chiaro, B., Chen, Y., Feigl, L., Kelly, J., Lucero, E., Mariantoni, M., O'Malley, P. J. J., Sank, D., Vainsencher, A., Wenner, J., White, T. C., Yin, Y., Zhao, J., Palmstrom, C. J., Martinis, J. M. & Cleland, A. N. Planar superconducting resonators with internal quality factors above one million. *Appl. Phys. Lett.* **100**, 113510–4 (2012).

[208] Doyle, S., Naylon, J., Mauskopf, P., Porch, A. & Duncombe, C. Lumped Element Kinetic Inductance Detectors. *Internat. Space THz Techn. Conf. Proc.* 8 (2007).

[209] Niemczyk, T. *From strong to ultrastrong coupling in circuit QED architectures.* Ph.D. thesis, Technische Universität München (2011).

[210] Mazin, B. A. *Microwave Kinetic Inductance Detectors.* Ph.D. thesis, California Institute of Technology (2004).

[211] Timoshenko, S. *Vibration Problems In Engeneering* (D. Van Nostrand Company, Inc: New York, 2008).

[212] Sattler, K. D. (ed.). *Handbook Of Nanophysics: Functional Nanomaterials*, chap. 8 (CRC press: Boca Raton, 2011).

[213] Gad-el Hak, M. (ed.) *The MEMS Handbook* (CRC press: Boca Raton, 2002).

[214] Imamura, T., Ohara, S. & Hasuo, S. Bias-sputtered Nb for reliable wirings in Josephson circuits. *IEEE Trans. Magnet.* **27**, 3176–3179 (1991).

[215] Hunklinger, S. & Raychaudhuri, A. Chapter 3: Thermal and Elastic Anomalies in Glasses at Low Temperatures. In Brewer, D. (ed.) *Progress in Low Temperature Physics*, vol. 9, 265–344 (Elsevier, 1986).

[216] Phillips, W. A. Two-level states in glasses. *Rep. Prog. Phys.* **50**, 1657 (1987).

[217] Hunklinger, S., Arnold, W., Stein, S., Nava, R. & Dransfeld, K. Saturation of the ultrasonic absorption in vitreous silica at low temperatures. *Phys. Lett. A* **42**, 253–255 (1972).

[218] Jäckle, J. On the ultrasonic attenuation in glasses at low temperatures. *Z. Phys.* **257**, 212–223 (1972).

[219] Black, J. L. & Fulde, P. Influence of the Superconducting State upon the Low-Temperature Properties of Metallic Glasses. *Phys. Rev. Lett.* **43**, 453 (1979).

[220] König, R., Esquinazi, P. & Neppert, B. Tunneling systems in polycrystalline metals: Absence of electron-assisted relaxation. *Phys. Rev. B* **51**, 11424–11432 (1995).

[221] Fefferman, A. D., Pohl, R. O., Zehnder, A. T. & Parpia, J. M. Acoustic Properties of Amorphous Silica between 1 and 500 mK. *Phys. Rev. Lett.* **100**, 195501 (2008).

[222] Landau, L. D. & Lifshitz, E. M. *Theory of Elasticity* (Pergamon: London, 1959).

[223] Anetsberger, G., Rivière, R., Schliesser, A., Arcizet, O. & Kippenberg, T. J. Ultralow-dissipation optomechanical resonators on a chip. *Nat. Photon.* **2**, 627–633 (2008).

[224] Gao, J., Zmuidzinas, J., Mazin, B. A., LeDuc, H. G. & Day, P. K. Noise properties of superconducting coplanar waveguide microwave resonators. *Appl. Phys. Lett.* **90**, 102507–3 (2007).

[225] Simmonds, R. W., Lang, K. M., Hite, D. A., Nam, S., Pappas, D. P. & Martinis, J. M. Decoherence in Josephson Phase Qubits from Junction Resonators. *Phys. Rev. Lett.* **93**, 077003 (2004).

[226] Martinis, J. M., Cooper, K. B., McDermott, R., Steffen, M., Ansmann, M., Osborn, K. D., Cicak, K., Oh, S., Pappas, D. P., Simmonds, R. W. & Yu, C. C. Decoherence in Josephson Qubits from Dielectric Loss. *Phys. Rev. Lett.* **95**, 210503 (2005).

[227] Neeley, M., Ansmann, M., Bialczak, R. C., Hofheinz, M., Katz, N., Lucero, E., O'Connell, A., Wang, H., Cleland, A. N. & Martinis, J. M. Process tomography of quantum memory in a Josephson-phase qubit coupled to a two-level state. *Nat. Phys.* **4**, 523–526 (2008).

[228] Grabovskij, G. J., Bushev, P., Cole, J. H., Müller, C., Lisenfeld, J., Lukashenko, A. & Ustinov, A. V. Entangling microscopic defects via a macroscopic quantum shuttle. *N. J. Phys.* **13**, 063015 (2011).

[229] Nayfeh, A. N. & Mook, D. *Nonlinear Oscillations* (John Wiley & Sons: New York, 1979).

[230] Gorodetsky, M. L., Schliesser, A., Anetsberger, G., Deleglise, S. & Kippenberg, T. J. Determination of the vacuumoptomechanical coupling rate usingfrequency noise calibration. *Opt. Express* **18**, 23236–23246 (2010).

[231] Marquardt, F., Clerk, A. A. & Girvin, S. M. Quantum theory of optomechanical cooling. *J. Mod. Opt.* **55**, 3329–3338 (2008).

[232] Clerk, A. A., Devoret, M. H., Girvin, S. M., Marquardt, F. & Schoelkopf, R. J. Introduction to quantum noise, measurement, and amplification. *Rev. Mod. Phys.* **82**, 1155 (2010).

[233] Clerk, A. A., Marquardt, F. & Harris, J. G. E. Quantum Measurement of Phonon Shot Noise. *Phys. Rev. Lett.* **104**, 213603 (2010).

[234] Nunnenkamp, A., Børkje, K., Harris, J. G. E. & Girvin, S. M. Cooling and squeezing via quadratic optomechanical coupling. *Phys. Rev. A* **82**, 021806 (2010).

[235] Arcizet, O., Molinelli, C., Briant, T., Cohadon, P.-F., Heidmann, A., Mackowski, J.-M., Michel, C., Pinard, L., Francais, O. & Rousseau, L. Experimental optomechanics with silicon micromirrors. *N. J. Phys.* **10**, 125021 (2008).

[236] Anetsberger, G., Arcizet, O., Unterreithmeier, Q. P., Riviere, R., Schliesser, A., Weig, E. M., Kotthaus, J. P. & Kippenberg, T. J. Near-field cavity optomechanics with nanomechanical oscillators. *Nat. Phys.* **5**, 909–914 (2009).

[237] Corbitt, T., Wipf, C., Bodiya, T., Ottaway, D., Sigg, D., Smith, N., Whitcomb, S. & Mavalvala, N. Optical Dilution and Feedback Cooling of a Gram-Scale Oscillator to 6.9 mK. *Phys. Rev. Lett.* **99**, 160801 (2007).

[238] Lee, K. H., McRae, T. G., Harris, G. I., Knittel, J. & Bowen, W. P. Cooling and Control of a Cavity Optoelectromechanical System. *Phys. Rev. Lett.* **104**, 123604 (2010).

[239] Schliesser, A., Rivière, R., Anetsberger, G., Arcizet, O. & Kippenberg, T. J. Resolved-sideband cooling of a micromechanical oscillator. *Nat. Phys.* **4**, 415–419 (2008).

[240] Teufel, J. D., Harlow, J. W., Regal, C. A. & Lehnert, K. W. Dynamical Backaction of Microwave Fields on a Nanomechanical Oscillator. *Phys. Rev. Lett.* **101**, 197203 (2008).

[241] Purdy, T. P., Peterson, R. W. & Regal, C. A. Observation of Radiation Pressure Shot Noise on a Macroscopic Object. *Science* **339**, 801–804 (2013).

[242] Schliesser, A. *Cavity Optomechanics and Optical Frequency Comb Generation with Silica Whispering-Gallery-Mode Microresonators.* Ph.D. thesis, Ludwig–Maximilians–Universität München (2009).

[243] Haus, H. A. *Waves and fields in optoelectronics* (Prentice-Hall: Englewood Cliffs, New Jersey, 1984).

[244] Braginsky, V. & Khalili, F. Y. *Quantum Measurement* (Cambridge University Press: Cambridge, 1992).

[245] Giovannetti, V. & Vitali, D. Phase-noise measurement in a cavity with a movable mirror undergoing quantum Brownian motion. *Phys. Rev. A* **63**, 023812 (2001).

[246] Gardiner, C. W. & Zoller, P. *Quantum Noise* (Springer.Berlin, 2004).

[247] Mollow, B. R. & Glauber, R. J. Quantum Theory of Parametric Amplification. I. *Phys. Rev.* **160**, 1076–1096 (1967).

[248] Saulson, P. R. Thermal noise in mechanical experiments. *Phys. Rev. D* **42**, 2437–2445 (1990).

[249] Vogel, M., Mooser, C., Karrai, K. & Warburton, R. J. Optically tunable mechanics of microlevers. *Appl. Phys. Lett.* **83**, 1337–1339 (2003).

[250] Stenholm, S. The semiclassical theory of laser cooling. *Rev. Mod. Phys.* **58**, 699–739 (1986).

[251] Wineland, D. J. & Itano, W. M. Laser cooling of atoms. *Phys. Rev. A* **20**, 1521–1540 (1979).

[252] Diedrich, F., Bergquist, J. C., Itano, W. M. & Wineland, D. J. Laser Cooling to the Zero-Point Energy of Motion. *Phys. Rev. Lett.* **62**, 403 (1989).

[253] Castellanos-Beltran, M. A., Irwin, K. D., Hilton, G. C., Vale, L. R. & Lehnert, K. W. Amplification and squeezing of quantum noise with a tunable Josephson metamaterial. *Nat. Phys.* **4**, 929–931 (2008).

[254] Clerk, A. A., Marquardt, F. & Jacobs, K. Back-action evasion and squeezing of a mechanical resonator using a cavity detector. *N. J. Phys.* **10**, 095010 (2008).

[255] Hertzberg, J. B., Rocheleau, T., Ndukum, T., Savva, M., Clerk, A. A. & Schwab, K. C. Back-action-evading measurements of nanomechanical motion. *Nat. Phys.* **6**, 213–217 (2009).

[256] LaHaye, M. D., Buu, O., Camarota, B. & Schwab, K. C. Approaching the Quantum Limit of a Nanomechanical Resonator. *Science* **304**, 74–77 (2004).

[257] Naik, A., Buu, O., LaHaye, M. D., Armour, A. D., Clerk, A. A., Blencowe, M. P. & Schwab, K. C. Cooling a nanomechanical resonator with quantum back-action. *Nature* **443**, 193–196 (2006).

[258] Dick, G., Santiago, D. & Wang, R. Temperature-compensated sapphire resonator for ultra-stable oscillator capability at temperatures above 77 K. *IEEE Trans. Ultrason. Ferroel. Frequ. Cont.* **42**, 812–819 (1995).

[259] Fleischhauer, M., Imamoglu, A. & Marangos, J. P. Electromagnetically induced transparency: Optics in coherent media. *Rev. Mod. Phys.* **77**, 633–673 (2005).

[260] Metzger, C., Ludwig, M., Neuenhahn, C., Ortlieb, A., Favero, I., Karrai, K. & Marquardt, F. Self-Induced Oscillations in an Optomechanical System Driven by Bolometric Backaction. *Phys. Rev. Lett.* **101**, 133903 (2008).

[261] Metcalfe, M., Boaknin, E., Manucharyan, V., Vijay, R., Siddiqi, I., Rigetti, C., Frunzio, L., Schoelkopf, R. J. & Devoret, M. H. Measuring the decoherence of a quantronium qubit with the cavity bifurcation amplifier. *Phys. Rev. B* **76**, 174516 (2007).

[262] Boyd, R. W. & Gauthier, D. J. Controlling the Velocity of Light Pulses. *Science* **326**, 1074–1077 (2009).

[263] Phillips, D. F., Fleischhauer, A., Mair, A., Walsworth, R. L. & Lukin, M. D. Storage of Light in Atomic Vapor. *Phys. Rev. Lett.* **86**, 783 (2001).

[264] Milonni, P. W. *Fast Light, Slow Light and Left-Handed Light* (Institute of Physics Publishing Bristol and Philadelphia, 2005).

[265] Lenz, G., Eggleton, B., Madsen, C. & Slusher, R. Optical delay lines based on optical filters. *IEEE J. Quant. Electron.* **37**, 525–532 (2001).

[266] Yanik, M. F. & Fan, S. Stopping Light All Optically. *Phys. Rev. Lett.* **92**, 083901 (2004).

[267] Notomi, M., Kuramochi, E. & Tanabe, T. Large-scale arrays of ultrahigh-Q coupled nanocavities. *Nat. Photon.* **2**, 741–747 (2008).

[268] Houck, A. A., Schuster, D. I., Gambetta, J. M., Schreier, J. A., Johnson, B. R., Chow, J. M., Frunzio, L., Majer, J., Devoret, M. H., Girvin, S. M. & Schoelkopf, R. J. Generating single microwave photons in a circuit. *Nature* **449**, 328–331 (2007).

[269] Bergeal, N., Schackert, F., Metcalfe, M., Vijay, R., Manucharyan, V. E., Frunzio, L., Prober, D. E., Schoelkopf, R. J., Girvin, S. M. & Devoret, M. H. Phase-preserving amplification near the quantum limit with a Josephson ring modulator. *Nature* **465**, 64–68 (2010).

List of publications

- Rosenfeld, W., Hocke, F., Henkel, F., Krug, M., Volz, J., Weber, M. & Weinfurter, H. Towards long-distance atom-photon entanglement. *Phys. Rev. Lett.* **101**, 260403 (2008)

- Niemczyk, T., Deppe, F., Huebl, H., Menzel, E. P., Hocke, F., Schwarz, M. J., Garcia-Ripoll, J. J., Zueco, D., Hümmer, T., Solano, E., Marx, A. & Gross, R. Circuit quantum electrodynamics in the ultrastrong-coupling regime. *Nat. Phys.* **6**, 772-776 (2010)

- Niemczyk, T., Deppe, F., Menzel, E. P., Schwarz, M. J., Huebl, H., Häberlein, M., Hocke, F., Danner, M., Baust, A., Hoffmann, E., Garcia-Ripoll, J. J., Solano, E., Marx, A. & Gross, R. Selection rules in a strongly coupled qubit-resonator system. *arXiv:1107.0810*

- Hocke, F., Zhou, X., Schliesser, A., Kippenberg, T. J., Huebl, H. & Gross, R. Electromechanically induced absorption in a circuit nano-electromechanical system. *N. J. Phys.* **14**, 123037 (2012)

- Zhou, X., Hocke, F., Schliesser, A., Marx, A., Huebl, H., Gross, R. & Kippenberg, T. J. Slowing, advancing and switching of microwave signals using circuit nanoelectromechanics. *Nat. Phys.* **9**, 179-184 (2013)

- Huebl, H., Zollitsch, C., Lotze, J., Hocke, F., Greifenstein, M., Marx, A., Gross, R. & Goennenwein S. T. B. High cooperativity in coupled microwave resonator ferrimagnetic insulator hybrids. *arXiv:1207.6039*

Danksagung

Eine Menge Menschen haben zum Entstehen dieser Arbeit auf ganz verschiedene Art und Weise beigetragen. Im Folgenden möchte ich ihnen danken:

Bei Rudolf Gross dafür, dass er mir ermöglicht hat dieses Projekt am WMI zu verfolgen. Seine Art, den Mitarbeiter*innen freie Hand in der Umsetzung ihrer Arbeit zu lassen und gleichzeitig bei Problemen immer ein offenes Ohr zu haben, trägt entscheidend zu der guten Atmosphäre am WMI bei.

Bei Hans Huebl, der mich und dieses Projekt sehr engagiert betreut für das Vertrauen und die Zeit, die er in mich investiert hat. Von seiner Herangehensweise an Fragestellungen und von seinem breiten Fachwissen habe ich stets profitiert und viel lernen können.

Bei Tomasz Niemczyk, der mich am Anfang mit viel Detailwissen, (schlechtem) Humor und komisch riechender Suppe in die meisten Geräte und die Qubit und Mikrowellen-Resonator Herstellung eingearbeitet hat.

Bei Achim Marx, der gerade am Anfang meiner Arbeit viel Zeit und Geduld in mich investiert hat und mir sowohl viel über die Welt der Qubits als auch über die Messapparaturen beigebracht hat.

Bei Tobias Kippenberg (EPFL Lauseanne), der zusammen mit Rudolf Gross dieses Projekt als Kollaboration ins Leben gerufen hat. Aus den Diskussionen mit ihm habe ich viel gelernt.

Bei Xiaoqing Zhou (EPFL Lauseanne) für die Probe und ihren großen Beitrag zum Gelingen dieses Projekts. Ohne die exzellente Arbeitsteilung wäre es schwierig gewesen solche Ergebnisse zu erzielen.

Bei Albert Schliesser (EPFL Lauseanne) für seinen Beitrag bei der Konzeption und Auswertung der Experimente. Es war inspirierend an seinem Wissen über Optomechanik teilhaben zu dürfen.

Bei Stefan Weis (EPFL Lauseanne), mit dem ich zu Beginn der Kollaboration an der Probenproduktion gefeilt habe.

Bei Matthias Pernpeintner für die engagierte Weiterführung der Elektromechanik am WMI. Seine Motivation und Zielstrebigkeit wird mit Sicherheit zu vielen interessanten Ergebnissen führen.

Bei meinem ehemaligen Diplomanden und jetztigem Kollegen Christoph Zollitsch. Durch seine motivierte Arbeitsweise und lustige Art hat es immer Spaß gemacht mit ihm